Light management

in thin-film silicon solar cells

O. Isabella

Light management

in thin-film silicon solar cells

Proefschrift

ter verkrijging van de graad van doctor
aan de Technische Universiteit Delft,
op gezag van de Rector Magnificus prof. ir. K. C. A. M. Luyben,
voorzitter van het College voor Promoties,
in het openbaar te verdedigen op maandag 28 januari 2013 om 10:00 uur
door

Olindo ISABELLA

Master of Science, University of Naples Federico II
geboren te Naples, Italië

Dit proefschrift is goedgekeurd door de promotoren:
Prof. dr. ir. M. Zeman

Samenstelling promotiecommissie:

Rector Magnificus	voorzitter
Prof. dr. ir. M. Zeman	Technische Universiteit Delft, promotor
Prof. dr. P. M. Sarro	Technische Universiteit Delft
Prof. dr. B. Rech	Technische Universität Berlin
Prof. dr. C. Ballif	École Polytechnique Fédérale de Lausanne, PVLAB
Prof. dr. R. E. I. Schropp	Technische Universiteit Eindhoven
Dr. A. H. M. Smets	Technische Universiteit Delft
Dr. J. Krč	University of Ljubljana
Prof. ir. L. van der Sluis	Technische Universiteit Delft (reservelid)

Alla mia dolce Joëlle
e ai miei gentitori
per essere fonte continua
di amore e sostegno.

Alea iacta est

Gaius Julius Caesar

Contents

Chapter 1

Introduction

In this chapter the photovoltaic research will be framed in a general context. Milestones in photovoltaics and modern solar cells technologies will be reviewed. Analyzing the production capacity and the availability of raw materials, thin-film silicon solar cells technology will be introduced. Opto-electronic properties of hydrogenated amorphous silicon and the concept of *optically thick* and *electrically thin* absorber layers will be addressed. The structure of basic devices and standard conditions for their characterization will be described, motivating the importance of light management techniques. Finally, the outline of this doctoral thesis and a summary of the contributions to the field will be given.

1.1   Photovoltaic potential

Studies on renewable energies and their applications in modern life play an essential role in the sustainable development of environment, economy, and society [1]. During past 2010, the average daily global energy consumption was over 400 Terawatt-hour [2, 3], mostly achieved burning fossil fuels which increase pollution to troublesome levels [4, 5]. Entering the declining phase of fossil fuels age [6], sustainable methods of energy production must be found. Such methods must deliver, in mid and long term, high conversion efficiency, low pollution impact, reliability, and scalability for meeting Mankinds energy demands, especially those of countries with fast growing economies [7]. Solar, geothermal, ocean, wind, hydro power and biomass are renewable energies that may fit this scenario. As reported in Fig. 1.1, solar energy alone possesses the potential of becoming the actual successor of fossil fuels [2], fulfilling the energetic needs of every country. Nowadays operating a photovoltaic (PV) system costs less or the same as other renewables thanks to restless research aimed to increase the conversion efficiencies and lower the production costs. Furthermore, this energy source is abundant and ubiquitous. The deployment of solar energy is also expected to give political stability to many areas of the planet because of more balanced distribution of a primary source of energy.

Solar energy can be transformed into electricity either thermodynamically [8] or electronically. The first method is indirect since the solar thermal energy, focused in specially designed optical collectors, is used in steam turbines or other heat engines to produce electricity (thermo-solar power systems). The second method instead converts directly the so-
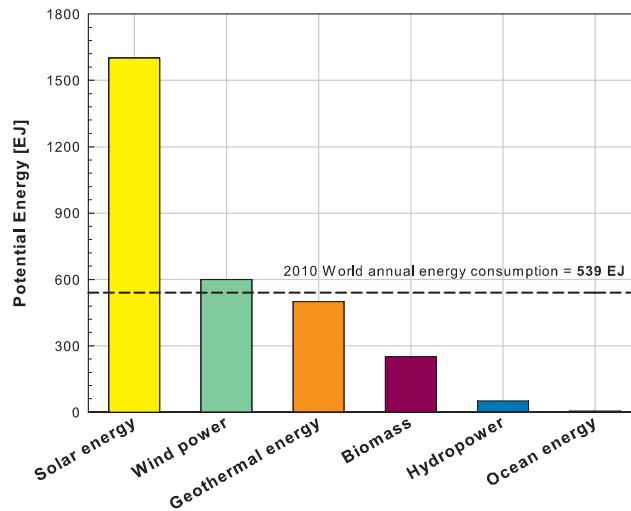
Figure 1.1: Potential energy production per year of various types of renewable energies.
The horizontal line indicates the world energy consumption in 2010. One exa-
joule (EJ = 10^{18} J) is equivalent to the amount of energy released by burning
roughly 2.4 millions of tons of crude oil.

lar energy into electricity by opto-electronic devices, called solar cells. Particularly, after
decades of research beginning with the first solar battery developed at Bell Labs [9], ef-
ficient production of electricity by means of solar cells is nowadays available. Although
photovoltaic technologies might be applied anywhere needed, it is remarkable that solar
panels with power conversion efficiency as low as 8% covering the area indicated by the six
spots in Fig. 1.2 could deliver enough electricity to power the planetary needs.

Moreover, PV conversion has already reached grid parity[1] in Australia [10] and is close
to it in Europe and in most of the United States with parity achievable already in 2013
[11, 12]. As terms of comparison, thermo-solar power systems are likely to reach the grid
parity within 2015 [13], whilst wind energy not before 2025 [14].

1.2   Milestones in photovoltaics

The photovoltaic effect - generation of a difference of potential at the junction between two
different materials under illumination - was discovered in 1839 by the physicist Alexandre-
Edmond Becquerel [16]. His experiment consisted in immersing platinum or silver elec-
trodes coated with light sensitive material (AgCl or AgBr) in an acidic solution and ap-
plying different types of illumination (sunlight, blue or ultraviolet) (see Fig. 1.3). In this
way the generation of electricity by means of the photovoltaic effect could be demonstrated.
After that, many other experiments were set-up, involving solid equipments and copper or
selenium as main photosensitive materials [17–21]. In the 1930s and 1940s a number of

---

[1]Grid parity is the ratio price to power at which energy produced with renewable means is cheaper than the
energy supplied by the grid. Standard grid parity target is 1 $ / Wp, where Wp, watt-peak, is the nominal power of
a solar device measured under standard illumination conditions.
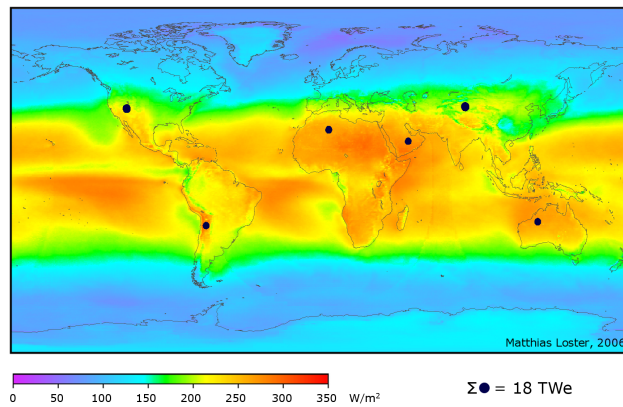
Figure 1.2: Total primary power density supply from sunlight. The colours show a three-year average of solar irradiance, including nights and cloud coverage [15]. TWe is Terawatt electrical power.
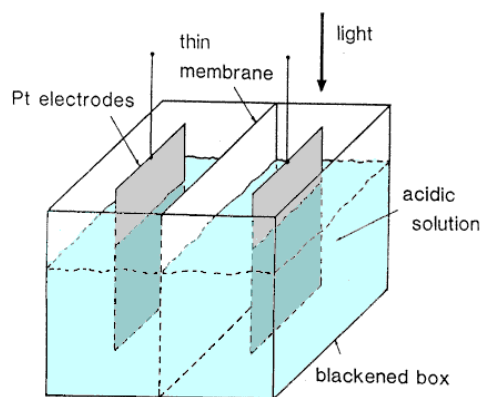
Figure 1.3: Schematic of the early solar device by Alexandre-Edmond Becquerel.

patents were filed to protect ideas on how to realize photovoltaic devices. However, it was only with the adaptation of the Czochralski process [22] for obtaining crystalline wafers of germanium or silicon by Teal and Little [23] in 1948 that the modern photovoltaic era began.

Thanks to the experience gained from early stages of microelectronics, such as wafer handling, doping and contacting, Chapin, Fuller, and Pearson from Bell Labs disclosed in 1954 the first *p-n* homojunction silicon-based solar cell [24]. The same year, Reynolds et al. presented the first heterojunction photovoltaic device based on CdS [25]. With conversion efficiencies constantly increasing from the initial 6% reported, theoretical studies were soon available on establishing the upper limit of the efficiency in *p-n* homojunction solar cells. Through a detailed argumentation, Shockley and Queisser demonstrated in 1961 that an efficiency as high as 30% could be achieved for an absorber material with a band gap of 1.1 *eV*. Such result was however carried out by considering strong ideal hypotheses:

(i) the incoming sunlight was assumed to be a blackbody radiation at 6000 K, (ii) the cell was kept at 300 K, and (iii) the only recombination mechanism of hole-electron pairs was considered radiative [26]. In 1970 Zhores Alferovs team created the first highly effective GaAs heterostructure solar cell for space applications [27, 28]. On the other hand, with explicit terrestrial application intents, Carlson and Wronski of RCA Laboratories reported in 1976 the first hydrogenated amorphous silicon (a-Si:H) based solar cell, having a conversion efficiency of 2.4% [29], after that Spear and Le Comber demonstrated the possibility to dope such material in 1975 [30]. The 1980s opened a new season in photovoltaic technologies: the concept of tandem solar cells, novel ternary and quaternary compounds, and wafer passivation were introduced to further increase the conversion efficiency. De Vos extended the previous detailed balance limit of the efficiency by Shockley and Queisser for an infinite number of homojunctions stacked on top of each other, showing that such ideal device may convert 68% of unconcentrated light [31]. University of Delaware published a thin-film solar cell using Cu_2S/CdS technology showing 10% efficiency [32]. Greens team at University of New South Wales (UNSW) reported in 1985 a solar cell on silicon wafer breaking the barrier of 20% conversion efficiency, in which passivation and light management were indicated as performance drivers [33]. Coming to the 1990s, in parallel to the further development of state-of-the-art silicon wafer based solar cells, thin-film silicon technology also saw important enhancements. Guha from United Solar Ovonic [34], Yamamoto from Kaneka Corporation [35], and Meier from University of Neuchâtel [36] (nowadays part of École Polytechnique Fédérale de Lausanne, EPFL) presented various designs of tandem double and triple junction devices based on amorphous silicon, nano-crystalline silicon (nc-Si:H) and alloys, such as amorphous silicon-germanium (a-SiGe:H). Remaining in Switzerland at EPFL, in 1991 O'Regan and Grätzel invented the dye-sensitized solar cell (DSSC), which is a photoelectrochemical device intended for low cost production [37]. During 2000s, solar cell technologies have been greatly improved and most of them have become commercially available, contributing to the cumulative 40 GW worldwide installation capacity in 2010 [38]. With more than 2700 journal papers [39] and more than 2300 patents [40] related to photovoltaic technologies published in 2011 only, even in a period of global economic downturn, scientific research and smart industrialization have not lost the momentum in pursuing better performance at the lowest price.

1.3   Modern solar cells technologies

Nowadays, PV technologies are classified in four classes: first generation, second generation, high efficiency solar cells, and third generation. The record conversion efficiencies for the different technologies reported in this section are updated until August 2012.

The first generation comprises single junction solar cells based on mono-/multi-crystalline silicon or III-V alloys. Major examples on silicon are crystalline UNSW PERL (Passivated Emitter with Rear Locally diffused) cell (25.0%) [41], Panasonic HIT (Heterojunction with Intrinsic Thin layer) cell (23.9%) [42], or FhG-ISE multi-crystalline cell (20.4%) [43]. On the other hand, FhG-ISE crystalline GaAs (26.4%), Spire crystalline epitaxial InP (22.1%) [44], or Alta thin-film[2] GaAs (28.8%) [45] are notable examples of III-V cells.

---

[2]This device is mentioned among the first generation since it is fabricated by epitaxial lift-off on a re-usable GaAs substrate.

The second generation includes solar cells fabricated on rigid or flexible substrates. The main difference with respect to the previous class is the thickness of the absorber layers, which can be as much as two orders of magnitude thinner (from hundreds of microns to microns). Thin-film solar cells based on binary, ternary, and quaternary absorber compounds examples are CIGS (Copper-Indium-Gallium-Selenide) device from ZSW (20.4%) [46] or First Solar CdTe (Cadmium-Telluride) cell (17.3%) show at this moment the highest efficiency. As for the amorphous silicon cells, they are available in single (Oerlikon: 10.1% [47] or Kaneka Corporation: 10.1% [48]), double (Kaneka: 12.3% [49] or Oerlikon: 12.2% [50]), and triple (United Solar: 12.4% [51], LG Electronics: 13.4% [52]) junction configurations[3]. Closing the roundup on the second generation, dye-synthesized solar cell (Sharp: 10.9% [53]) and organic solar cell (Konarka: 8.3% [54]) constitute alternative technologies for low-cost solar energy production.

The high efficiency class regards those multi-junction and wafer-based solar devices designed to operate in space environment or under concentrated light, whereas the first two generations are aimed mainly for terrestrial applications and perform under unconcentrated light (i.e. 1 x Sun). Triple junctions devices from Solar Junction (lattice matched, 43.5%, 418 x Sun) [55] and from Spire (metamorphic[4], 42.3%, 406 x Sun) [56] are the latest record solar cells of this class. The so-called concentrated photovoltaic (CPV) is primarily based on the latter technologies.

The third generation of solar cells is expected to combine the best aspects of the first and second generation, i.e. high efficiency and low costs, respectively. To demonstrate efficiency higher than 30% with small usage of raw materials and cost effective production methods, a number of different approaches has been suggested, mainly based on the tuneability of the fluorescence inside the solar devices. Even though this generation is still in early stages, promising approaches like quantum dots [57], up-down converters [58–62], and plasmonic structures [63] are being investigated for an optimal absorption of the incoming light.

1.4 Production capacity

For large scale production, solar cells are usually arranged in rigid or flexible frames, called modules, for ease of mounting and meeting markets demands of high wattage. At present time, the PV market is dominated by first and second generation technologies, CPV occupies 0.1% of the total power installed worldwide in 2011, and other technologies are still too little or too expensive for a realistic market breakthrough in a near future.

The most successfully commercial solar cells in the first generation are those fabricated on mono- and multi-crystalline silicon wafers, as they offer a very interesting price/performance ratio that can be as low as the grid parity target of 1 $ / Wp. In the frame of an expected growth in cumulative production capacity of more than 200% by 2015, the production capacity of second generation solar cells will grow by $\sim$ 40% reaching 23 GW in 2015 (see Fig. 1.4).

---

[3]Reported efficiencies for single, double, and triple junction thin-film silicon solar cells are stabilized (see Sec. 1.5.

[4]Metamorphic, from metamorphism (i.e. change in form), refers to slight changes in the lattice constant of the triple junction layers with respect to the GaAs wafer substrate.
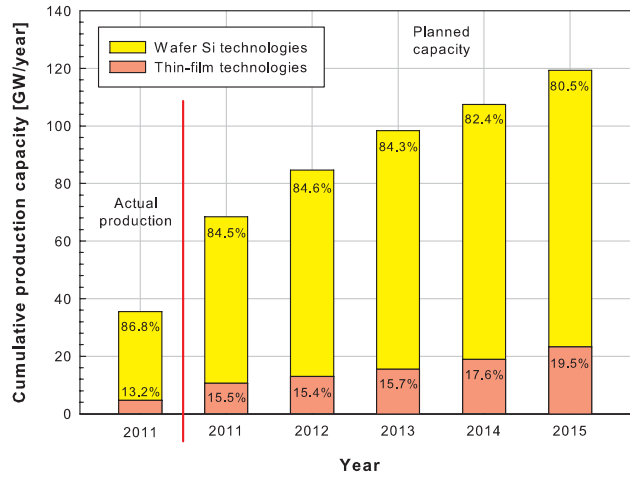
Figure 1.4: Production capacity in 2011 and planned until 2015 of the first and second technologies of solar cells. Reported percentages are market shares in 2011 and forecast until 2015 [64, 65].
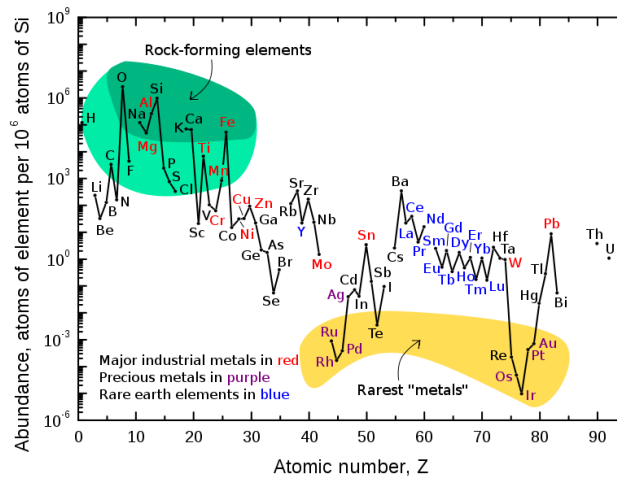
Figure 1.5: Abundance (atom fraction) of the chemical elements in Earths upper continental crust as a function of atomic number. Many of the elements are classified into (partially overlapping) categories: (1) rock-forming elements (major elements in green field and minor elements in light green field); (2) rare earth elements (lanthanides, LaLu, and Y; labeled in blue); (3) major industrial metals (global production $> \sim 3 \cdot 10^7$ kg/year; labeled in red); (4) precious metals (purple); and (5) the nine rarest metals the six platinum group elements plus Au, Re, and Te (a metalloid) (yellow field) (source [66]).

A large part of the second generation solar cells market share will be ascribed to thin-

film silicon, because of low fabrication temperatures and small usage of raw materials. As plasma-based techniques are mainly used to deposit the films forming the photovoltaic junction, large area deposition is enabled up to the so-called GEN8.5 size (2.2 *m* x 2.6 *m*), although the most successful market products are currently based on GEN5 size (1.1 *m* x 1.3 *m*). Another important aspect is the monolithic integration of a number of solar cells in series directly at production stage. These aspects contribute to lower the energy pay-back time[5], which is around one year for this technology [67]. In addition, the large availability of source materials (see Fig. 1.5) and no environmental hazards render this technology suitable for terawatt scale production. On the other hand, concerns on CI(G)S cells stability against moisture [68], risks related to safety and pollution because of cadmium [69], and scarcity of raw materials [70], if not tackled, will curb the widespread use of these other thin-film technologies [71].

1.5   Amorphous silicon

Silicon is the second most abundant natural element on Earth but is rarely found in its elemental form. Usually extracted from its oxides and silicate, it can be industrially prepared in crystalline or amorphous form. Crystalline silicon (c-Si) is an indirect semiconductor with band gap 1.12 *eV*. It is grown rod-shaped using Czochralski or Float Zone [72] methods and subsequently cut in circular or squared wafers of various dimensions and thicknesses for opto-electronic applications. On the other hand, the amorphous silicon is deposited in thin films using low-temperature large-area plasma-assisted methods where silane (SiH_4) or disilane (Si_2H_6) are major gas precursors.

Amorphous silicon (a-Si) differs from crystalline silicon for its disordered and porous lattice. Even though the tetravalency of the material is maintained, amorphous silicon lattice does not present the usual bond lengths and angles typical of crystalline silicon [73]. Furthermore, nano- and micro-voids can be present where some atoms share only three of the four outer-shell electrons causing disruptions in the lattice [74]. Such intrinsically occurring imperfections are efficient recombination centres and decrease the electron and hole diffusion length with respect to crystalline silicon. The situation is partially improved by the presence of hydrogen atoms during the deposition. This material is referred as hydrogenated amorphous silicon (a-Si:H). In particular, hydrogen atoms can share their electron with the silicon atoms, thus passivating the voids and reducing the amount of defects. Because of its amorphous nature, a-Si:H material behaves similarly to a direct semiconductor and can exhibit band gap varying between 1.7 *eV* and 1.9 *eV*, depending on deposition conditions. However, diluting silane or disilane with increasing flows of hydrogen and spanning regimes of high pressure and high power result in the formation of a crystalline phase within the amorphous tissue. Such kind of material is called hydrogenated nano-crystalline silicon (nc-Si:H) and exhibits a band gap close to that of crystalline silicon.

Alloying a-Si:H with other chemical elements is relatively easy by using additional precursor gases. Amorphous silicon can be combined with materials like germanium [34], tin [75], oxygen [76], or carbon [77] to form semiconductors with quite different opto-electronic properties. All these alloys, presenting band gap values either above or below the

---

[5]The energy pay-back time is the time required for an energy conversion system or device to produce as much energy as is consumed for its production.
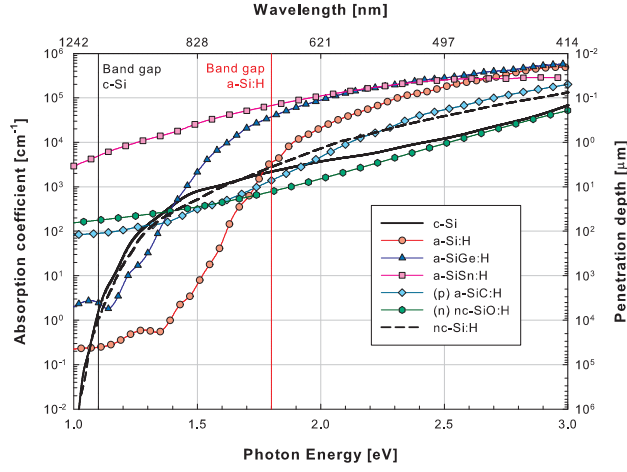
Figure 1.6: Absorption coefficient of c-Si, nc-Si:H, a-Si:H, and some of its alloys as function of energy (i.e. wavelength). On the secondary vertical axis, the penetration depth δ is also reported.

one of pure a-Si:H, can be profitably used in thin-film silicon multi-junction solar cells as absorber, window or intermediate layers.

Looking at the absorption coefficient[6] α of a-Si:H and some of its amorphous alloys in the range of the electromagnetic spectrum between 1 *eV* and 3 *eV*, it is evident the higher absorption with respect to the reference c-Si is due to the disorder in their atomic structures, aside from the case of n-type nc-SiO:H (see Fig. 1.6). This property allows making thinner solar devices, which is one key point for choosing to fabricate thin-film silicon solar cells. For example, in the visible wavelength range, an ideal single junction solar cell provided with a broad-band anti-reflective coating, perfect back reflector and a-Si:H absorber layer (band gap 1.8 *eV* and thickness 1 *μm*) would convert up to 87% of the usable energy, while, in the same wavelength range, a similar cell using c-Si absorber layer would convert only 61%. However, in the infrared wavelengths the penetration depth δ (secondary vertical axis in Fig. 1.6, δ = 1/α) becomes large for both a-Si:H and nc-Si:H, suggesting the usage of light management techniques to keep high the absorption of light in thin layers [78]. Furthermore, as anticipated in Sec. 1.2 and Sec. 1.3, the crossing points at which nc-Si:H absorbs more than a-Si:H ($h\nu \sim 1.75$ *eV*) and at which a-SiGe:H absorbs more than nc-Si:H ($h\nu \sim 1.45$ *eV*) indicate these three materials as perfect matches for double and triple junction thin-film silicon solar cells.

A crucial issue in amorphous silicon technology is the light induced degradation effect (LID) [79]. Discovered in 1980, it deals with the electronic degradation amorphous silicon undergoes after a long exposure to light. The decrease of dark- and photo-conductivity seems to be related to changes in defect density of the material. This effect is reversible, so that an a-Si:H layer annealed above 150 °C recovers its initial opto-electronic properties. The LID induces a relative 10-20% efficiency drop to a-Si:H based solar cells with respect

---

[6]Given a material with wavelength dependent complex refractive index $\tilde{n}(\lambda) = n(\lambda) + jk(\lambda)$, the absorption coefficient $\alpha(\lambda)$ is equal to $4\pi k/\lambda$.

to initial performance. Such effect saturates after around two months of light soaking. Al-though the LID is not completely understood yet, the research has recently shifted the focus from mid gap defect states reckoned too fast to contribute to LID to the defect states located closer to the valence/conduction band. Since these states are efficient hole recombination centers under illumination, minimizing their presence with tailored nanostructure engineer-ing is expected to greatly improve cell stability [80]. Recognized to be a bulk effect [81], the LID can be reduced by depositing thinner a-Si:H layers. On the other hand this strate-gy decreases the conversion efficiency of a-Si:H based solar devices since it leads to films exhibiting lower absorption. This issue kicks off the application of light trapping in a-Si:H pursuing the concept of *optically thick* and *electrically thin* absorber layers. As it will be described in the following chapter, light trapping is one of the light management techniques and it is the focal point of this doctoral thesis.

1.6   Thin-film silicon solar cells

The values of electronic properties such as diffusion length and mobility for both electrons and holes in a-Si:H are smaller than c-Si. As doped a-Si:H layers have two or three orders of magnitude more defect states than intrinsic layers, it becomes clear that *p-i-n* junction needs to be used rather than a conventional *p-n* junction for solar cells based on thin-film silicon technology. In the intrinsic absorber layer, sandwiched between doped layers which build up the high electric field across the junction, the photo-generated charge carriers are sepa-rated and pushed towards the relative terminals to be collected. For this reason solar cells fabricated with thin-film silicon technology are *drift* devices in contrast with c-Si *diffusion* devices.

The standard structure of thin-film silicon solar cells comprises in general four different types of materials. In the order of deposition on see-through glass carrier (from 0.6 to several mm): (i) front transparent conductive oxide (TCO) is the window and contact layer (from 0.6 to 2 μm) collecting holes, (ii) p-type, intrinsic, and n-type silicon-based layers form the *p-i-n* junction, (iii) back TCO acts as diffusion barrier layer (around 60-70 nm), and (iv) metal is the rear contact layer collecting electrons. The doped layers are usually one order of magnitude thinner than the absorber (from hundreds to thousands of nm). In such kind of device, the generation of charge carriers happens mainly in the front part and, because the hole diffusion length in a-Si:H is smaller than the electron counterpart, the deposition of the p-layer comes preferably first in the formation of the junction so that the holes move over a shorter distance to the electrode. At the rear side, the combination of back TCO and metal operates also as standard back reflector increasing the path of light and hence enhancing the absorption. However it is possible to couple a more conductive (usually thicker) back TCO and a dielectric back reflector to avoid the use of any metal. Bringing at least another type of material in thin-film silicon solar cells technology, this matter has not only economic relevance, but has also effect on the conversion efficiency, as it will be addressed in the next chapter.

The listed deposition sequence is known as *pin* or *superstrate* configuration. The major advantage of this sequence is the possibility to deposit excellent front TCO (highly transpar-ent and conductive) at temperatures as high as glass can withstand. However, since device quality intrinsic and doped silicon-based layers are usually deposited at temperatures below
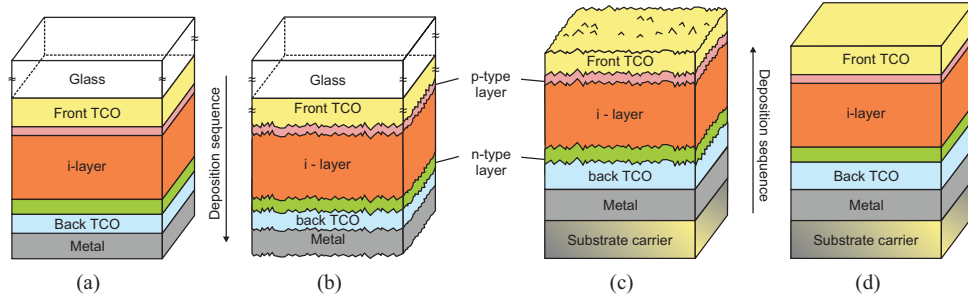
Figure 1.7: Schematic sketch of thin-film silicon solar cells in pin (a-b) and nip (c-d) configurations with flat (a-d) or rough (b-c) interfaces.

250 °C, the fabrication of thin-film silicon solar cells is also possible on flexible substrates, such as plastic foils or metallic laminates. In this case, the carrier substrates are not transparent anymore; therefore an inverted deposition sequence is applied to place the p-type layer anyway at the front side. This sequence is called *nip* or *substrate* configuration, where the n-type layer is deposited first on the back reflector before the other layers forming the junction. In Fig. 1.7 schematic sketches of both *pin* and *nip* sequenced thin-film silicon solar cells are reported. As it is possible to note, the interfaces between the layers may not be just flat. A random texturization is usually introduced at front TCO / p-layer interface for *pin* cells and at back TCO / n-layer interface for *nip* cells to scatter light in directions different than specular. In this way the path of light inside the i-layer (i.e. absorber layer) can be increased and absorption enhanced.

Next to standard single junction solar cells, more advanced structures have been developed to achieve higher conversion efficiency. Double or triple junction thin-film silicon solar cells in both *pin* [49, 50, 52] and *nip* [82, 83] configurations hold the efficiency records with this technology. The increased fabrication complexity is balanced by higher conversion efficiency, which is in turn given by higher voltage and better use of spectral irradiance. In the next chapter the multi-junction approach will be addressed as one of the light management techniques.

1.6.1   Spectral irradiance, *J-V* and *EQE*

The spectral irradiance of sunlight $P(\lambda)$ (spectral power density) provides the input power density used to calculate the conversion efficiency of a solar cell and the incident photon flux for correctly measuring its photo-generated current. Integrating $P(\lambda)$ over the wavelength range $[\lambda_1, \lambda_2]$ the input power density or irradiance is obtained[7]:

$$P_{IN} = \int_{\lambda_1}^{\lambda_2} P(\lambda)d\lambda = \left[\frac{W}{m^2}\right].\tag{1.1}$$

As any other type of solar device in unconcentrated regime of illumination, to qualify and quantify the performance of a thin-film silicon solar cell, the current density voltage (*J-V*) characteristic and the external quantum efficiency (*EQE*) are standardized and must meet

---

[7]In this thesis physical units are reported within square brakets "=[ ]".
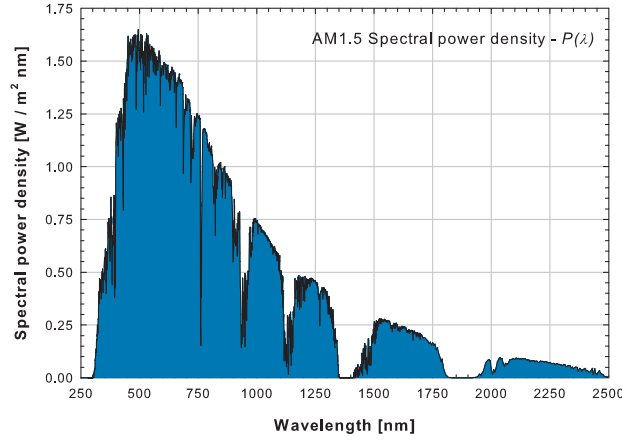
Figure 1.8: AM1.5 spectral power density, also known as spectral irradiance [84].

the following experimental conditions: (i) the spectral irradiance is relative to the AM1.5[8], (ii) the value of irradiance is 1000 W/m^2, and (iii) the measurements are carried out at 25 °C. In Fig. 1.8 the standard AM 1.5 spectral power density is shown.

The J-V characteristic describes the electrical behavior of the solar cell under illumination condition following the standard diode equation:

$$J(V) = J_0 \left[exp\left(\frac{qV}{i_f \cdot k_B \cdot T} \right) - 1 \right] - J_{PH} \Rightarrow \begin{cases} V = 0 \Leftrightarrow J_{SC} = -J_0 - J_{PH} \approx -J_{PH} \\ J = 0 \Leftrightarrow V_{OC} = \frac{i_f \cdot k_B \cdot T}{q} ln\left(\frac{J_{PH}}{J_0} + 1 \right) \end{cases} \quad (1.2)$$

where J_0 is the saturation current, q is the elementary charge, i_f is the ideality factor, k_B is Boltzmann constant, T is the absolute temperature, and J_{PH} is the photo-generated current density. In Fig. 1.9(a) especially three points are of interest: the open-circuit voltage (V_{OC}), the short-circuit current density (J_{SC}), and the maximum power point (*MPP*), obtained from the product of its voltage (V_{MPP}) and current density (J_{MPP}). With these points it is possible to calculate the conversion efficiency:

$$\eta = \frac{P_{OUT}}{P_{IN}} = \frac{MPP}{P_{IN}} = \frac{V_{MPP} \cdot J_{MPP}}{P_{IN}} = \frac{FF \cdot V_{OC} \cdot J_{SC}}{P_{IN}} \quad (1.3)$$

where P_{IN} is the aforementioned standard irradiance value, while FF is the fill-factor, which is a quantity linked to the recombination in the solar cell and is defined as the ratio between the areas A and B in Fig. 1.9(a). For calculating the conversion efficiency the assumption is made that the solar cell under test is working at the *MPP*, condition that in reality may not be met during daily operations but that can be reached using so-called power trackers. Such assumption is taken for granted in the rest of this work.

---

[8]The Air Mass (AM), defined as $1/cos(90° - \theta)$ with θ angle above the horizon, quantifies the reduction in the power of light as it passes through the atmosphere. AM1.5 is widely accepted standard for comparing solar systems ($\theta = 48.2°$).
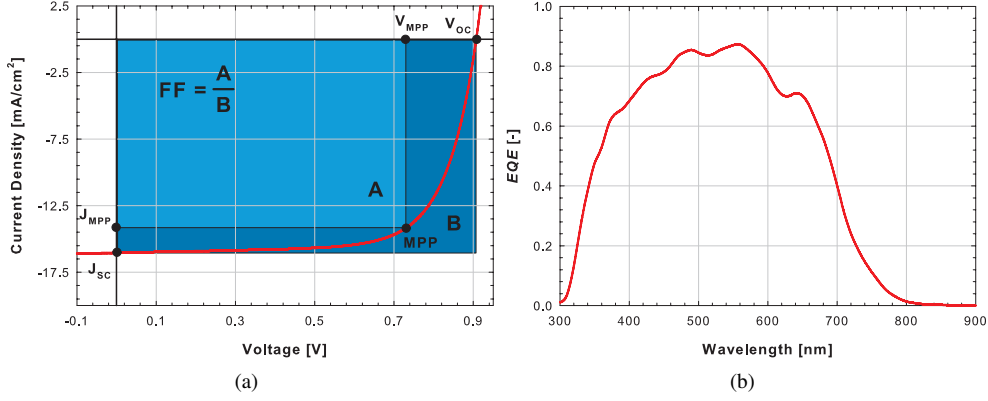
Figure 1.9: (a) J-V *curve and (b)* EQE *of a typical* pin *single junction thin-film silicon solar cell fabricated in PVMD group at Delft University of Technology.*

The *EQE* is a wavelength dependent quantity which measures the spectral sensitivity of a solar cell (spectral response $SR(\lambda)$ at $0\ V$ bias, see Fig. 1.9(b)). Reading the wavelength (i.e. the energy) at 50% of its maximal peak, it is possible to get a reasonable indication of the absorber layer band gap [85]. Given the incident photon flux $\Phi(\lambda)$ number of photons per unit time, per unit area, and per unit wavelength:

$$\Phi(\lambda) = \frac{\lambda \cdot P(\lambda)}{h \cdot c} = \left[\frac{photons}{s \cdot m^2 \cdot nm} \right] \qquad (1.4)$$

where h is the Planck constant and c is the speed of light, the *EQE* is defined as follows:

$$EQE(\lambda) = \frac{J_{PH}(\lambda)}{-q \cdot \Phi(\lambda)} \qquad (1.5)$$

that is nothing but else the ratio of the number of electrons per unit time, per unit area, and per unit wavelength over the incident photon flux. Rearranging Eq. 1.5 and integrating with respect to the wavelength range $[\lambda_{min}, \lambda_{max}]$ the total photo-generated current density in the device can be calculated:

$$J_{PH} = -q \int_{\lambda_{min}}^{\lambda_{max}} EQE(\lambda) \cdot \Phi(\lambda) \cdot d\lambda = \left[\frac{A}{m^2} \right]. \qquad (1.6)$$

Neglecting J_0, J_{PH} can be approximated to the J_{SC}. The *EQE* is therefore linked to both absorption of photons in the absorber layer and collection of electrons through the doped layers: an ideal device collecting all the electron-hole pairs generated by incoming photons at any wavelength would have an equally ideal *EQE* having constant value one (the so-called Shockley-Quessier limit [26]). Another way to look at the *EQE* is the proportionality to the absorptance in the absorber layer $A(\lambda)$:

$$EQE(\lambda) = \beta \cdot \gamma \cdot A(\lambda)_{|\beta=1, \gamma<1} \qquad (1.7)$$

where factors β and γ indicate, respectively, that each absorbed photon creates an electron-hole pair and the probability of created charge carries to be collected at the terminals. In reality β, also known as generation quantum efficiency, is always one, since no multiple generation is expected in a-Si:H, while γ is generally lower than one, as recombination and thermalization losses do occur even in device grade material. Finally, introducing the spectral generation $G(\lambda) = \beta \cdot \Phi(\lambda) \cdot A(\lambda)$, which represents the number of electron-hole pairs generated per unit time, per unit area, and per unit wavelength, the EQE can be equivalently expressed as follows:

$$EQE(\lambda) = \gamma \cdot \frac{G(\lambda)}{\Phi(\lambda)}. \qquad (1.8)$$

The spatial derivative of $G(\lambda)$, $g(r,\lambda)$, known as spectral generation rate, will be used in the next chapter as studying function for optical modeling.

The external parameters in Eq. 1.3 must be manipulated to increase the conversion efficiency. The application of light management techniques in thin-film silicon solar cells technology involves mainly actions on V_{OC} and J_{SC} with sometimes consequences for the fill-factor (see Sec. 2.3.1). In the next chapter such techniques will be analyzed before focusing mainly on J_{SC}. Light trapping has a direct impact on the spectral response and thus on the photo-generated current density, especially for wavelengths longer than green color. For this reason, Eq. 1.6 and Eq. 1.7 were intensively used for extracting J_{PH} and EQE from mono- and three-dimensional simulations or measurements carried out on fabricated samples. In the course of this thesis, even being aware of the aforementioned differences between $EQE(\lambda)$, $SR(\lambda)$ and $A(\lambda)$, when referring to optical simulations, external quantum efficiency, spectral response and absorptance will be considered synonyms.

1.7 Aim of this work

Together with efficient back reflector, the random texturization constitutes the basic light trapping scheme for fabricating highly efficient and extremely thin solar cells based on a-Si:H technology. The aim of this doctoral thesis is to investigate and optimize novel approaches of ligth trapping in thin-film silicon solar cells. In particular, (i) periodic diffraction gratings will be used as an alternative way to scatter light inside thin-film silicon solar cells; (ii) the typical random morphology of TCO layers will be superimposed to larger and deeper surface texturization fabricated on glass substrate introducing the concept of modulated surface textures (MST) for increased light scattering; (iii) mono-dimensional laminated structures will be used as dielectric distributed Bragg reflectors (DBR) forming, in combination with back TCO, efficient back reflectors; and (iv) optimal two-dimensional flattened periodic grating, also known as Flattened Light-Scattering Substrate (FLiSS), used as conductive back reflectors will be modeled for highly efficient single, double and triple junction *nip* thin-film silicon solar cells.

1.8 Outline of the thesis

Chapter 1 gives an overview and motivation of the thesis. **Chapter 2** is focused on light management. Motivations leading to the deployment of photonic techniques for increasing

current and voltage in thin-film silicon solar cells are analyzed. After looking at state-of-the-art light management approaches, advanced and novel techniques are presented and finally the main topics of this thesis are introduced. **Chapter 3** deals with the description of deposition machines, measurements setups, and computer simulators used to carry out the presented results. **Chapter 4** is about 1-D periodic diffraction gratings. After the morphological and optical analysis, the modelling of the optical behaviour is presented. 3-D simulations to find optimal combination between period and height for *pin* single junction devices are shown and the opto-electrical characterization of *pin* single junction devices are reported. **Chapter 5** shows the results on manipulation of surface textures. The concept of MST is first introduced with proof in Fourier domain. The analysis of in-house developed modulated textures follows with the practical demonstration of superposition from both morphological and optical point of view. Finally MST are applied in *pin* single and tandem solar cells. **Chapter 6** presents dielectric DBR. Properties and design rules are evaluated and fabrication of multi-layer stacks is reported together with their optical characterization and modelling. Single junction solar cells in *pin* and *nip* configuration on both flat and textured substrates are analyzed. **Chapter 7** describes the opto-electrical modelling of optimized FLiSS for *nip* single and multi-junction solar cells. After the optical study of different geometrical configurations with diverse constituting materials, the most promising design is embedded in complete solar cells showing a potential initial efficiency up to 16% for triple junction solar cells. **Chapter 8** reports the conclusions and puts forward future developments of the light management techniques presented throughout this thesis.

1.9   Novel contributions to the field

This doctoral thesis collects a series of results exploring novel light management techniques for application in thin-film silicon solar cells.

Regarding the studies conducted on 1-D periodic gratings, the application of Harvey-Shack scattering model served for the prediction of angular intensity distributions and haze parameters of 1-D gratings, while finite element method in its 3-D declination was used for the first time to study the optimal combination of geometrical parameters of 1-D gratings in *pin* thin-film silicon solar cells. Also the optimized deposition of solar devices on 1-D gratings demonstrated the possibility to use periodic textures in *pin* configuration.

The concept of surface modulation, allowing the fabrication of novel surface textures, was developed with the idea of enhancing the scattering at front TCO / p-layer interface. The optical efficiency of surface modulated textures was explained in terms of superposition of different scattering mechanisms ranging between the scalar scattering theory and Mie solution of Maxwell equations. The integration of surface modulated TCO in single and double junction *pin* solar cells was tested for the first time leading to state-of-the-art results.

The use of dielectric DBR was introduced and tested as alternative to metallic reflectors. Low temperature DBRs were successfully fabricated, optically measured, and modeled with computer software. Dielectric DBR were for the first time embedded in flat and textured thin-film silicon solar cells in both *pin* and *nip* configuration, showing opto-electonic behavior comparable to reference solar cells endowed with metallic back reflector thanks to a quasi omni-directional behavior of the DBR.

Finally, FLiSS was optimized for application in *nip* single and multi-junction solar cells.

The optimization was achieved by coupling 3-D optical simulations with 1-D electrical modeling. Results of the study showed the possibility to reach high initial efficiency. Because of FLiSS excellent scattering properties, very thin absorber layers could be used thus expecting also low degradation.

Chapter 2

Light management in thin-film silicon solar cells

A number of optical methods used in thin-film silicon solar cells to increase the conversion efficiency fall under the definition of *light management techniques.* In this chapter the motivation of their application in real devices will be clarified, state-of-the-art methods will be described and finally advanced and novel techniques will be introduced.

2.1 Introduction

The efficiency of thin-film silicon solar cells has to achieve a level of 20% on a laboratory scale in order to stay competitive with bulk crystalline silicon solar cells and other thin-film solar cell technologies, thus fitting the growth scenario discussed in the previous chapter. Controlling the way how the light is reflected, absorbed in the active layers and lost in supporting layers[1] is a strategic matter for improving the performance of thin-film silicon solar cells. This type of devices has absorber layers much thinner[2] than 1 μm, because a-Si:H suffers from a lack of absorption for wavelengths longer than 750 nm ($\sim$ 1.74 eV). For wavelengths longer than such threshold the absorption coefficient quickly decays, the penetration depth increases and the thin active layer becomes transparent. Therefore, the aim of the light management is the effective use of the energy of the solar radiation to maximize the absorption in the active layers and minimize the losses in supporting layers as well as the total reflectance of the device.

---

[1]Supporting layers are the films and substrates which do not contribute to the photo-current density of the solar cell. In thin-film silicon technology, glass and opaque substrates, TCOs, and doped layers can be so regarded. Their (eventual) intrinsic absorption is considered a loss, but their presence is seminal for the optical situation inside the absorber layer(s).

[2]If the thickness of a thin-film silicon single junction solar cell (excluding glass, $< 1.5 \ \mu m$) were comparable with the height of a man (factor scale: 1,200,000), a typical laboratory scale contact area of 4 x 4 mm^2 would have an area of 2160 soccer fields.

2.1.1 Optical limits

Light management involves actions on short-circuit current density and open-circuit voltage (see Sec. 2.3.1) of the solar device. Particularly, the increasing of absorptance in the absorber layers is a key issue for achieving high photo-current density and thus high efficiency. For solar cells the energy conservation can be written as follows:

$$R_{front}(\lambda) + \sum_{i=1}^{m} A_i(\lambda) + T_{back}(\lambda) = 1 \qquad (2.1)$$

where $R_{front}(\lambda)$ is the so-called primary reflectance, measured at the first interface air / device, $A_i(\lambda)$ is the absorptance of the $i-th$ layer constituting the device, and $T_{back}(\lambda)$ is the transmitted light at the rear side of the device, which is usually negligible especially in presence of a thick enough back reflector. Re-thinking the aim of light management in terms of energy conservation makes evident how actions taken in any part of the device (front side, rear side, and supporting layers) influence the absorptance in the absorber layer. Even with the application of light management techniques towards an ideal *EQE*, so-called optical limits set lower and upper bounds achievable for the absorptance in the absorber layer.

In 1982 Yablonovitch and Cody [86] calculated the upper limit for light intensity in a slab of dielectric material having refractive index n and sandwiched *in vacuo*. Using a statistical-mechanics approach, in the hypothesis of equilibrium and full randomization of light[3] inside the dielectric, the intensity of light within the slab was found to be n^2 times greater than the external blackbody radiation or $2n^2$ times greater in case of a white reflective plane placed at the opposite of the illumination side.

Soon after, such approach was applied on an ideal structure closer to a real solar cell to find an upper limit for light absorption [87]. From the irradiation side, such optical system is formed by air half-space, brushing a surface-textured morphology in the role of broadband perfect anti-reflective coating ($R_{front}(\lambda) = 0 \; \forall \lambda$), a dielectric slab with thickness d, and a perfect back reflector ($R_{front}(\lambda) = 1 \; \forall \lambda$). In the hypotheses of light randomization, small absorption ($\alpha d < 1$), and ideally diffused light scattering, the upper limit absorption probability (i.e. absorptance $A \in [0,1]$) can be expressed as follows:

$$A_{UL} = \frac{\alpha}{\alpha + \frac{1}{4n^2 d}} \qquad (2.2)$$

where the dependency of A_{UL}, α and n from wavelength is omitted for brevity. Eq. 2.2 effectively depicts the highest absorption achievable in a solar cell absorber layer since it neglects both primary reflection loss and parasitic losses. This is the so-called *classical Yablonovitch limit* or $4n_2$ *limit*.

In 1983, taking into account the total reflection loss and parasitic losses and considering the same aforementioned hypotheses, Deckman *et al.* proposed a more realistic ideal absorptance, A_D [88]. Using a geometric progression to deal with multiple internal reflections

---

[3]By definition, light is randomized in a dielectric slab when all correlation of the internal rays with the external angle of incidence is lost almost immediately on the rays' entering the medium and/or on their averaging over the illuminated surface [86].

Table 2.1: Hypotheses for the calculation of optical limits.

	R_{front}	R_{back}	A_{SL}	αd	**Light**	**Scattering**
A_{UL}	0	1	0	< 1	Randomized, many passes	Ideally diffused
A_D	> 0	< 1	> 0	< 1	Randomized, many passes	Ideally diffused
A_{LL}	0	1	0	< 1	Not randomized, two passes	No

and defining with A_{SL} the absorptance in the supporting layers[4], an enhancement factor (F^{enh}) for the absorber layer can be written, for example, with respect to the thin-film silicon solar cell structure reported in Fig. 1.7(a) (single junction flat *pin* thin film silicon solar cell):

$$F^{enh} = \frac{1 - A_{SL}e^{-2\alpha d} - (1 - A_{SL}e^{-4\alpha d})}{1 - (1 - A_{SL})e^{-4\alpha d} + (1 - A_{SL})n^{-2}e^{-4\alpha d}}. \tag{2.3}$$

F^{enh} must be scaled with some pre-factors in order to consider the primary reflectance at air / glass interface (R_{front}) and the losses in the front TCO ($A_{frontTCO}$) and in the p-type layer ($A_{p-layer}$), thus obtaining A_D:

$$A_D = (1 - R_{front})(1 - A_{fronTCO})(1 - A_{p-layer})F^{enh}. \tag{2.4}$$

This approach is more realistic than the previous since to calculate Eq. 2.3 and Eq. 2.4 one needs to measure independently the primary reflectance (air / glass interface in the reported case) and all the absorptances forming A_{SL}. This makes A_D conceptually very close to the measured EQE of a device fabricated with the same layers and materials [89].

A lower limit for the absorptance in the absorber layers can be written by considering the exponential absorption that light undergoes within two passes in a dielectric slab having thickness d:

$$A_{LL} = 1 - e^{-2\alpha d}. \tag{2.5}$$

To ensure the two passes for impinging light, R_{front} and R_{back} are here rigidly set to 0 and 1 $\forall \lambda$, respectively, but unlike the upper limit case no scattering is considered. The hypotheses needed to correctly calculate the optical limits are summed up in Tab. 2.1. From now on, unless explicitly stated, R_{front} and T_{back} will be simply named R and T.

Fig. 2.1(a) reports a comparison between the described optical limits and the $A_{i-layer}$ of a flat *pin* thin-film silicon solar cell. Such absorptance presents interference fringes that, due to the coherence of light in the absorber layer (here 300 *nm* thick), result in constructive and destructive peaks. Especially at wavelengths longer than 600 nm $A_{i-layer}$ is close to A_{LL} indicating that those photons bounce once on a flat device. On the other hand, for wavelengths shorter than 600 *nm* the lower limit overestimates the absorption, since it does not take into account neither primary reflectance nor parasitic absorptance. This is also the case of A_{UL}, which in turns stays higher than $A_{i-layer}$ for longer wavelengths thanks to the randomized and diffuse scattered light hypotheses. As anticipated, of the three discussed limits, A_D is the closest absorptance to the real device. A_D highlights what effectively the

---

[4]The absorptance in supporting layers is given by the sum of single layers absorptance:
$A_{SL} = A_{frontTCO} + A_{p-layer} + A_{n-layer} + A_{backTCO} + A_{Metal}.$
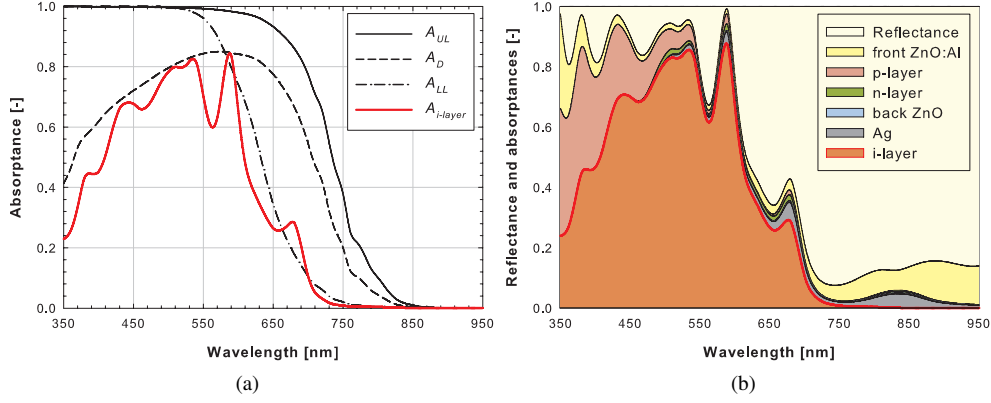
Figure 2.1: (a) Optical limits and i-layer absorptance and (b) reflectance and absorptances for a flat pin thin-film silicon solar cell.

device can gain from using light management techniques. Particularly, A_D envelops the short wavelength peaks while for longer wavelengths settles between upper and lower limits taking into account the randomization and scattering of light and the inclusion of absorptance in supporting layers.

Comparing Fig. 2.1(a) with 2.1(b) and using the concept of penetration depth, for which short wavelength photons are absorbed in the first few nanometers of the absorber layer while long wavelength photons are less efficiently absorbed, the higher absorptance of A_D with respect to $A_{i-layer}$ puts into evidence the strategic importance of (i) low absorption in supporting layers (primarily front TCO and p-layer), (ii) anti-reflective (AR) effect for light in-coupling and (iii) scattering effect for efficient absorption of short and long wavelengths.

2.2   Optical modelling and light management

The structure of present day thin-film silicon solar cells is really advanced. As a result of optical methods applied or number of optimized layers involved, solar cells complexity has significantly evolved from simple flat single junction to textured double or triple junction multi-layered stack with a great deal of optically active layers.

To exploit the potential of light management in the absorber layer(s) and locate where actual absorption losses take place, optical modelling has become extremely important. It is easy to guess that light management techniques influence the spectral generation rate, $g(r,\lambda)$, which is the number of electron-hole pairs generated at the point with coordinates $r = (x,y,z)$ per unit time, per unit volume, and per unit wavelength. Such quantity is directly proportional to the spectral absorption rate $a(r,\lambda)$ via the generation quantum efficiency β and the incident photon flux $\Phi(\lambda)$:

$$g(r,\lambda) = \beta \cdot \Phi(\lambda) \cdot a(r,\lambda) = \left[\frac{e-h}{s \cdot m^3 \cdot nm} \right]. \qquad (2.6)$$

Integrating the spectral absorption rate along a distance equal to single layer thickness, one gets the spectral generation $G(\lambda)$, introduced in Ch. 1:

$$G(\lambda) = \beta \cdot \Phi(\lambda) \cdot \int_0^d a(r,\lambda)dr = \beta \cdot \Phi(\lambda) \cdot A(\lambda) = \left[\frac{e-h}{s \cdot m^2 \cdot nm} \right]. \qquad (2.7)$$

On the other hand, integrating over the wavelength range, the optical generation rate $G_L(r)$ from the spatial absorption rate $A_L(r)$ can be obtained:

$$G_L(r) = \beta \cdot \int_{\lambda_{min}}^{\lambda_{max}} \Phi(\lambda) \cdot a(r,\lambda)d\lambda = \beta \cdot A_L(r) = \left[\frac{e-h}{s \cdot m^3} \right]. \qquad (2.8)$$
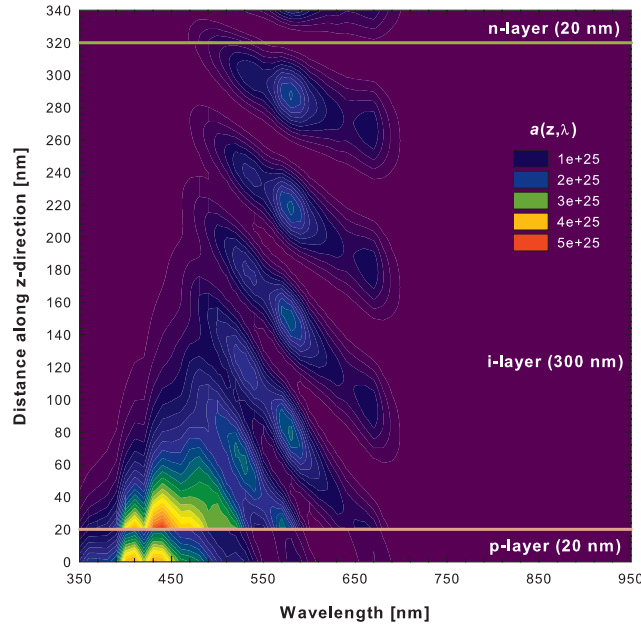
Figure 2.2: Spectral absorption rate $a(z,\lambda)$ in flat pin single junction thin-film silicon solar cell. Illumination side is the bottom of the plot, horizontal lines demarcate the p/i and i/n interfaces.

Considering again the single junction flat *pin* solar cell depicted in Fig. 1.7(a), both optical and electrical behaviour can be considered as a mono-dimensional problem along z-axis (growth direction). In Fig. 2.2 the spectral absorption rate reduced to only one dimension $a(z,\lambda)$ and zoomed on the *pin* junction is reported. As predicted by the increase of penetration depth for longer wavelength, the absorption is high in the first part of the i-layer then rapidly decreases with oscillations towards its rear side. The p-layer absorbs a lot in its entire thickness for wavelengths until 650 nm (see also Fig. 2.1(b)), while the n-layer, following the wavy pattern of the i-layer, absorbs (weakly) only between 500 nm and 700 nm. Finally, observing the alignment of local maxima and minima in the i-layer with respect to wavelength, it is possible to track noticeable peaks in Fig. 2.1(a), like those 530, 590, and 670 nm. In Fig. 2.3(a) a comparison between the incident photon flux and the

spectral generation in the i-layer is reported, clearly showing that the higher is $A_{i-layer}(\lambda)$, the closer is the number of generated electron-hole pairs to the incident number of photons. In Fig. 2.3(b) the optical generation rate, also reduced to the z-direction, is presented. In the p-layer the optical generation rate is higher than in the front side of the i-layer, suggesting once again the importance of researching low absorption window layers. In the i-layer, $G_L(z)$ exponentially decays from the high values of the front side to the low values of the rear side. Finally a further drop in the optical generation rate happens in the n-layer where mostly long wavelength photons arrive. In this case n-layer penetration depth is simply too large to have an efficient absorption, thus leading to a limited loss in this part of the device. The n-layer, however, senses the improved internal reflectance given by the presence of back zinc-oxide layer (see the ripple at i/n interface in Fig. 2.3(b)).
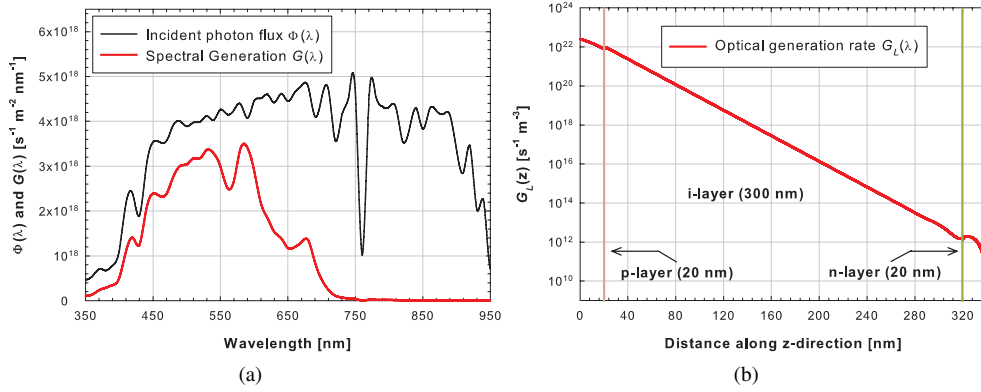
Figure 2.3: (a) Comparison between the incident photon flux $\Phi(\lambda)$ and the spectral generation $G_{i-layer}(\lambda)$ and (b) optical generation rate $G_L(z)$ of the flat pin single junction thin-film silicon solar cell (logarithmic scale, illumination is applied on left side, vertical lines indicate the p/i and i/n interfaces).

The optical generation rate is instrumental in solar cells: once plugged in the continuity equations for electrons and holes, together with Poisson equation and current density equations, it enables the calculation of the device electrical behaviour under illumination. After the publication of the aforementioned limits, several software were developed embedding optical models dealing with the emerging light management techniques, above all the light scattering arising from surface texturing (see Sec. 2.3.3). Coupled or not with semiconductor equations, such software are able to calculate at least one-dimensional optical generation rate. As sufficient computational power has become largely available, advanced three-dimensional structures can be studied or, if already fabricated, modelled and thus optimized. Nowadays optical modelling, either described by closed (empirical) formulae or by full-wave three-dimensional analysis, can be used as a way to predict the optical situation inside a (real) solar device and to lay the basis for further optimization.

Table 2.2: Light management techniques sorted by application area and novelty. Highlighted in italic the topics of this doctoral thesis.

	Solar spectrum	**Minimizing losses**	**Light scattering**
Present	Multi-junction	Anti-reflection	Random Textures
Novel	Intermediate reflectors	Low absorption TCOs Low absorption doped layers	*1-D or 2-D Gratings FLiSS*
Advanced	Quantum Dots Up / Down Converters Nanowires High Aspect-ratio	*Distributed Bragg Reflectors* White Paints	*Modulated Surface Textures* Metal nano-particles Plasmonics

2.3 Light management techniques

Light management in thin-film solar cells is accomplished by optical techniques related to the following areas (see Tab. 2.2): (i) effective use of the energy of the solar spectrum, (ii) low primary reflectance and low optical losses in supporting layers, and (iii) trapping of photons inside the absorber layers. The latter is achieved by the conjoined action of high reflectance at the rear side and light scattering at textured interfaces. In the following, a review of the light management techniques currently used in commercial, state-of-the-art, and R&D devices is given. The topics of this doctoral thesis are indicated in italic in Tab. 2.2 and will be reported in next chapters.

2.3.1 Effective use of solar spectrum energy

In previous sections, supporting layers and primary reflectance have been indicated as source of optical losses that are independent from the absorber layer. In addition, there are two intrinsic optical losses that strongly reduce the energy conversion efficiency of todays solar cells. Both losses are related to the spectral mismatch of the energy distribution of photons in the solar spectrum and the band gap of a semiconductor material that serves as the absorber in a solar cell. The first loss is the non-absorption of photons with energy lower than the band gap energy of the absorber ($E_{ph} < Eg_{i-layer}$). These photons are in principle not absorbed in the absorber and therefore do not contribute to the energy conversion process. The second process is the *thermalization*. In this process the electrons and holes generated by photons with energy higher than the band gap of the absorber release the extra energy as heat into the semiconductor atomic network. In Fig. 2.4(a) the mismatch between the spectral power density $P(\lambda)$ and a-Si:H semiconductor ($Eg \approx 1.8\ eV$) between 300 and 1200 *nm* is shown. In such wavelength range, around 13% of the incident energy is lost for thermalization ($E_{ph} > 1.8\ eV$), while the amount of non-absorbed energy is around 45% ($E_{ph} < 1.8\ eV$).

Standard approach to the effective utilization of the solar spectrum energy is the multi-junction structure (also known as tandem). The concept of a multi-junction solar cell is already widely used in thin-film silicon solar cell technology. In this structure two [49,
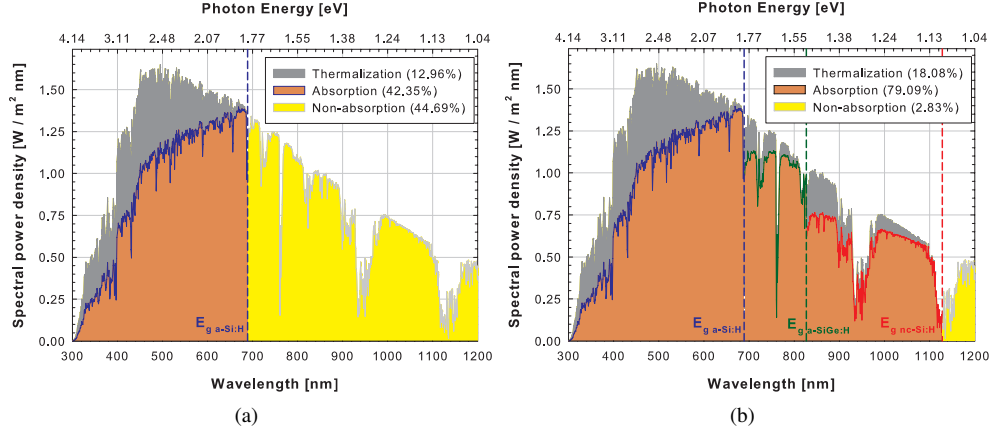
Figure 2.4: (a) Spectral mismatch for a-Si:H semiconductor and (b) spectral mismatch for a stack of three semiconductor materials (a-Si:H, a-SiGe:H, and nc-Si:H).

50] or more [34] solar cells are stacked on top of each other. Typical absorber layers in tandem thin-film silicon solar cells are based on a-Si:H and its alloys, like a-SiGe:H and nc-Si:H. Recently, also hydrogenated nano-crystalline silicon-germanium alloy (nc-SiGe:H) has been considered as efficient candidate for bottom cell absorber layer in triple junction solar cells thanks to its low band gap [90]. In fact, multi-junction solar cell approach means that the absorber layer in each component cell is tailored to a specific part of the solar spectrum. Top cells efficiently absorb short-wavelength part of the spectrum (high energy photons), whereas bottom cells absorb the remaining long-wavelength part of the spectrum (low-energy photons) (see Fig. 2.5). In Fig. 2.4(b) the mismatch between $P(\lambda)$ and a stack of a-Si:H, a-SiGe:H, and nc-Si:H semiconductors is reported. Even though the total thermalization loss is slightly increased to 18% with respect to the previous case, thanks to the multi-junction approach the absorption range of the device is greatly increased, leading to less than 3% of energy lost for non-absorption.

Passing from single junction to tandem solar cells, light management actions shift from purely increasing J_{SC} to manipulating both J_{SC} and V_{OC}. In single junction cell, once chosen the absorber material, which ideally fixes the V_{OC} [91], the efficiency of the solar cell is enhanced by increasing the i-layer absorptance (i.e. higher short-circuit current density). In tandem structure instead, since the stacked junctions are connected in series, the V_{OC} is increased while the J_{SC} must be properly distributed such that it is ideally the same in each junction, achieving the so called current-matching. For a triple junction cell, Eq. 1.3 can be re-written as follows:

$$\eta = \frac{FF \cdot V_{OC-T} \cdot J_{SCmin}}{P_{IN}} = \frac{FF \cdot (V_{OC1} + V_{OC2} + V_{OC3}) \cdot J_{SCmin}}{P_{IN}} \tag{2.9}$$

where V_{OC-T} is the total open circuit voltage, given by the sum of single open circuit voltages, and J_{SCmin} is the minimal short circuit current density among those developed by the single sub-cells. Passing from single to multi-junction approach, the fill factor is expected
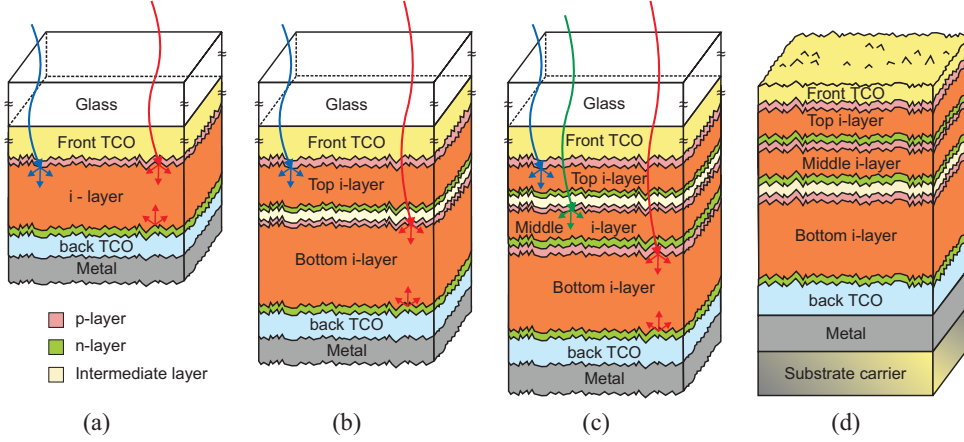
Figure 2.5: Sketches comparing (a) single junction, (b) double junction, (c) pin and (d) nip triple junction thin-film silicon solar cells.

to rise thanks to a more favourable ratio between electrical power loss ($R_{sh}J_{MPP}^2$) and the maximum achievable power ($V_{MPP}J_{MPP}$). In this respect, the model proposed by Hanak [92] can be used to estimate the FF [93] as follows:

$$FF = 1 - \left(\frac{R_{sh}J_{MPP}}{V_{MPP}} \right) \frac{w^2}{3} - \Delta FF \qquad (2.10)$$

where R_{sh} is the sheet resistance of the front electrode, w is the width of the solar cells and ΔFF takes into account other losses in silicon layers, back electrode, contact resistances and recombination junction resistance between the sub-cells. This positive aspect is however jeopardized by using extremely rough interfaces. In fact, if textured morphologies enable higher current densities thanks to light scattering (see. Sec. 2.3.3), on the other hand they prevent the optimal growth of absorber layers thus lowering both ΔFF and V_{OC}. This is a typical problem especially in case of nano-crystalline silicon, since cracks can form during the deposition in correspondence of so-called V-shaped deep features [94].

Optimal current matching in multi-junction structures is not straightforward since two opposite requirements should be satisfied: (i) thinner absorber layers to limit the degradation affecting a-Si:H and a-SiGe:H and (ii) higher absorption to raise J_{SCmin}. An advanced approach to deal with this trade-off is the implementation of intermediate reflectors. Such layers act as optical filters reflecting part of light (e.g. short wavelengths) and letting pass through them another part (e.g. long wavelengths). In this way the thickness of the top and middle absorber layers can be kept as thin as possible, thus lowering the LID effect; at the same time, the bottom absorber layer, which is characterized by higher absorption coefficient at long wavelengths, can efficiently absorb (near) infrared photons. Therefore intermediate reflectors must exhibit low refractive index and low absorption for long wavelengths. Materials like ZnO [95, 96] or doped SiO [97] fit such scenario. Especially the latter is nowadays broadly used not only for the ease of tuning of their opto-electronic properties, but also for the resilience it offers against cracks formation in case of surface textures with large and deep features [76].
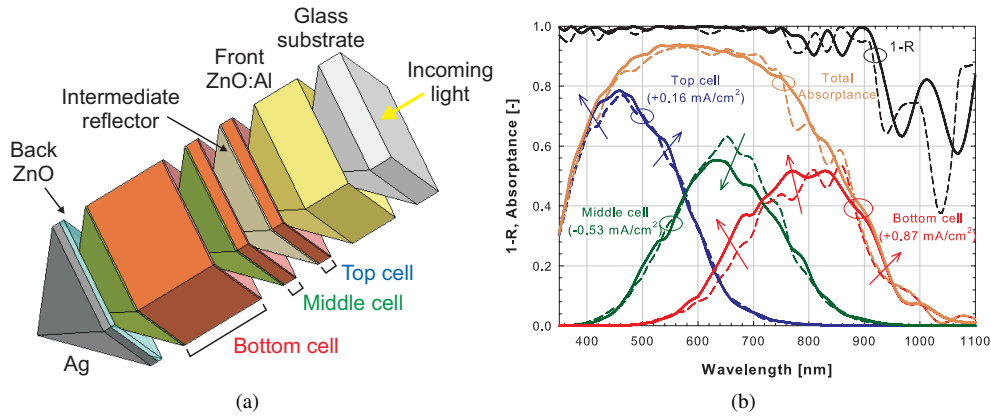
Figure 2.6: (a) Sketch of a novel triple junction (a-Si:H / a-SiGe:H / nc-Si:H) with top n-type
a-SiO:H intermediate layer on two-dimensional gratings; (b) effect of inter-
mediate layer on the i-layers absorptance as indicated by simulations (dashed
curves: triple junction with typical top n-type a-Si:H, continuous lines solution
with a-SiO:H).

Current matching is a typical modeling problem. Once solved, it is possible to mi-
nimize the amount of samples to fabricate in order to test the efficiency of multi-junction
solar cells. In Fig. 2.6, for example, a novel triple junction device on inverted pyramid
in the role of two-dimensional periodic gratings (see Ch. 4) simulated by means of Finite
Element Method [98] is sketched. The thickness of a-Si:H, a-SiGe:H and nc-Si:H i-layers
are, respectively, 150, 150, and 1050 nm. With such thicknesses and not using any inter-
mediate layer, the middle cell absorbs too much (9.6 mA/cm^2), making the device bottom
limited (8.2 mA/cm^2). Using an n-type a-SiOx:H instead of the typical n-type a-Si:H as
intermediate reflector enables the redistribution of absorption along top, middle and bottom
junctions, thus achieving the current matching (9.06, 9.06, and 9.07 mA/cm^2, respectively).

Intermediate reflectors based on periodic structures are also under development. The
wavelength selective behaviour of photonic band gap structures can be opportunely tuned to
achieve high reflectance in a given wavelength range while conserving a sufficient conduc-
tivity. Three-dimensional inverted opal structured ZnO [99] or distributed Bragg reflectors
(DBR) formed by alternating layers of n-type a-Si:H / ZnO [100], SiO / C [101], and ITO
/ ZnO [99, 102] are notable examples of periodic intermediate reflectors for multi-junction
devices. In Ch. 6 the study and implementation of dielectric DBR as efficient back reflector
will be reported.

Recently novel absorber materials and cell concepts based on spectrum splitting on two
or more laterally dislocated cells [103], up- and down-converters [104–106], absorbers with
quantum dot superlattices [107], intermediate-band cells [108] have been investigated for
a generic approach of all-silicon tandem solar cells. Furthermore, nanowires [109, 110],
pillars [111], and high-aspect ratio structures [112, 113] promise maximized absorption by
enabling a pronounced AR effect within very thin absorber layers.
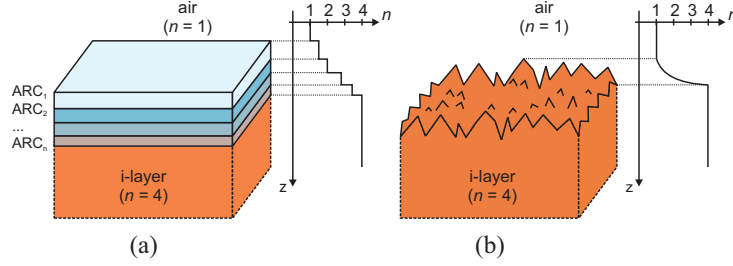
*Figure 2.7: Anti-reflection schemes between air ($n_{air} = 1$) and i-layer ($n_{i-layer} = 4$): (a)
multi ARC, giving step-wise refractive index matching, and (b) front nano-
texture, giving gradual refractive index matching.*

2.3.2 Low primary reflectance and optical losses in supporting layers

The primary reflectance, arising from the refractive index mismatch between incident me-
dium and irradiated device, can be reduced by using two techniques: anti-reflective coatings
(ARC) and front nano-textures (see Fig. 2.7). In the first case one or more coating layers
can be used to produce a step-wise change of the refractive index from air ($n_{air} = 1$) to
absorber layer ($n_{i-layer}$). An ARC is characterized by its refractive index and thickness.
The ideal anti-reflective coating refractive index is obtained by calculating the geometric
mean between incident and absorptive media [114]:

$$n_{ARC} = \sqrt{n_{air}n_{i-layer}} \tag{2.11}$$

while the thickness d_{ARC} follows the principles of interference:

$$d_{ARC} = \frac{\lambda}{4} = \frac{\lambda_0}{4n_{ARC}} \tag{2.12}$$

where λ_0 is the wavelength *in vacuo* and the $\lambda/4$ rule assures π radians phase shift between
the air/ARC and ARC/i-layer reflectances, resulting in their cancellation at the designed
wavelength. However this technique is only indicative, since the ideal index may not cor-
respond to any material and, depending on the material chosen, a controlled thickness may
be difficult to achieve. Furthermore, the wavelength range for which there is an actual de-
crease of the primary reflectance is usually quite narrow. In order to widen such wavelength
range a multi-ARC could be fabricated by choosing specific materials and designing their
thicknesses. The ARC approach is mostly used in c-Si based solar cells, where a thin layer
of silicon nitride covers the front side of the wafer.

In thin-film silicon solar cells technology, the intrinsic multi-layer structure of devices
calls for a preliminary decision on where to use an ARC. For example, anti-reflective ma-
terials for *pin* thin-film silicon solar cells can be deposited onto the glass substrate, like
magnesium fluoride ($n_{MgF_2} = 1.38$) [115], or placed between the front TCO and the p-layer,
like titanium oxide ($n_{TiO_2} = 3$) [116]. In case of *nip* solar cells, the used front TCO is usual-
ly indium-doped tin-oxide (ITO), whose thickness can be tuned to meet both conductance
and anti-reflection requirements.

The usage of nano-textures in thin-film silicon solar cells is also appealing, especially
for multi-junction applications. The presence of an appropriate front texturization assures a

broader wavelength range of anti-reflection and, at the same time, triggers light scattering (see Sec. 2.3.3). A surface morphology containing features with vertical and lateral dimensions smaller than the incoming wavelength will prevent light interacting with smallest details. In this case refractive index spatially varies (see Fig. 2.7(b)) and smoothly matches the indexes of incident and irradiated media, thus decreasing the primary reflectance. Mainly focusing at the interface air / device, several anti-reflection schemes mimicking moth-eye have been lately proposed [117–119]. However, also the texturization of internal interfaces in thin-film silicon solar cells, particularly the TCO / p-layer interface, promotes a gradual change in the refractive index. A combination of nano- or micro-texturization *outside* the device (air / glass interface) and textured interfaces inside the device is also possible and holds a good potential in lowering the primary reflectance, as shown lately in [120].

Not only primary reflectance but also absorption of light in supporting layers such as doped semiconductor layers and transparent and metal electrodes leads to optical losses in the solar cell. In principle, photons that are absorbed in these supporting layers do not contribute to the energy conversion process and therefore the absorption in these layers has to be minimized. Recently a lot of effort has been dedicated to the development of transparent conductive oxides (TCO) with low absorption in a wavelength region of interest (300 $nm < \lambda < 1200$ nm) [121–125]. A continuous attention is also paid to the development of wide band gap doped semiconductors based on a-Si:H and μc-Si:H such as hydrogenated amorphous/microcrystalline silicon carbide (a-SiC:H/μc-SiC:H) and hydrogenated amorphous/microcrystalline silicon oxide (a-SiO:H/μc-SiO:H) [126, 127]. Finally, alternative solutions to metallic back reflectors, i.e dielectric-based reflectors, are investigated to avoid parasitic plasmonic absorption on the textured metal surfaces [128]. Examples of such novel reflectors are white paint [129, 130] or photonic crystal solutions [131–134]. The latter allow the manipulation of reflection and transmission at a particular interface inside a solar cell. This specially designed optical interface results in a wavelength-selective management of (high) reflection or transmission of light (see Ch. 6).

2.3.3   Scattering and trapping of photons inside the absorber layers

The purpose of light trapping is to lead a photon through a solar cell into the absorber layer and once it enters the absorber to trap it there until it is absorbed. The most important role of light trapping is to keep the physical thickness of the absorber layer as thin as possible and to maximize its effective optical thickness. Calculating the spectral absorption of 300 nm thick a-Si:H layer, when the effective optical thickness of the layers is increased 10 and 50 times, result in 52% and 78% potential enhancement of the photo-current density, respectively, with respect to the situation where the physical thickness is equal to the optical thickness. In case of nc-Si:H material, light trapping plays an even more important role. Increasing the optical thickness of 1 μm thick nc-Si:H layer 10 and 50 times results in 90% and 138% enhancement of the photocurrent, delivering potential photo-current density of 28 and 35 mA/cm^2, respectively [135].

The following techniques are usually combined, constituting so-called light trapping schemes: (i) front side in-coupling of incident photons, (ii) intermediate reflectors in tandem solar cells, (iii) back side reflection, and (iv) scattering at rough interfaces or at metallic nano-particles. The first three techniques, discussed in previous sections, deal with the manipulation of photon propagation throughout a solar cell. They are related to the deve-
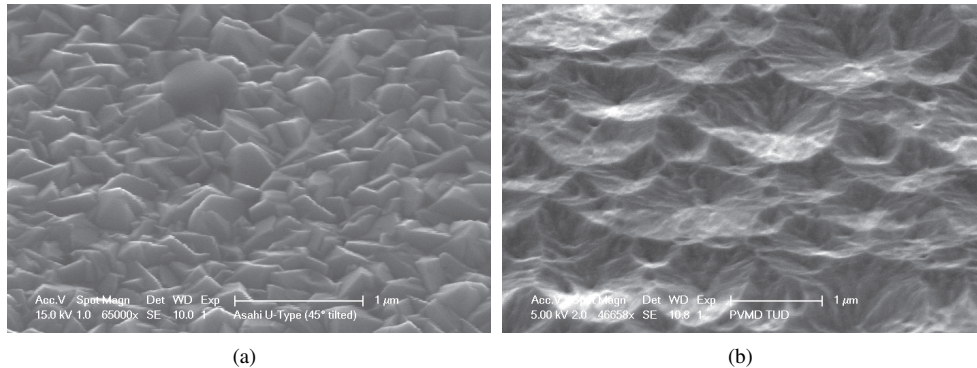
Figure 2.8: SEM micrographs of two examples of randomly textured front TCOs: (a) SnO$_2$:F (FTO) Asahi U-type and (b) wet-etched ZnO:Al (AZO).

lopment and implementation of optically-active layers that let photons to reach the absorber layer. In contrast, the last technique deals with the enhancement of an average photon path length inside the absorber layer. Scattering of light at rough interfaces and/or metallic nano-particles is related to the design and fabrication of a surface texture on substrate carriers, which in turn introduce rough interfaces into the solar cell structure. Scattering at rough interfaces prolongs the effective path length of photons and partially leads to the total internal reflection between the back and front contacts confining light inside the absorber. Recently, layers of metallic nano-particles and composite materials with embedded metal nano-particles [136–139] for efficient in-coupling and scattering of light into the absorber layer have attracted a lot of attention [140–144].

However, in state-of-the-art thin-film silicon solar cells light is scattered at rough interfaces introduced by substrate carriers coated with a randomly surface-textured TCO. Typical examples are fluorine-doped tin oxide (FTO) or boron-doped zinc oxide (BZO) with a pyramidal-like surface structure [127, 145] (see Fig. 2.8(a)) and sputtered-etched gallium-doped or aluminum-doped zinc oxide (GZO or AZO) that show a crater-like surface texture [90, 146] (see Fig. 2.8(b)). Alternative approaches for enhanced light scattering are periodic diffraction gratings or modulated surface morphologies. The first approach, often referred as the angle-selective management of scattered light at textured interfaces, deals with the manipulation of light scattering into (pre-) selected angles (see Ch. 4). Diffraction gratings can be also arranged in flattened substrates and used as efficient back reflectors (see Ch. 7). The approach based on the use of modulated surface textures allows manipulation of scattering in a broad wavelength range (see Ch. 5).

Chapter 3

Tools for thin-film deposition, characterization and opto-electrical modelling

In this chapter, tools used for carrying out the results of this doctoral thesis will be described. Firstly, techniques for vacuum deposition and patterning of thin-films will be introduced, then methods for their characterization will be illustrated, and finally computer programs for opto-electrical modelling will be presented.

3.1 Techniques for vacuum deposition and patterning

3.1.1 Radio-frequency magnetron sputtering

As introduced in previous chapters, front conductive oxides for both *pin* and *nip* configurations hold important opto-electrical role in thin-film silicon solar cells. Among various technologies to deposit high quality TCOs for photovoltaic applications, radio-frequency (RF) magnetron sputtering is the method of choice for devices presented and discussed throughout this thesis.

Using RF sputtering, (semi-)conducting and dielectric films can be fabricated by depositing on a substrate (anode) atoms released from a solid target (cathode). The target is bombarded by ions or highly energetic atoms, which are present in a glow discharge initiated with Ar flow and bias voltage between the anode and cathode [147]. Specific benefits of RF sputtering are: (i) possibility to predict the layer structure and thickness, (ii) capability of sputtering compound materials without losing target stoichiometry, (iii) deposition of well adhering and highly dense films, and (iv) high deposition uniformity [148]. Furthermore, thanks to radio-frequency (usually 13.56 *MHz*), the target is alternatively attacked by ions and electrons thus avoiding charge built-up at not-conducting targets surface. Glow discharge is mainly driven by ionizing electrons which perform an oscillating motion within the plasma body. This is because the electrons are able to follow the RF frequency, whilst the ions are not for their large inertia.
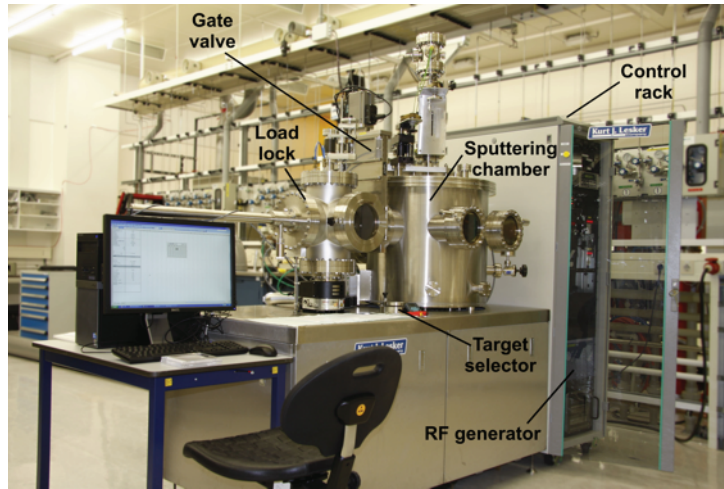
Figure 3.1: Photo of Kurt J. Lesker sputtering machine in PVMD/DIMES clean room (photo courtesy of Stefaan Heirman, PVMD).

By adding magnets underneath the cathode surface, trapping of electrons close to the sputtering target is enabled. Since the residence time of the electrons in the plasma is considerably enhanced, the chance of making ionizing collisions is also much greater. This increased ionization efficiency results in a denser plasma, which makes possible to sustain much higher current at a significantly lower voltage. Extensive studies on planar magnetron sputtering carried out by Thornton [149] and further developed by Kluth *et al.* [150] led to the so-called modified Thornton model, in which substrate temperature and sputter pressure are indicated as main parameters for changing the opto-electrical properties of the deposited material and influencing the eventual post-deposition etching. In addition, aiming to optimize the whole device, such properties can be finely tuned by adapting the RF power, the Ar flow, the target-to-substrate distance, and the initial background pressure.

The RF magnetron sputtering system used in this work is a manually operated multi-target system by Kurt J. Lesker Company. The system, displayed in Fig. 3.1, consists of a load lock chamber which is connected to the actual process chamber by a gate valve. Inside this chamber, three ceramic targets with a diameter of seven inches are present, each located on top of a so-called magnetic torus. One target has a composition of 10% SnO_2 in 90% In_2O_3 for deposition of indium-doped tin oxide (ITO). The other two share the same composition (2% Al_2O_3 in 98% ZnO) for deposition of aluminum-doped zinc oxide (AZO). The targets are separated from each other by vertical shields placed between them. A rotating shutter, positioned slightly above the targets, is used during pre-sputtering to protect the substrate holder assembly and process chamber walls from unwanted deposition. The substrate holder assembly, whose distance from the bombarded target can be tuned, is formed by a closed box containing three halogen lamps for heating purposes. The actual substrate holder is clamped to this box by heat resistant Nimonic springs. The temperature of the substrate holder is controlled by a 2408 Eurotherm which has a thermocouple positioned inside a metal housing and sandwiched between the assembly and the back of the substrate holder. A maximal temperature of 750 °C is allowed. Under the sputtering chamber, three
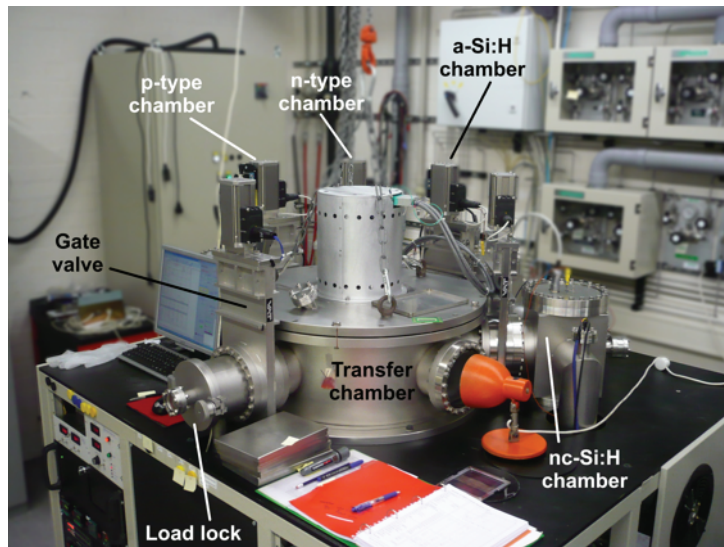
Figure 3.2: Photo of AMOR cluster tool in PVMD/DIMES clean room.

impedance-matching networks between the power supply and the magnetic tori are mounted together with a flowing water circuit to keep the circuitry cool during operation.

3.1.2 Plasma-enhanced chemical vapour deposition

The fabrication of *p-i-n* junctions was carried out by means of RF plasma-enhanced chemical vapour deposition (RF PE-CVD). The usage of this technique in thin-film silicon solar cells technology is preferred as it enables low operation temperatures, deposition of high quality films, and good coverage of textured morphologies, adhesion, and uniformity. Thin-film growth takes place through the adsorption on the substrate of so-called reactants formed in the plasma.

Specifically, silane and other gases like molecular hydrogen or dopants are introduced in the reaction chamber. There, gases are mixed and transformed into reactive radicals, ions, neutral atoms and molecules because of collisions in a glow discharge triggered by RF power. In this way, the substrate can be maintained at a low temperature as reactive and energetic species are formed in gaseous phase. Since the substrate is kept grounded with a lower potential than the plasma, only neutral or positively charged particles can diffuse towards it, thus forming the thin-film layer [151]. Deposition rate and physical properties of the film, such as refractive index, density or dark- and photo-conductivity, can be tuned by acting on background pressure of the chamber, RF power, temperature and gas flows.

So-called AMOR ultra-high vacuum (UHV) multi-chamber cluster tool by Elettrorava S.p.A. was used for depositing *p-i-n* junctions and multi-layer structures presented in this work[1]. The system, shown in Fig. 3.2, is operated via software and consists of a load lock and four reaction chambers connected through the transfer chamber, where a robotic

---

[1]Micromorph tandem solar cells presented in Ch. 5 were deposited in a Oelikon A. G. KAI reactor at IMT-PVLAB, Neuchâtel (Switzerland).

arm is located. Reaction chambers, that can accommodate substrates up to 10x10 cm^2 area, contain parallel electrodes and are individually deployed for p-type, n-type, intrinsic amorphous, and nano-crystalline silicon layers, respectively. The latter can be also used for depositing other alloys like hydrogenated amorphous silicon-nitride (a-SiN$_x$:H, see Ch. 6). An oscillating signal at 13.56 MHz is applied to the chambers electrodes through an impedance-matching network for maximizing the injected forward power. Under each reaction chamber, turbo molecular and rotary pumps provide the necessary background vacuum level and a butterfly valve controls the pressure during operations. Finally, mass flow controllers precisely control the composition of gas mixture inside reaction chambers.

3.1.3 Physical vapour deposition

Metal evaporation is the technique used in this work to fabricate metal contacts in solar cells. It consists in the evaporation of a metallic source which condensates onto the substrate. The reaction chamber is kept at high vacuum to reduce chances of fabricating (slightly) oxidized metallic films and to better control the deposited thickness. The deposition rate achievable with evaporation is generally higher than sputtering methods with also lower surface damage [152]. To improve deposition uniformity and step coverage, substrates are usually mounted on a rotating stage. For melting metals and creating metallic vapour, two basic ways are considered here. They both involve heat resistant ceramic or tungsten-based crucibles which contain the metallic source: (i) flowing high current through the *boat*-crucible (thermal evaporation) or (ii) irradiating the crucible with high energy electrons from a glowing tungsten filament (electron beam method).
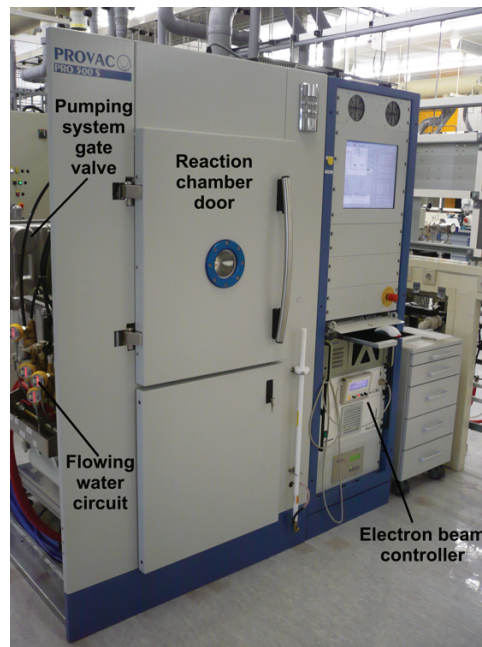
Figure 3.3: Photo of PRO500S metal evaporator in PVMD/DIMES clean room.

A high vacuum PRO500S metal evaporator by Provac is in use at PVMD/DIMES. The system, depicted in Fig. 3.3, is fully controllable via software (pressure cycles, material choice, and deposition recipes). Behind the door of the reaction chamber, it contains parts for both aforementioned evaporating approaches: a tungsten boat used for depositing Ag and four ceramic crucibles, each containing a different material, used for evaporating Al or other metals. The reaction chamber, equipped with a rotating stage, can accommodate up to four 10x10 cm^2 substrates. At the rear side of such chamber, pumping system and flowing water circuit are located. For solar cells in *pin* configuration, a 4x4 mm^2 device area is defined upon the deposition of the back contact using a shadow mask. In *nip* configuration, the metallic back contact is deposited on the entire area of the substrate before sputtering the back TCO. In this case the sputtered front ITO defines the device area afterwards.

3.1.4 Reactive Ion Etching

In order to precisely define solar cells endowed with back dielectric distributed Bragg reflectors (see Ch. 6), reactive ion etching technique (RIE) was used. This method allows for selectively removing patterned films through plasma-driven chemical reactions. In the glow discharge formed between two parallel plates and triggered/sustained by RF power, different gaseous species with large molecular weights are mixed and ionized. The difference of potential built up between the plates accelerates the negative ions towards the positively charged substrate where they chemically react with the patterned film, resulting in its etching. This technique is especially appealing when anisotropic etching is needed.
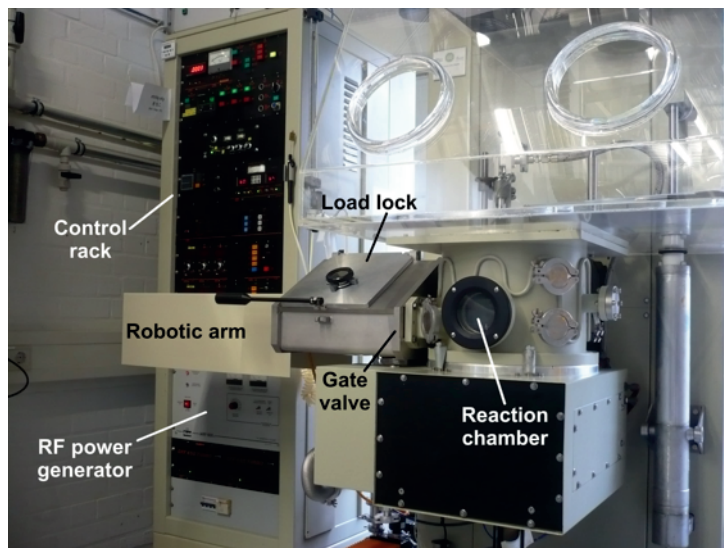
Figure 3.4: Alcatel plasma etcher in PVMD/DIMES clean room.

An Alcatel plasma etcher installed in PVMD/DIMES facilities, shown in Fig. 3.4, was used as RIE system. The substrate (max area 10x10 cm^2) can be mounted on the substrate holder located in the load lock chamber. After starting the pumping system (not shown in the figure), the gate valve opens, letting the robotic arm to introduce the substrate holder in

the reaction chamber. There selected gases, such as CF_4, SF_6, CHF_3, BCL_3, Cl_2, O_2, N_2 or He, are mixed at a certain set point pressure. After the RF power generator is properly set up, plasma is triggered and the etching begins.

3.2 Characterization methods

3.2.1 Scanning electron microscopy

Scanning electron microscopy (SEM) was used for the visualization of micro- and nano-scale features present on the surface of textured substrates. SEM working principle is essentially based on the detection of electrons emitted by the specimen under observation, being irradiated by a highly energetic electron beam (from 0.2 to 40 *keV*). Such beam, emitted by a LaB_6 crystal, is focussed through one or two lenses and is deflected along *x*- and *y*- direction by means of scanning coils. In this way a so-called raster scan of the specimen surface is enabled. In the most basic embodiment of this technique, secondary electrons emitted by the specimen are detected and interpreted as brightness and contrast signals. Images plotted on old-style cathode ray tubes or up-to-date computer screens are, respectively, analog and digital versions of such signals. A scanning electron microscope can inspect wide areas with many levels of zoom and typical achievable resolution is in the order of hundreds or tens of nanometers. The already high detail achievable with this technique can be further enhanced tilting the specimen by several degrees with respect to the incoming electron beam, resulting in a three dimensional-like image.

Figure 3.5: Philips XL-50 SEM system in PVMD/DIMES clean room.

SEM images presented in this work were carried out either with a Philips SEM525M or with a Philips XL-50 (see Fig. 3.5). The electron beam energy ranged between 5 and 15 *keV* depending on the conductivity of the specimen. Tilted images were taken at 45°

inclination angle. In case of non-conductive samples, a thin layer of silver (<30 *nm*) was evaporated to reduce charging effect.

3.2.2 Atomic force microscopy

Atomic force microscopy (AFM) was also extensively used not only for the 3-D visualization of textured morphologies, but also for the numerical study of statistical parameters related to their surfaces. In AFM a laser beam, reflected by a metal-coated silicon-based cantilever and detected by photodiodes, indirectly furnishes the surface image. On the non coated side, the cantilever has a tip with radius of curvature of few nanometers, which is used to scan the surface.

More in detail, an atomic force microscope operates through four main parts (see Fig. 3.6). The substrate to scan is mounted on a (i) piezo-electric (PZT) stage which can translate electrical inputs in small movements in *x*-, *y*-, and *z*-direction, the so-called scan-by-sensor configuration. Through a closed loop control system, the stage is smoothly lifted up in *z*-direction until when the cantilever, mounted on (ii) a holder, starts to deflect. This effect is due to the interaction between the nano-scale cantilevers tip and forces established at nanometric distances. Such effect, initiated at substrate-to-tip side, is sensed indirectly at the coated side by (iii) two photodiodes. In fact, the difference of their optical response, related to (iv) the laser beam reflected by the metallic coating, is proportional to the cantilevers deflection. After such landing step, the average distance between substrate and cantilevers tip is also controlled by the closed loop system. Finally, depending on the appropriate AFM operation mode (contact, non-contact, or tapping mode), the PZT stage moves in *x*- and *y*-direction the substrate, thus allowing the scan of the surface though the cantilever.
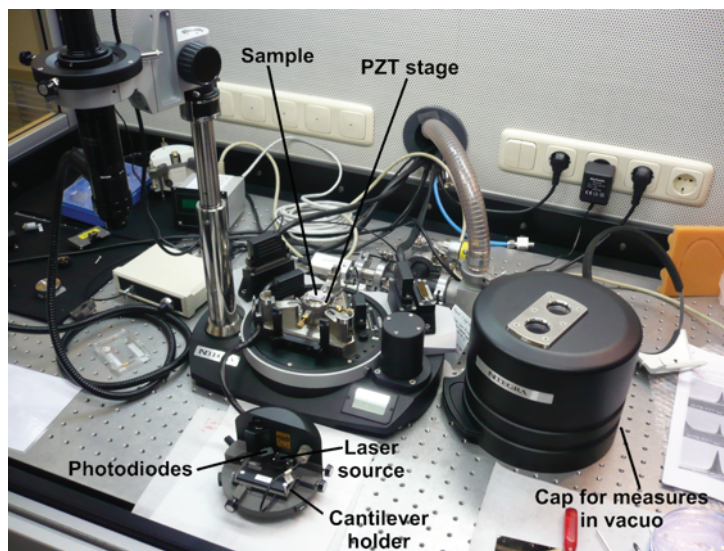

Figure 3.6: nTegra NT-MDT atomic force microscope located in a PVMD measurement room.

AFM systems present resolutions in the order of nanometers, thus higher than scan-

ning electron microscopes. However the reachable area without physically displacing the specimen is in the order of 100x100 μm^2 - 200x200 μm^2, depending on the model and on the scan configuration. To further improve the resolution or the image quality, a cap can be mounted on the measurement equipment to perform measurements in vacuo. In this way the natural meniscus of humidity present on the specimen can be removed, resulting in higher signal-to-noise ratio. An important benefit of AFM with respect to SEM is the possibility to numerically post-process the surface morphology $z(x,y)$. Typical statistical parameters like surface roughness or correlation length can be therefore easily extracted and fast Fourier transform (FFT) of the surface efficiently calculated for optical modelling purposes (see Ch. 4 and 5 or [153]).

The atomic force microscope used in this work was a nTegra by NT-MDT (see Fig. 3.6). Silicon cantilevers with gold coating and whisker tip (10 nm radius, 10° inclination angle) were deployed in tapping mode. Scan frequency was set to 1 line / second and final digitized surfaces were formed by either 256x256 points or 512x512 points. Like in SEM inspection, a thin layer of silver was evaporated onto non-conductive samples.

3.2.3   Statistical parameters

A number of statistical quantities, describing vertical and lateral components of the surface morphology, can be calculated from a sample scanned with AFM method. Especially those related to the aspect ratio of surface textures are nowadays of practical interest for modeling light scattering intensity (see Sec. 5.4), quantifying the accuracy of recent nano-imprinting techniques [141, 154], or analyzing different advanced surface morphologies (see Sec. 5.8).

The peak-to-peak $P2P$ height and the surface root mean square roughness σ_{RMS}, both usually measured in nm, deal with the vertical components of surface textures. The $P2P$ is the absolute vertical distance between the maximal and minimal heights of the morphology, while σ_{RMS} indicates the vertical deviation of surface features from their average value. It is defined as follows:

$$\sigma_{RMS} = \sqrt{\frac{1}{N}\sum_{i=1}^{N}(z_i - \hat{z})^2} \qquad (3.1)$$

where N is the number of data points, $\hat{z}$ is the average surface level and z_i is the height of the i_{th} data point in an AFM scan. On the other hand, the correlation length L_C, typically measured in μm, represents the average lateral component of surface features. It is determined as the diameter of a disc obtained by cutting the peak of AFM image autocorrelation function (ACF) [155] at $1/e$ of its maximum. For a not Gaussian surface height distribution, the extracted ACF is not a 2-D Gaussian function and the cut disc used to determine L_C is elliptic with major and minor axis not aligned with x- and y- directions. In this case the generalized correlation length L_{CG} is defined as the diameter of a disc having the area of the elliptic cut [154]. The dimensionless ratio between surface roughness and (generalized) correlation length is called aspect ratio, $Aspect_R$.

The angle distribution and especially its mean slope value S_M, measured in degrees, holds a prominent role in assessing the scattering properties of surface features (see Sec. 5.8). Considering the plane passing through each three points of an AFM scan (facet) and the normal versor of such plane, the slope distribution keeps track of all the angles between

facets versor and the versor of flat projected area A_P. The area ratio $Area_R$ is given by the following relation:

$$Area_R = \frac{A_S - A_P}{A_P} 100\% \tag{3.2}$$

where A_S is the surface area. $Area_R$ denotes the warping degree of a textured morphology with respect to an ideally flat surface. The distribution of grains diameter and its mean value D_M, measured in μm, provide information on cavities present on the morphology.

3.2.4 Sheet resistance

The sheet resistance R_{sq}, measured in $\Omega/\square$ and defined as the ratio of resistivity to thickness of the measured film, is an important figure of merit for the characterization of TCO. The method involving four probes mounted in line is the reference for this kind of measurements. As the external probes (1st and 4th) apply a current and the internal probes (2nd and 3rd) measure the voltage, the sheet resistance is thus determined without any influence of the contact resistance, which can be significant for materials with a high conductivity. For sputtered materials used in this work, the linear four probes system CMT-SR2000NW by Advanced Instruments Technology was used (see Fig. 3.7).
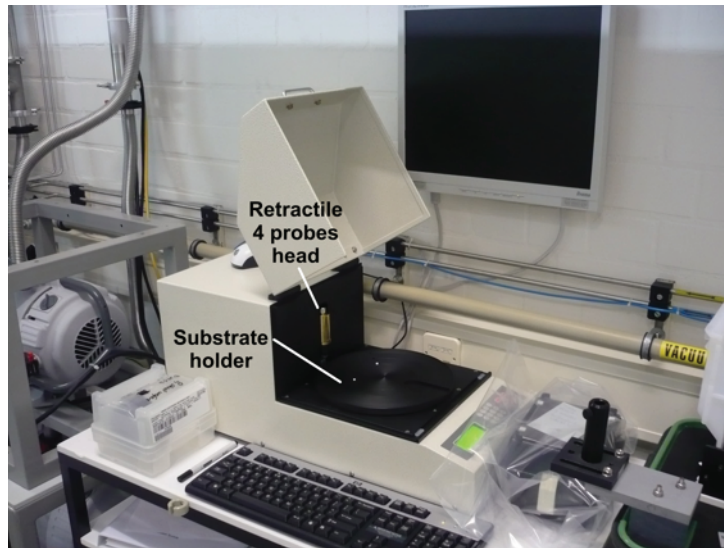
Figure 3.7: CMT-SR2000NW sheet resistance setup in PVMD/DIMES clean room.

3.2.5 Profiling

The profiling is a very sensible electro-mechanical method useful to find the thickness of a film. Steps from tens of nanometers to several millimetres can be easily measured and the operation sequence is quite simple. A sharp needle, whose height position is controlled by a computer software, is smoothly landed on the specimen. The latter is placed on a moving

the stage that can usually move only in one direction. After the landing, the stage moves under the needle and any height variation is digitally recorded and reported on a computer screen. For trustworthy measurements a step-like boundary should be present between the substrate and the top surface of the film under test. Fig. 3.8 depicts the system Dektak 150 by Veeco used in this work.
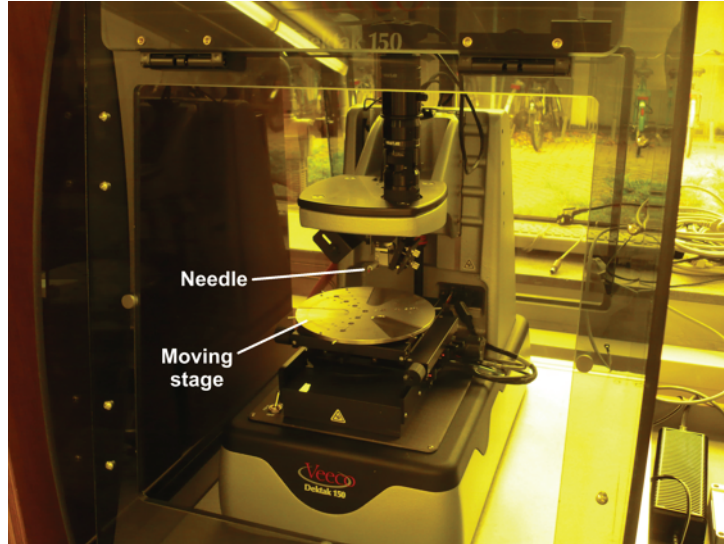
Figure 3.8: Veeco Dektak 150 profilometer in a PVMD/DIMES clean room.

3.2.6   Spectrophotometry

For the optical characterization of absorber layers and supporting layers, spectrophotometry was extensively used. This technique allows the measurement of transmittance and reflectance of a specimen with respect to the wavelength of incoming light. In typical spectrophotometer, a source of light impinges on diffraction gratings, able to select specific wavelengths. Through a series of mirrors and other optical elements the path of wavelength-selected beam of light is directed to the specimen. The light transmitted or reflected by the sample is captured with an optical detector sensitive in a wavelength range compatible with the selected beam. Information from the detector is then compared wavelength by wavelength to reference transmittance and reflectance spectra. Measured spectra are thus reported in percentage.

A spectrophotometer Lambda 950 by Perkin Elmer was deployed for optical measurements (see Fig. 3.9). This spectrophotometer has two light sources, a deuterium arc lamp for ultraviolet light and a tungsten-halogen lamp, for which a wavelength spectrum between 175 *nm* and 3300 *nm* can be covered. Two different accessories could be mounted on the spectrophotometer: the Integrating Sphere (IS) and the Absolute directional Reflectance/Transmittance Accessory (ARTA). The latter is from OMT Solutions B.V. and enables the Variable Angle Spectrometry (VAS) technique [156]. Both accessories contain two detectors: a photomultiplier for ultraviolet and visible regions of the spectrum and a PbS
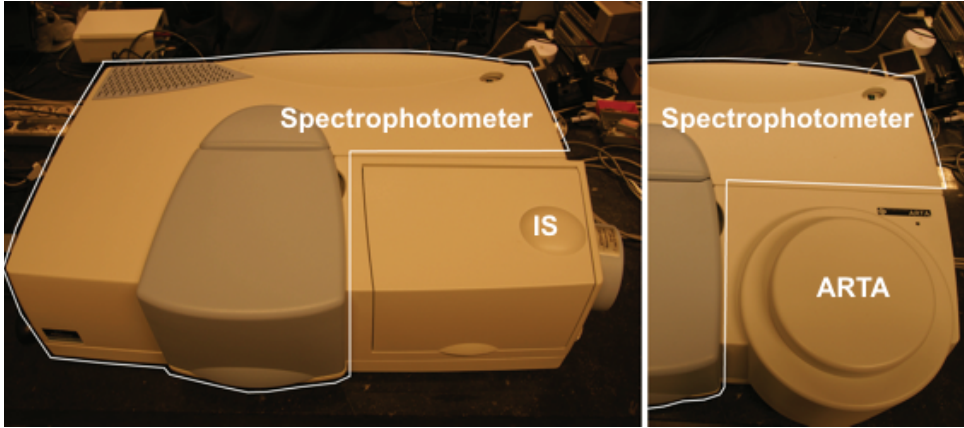
Figure 3.9: Perkin Elmer Lambda 950 spectrophotometer with mounted IS (left) or ARTA (right) accessories.

detector that deals with the near infrared range. The switching between the two detectors happens at 860.60 *nm* which is the weakest region for both detectors [157, 158].

The IS has a diameter of 150 *mm* and it is internally coated with Spectralon, which is a highly reflective material with a Lambertian behavior[2]. When light enters though the sample at the transmittance port (see Fig. 3.10a), due to multiple internal reflections, the electromagnetic field in the sphere becomes homogeneous and allows for measuring the total (diffuse + specular) transmittance $T_T(\lambda)$. To measure the diffuse transmittance $T_D(\lambda)$, it is possible to remove a cap at the reflectance port (a Spectralon mirror), opening a hole through which the specular transmitted light can leave the sphere. With these measurements, the haze of transmitted light $H_T(\lambda)$ can be calculated according to the following equation:

$$H(\lambda) = \frac{T_D}{T_T}. \tag{3.3}$$

Similarly to the transmittance, mounting the sample at the reflectance port of the IS, the total reflectance $R_T(\lambda)$ can be measured as well as the diffuse part $R_D(\lambda)$, once another cap is removed to allow the specular reflected light to depart from the sphere. Knowing both total transmittance and reflectance, it is possible to calculate the absorptance of a film ($A_{film} = 1 - R_T - T_T$) in the hypothesis that the substrate carrier does not absorb light in the inspected wavelength range.

The ARTA, schematically shown in Fig. 3.10(b), has a diameter of 180 *mm* and it is typically used for VAS measurements. In fact, the determination of specular transmission and reflection (T_S and R_S, respectively) at different incident angles is possible, since the sample is mounted on a rotating stage. However, keeping the sample position fixed and rotating the small IS around it, ARTA can be used also as Angular Resolved Scattering (ARS) setup. In this way it is possible to measure the Angular Intensity Distribution (*AID*) in a broad spectrum, because the ARTA can use the wavelength range provided by the spectrophotometer.

---

[2]A surface that ideally scatters light in all directions is called Lambertian and obeys the cosine law: $I = k \cdot cos(\theta)$, where I is the intensity of light, k is a proportionality factor and θ is the scattering angle.
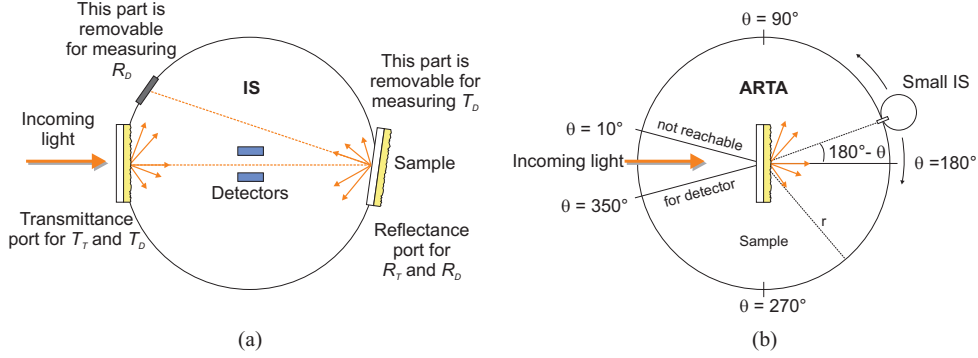
Figure 3.10: Conceptual sketches of (a) IS and (b) ARTA accessories for Perkin Elmer Lambda 950 spectrophotometer (ARTA sketch courtesy of dr. K. Jäger).

This accessory is further equipped with a polarizer that enables the measurement of optical properties for arbitrary polarizations (see Sec. 3.2.7). The aforementioned detectors are situated in the small IS, that can rotate in an angular range between 10° and 350°. The incident angle for the rotating stage can be set between 90° (normal incidence of the light beam on the sample surface) and 180° (parallel incidence). While for the normal incidence the whole transmitted light can be measured, this is not possible for the reflected light since the small IS cannot move on the light beam. With the ARTA the absorbance A is measured, which is related to the *AID* via:

$$AID(\lambda; \theta, \varphi) = 10^{-A(\lambda; \theta, \varphi)}. \tag{3.4}$$

The *AID* is a function of wavelength, scattering angle θ, and azimuth angle φ, for which it is necessary to repeat the measurements for different azimuths of the sample. However, for isotropic samples, like randomly textured TCOs, this is not necessary and the *AID* depends only on wavelength and scattering angle. Before a measurement starts, the ARTA is calibrated so that $A \equiv 0$ when no sample is present.

3.2.7   Extraction of refractive index from VAS measurements

Together with surface morphology and layers thickness, the optical properties of materials involved in computer simulations hold a key role in the proper calculation of primary reflectance and absorptance in each layer. Refractive indexes of several materials used in simulations presented in this thesis were carried out with an accurate characterization method based on VAS [159]. With such method, the optical properties are obtained from simultaneous fitting of simulated T_S and R_S spectra to spectroscopic measurements for different polarizations and light incidence angles. The operative flow chart of such method is reported in Fig. 3.11(a). Measured spectra are imported in SCOUT software [160], where they are compared to simulated spectra from the application of Fresnel equations to the defined multi-layer system. Such system is given by incident light / air / surface mix model / film under test / substrate / air, which resembles the actual optical system during the measurement session. The fitting is operated by iterative adjustment of several parameters which
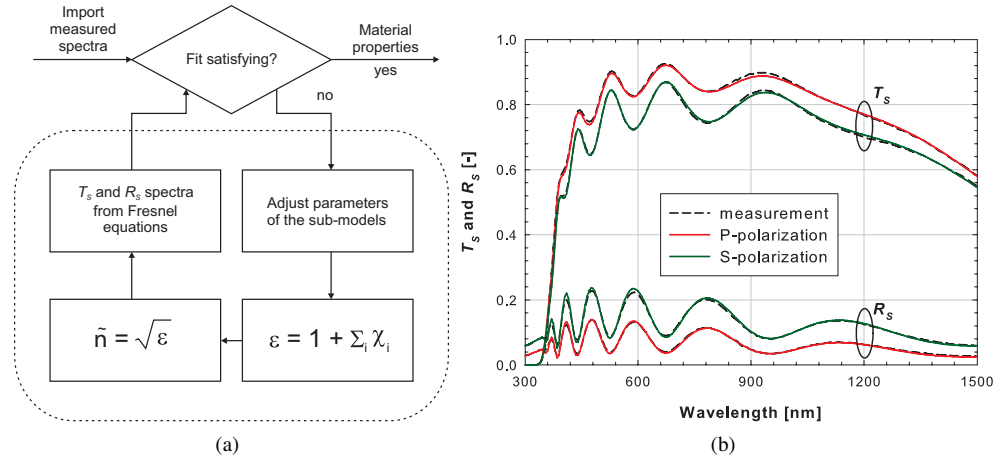
Figure 3.11: (a) Operative flow chart for fitting simulated T_S and R_S spectra on VAS measurements; (b) example of fitted ZnO:Al spectra measured at 30° of light incidence and for both S- and P-polarizations (courtesy of J. A. Sap).

define a set of susceptibility sub-models (χ_i). The sum of all χ_i allows calculating the complex permittivity of the film and then its complex refractive index. Finally this information is used in Fresnel equations, thus closing the feedback loop. Each sub-model provides susceptibility as a function of wavelength and is most accurate in a specific part of the spectrum. Intrinsic a-Si:H and nc-Si:H layers were modeled with the O'LearyJohnsonLim interband transitions model [161] for the description of band gap and tail states, with a Brendel oscillator for normal mode vibrations [162], and with Bruggeman effective medium approach in case of optically flat layers in order to consider native roughness [163]. For doped layers and wide band gap materials, like n-type nc-SiO$_x$:H or TCO films, the extended Drude model [164, 165] was also deployed to take into account the free carrier absorption observable in the considered wavelength range (300 *nm* 1500 *nm*). Finally, for textured films, light scattering effects from the surface were modeled with scalar scattering theory [166, 167]. In Fig. 3.11(b) an excellent fit is shown for ZnO:Al spectra measured at 30° of light incidence for both S- and P-polarizations. All physical models are effective in the entire considered wavelength range. However, the underlying equations cause the effects of each single model to be strong in a specific part of the spectrum. Superposition of the physical models creates a combined model that includes all effects occurring in the thin-films. This method of superposition has also been demonstrated in combination with ellipsometry measurements of ZnO:Al thin films [168]. The reliability of refractive indexes carried out with VAS-based method was repeatedly tested in thin-film silicon solar cells simulations, achieving good agreement with measured spectra such as primary reflectance and *EQE*.

3.2.8   Solar simulators

The electrical performance of solar cells is measured using so-called solar simulators. Such setups embed one or more light sources, whose combined and optically filtered spectral irradiance resembles the standard spectral power density of sunlight $P(\lambda)$ (see Sec. 1.6.1). Placing the device under this synthetic light source and sweeping the voltage across the solar cell electrodes, the illuminated *J-V* characteristic can be measured. In completely dark conditions and with light source opportunely shielded, the dark *J-V* characteristic can be tested with the same apparatus.

J-V characteristics and external parameters of solar cells presented in Ch. 4 and 6 were measured with a continuous type solar simulator. This is manually operated and formed by an Oriel He-Xe light source and a Hewlett Packard 4145B parameter analyzer (see Fig. 3.12(a)). As for the solar cells results discussed in Ch. 5, a flash type Pasan solar simulator with automatic probing stage was used (see Fig. 3.12(b)). In this case pulses of light 4 *ms* short were deployed while measuring the current-voltage characteristics. With this setup only *pin* cells could be measured.

(a)   (b)
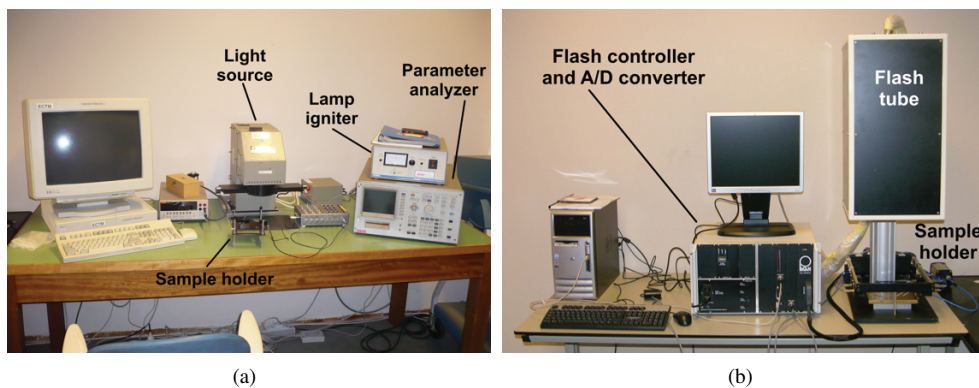
Figure 3.12: (a) Continuous type and (b) Pasan flash type solar simulators located in a PVMD measurement room.

Thin-film silicon solar cells reported in this work were fabricated on substrates capable to accommodate up to 30 dots. Measured *pin* solar cells had 4 x 4 mm^2 area, except those discussed in Ch. 6 that were measured with a 3 x 3 mm^2 area mask. The same mask was also deployed in case of *nip* cells. From both solar simulators, open circuit voltage and fill factor can be known with a good degree of confidence as long as measurements are taken in a temperature controlled environment and relatively quickly in case of continuous type. In reality, even exposing the cell for few seconds only to the continuous light, slightly lower V_{OC} might be measured for the heat transferred to the substrate. The J_{SC} from solar simulator is generally less reliable than the one obtained using Eq. 1.6. This is because the current measured under the solar simulators could result from the carriers collection of neighbouring dots not perfectly masked (*pin* case) or because of not well defined front TCO contact area (*nip* case).

3.2.9 Spectral response

A spectral response setup allows the measurement of voltage-biased External Quantum Efficiency (*EQE*). By means of a monochromator, light source is wavelength-selected and aimed at the device. To minimize the effects of peripheral light, the light beam is chopped and, thanks to a lock-in amplifier, metallic probes connected to the solar cell electrodes allow to measure the photo-generated current.

The setup used in this work was built in house and comprises a Newport illuminator/monochromator, a chopper, a substrate holder with magnetic pads to hold the probes, and a lock-in amplifier. In addition, since the output light of a monochromator may exhibit a preferential polarization due to its gratings, in order to ensure a (pseudo-) random output polarization, a wedge depolarizer made up of quartz and fused silica lenses is mounted after the output port (see Fig. 3.13).
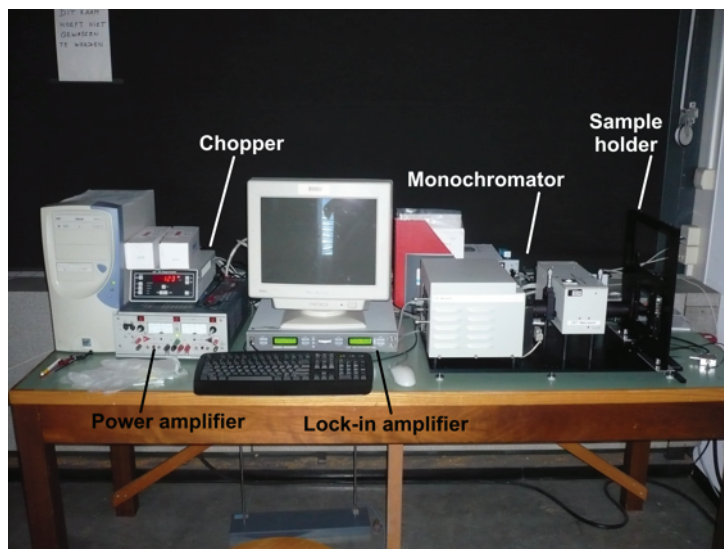
Figure 3.13: EQE equipment located in a PVMD measurement room.

3.3 Computer programs for opto-electrical modeling

3.3.1 Overview of rigorous modeling approaches for analysis of thin-film solar cells

The Finite-Difference Time-Domain (FDTD) method [169] has been commonly used to solve electromagnetic problems in thin-film optoelectronic devices [170]. A complete analysis over a wide wavelength range can be carried out by one simulation run since the method works in time domain. The electric and magnetic field components in a volume of space are evolved in time until the desired transient or steady-state electromagnetic field behaviour is fully reached. In the simple case of single wavelength calculation, FDTD modelling does not require parameterized optical properties of materials. However, for more

complex and realistic cases, wavelength-dependent complex refractive indexes of layers have to be represented by dielectric functions parameterized with Lorentz-like oscillators [171]. For semiconductor materials like amorphous silicon more than three oscillators have to be superimposed to mimic the wavelength behaviour of desired dielectric functions [172]. This leads to convergence problems in finding solution or, at least, in long computational time, if the calculation conditions are not properly chosen. Such problem affects also other numerical calculation methods. Another difficulty when using FDTD for the analysis of thin-film photovoltaic devices is related to metal back contacts. If realistic optical properties of metals such as silver or aluminium are used in simulations, convergence problems may arise. For this reason most of recent commercial FDTD software have algorithms that prevent divergence in the calculation of a model including metals.

The Finite Integration Technique (FIT) is a spatial discretization scheme to numerically solve electromagnetic field problems in time domain. The basic idea of this approach is to apply Maxwell equations in integral form to a set of staggered grids [173]. This method stands out due to high flexibility in geometric modelling and boundary handling as well as incorporation of arbitrary material distributions and material properties such as anisotropy, non-linearity and wavelength dependency. The use of a consistent dual orthogonal grid in conjunction with an explicit time integration scheme leads to memory-efficient algorithms. Successful use of FIT in simulations of thin-film silicon solar cells can be found in recent publication [174].

The Rigorous Coupled-Wave Analysis (RCWA) is an accurate computational method for evaluating the electromagnetic modes in periodic dielectric configurations [175]. Maxwell equations, arranged in partial differential form, as well as the boundary conditions, are expanded in terms of Floquet functions and turned into infinitely large algebraic equations. Depending on the accuracy and convergence speed needed, such system can be made finite and thus solvable numerically by properly filtering out higher order Floquet functions. RCWA has been efficiently applied in simulations of thin-film silicon solar cells with periodically textured interfaces [176, 177].

Another approach to solve partial differential equations, such as Maxwell equations, is the Method of Moments (MoM) [178]. In this method, calculations are executed only at a designed closed surface, rather than throughout the volume of space contained in it. For this reason MoM is more efficient than other approaches for small surface-to-volume ratio problems. The boundary element formulations and the treatment of fields only in linear homogeneous media are among the disadvantages of this approach, which lead, respectively, to computational time growing with the square of the problem size and considerable restrictions on the range of problems solvable with this method. Usage of MoM in electromagnetic problems related to photovoltaics has been recently reported [179].

3.3.2 Finite Element Method

FEM is a numerical technique for finding approximate solutions of Maxwell equations. The volume of the simulated structure is meshed (i.e. discretized) with tetrahedrons and the electromagnetic field components are computed at their vertices (nodes). In this method the Faraday and Ampere-Maxwell laws in the frequency domain are combined together to yield a single vector wave equation [180] in terms of the electric field $\mathbf{E}$, or alternatively the magnetic field $\mathbf{H}$, as follows:

$$\bigtriangledown \times \frac{1}{\mu_r} \bigtriangledown \times \mathbf{E} - k_0^2 \varepsilon_r \mathbf{E} = i k_0 Z_0 \mathbf{J} \qquad (3.5)$$

where $\mathbf{J}$ is the current density, ε_r and μ_r denote, respectively, the relative permittivity and magnetic permeability of the medium, $k_0 = 2\pi f \sqrt{\mu_0 \varepsilon_0}$ and $Z_0 = \sqrt{\mu_0/\varepsilon_0}$ are the propagation constant and characteristic impedance of free space. Using either the variational approach [181] or the method of weighted residuals [182, 183] the Eq. 3.4 and its dual equation on the magnetic field can be cast in a matricial form, $\underline{\mathbf{A}} \cdot \mathbf{x} = \mathbf{b}$. The vector $\mathbf{x}$ contains the unknown spatial components of the electromagnetic field, whereas the known vector $\mathbf{b}$ is determined on the basis of boundary conditions and forced excitation. The coefficient matrix $\underline{\mathbf{A}}$ is square, sparse, and symmetric, whose elements indicate the material properties at the nodes. Once such system of equations has been set up, its solution is achieved by the application of an iterative or direct solving technique [184]. Direct methods are suited for reduced size problems only, since they are computationally very demanding. In typical problems regarding realistic 3-D optical devices, iterative method-based procedures are widely used by virtue of the efficient handling of sparse linear systems [185]. It must be emphasized that the mesh generation within FEM can be cumbersome for large three-dimensional structures (e. g. large amount of random access memory (RAM) needed) [186] and, indeed, mesh set-up times exceeding the solution time of the electromagnetic problem have been outlined in the scientific literature.

In FEM, besides tetrahedrons, also conformal elements can be employed to better approximate curved geometries. In this way, an accurate modeling of inhomogeneous materials and complex non-conformal geometries can be achieved in a straightforward manner [181]. Such flexible meshing capability is a clear advantage over FDTD or FIT schemes based on Cartesian meshes, wherein each cell of the computational lattice is implicitly assumed to be filled by a homogeneous material [173, 187] and therefore a stair-case approximation of the morphology has to be used. Another appealing feature of FEM is the simple handling of arbitrary wavelength-dependent relative permittivity of the materials simulated. Furthermore, optical effects occurring at corrugated metal surfaces or metal nano-particles can be efficiently modeled with FEM. It is worth mentioning that FEM-based algorithms feature a reduced frequency scaling of the computational burden compared to the other methods [188], making the calculations in a 3-D space with this method very fast, provided that an adequate amount of RAM is available. Finally, FEM can be easily used for accurate multi-physics simulations, providing the capability to couple the electromagnetic field-based characterization with, for instance, mechanical or thermal modeling [189]. Such feature allows for the enhanced modeling of solar cells with dispersive materials having temperature-dependent electrical properties [190]. The FEM is a good choice for solving the electromagnetic problems over complicated structures. The method appears to be very effective also for evaluating the optical situation in thin-film PV devices [191].

3.3.3   A 3-D FEM software: HFSS

A commercial implementation of FEM called the High Frequency Structure Simulator (HFSS) [192, 193] was used in this work. Its optimized algorithm is capable to solve 3-D electromagnetic problems also at optical frequencies. By taking advantage of multi-core architectures and providing a wide range of boundary conditions as well as symmetry capa-

bilities, the HFSS performs simulations in short times. Furthermore the CAD-like graphic user interface allows designing complex structures easily. The HFSS runs on a relatively inexpensive workstation (dual six-core X5670 Intel Xeon architecture equipped with 24 GB DDR3-1333 type RAM memory).

Once the simulation of the design is set up (structure, boundary conditions, excitation(s), wavelength range, initial wavelength, and materials properties), FEM-based algorithms in HFSS operate through three phases: *meshing*, *solving*, and *sweeping*. In the first phase, for a given wavelength, the volume of the design is discretized in tetrahedrons. During the second phase, the resulting system of equations, $\underline{\mathbf{A}} \cdot \mathbf{x} = \mathbf{b}$, is iteratively solved. At each iterated steps, the volume of the design is approximated more thoroughly by raising the number of tetrahedrons (*mesh adaptation*). If the difference between the values of $\mathbf{x_i}$ calculated at the ith iteration step and the values of $\mathbf{x_{i-1}}$ calculated at the $(i-1)^{th}$ iteration step is smaller than a certain threshold value, the iteration stops and the system of equations is considered *converged*. From this state, the last phase starts, during which the electromagnetic field in the meshed volume for each wavelength previously set up is calculated. Therefore, once the initial wavelength is specified, each simulation solves at least two iteration steps before starting the wavelength sweep. To improve the numerical stability for the simulations reported in this thesis, the sweeping phase was set to start only after at least three converged iteration steps in a row. The schematic flow chart of FEM-based algorithm is reported in Fig. 3.14 with highlighted parts: input, adaptive part, iterative part and output.
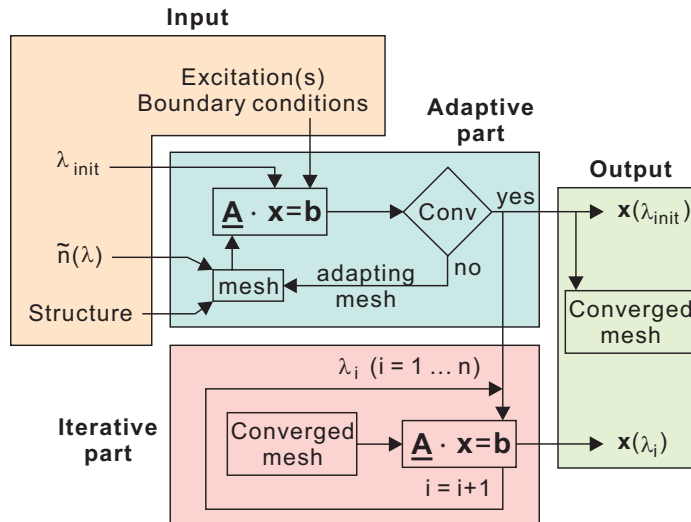
Figure 3.14: Schematic flow chart of FEM-based algorithm (the rhombic conditional block checks if the convergence has been reached).

3.3.4   A 1-D opto-electrical simulator: ASA

Solar cell is a semiconductor device, obeying Poisson, current density, and continuity equations. The Advanced Semiconductor Analysis (ASA) software was deployed to simultaneously solve these equations. ASA is developed at Delft University of Technology and widely

used in the field of thin-film silicon technology [194–197]. This fast software is especially designed for simulating devices based on amorphous and (nano-) crystalline semiconductors. It is a one-dimensional (1-D) solver, which uses the free electron concentration, n, the hole concentration, p, and the electrostatic potential, ψ, as variables. Boundary conditions can be either ohmic or Schottky-type, whilst parallel and series resistances can be varied with external circuit settings. After reading structure statements from an input file, the ASA engine generates a grid along z-direction (depth of the device) and calculates the density of states. After that, it carries out the spectral absorption rate (or reads it from an external file) and solves the Poisson equation at thermal equilibrium. Finally the current density-voltage characteristic is computed upon solving semiconductor equations using numerical techniques such as Newton [198] or Gummel [199] methods.

3.3.5 Coupling HFSS and ASA

The link between optical and electrical behaviour of a solar device is represented by the optical generation rate $G_L(r)$ (see Sec. 2.2):

$$G_L(r) = \beta \cdot \int_{\lambda_{min}}^{\lambda_{max}} \Phi(\lambda) \cdot a(r,\lambda) d\lambda. \qquad (3.6)$$

where r denotes the Cartesian triplet (x, y, z), λ_{min} and λ_{max} constitute the wavelength range of interest, $\Phi(\lambda)$ is the incident photon flux, $a(r,\lambda)$ is the spectral absorption rate measured in m^{-1}, and β is the generation quantum efficiency (equal to one).

As described in previous section, ASA program can read the spectral absorption rate from an external source. This feature enables to plug in the continuity equation the optical generation rate carried out with other means, like a 3-D Maxwell equation solver. However, since ASA can describe the opto-electronic behaviour of the device along z-direction, a numeric compression from 3-D $a(r,\lambda)$ to 1-D $a(z,\lambda)$ must be carried out. In Sec. 7.3.2 a procedure will be introduced to handle this matter.

Chapter 4

Periodic diffraction gratings

This chapter will deal with the investigation and implementation of transparent rectangular periodic diffraction gratings in thin-film silicon solar cells. Morphological characteristics and optical behaviour of these textures will be analyzed. Results obtained on single junction solar cells in *pin* configuration fabricated on 1-D periodic gratings spanning different periods and groove heights will be shown. Later, a 3-D optical modelling will be introduced to find the optimal combination of geometrical parameters characterizing both 1-D and 2-D transparent rectangular gratings.

4.1   Introduction

The manipulation of light is instrumental for increasing performance of thin-film silicon solar cells. As discussed in Ch. 2, the term light management covers a broad field of approaches aimed at the enhancement of light absorption inside the absorber layers. Among these approaches, textured surfaces allow light scattering for achieving high photo-current density. State-of-the-art random textures scatter continuously light from specular direction to wide angles (i.e. close to $90°$) with intensity decaying towards large angles. Diffraction gratings with sub-micron periodicity are attractive alternative to this paradigm. In fact, they enable angle-selective scattering [200] for which light is intensively diffracted only at specific angles. This effect can be manipulated by controlling gratings geometrical features. In the left-hand side of Fig 4.1(a) 1-D periodic diffraction grating on a transparent substrate is schematically shown. Light impinging on such type of texture splits in a number of diffraction modes (m_i for different scattering angles θ_i) aside the so-called specular component 0th order mode (m_0). The arising of such modes, their number, and the intensity of light associated with them depend on the wavelength and incident angle of exciting light, on the incident and diffractive media (n_1 and n_2, respectively), and on grating geometrical features, such as shape, period (P), groove height (h) and duty cycle[1] (d_C). It will be shown that the period sets the highest wavelength for which scattering occurs, while the groove height is somewhat proportional to the intensity of such scattering. In this respect the flat interface

---

[1]The duty cycle is usually defined as the percentage ratio between the distance for which the grating presents the highest value and the grating period.

can be seen as a periodic grating with groove height equal to zero, where the scattering is suppressed (i.e. only specular component of light is allowed). For 2-D gratings similar properties hold but with an expected higher intensity of scattered light. In this case, in fact, two families of diffraction modes arise from the texture diffracting light more efficiently. These two groups of diffraction modes are rotated with respect to each other by 90° in case of square lattice or by an angle θ_L, defining the deformation degree of the lattice from squared to triangular (see right-hand side of Fig. 4.1(a)).

The optical behavior of diffraction gratings in solar devices depends, however, also on other factors. For instance, it has been shown that finding an optimal combination of geometrical features for a type of absorber layer may not be the optimal combination when switching to another kind of absorber layer or just changing its thickness [191, 201, 202]. Another important factor is the non-conformal growth of TCOs or amorphous and nanocrystalline materials on textured substrates, that results in the so-called leveling effect (see Sec. 4.4.1) [203]. Easily detectable by cross-sectional SEM imaging, such effect tends to progressively flatten layer by layer the initial grating morphology by rounding the gratings shape and reducing the groove height while remaining unaltered the periodicity. In such practical scenario, deep grooves would be the natural choice to balance the leveling effect and ensure the light scattering, especially when dealing with thick absorber layers. However, depending on thickness and deposition conditions, coating layers may self-organize in bulb-like features around gratings grooves creating voids potentially detrimental for electrical performance of the solar cell [141, 147]. Therefore a reasonable aspect ratio (h/P) is desirable for achieving the trade-off between optical and electrical performance. To take full advantage of light scattering delivered by periodic diffraction gratings, it is necessary to find the right combination of all aforementioned factors. This represents an extremely significant optimization task that can be handled with 3-D modeling, as it will be shown in Sec. 4.5.

In recent years, with the advent of nano-metric patterning techniques like laser scribing or (electron beam) lithography and with the usage of nano-imprinting techniques on transparent polymers [154], many sorts of 1-D and 2-D periodic diffraction gratings with well defined geometrical features have been prepared on glass, c-Si wafers and on plastic or metallic foils. For example, in Fig. 4.2 the highly detailed AFM scan of a transparent 1-D grating texture on glass substrate used in this work is reported. The viability of these technologies for photovoltaic applications has been demonstrated with the fabrication of single and multi-junction thin-film silicon solar cells in both *pin* [204–207]and *nip* [141, 208–210] configurations. With respect to solar cells on flat substrates, solar cells on optimized gratings show enhanced absorption. The implied photo-current of such solar cells is similar to that of randomly-textured solar cells, in spite of generally different behavior for long wavelengths of the external quantum efficiency. In fact, in case of random textures, the EQE just smoothly decays to zero, whereas in case of gratings the EQE may exhibit resonance peaks while falling to zero.

4.1.1 Resonance peaks, absorption limits and comparison to random textures

Resonance peaks in *EQE* of gratings-based solar devices have been explained in the framework of waveguide theory [211]. Thin-film silicon solar cell is ideally treated as planar
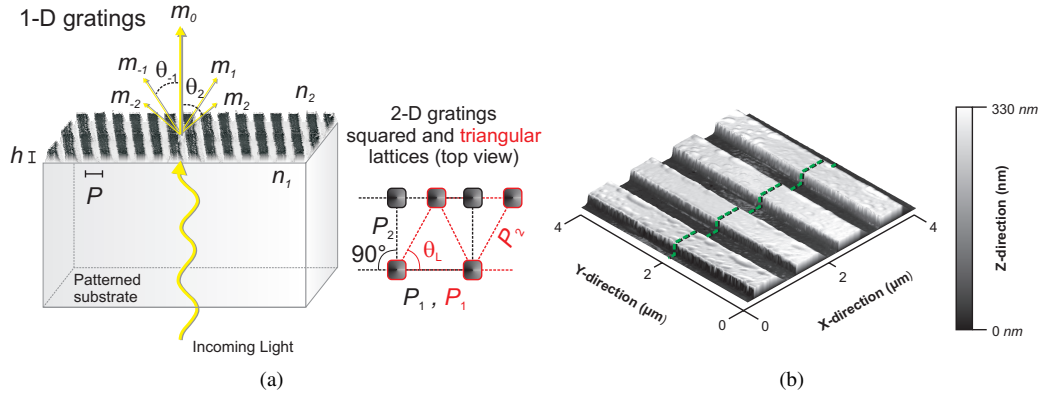
Figure 4.1: (a) Sketch of a 1-D grating on transparent substrate developing diffraction modes; (right) top view of 2-D gratings squared and triangular lattices. P_1 and P_2 indicate the periods along the 2-D lattice; (b) AFM scan of one of the rectangular 1-D grating on transparent substrate deployed in this work (P = 1000 nm, $h \sim 300$ nm, $d_C \sim 50\%$). Arbitrary cross-section is highlighted with the dashed green line.

multi-layer structure, where supporting and absorber layers are sandwiched be-tween the textured front TCO and the metallic back contact (so-called cladding layer). In such an optical system, wave guiding can effectively take place. Light incident on the textured surface is coupled in thin-films passing from vertical incidence above the front texture to horizontal propagation and (partial) absorption in the layers beneath. Wave guiding, which is not allowed in case of flat interfaces due to energy and momentum conservation [212], applies to both randomly and periodically textured interfaces. This is because they have essentially the same physical background. A random texture can be seen in fact as a superposition of sinusoidal gratings via spatial Fourier expansion (see Sec. 5.3). The main difference between these two classes of textures is the wavelength-dependent distribution of guided modes [206]. Random textures, scattering light continuously over all angles, are capable to couple light in a continuum of modes. On the other hand, periodic textures can couple light only at specific wavelengths (i.e. energies), since light is scattered only at well-defined angles. These wave guiding behaviors are ultimately reflected in different EQEs at long wavelength range.

The question whether periodic textures can exhibit similar or better scattering performance with respect to random textures when embedded in solar cells has been recently addressed both theoretically and experimentally.

From theoretical point of view, a newly-developed concept of upper absorption limit allows for the calculation of enhancement factor when dealing with periodic textures [213]. As special case, it also contains the previously discussed A_{UL} limit (see Sec. 2.1.1), considering random textures like periodic gratings having periodicity equal to infinity. The enhancement factor in such broader concept of absorption limit is proportional to the ratio

between the number of guided modes in the absorber layer and the number of *channels*[2]. In case of 2-D periodic textures, the enhancement factor can be higher than the classical $4n^2$ limit, reaching a maximal value of $4\pi n^2$ at $P = \lambda$ for squared gratings lattice or $8\pi n^2/\sqrt{3}$ at $P = 2\lambda/\sqrt{3} \approx 1.15\lambda$ for triangular grating lattice. However, such enhancement factor assures higher absorption only in narrow wavelength ranges around the resonance peaks, holds only for normal incidence because of its strong angular dependency, and tends anyway to $4n^2$ limit for $P >> \lambda$. Given the same caveat, in case of 1-D gratings the enhancement factor is $2\pi n$ achieved at $P = \lambda$ and decaying to πn for $P >> \lambda$. Although characterized by a lower enhancement factor, 1-D periodic gratings are interesting textures for studying purposes. Thanks to their polarization dependency, 1-D gratings used in solar cells offer a good tool for sampling guided modes from angle resolved and polarization dependent *EQE* measurements [214].

From waveguide theory and from the introduced theoretical limits, it appears that gratings periodicity should be chosen in order to maximize the number of guided modes per channel in the spectral region of weak absorption of the absorber layers. The arising of such modes is directly linked to the intensity of diffraction modes in the angle-selective scattering, which in turn depends on gratings height. Once again, the aspect ratio of gratings plays a key role in achieving optimized scattering. Something similar is important for random textures as well, where taller features are required to efficiently scatter light at large angles (see Sec. 5.8). With this type of texture as well, one should pay attention to the right balance between optical and electrical performance [127]. Furthermore, regardless the type of texture used in fabricated devices, expected enhancements should be corrected with a more realistic interpretation of the theoretical limits. Thick front TCOs with relatively low refractive index are practically used for state-of-the-art solar cells. In this respect, guided modes are enabled also in the front electrode and if its extinction coefficient is not negligible, parasitic absorption can take place here. For this reason, in all discussed enhancement factors for silicon absorber layers, n_{Si}^2 should be replaced with $n_{Si}^2 - n_{TCO}^2$ when dealing with realistic structures [215].

From experimental point of view, since the first attempts of solar cells deposited on periodic gratings, comparisons with available random textures have been presented and discussed. The usual evaluation is assessed by superposing measured *EQE*s from differently textured cells and calculating implied photocurrent density enhancement with respect to a reference flat cell. However, this type of evaluation should not be considered *conclusive* since the configurations under test might not be optimal with respect to either random or periodic textures. This is because of different materials constituting or covering the textured surface, as-grown morphologies of deposited layers and deposition temperatures.

In case of *pin* configuration, for example, standard textured front TCOs deposited on transparent superstrates may present similar morphologies but different absorptance, like in case of SnO_2:F and ZnO:B, or may grow optically flat, like ZnO:Al or In_2O_3:SnO_2, but once again with different opto-electrical properties. The main challenge is therefore to deposit solar cells on the same TCO but endowed with different textures, in order to decouple the optical behaviour (EQE and JSC) from the electrical behaviour (V_{OC} and *FF*). Only recently, with the successful implementation of periodic 2-D pattern via RIE or random textures via nano-imprinting technique on glass and the development of hydrogenated

---

[2]A channel is defined as a plane wave that couples to the guided mode [215].

indium-oxide TCO (In_2O_3:H, IOH) [123], an unbiased comparison could be done for a-Si:H single junction solar cell [206]. In this case, despite having chosen an optimal periodicity for the used 2-D grating, *pin* cells on both types of textures showed the same J_{SC} and η. The trade-off between optical and electrical response related to the aspect ratio of the surface features was indicated as major issue to tackle for pushing higher the efficiency of both cells. Therefore the question remains still open whether 2-D gratings can outperform random textures using, for instance, rougher morphologies together with SiO_x-based materials [97].

In case of *nip* configuration, the comparison is in principle slightly simpler, because ITO is almost always chosen as front electrode TCO and the back reflector is usually given by the same pair of materials: Ag with a thin ZnO layer on top. In particular, Ag coats the morphology present on the substrate or determines itself the morphology, like in case of hot Ag [216]. After some attempts [141, 209, 217], however, a more impartial approach is still needed regarding the choice of morphologies to compare.

Despite theory predicting a better optical response for solar cells on 2-D periodic gratings with respect to random textures, reported solar cells on both types of textures still exhibit pretty similar behavior. A *conclusive* method, valid for both *pin* and *nip* configurations, would be to experimentally compare the best textures of both kinds specifically designed for the same solar cells structure and the same absorber layers. Of course, the same front TCO and the same back reflector materials should be deployed as well as doped SiO_x layers. Materials and design tools to approach such method do exist. Particularly, using waveguide theory it is possible, together with 2-D or 3-D optical modeling, to indicate an optimal grating design for specific solar cell structure and absorber layers. On the other hand, using Perlin noise algorithm, it is possible to generate randomly-textured surfaces optimized for broadest AID, highest haze, and maximal absorption [218].

4.1.2 Studying approach

1-D gratings on transparent glass substrates with ideally rectangular shape were chosen as periodic textures for studying the effect of angle-selective light scattering in thin-film silicon solar cells. Morphological and optical properties were studied and compared to the reference randomly textured Asahi-U substrate. The adaptation of a baseline process for *pin* configuration led to the fabrication of a-Si:H single junction solar cells on 1-D gratings for different periods, different groove heights, and Ag back reflector.

The following step was to study the implementation of a back reflector formed by ZnO and Ag. It has been shown, in fact, that in the vicinity of textured interface between n-type layer and bare Ag, the lowest P-polarized mode (P_0) behaves like a surface plasmon polariton [219]. As the electro-magnetic (E-M) field resonates along the corrugated border between the two materials, parasitic absorption takes place [128]. The insertion of a ZnO film between n-layer and Ag, besides preventing silver from diffusing into silicon layers, mutates the aforementioned P_0 mode into a regular wave guided mode [219], potentially enhancing the absorption in the absorber layer.

With an accurate 3-D optical modeling based on finite element method (see Sec. 3.3.2), not only best combinations of P and h were found for a-Si:H single junction solar cells on 1-D and 2-D rectangular gratings, but also the optical losses occurring in the supporting layers were calculated. It will be shown that the parasitic losses in the n-layer are mostly

suppressed while the ZnO layer takes on the major part of losses at the back side of the solar cell structure.

4.2   Morphological analysis

Results reported were achieved using several 1-D periodic gratings on glass with nominal P in the range from 400 *nm* to 1000 *nm*, h from 50 *nm* to 300 *nm*, d_C equal to 50%, and rectangular cross-section. A process developed by OM&T B.V. MoserBaer for production of Blu-ray^{TM} discs [220], involving the pattering of a UV-curable lacquer spun on glass, was deployed to fabricate these structures. The obtained textured substrates are rigid, transparent and nano-textured, therefore suitable for *pin* configuration.

The morphological analysis of gratings was done by means of AFM. As an example of such study,Fig. 4.2 presents arbitrary cross-section, height distribution, autocorrelation function (ACF), and angle distribution of the 1-D grating shown in Fig. 4.1(b) ($P = 1000$ *nm*, $h \sim 300$ *nm*, $d_C \sim 50\%$) compared to those of Asahi-U type TCO (reference random texture). In this context the height h is the peak-to-peak groove depth.

Comparing the two arbitrary cross-sections (see Fig. 4.2(a)), the intrinsic difference between the two morphologies is evident: Asahi-U texture shows the expected random behavior and the 1-D grating exhibits a shape quite close to the nominal rectangular and values of height alternating between the bottom of the pattern (close to 0 *nm*) and the top of the periodic ridges (close to 300 *nm*). In addition, nano-ripples due to fabrication process are present on flat parts of the pattern, while height and duty cycle are slightly smaller than the nominal values. These facts are visible in the discrete nature of the height distribution of 1-D grating calculated over the entire AFM scan area (see Fig. 4.2(b)). The two peaks, representing the bottom and the top parts of the grating, are not placed around $h = 0$ *nm* and $h = 300$ *nm*, but slightly shifted around $h = 5$ *nm* and $h = 270$ *nm*, respectively. Furthermore, since the values of these peaks are not the same, it is possible to carry out a more realistic value for the duty cycle close to 65%. On the other hand, the height distribution of Asahi-U morphology is not discrete and follows a Gaussian shape, highlighting the random nature of such texture. Regarding the period of 1-D grating, the nominal value is instead verified, since consecutive local maxima or minima in the *ACF* are spaced by 1 *μm* (see Fig. 4.2(c)). In case of Asahi-U, the *ACF* decays quickly to zero with very limited and random oscillations. Finally, the steepness of the 1-D grating walls is confirmed with the angle distribution, where almost vertical slopes are measured around 77° (see Fig. 4.2(d)). Slopes close to 0° indicate instead the general flatness of top and bottom parts of the patterns. In case of Asahi-U facets, the angle distribution extends continuously from 0° to around 65° with an average of 27.5°.

The morphological analysis of other gratings is omitted for brevity, as the discussed *discrete* properties hold for different shapes, periods, heights, and duty cycles. In the following, AFM technique will be used again for studying the evolution of surface roughness in solar cells (see Sec. 4.4.1) and for carrying out the spatial frequency surface representation (see Sec. 5.3).
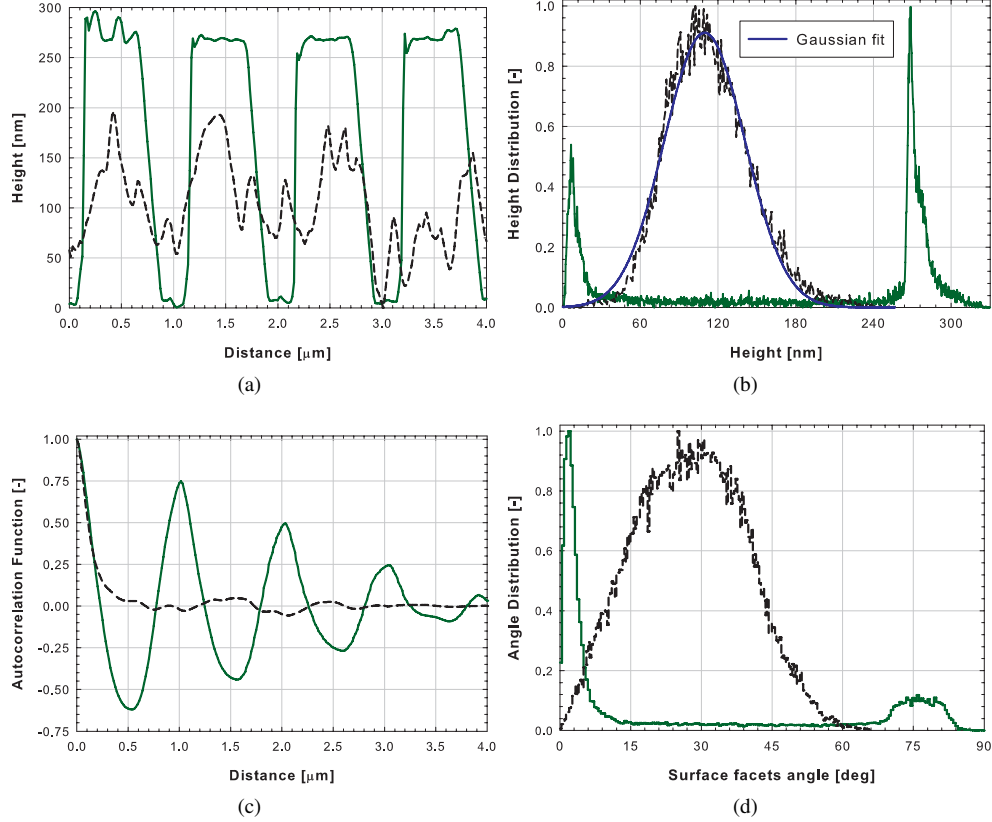
Figure 4.2: (a) Arbitrary cross-section, (b) height distribution, (c) ACF, and (d) angle distribution of 1-D grating (P = 1000 nm, h ∼ 300 nm, d_C ∼ 50%, green dashed lines) and Asahi-U type TCO (black lines). Blue line in (b) is the fit of Asahi-U type TCO height distribution operated with Gaussian distribution.

4.3 Scattering properties of 1-D periodic gratings

Scattering properties of transparent diffraction gratings are analyzed by looking at the angular intensity distribution and haze parameter in transmittance (AID_T and H_T, respectively, see Sec. 3.2.6). The AID_T measures the intensity of specular component and diffraction modes for different wavelengths. The H_T, which is fundamentally the integration of AID_T over the scattering hemisphere [158], evaluates the wavelength-dependent fraction of scattered light.

4.3.1 Angular intensity distribution

Periodic gratings scatter light in well-defined angles at different wavelengths. The AIDT of a 1-D periodic grating (P = 1000 nm, h ∼ 150 nm, d_C ∼ 50%) on glass measured in air

and for perpendicular incidence is shown together with its contour plot in Fig. 4.3. The optical system was given by incident light impinging on the glass substrate, going through the lacquer, and finally exiting at patterned lacquer / air interface. The 1-D grating under test was mounted vertically. In this way diffraction modes laid on the rotation plane of ARTAs small IS (see Fig. 3.10) and could be measured. Light impinging on such optical system scatters in six different diffraction orders and the intensity of scattered light decreases for higher orders. For all wavelengths, some part of light passes straight through the periodic texture (0th mode or specular transmittance). In these measurement conditions, the higher order diffraction modes are symmetric with respect to the $0th$ mode and can be grouped in *pairs*, each formed by modes having the same integral number but with opposite sign.

In Sec. 4.3.2 light intensity associated with diffraction modes will be discussed, while a condition to suppress the 0th order mode will be presented in Sec. 4.3.3. At this stage the focus is on the scattering angles provided by the periodic grating. The diffraction equation predicts such scattering angles [221]:

$$\theta_m = arcsin \left[\frac{m\lambda}{n_2 P} + \frac{n_1}{n_2} sin(\theta_{inc}) \right] \qquad (4.1)$$

where θ_m is the $m-th$ wavelength dependent scattering angle, m is a positive or negative integer number, λ is the wavelength *in vacuo*, P is the grating period, θ_{inc} is the angle of incidence, and n_1 and n_2 are the refractive indices of the incident and diffractive media, respectively. For $m = 0$ Eq. 4.1 simply reveals Snell law. From the diffraction equation follows that the scattering angles θ_m do not depend on the particular shape of the grating.

Simplified to accommodate measurement conditions ($\theta_{inc} = 0°$ and $n_2 = 1$), Eq. 4.1 gave the lines superposed on the contour plot in Fig. 4.3(b). Measured wavelength-dependent scattering angles closely match calculated theoretical values. Not shown in Fig. 4.3 is the threshold wavelength $\lambda_0 = n_2 \cdot P$. For $\lambda > \lambda_0$ and $m = \pm 1$ the argument of *arcsin* function is higher (lower) than 1 (-1), leading to imaginary scattering angles. Therefore, in such wavelength range also the 1st order diffraction modes vanish and only specular component remains. In case of the 1-D grating under test λ_0 is $n_2 \cdot P = 1000\ nm$. Another interesting property is noticeable for $\lambda < \lambda_0$, where sub-ranges of wavelengths contain a certain number of diffraction modes. In Fig. fig:Fig.4.3b, for wavelengths between $P/2$ and P, only the 1st order modes are present; for wavelengths between $P/3$ and $P/2$ also the 2nd order modes appear; and so on. Generalizing, for $m \geqslant 1$, the first $2m$ diffraction modes coexist in the wavelength range $[n_2 P/(m+1), n_2 P/m]$.

Using Eq. 4.1 for $\theta_{inc} = 0°$, calculated diffraction modes from a grating with $P < 1000\ nm$ or $n_2 \neq 1$ are shown in Fig. 4.4(a) and 4.4(b), respectively. In the first case ($P = 600\ nm$ and $n_2 = 1$), the first diffraction mode moves as expected to shorter wavelengths. Fewer diffraction modes than in case of $P = 1000\ nm$ can be accommodated in the wavelength range of interest (usually from $300\ nm$). In the second case ($P = 400\ nm$ and $n_2 = n_{a-Si:H}$), since $n_2 > 1$ in the wavelength range of interest, up to seven pairs of diffraction modes can be triggered. These calculations show that both period and diffractive medium contribute to the development of diffraction modes. In thin-film silicon solar cells on gratings, the periodic morphology is transferred at each separation interface. Several combinations of n_1, $n_2 \cdot P$, and h coexist simultaneously; therefore looking for the optimal arrangement is not a trivial task. In the following, given a thin-film silicon solar cell structure (i.e. sequence of pairs of n_1 and n_2), numerical modeling will be deployed to find the optimal combination
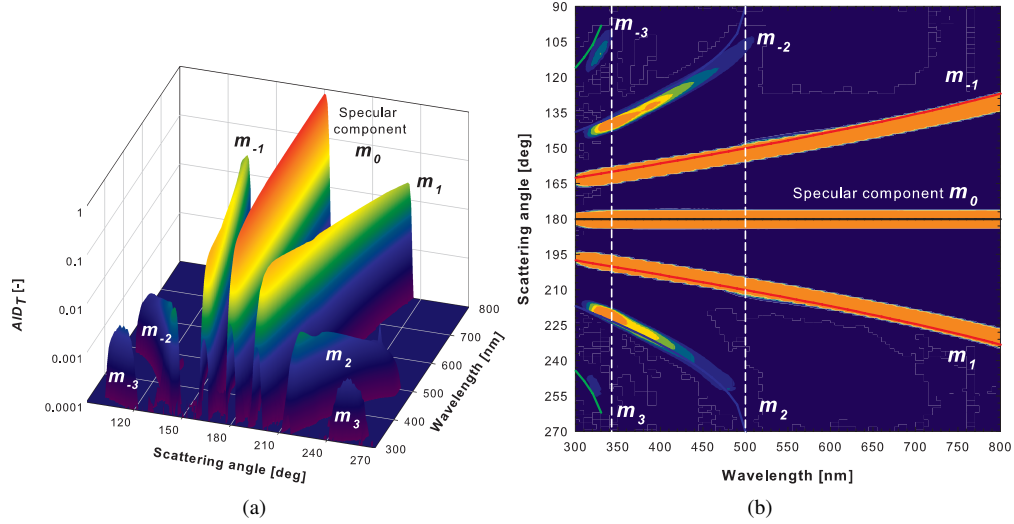
Figure 4.3: (a) AID_T measured in air ($n_2 = 1$) and at perpendicular incidence ($\theta_{inc} = 0°$) of a 1-D periodic grating (P = 1000 nm, h ~ 300 nm, d_C ~ 50%) and (b) its contour plot with superposed lines calculated from Eq. 4.1. AID_T is represented in logarithmic scale; vertical white dashed lines in (b) mark different wavelength sub-ranges.
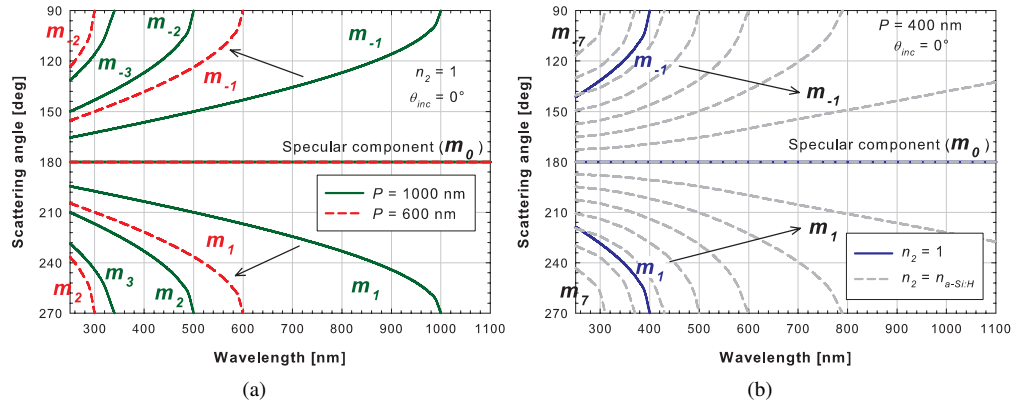
Figure 4.4: Calculated wavelength-dependent scattering angles (a) for two different periods (P = 1000 nm and P = 600 nm) in air and (b) for two different diffractive media n_2 (air and real a-Si:H) considering P = 400 nm. In both cases $\theta_{inc} = 0°$.

between period and height.
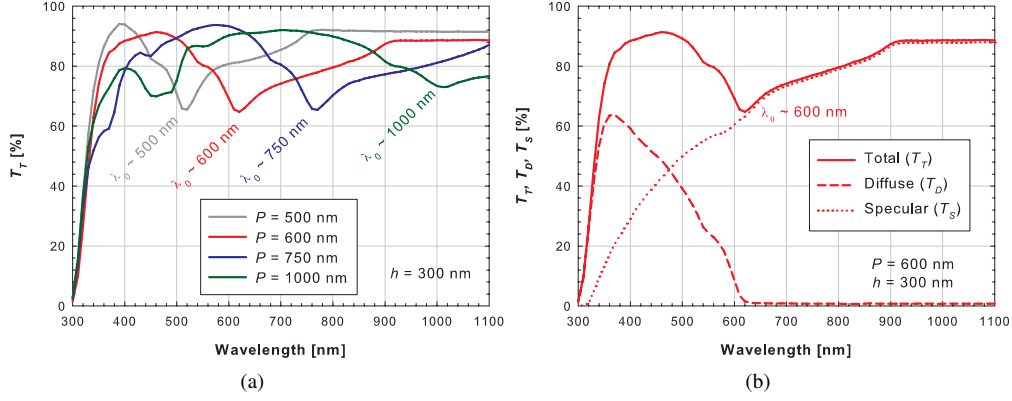
Figure 4.5: (a) Measured T_T of gratings with different periods but same nominal height (h = 300 nm); (b) decomposition of T_T in T_D and T_S components for the grating characterized by P = 600 nm and h = 300 nm.

4.3.2 Optical analysis of transparent diffraction gratings

The IS accessory was used to measure the total and diffuse transmitted light through the 1-D gratings (T_T and T_D, respectively) and the total reflectance (R_T) at perpendicular incidence. From such spectra, specular component (T_S) and haze parameter (H_T) in transmission could be easily calculated (see Sec. 3.2.6) as well as the absorptance of the patterned substrate ($A_{grating} = 1 - R_T - T_T$). Incident light was un-polarized and the optical system was set up as described in previous section. In Fig. 4.5(a) T_T of several gratings with different periods and nominal h = 300 *nm* is reported. The investigated substrates present portions of spectrum around or above 90% and dips down to 70%.

These dips blue-shift for smaller periods and are located in the vicinity of specific wavelengths. They can be recognized as the aforementioned threshold wavelengths λ_0 characterizing each diffraction grating. In fact, decomposing the total transmittance of one of the gratings under test in diffuse and specular components (see Fig. 4.5(b)), the rise of T_D is seen for $\lambda < \lambda_0$, while for $\lambda < \lambda_0$ only T_S is allowed. In case of P = 1000 *nm*, it is also possible to recognize the onset of the 2nd order modes, whose presence is expected for λ ¡ 500 *nm*. Threshold wavelengths are indicated in Fig. 4.5 with $\sim$ sign to address small fluctuations from the nominal value of P occurring at the fabrication stage of the diffraction gratings.

The dips in transmittance observed in Fig. 4.5(a) can be explained in terms of absorptance and total reflectance. Fig. 4.6(a) shows T_T, R_T and $A_{grating}$ of a periodic grating. Peaks are present also in absorptance and total reflectance, located in correspondence with the threshold wavelength $\lambda_0 = P$. It can be argued that (i) the absorption peak accounts for a certain light coupling in the patterned lacquer and (ii) the reflectance peaks to the left and to the right of λ_0 regulate the passage from pure specular to diffracted regime in transmittance, ensuring the conservation of energy.

In Fig. 4.6(b), the haze parameter of the investigated 1-D gratings is shown. Following
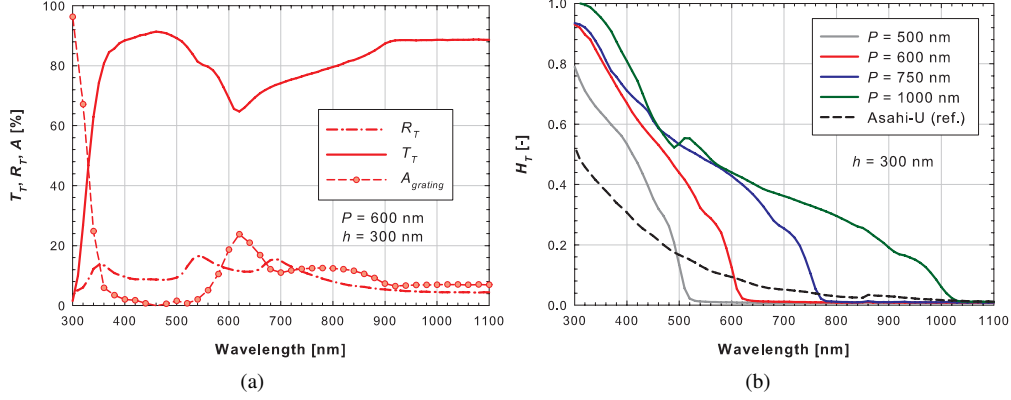
Figure 4.6: (a) Total transmitted and reflected light for a 1-D grating (P = 600 nm and h = 300 nm). A$_{grating}$ refers to the patterned substrate (red symbols); Haze in transmission of gratings with different period and constant height (h = 300 nm). Asahi-U (black-dashed line) is present as reference (exponential decay).

from the nature of diffuse transmittance in diffraction gratings and from Eq. 3.3, the haze parameter assumes values higher than zero only for $\lambda < \lambda_0$. Since $\lambda_0 = n_2 \cdot P$ and having taken measurement in air, reported hazes shrink towards shorter wavelengths for smaller periods. It has to be noted, however, that such optical situation radically changes when the diffractive medium is different than air (see Fig. 4.4(b)). For example, considering as diffraction medium a-Si:H, the haze parameter will enlarge beyond the threshold wavelength in the air, therefore even a diffraction grating with small period can potentially scatter light in the region of weak absorption of a-Si:H. The maximum value of these hazes (H_{T-max}) occurs in the neighborhood of $\lambda = h = 300$ *nm*. In the next section a condition relating groove depth and H_{T-max} will be given. In the same plot, the haze in transmission of Asahi-U type TCO is also reported as prominent example of wavelength dependent exponential decay, which characterizes randomly textured morphologies (see Sec. 5.4).

If the number of diffraction modes and their wavelength ranges depend on the gratings period, the intensity of diffracted light is regulated by the groove depth. Decreasing such height, the haze parameter also decreases as the textured substrate approaches an optically flat configuration. To asses this relation, it must be noticed that the intensity of light scattered in each diffraction mode can be related to either specular or diffuse components of transmitted light. In particular, intensity I_0 of the 0$^{\text{th}}$ order mode is T_S, while, for $m \neq 0$, intensities I_m are added up provide T_D.

For perfectly conducting (*opaque*) 1-D sinusoidal gratings in paraxial conditions ($\lambda < \lambda_0/2$) and for S-polarization[3], I_m for different m depend on the height of the grating through the argument of squared Bessel functions of the first kind (J_m^2) [221]:

---

[3]Incident light is said P-polarized if the electric field component is parallel to the 1-D grating. On the other hand, if the electric field component is perpendicular to the grating, the incident light is said S-polarized.

$$I_m \sim J_m^2 \left(\frac{2\pi}{\lambda} \cdot h \right) . \tag{4.2}$$

In non-paraxial ($\lambda/2 < \lambda < \lambda_0$) and in smooth surface conditions ($\lambda > \lambda_0$), Eq. 4.2 can be modified to properly probe the optical behavior of the diffraction grating in the passage from diffracted to pure specular regime [222]:

$$I_m \sim J_m^2 \left[\frac{2\pi}{\lambda} \cdot \frac{h}{2} \cdot (cos\theta_{inc} + cos\theta_m) \right] \tag{4.3}$$

where θ_m is the scattering angle. The haze parameter in reflection of such opaque gratings in case of S-polarization (H_R^S) can be written as:

$$H_R^S \hat{=} \frac{R_D^S}{R_S^S + R_D^S} = \frac{\sum\limits_{m \neq 0} J_{m_n}^2}{J_{0_n}^2 + \sum\limits_{m \neq 0} J_{m_n}^2} \tag{4.4}$$

where R_D^S and R_S^S are, respectively, diffuse and specular components of reflected light in case of S-polarization, and the subscript n indicates that the squared Bessel functions are normalized as follows:

$$J_{m_n}^2 = \frac{J_m^2}{J_0^2 + \sum\limits_{m \neq 0} J_m^2 \Big|_{\forall m}} . \tag{4.5}$$

Thanks to this normalization procedure the light intensity is distributed only in the propagating diffraction modes [223], contributing to a more precise prediction of the haze in reflection. However, from the measurement of realistic opaque sinusoidal gratings not only diffraction modes influence the intensity of scattered light but also other optical phenomena like wave guided modes in case of multi-layer structures or surface plasmon polariton resonances occurring at metal / dielectric interface. Furthermore, for the P-polarization, only a solution for the first diffraction order valid in paraxial conditions exists [224]. These difficulties have been lately overcome by using an approach based on plane wave expansion that is capable to correctly predict, for both polarizations, diffraction modes, wave guided modes, and surface plasmon polariton resonances also in case of realistic permittivities [224].

Although an exact theory based on numerical computations was developed for opaque rectangular gratings [221], at the best of our knowledge, closed expressions for transparent rectangular gratings are not readily available. In the following, a semi-empirical approach is discussed only to qualitatively show the influence of groove height on diffraction modes and thus on the diffuse component of transmitted light.

Removing the hypotheses of the gratings conductivity and polarization of light from the treatment of opaque sinusoidal gratings, it was found that the H_T of 1-D gratings measured in air, at perpendicular incidence, and for un-polarized light could be predicted by making use of a modified version of Eq. 4.3. Deploying the aforementioned non-paraxial correction, the intensity of light related to the mth diffraction mode in transparent rectangular gratings was calculated as follows:

$$I_m \sim J_m^2 \left[\frac{2\pi}{\lambda} \cdot \frac{h}{2 \cdot K} \cdot (cos\theta_{inc} + cos\theta_m) \right] \tag{4.6}$$

which is basically Eq. 4.3 with the introduction of a constant K. The value of K was found to be equal to 3 and successfully deployed in predicting the H_T of several transparent 1-D gratings. Constant K takes into account the following aspects: (i) the reflections occurring at air / glass, glass / lacquer, and patterned lacquer / air interfaces, which may cut down the effective groove depth experienced by light, (ii) the shape change from sinusoidal (original approach) to rectangular-like, and (iii) the effects of polarization.

Considering a combination of period and height, calculating θm from Eq. 4.1, and applying the normalization procedure to the squared Bessel functions as in Eq. 4.5, the H_T for transparent gratings could be calculated in the same way of H_R^S:

$$H_T = \frac{\sum\limits_{m \neq 0} J_{m_n}^2}{J_{0_n}^2 + \sum\limits_{m \neq 0} J_{m_n}^2}. \tag{4.7}$$

Similarly to Eq. 4.7, it was possible to calculate the parameter S_T, defined as the ratio of specular to total transmitted light:

$$S_T = \frac{J_{0_n}^2}{J_{0_n}^2 + \sum\limits_{m \neq 0} J_{m_n}^2} \tag{4.8}$$

Referring for example to a 1-D grating with P = 1000 nm and h = 300 nm, intensities of diffraction modes and their normalized counterparts are grouped in pairs, summed up, and shown in Fig. 4.7(a), while a comparison between measured and calculated H_T and S_T is reported in Fig. 4.7(b). It is possible to notice that (i) three pairs of diffraction modes contribute to the haze parameter, as predicted by diffraction equation (Eq. 4.1 or see Fig. 4.4(a), (ii) the normalization procedure affects mainly the 0th and the 1st order diffraction modes, and (iii) the general behavior of H_T and S_T is reproduced.

Afterwards, from the measurement of T_T and the calculation of H_T, T_D could be carried out as superposition of light intensities distributed in different diffraction modes ($T_D = H_T \cdot T_T$). In Fig. 4.8, the effect of height on the transmitted light for two pairs of 1-D gratings is reported. The first pair has fixed P = 600 nm and h = 300 nm or 150 nm (see Fig. 4.8(a)), while the second pair has fixed P = 1000 nm and h = 300 nm or 150 nm (see Fig. 4.8(b)). In both pairs, passing from higher to lower groove depth, the intensity of diffracted light drops as the argument of $J_m{}^2$, for $m \neq 0$, becomes smaller. As a result, the diffuse component of transmitted light decreases. On the other hand, for smaller argument, $J_0{}^2$ becomes bigger, thus increasing the specular component. In this way the total transmittance becomes higher in the region of dips caused by the passage from pure specular to diffracted regime. The described trend low h low H_T is valid as long as the groove depth approaches small values or, to the limit, becomes null (flat surface). Conversely, increasing h will red-shift H_{T-max} in correspondence of a wavelength for which $J_0{}^2$ is minimized.

Modeled H_T and T_D present steep edges at the threshold wavelengths due to the abrupt vanishing of the 1st order diffraction modes from calculation point of view. In case of gratings with P = 1000 nm, such effect should be reiterated at 500 nm where also the 2nd order
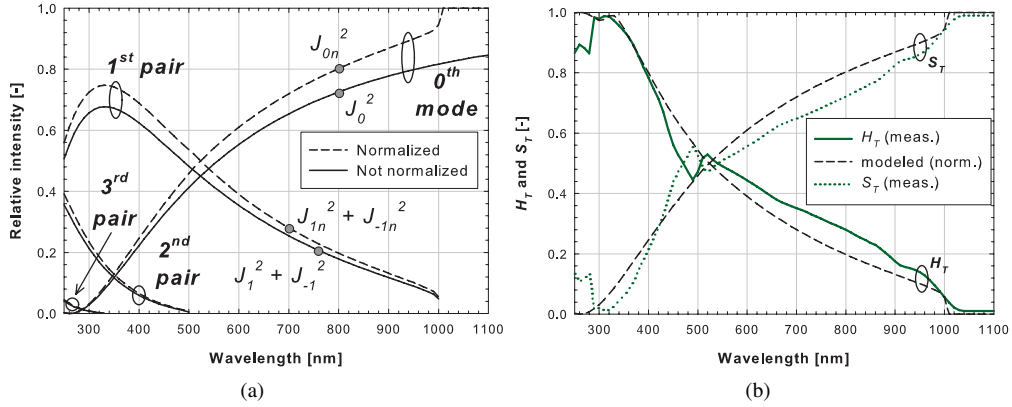
*Figure 4.7: Referring to a 1-D grating characterized by P = 1000 nm and h = 300 nm: (a)
relative intensity in different diffraction modes with and without normalization
and (b) measured and modeled H_T and S_T.*
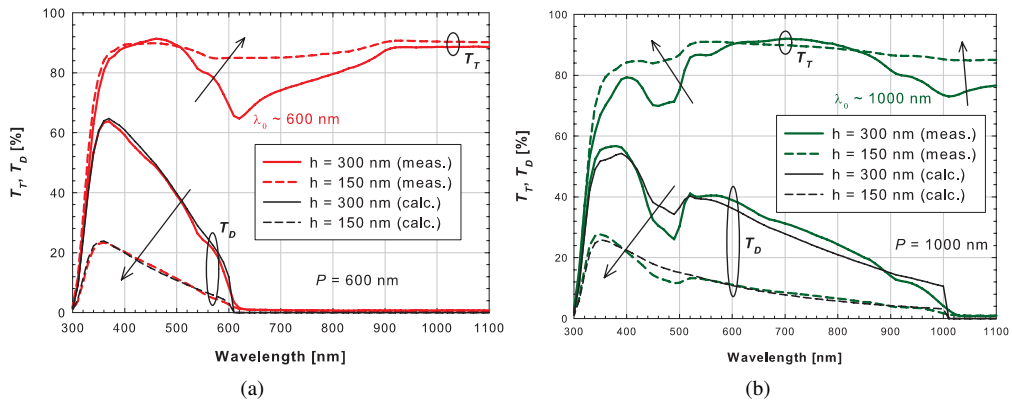
*Figure 4.8: Effect of height on measured transmittance for 1-D periodic gratings charac-
terized by (a) P = 600 nm and (b) P = 1000 nm. Diffuse components are also
modelled (black lines).*

modes disappear. However, the semi-empirical approach fails to properly describe this fea-
ture yet present in measurements, especially for the shallower grating (see Fig. 4.8(b)). It is
clear that the proposed usage of the scattering theory of opaque sinusoidal gratings, besides
being modified with a somewhat arbitrary constant, is not satisfactory and calls for a closer
examination. Nevertheless, it has been shown that this semi-empirical approach is capable
to approximate the measured H_T of transparent rectangular gratings in air and to super-
pose the intensity of propagating diffraction modes thus describing the diffuse component
of transmitted light.

4.3.3   Effect of shape, duty cycle and groove depth

The semi-empirical approach previously discussed cannot be used to address the effect of grating shape and duty cycle on the haze parameter, because the only relevant geometrical parameters in the original theory for sinusoidal gratings are the period and the groove depth. A different approach should be therefore deployed to take into account the realistic shape of available gratings.

In scalar scattering theory, the approach known as the Harvey-Shack (H-S) model [223] has recently gained attention, since it has been successfully applied in the study of scattered transmitted light from randomly textured interfaces [225] and later further expanded also to model the scattered reflected light [153]. Restricting the discussion to the sole transmitted light as of interest in this context and using the notation as in [153], this model considers the scalar field U in k-space as the Fourier transform of a *pupil function* P:

$$U(k_x, k_y, k_z) = \frac{1}{2\pi} \iint\limits_{\mathbb{R}^2} P(x, y, z) \cdot e^{-i(k_x x + k_y y)} dx dy. \tag{4.9}$$

The pupil function P represents the aperture where diffraction occurs and takes into account the phase shift due to the morphology $z(x, y)$:

$$P(x, y, z) = \sqrt{\frac{T_T}{A}} \cdot e^{ik_0 z(x,y)(n_1 - n_2)}. \tag{4.10}$$

In both Eq. 4.9 and Eq. 4.10 the wavelength dependency is due to the wavenumber in vacuo $k_0 = 2\pi/\lambda$ and to the incident and diffractive media n_1 and n_2, provided that they do not suddenly change with the wavelength. The constant $\sqrt{\frac{T_T}{A}}$, making sure that the amount of light going through the area A of the aperture is the same as the total transmittance, ensures the energy conservation. Finally, the morphology $z(x, y)$ is provided in a discrete fashion by AFM scan.

Using a fast Fourier transform, it is possible to calculate the scalar field U in a discrete k-space in which integrals are substituted with sums. Only k-vectors inside the circle with radius $k_0{}^2 \cdot n_2$ are related to propagating waves, while those outside the circle denote evanescent waves, which ultimately do not contribute to the transmitted light. As the intensity of light is linked to the quantity $|U|^2$, the haze parameter can be carried out as follows:

$$H_T = \frac{T_D}{T_T} = \frac{T_T - T_S}{T_T} = \frac{\sum\limits_{k_x^2 + k_y^2 \leqslant k_0^2 \cdot n_2} |U(k_x, k_y)|^2 - |U(0,0)|^2}{\sum\limits_{k_x^2 + k_y^2 \leqslant k_0^2 \cdot n_2} |U(k_x, k_y)|^2} \tag{4.11}$$

where only propagating modes are considered with the condition $k_x{}^2 + k_y{}^2 \leqslant k_0{}^2 \cdot n_2$. Using the H-S model, a normalization procedure to redistribute all the energy only in propagating modes would be required to properly estimate the AID_T. Such procedure aims to carry out a constant value k_{HS} defined as follows, which is then multiplied by the quantity $|U|^2$:

$$k_{HS} = \frac{\iint\limits_{\mathbb{R}^2} |U|^2 dk_x dk_y}{\iint\limits_{k_x^2 + k_y^2 \leqslant k_0^2 \cdot n_2} |U|^2 dk_x dk_y} \Rightarrow |U|_n^2 = k_{HS} \cdot |U|^2 \tag{4.12}$$
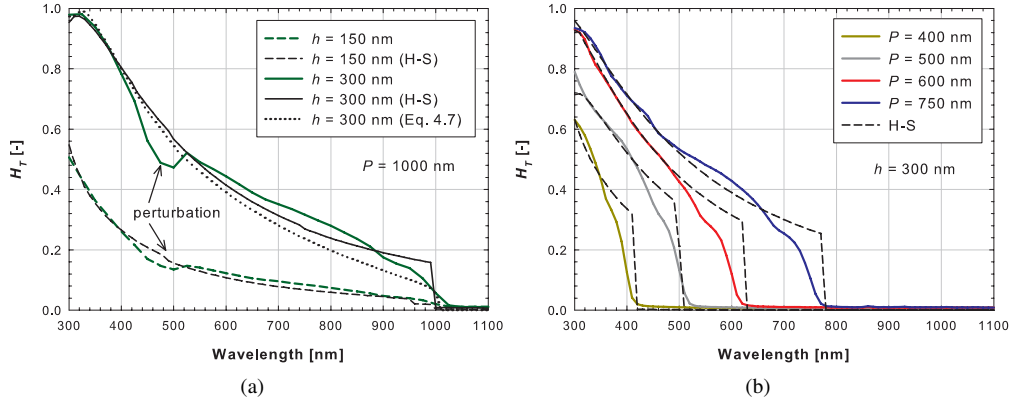
Figure 4.9: Measured and calculated haze parameters for 1-D gratings with different height and fixed period (P = 1000 nm) (a) and for 1-D gratings with different periods and fixed height (h = 300 nm) (b).

with the subscript *n* indicating the normalized quantity. However, for calculating only the haze parameter, such procedure can be avoided, as the factor k_{HS} cancels out being present in both numerator and denominator of Eq. 4.11. In the described form, the H-S model deals with two materials (n_1 and n_2) separated by the morphology $z(x, y)$.

AFM scans of some periodic textures were used to test the predictive power of the H-S model applied to 1-D gratings investigated under un-polarized and perpendicular incident light. In these calculations n_1 was set to 1.5. In Fig. 4.9(a) the haze parameter of 1-D gratings with *P* = 1000 *nm* and two different heights (150 *nm* and 300 *nm*) are compared with calculated H_T. In addition, also the H_T calculated with Eq. 4.7 is reported for the deeper morphology. The H-S model was capable to deliver the general behavior of haze parameter for the considered gratings. With respect to the Eq. 4.7, a closer match with measurements is found between 550 *nm* and 900 *nm*. Furthermore the curves computed with the H-S model show small perturbations of the haze parameter around 500 *nm* (indicated with arrows in the plot), that were not reproduced using Eq. 4.7. Around the threshold wavelength of the deeper grating, the H-S model slightly overestimates the haze. This issue is also present when calculating the haze parameter for other 1-D gratings with *h* = 300 *nm* and different periods (see Fig. 4.9(a)). It appears that in real gratings the passage from pure specular regime to diffracted regime happens more gradually than calculations would admit. This effect may result from an optical disturbance due to the aforementioned nano-ripples present on flat parts of the patterns (see Sec. 4.2). Anyway, for $\lambda < \lambda_0$, the agreement between measured and calculated hazes is quite close. This justifies the utilization in the following of the H-S model for the qualitative study of shape and duty cycle influence on the haze parameter.

To investigate the effect of gratings shape, six synthetic 1-D gratings with 5x5 μm^2 area were considered. In Fig. 4.10(a-c) arbitrary cross sections of the used shapes are shown. Indicated with Roman numbers they are (I) saw-tooth, (II) triangular, (III) dimple, (IV) sinusoidal, (V) trapezoidal, and (VI) rectangular. The period and the height of such

gratings were fixed to 1000 *nm* and 300 *nm*, respectively. The tilt angle of walls of the considered trapezoidal shape was 59°. These six synthetic morphologies were used as input in H-S model setting $n_1 = 1.5$ and $n_2 = 1$. In Fig. 4.10(d), the H_T resulting from H-S model for different shapes is reported. Even bounded to the threshold wavelength of 1000 *nm*, the haze parameter progressively increases and the perturbation indicating the onset of the 2nd diffraction modes progressively decreases when sweeping the gratings shape from type (I) to type (VI). It must be noted that such enhancement should not be interpreted as having found an optimal shape for application in real devices. In fact, since the H-S model involves only two materials with a separation surface, a number of optical effects present in realistic multi-layer solar cells are here not taken into account (internal reflection, escaping light, absorption, etc.). These simulations rather serve to test the responsiveness of the model when changing the shape. In this respect, the H_T previously shown in Fig. 4.9 and calculated also with H-S model but using an AFM scan as input is reproduced in Fig. 4.10(d). Such haze settles between those due to trapezoidal and pure rectangular shapes. This is in accord with the angle distribution of the AFM scanned 1-D grating reported in Fig. 4.2, which is characterized by a tilt angle of walls around 77°.

For the analysis of duty cycle, pure rectangular 1-D grating characterized by $P = 1000$ *nm* and $h = 300$ *nm* was considered. In this case eleven versions of the synthetic periodic texture were tested, sweeping d_C from flat interface (0%) to 50% to flat interface again (100%) with incremental steps of 10%. Results of the simulation are in Fig. 4.11(a). The calculated haze parameter for $d_C = 0\%$ or 100% is null, as expected in case of flat interface. Raising d_C, the haze parameter reaches its apex for $d_C = 50\%$, while for $60\% < d_C < 90\%$ H_T decreases again towards minimal values. For intermediate d_C values, step-like features around 500 *nm* and 330 *nm* are observable, indicating a higher influence of 2nd and 3rd order diffraction modes on the haze parameter with respect to the 1st order diffraction modes.

The H-S model was finally used to calculate the haze parameter of pure rectangular 1-D gratings with $P = 1000$ *nm*, $d_C = 50\%$, and with h ranging from 150 to 750 *nm*. Even though very deep grooves are difficult to fabricate for the given periodicity, the analysis of heights exceeding those characterizing the available substrates allows for a broader view of the haze parameter. Calculated haze parameter for five different heights is reported in Fig. 4.11(b). As mentioned in the previous section, considering deeper grooves modifies H_T by *red*-shifting H_{T-max} towards the gratings threshold wavelength. This optical behaviour can be approximated with the following equation[4]:

$$H_T = \frac{1}{2}\left[1 - cos\left(\frac{2\pi}{\lambda} \cdot h \cdot |n_1 - n_2|\right)\right] \tag{4.13}$$

in which the argument of cosine part is similar to that of Bessel functions discussed in Eq. 4.2 and takes into account the passage from incident to diffractive medium. Eq. 4.13 is maximized for $\lambda_{max} = 2h \cdot |n_1 - n_2|$, at which H_{T-max} occurs. This condition is equivalent to the suppression of the 0th mode in the neighborhood of λ_{max}.

4.3.4 Wrap-up of scattering properties

The absence of a theory, that properly explains the scattering of light from transparent rectangular periodic gratings, led to the usage of scattering models initially developed either

---

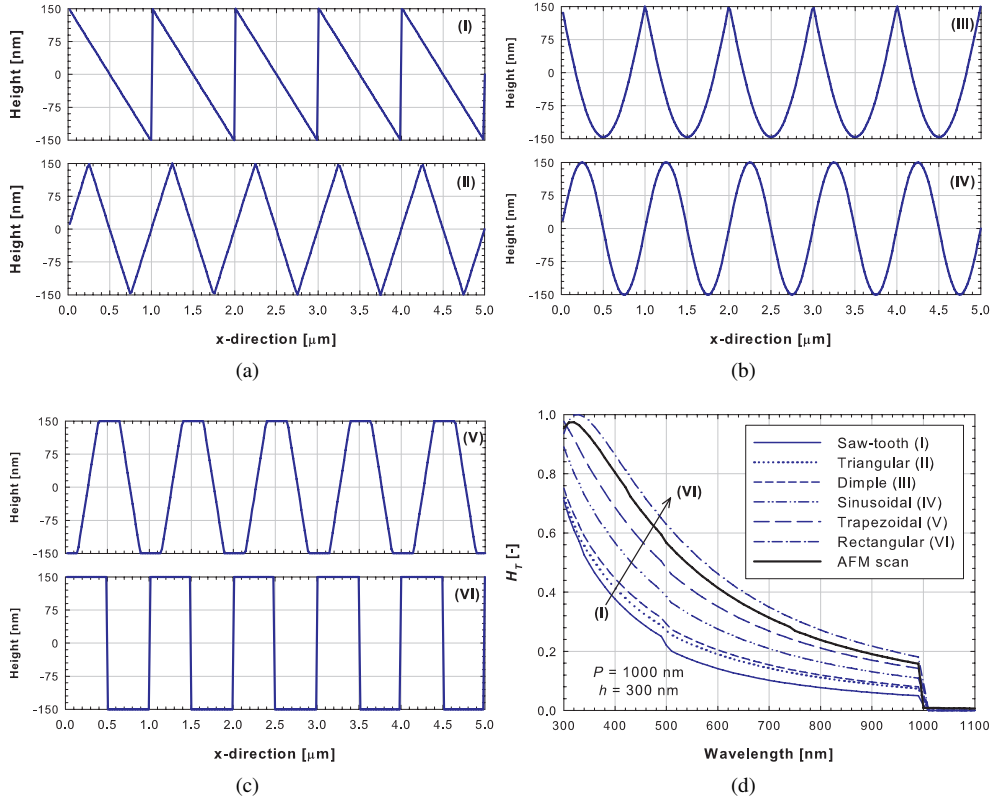[4]This equation was proposed by H. de Groot at OM&T B.V. MoserBaer

Figure 4.10: (a-c) Cross sections of synthetic 1-D gratings with (I) saw-tooth, (II) triangular, (III) dimple, (IV) sinusoidal, (V) trapezoidal, and (VI) rectangular shape; (d) calculated (H-S model) haze parameter of the synthetic 1-D gratings and of a real 1-D grating (AFM scan, see Fig. 4.1(b) and Fig.4.9(a)).

for opaque substrates or for (transparent) random textures. Measurements taken in conditions of un-polarized and perpendicular incident light helped adapting such models to the tested optical systems. It is undeniable that a more rigorous approach is needed to model the light scattering from transparent gratings, primarily based on different angles of incidence and on their polarization-dependent behavior. Nevertheless, from the discussed optical analysis of transparent rectangular 1-D gratings, concepts linked to their geometrical parameters emerged as instrumental for the understanding of featured scattering properties.

The threshold wavelength λ_0, related to the period of the grating and to the diffractive material, indicates the maximal wavelength for which a grating scatters light in diffraction modes different than the 0th order mode. Its fingerprint is recognizable especially in the transmittance spectra where the transition from specular-only to diffraction regime occurs. This concept, independent from the grating shape, descends from the diffraction equation (Eq. 4.1), generally used to predict how many diffraction modes a periodic grating develops,
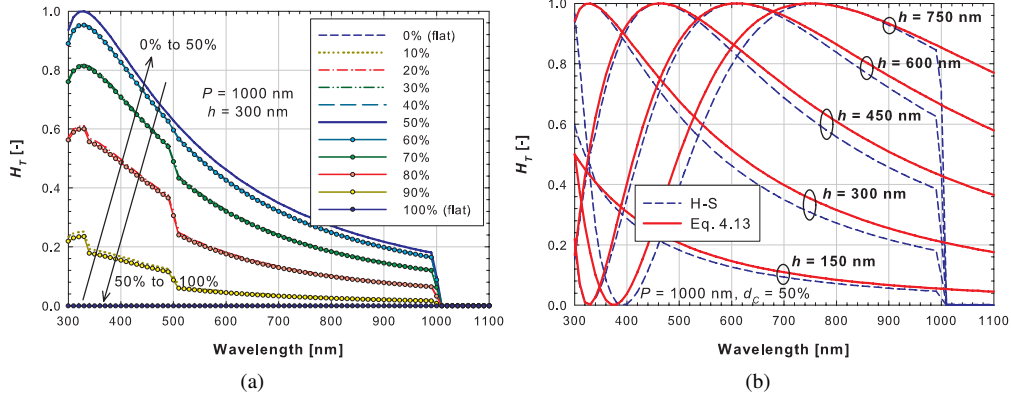
Figure 4.11: (a) Effect of duty cycle variation (0% to 100%) on haze parameter using H-S model for a pure rectangular grating (P = 1000 nm and h = 300 nm); (b) Effect of deep grooves on haze parameter using H-S model for a pure rectangular grating (P = 1000 nm and d_C = 50%).

depending on refractive indexes of incident and diffractive media. The same equation is also involved in the non-paraxial correction for a more precise estimation of light intensity distributed in each diffraction mode (Eq. 4.3).

High order squared Bessel functions ($m \neq 0$), containing the height of the grating in their argument, can be superposed to qualitatively explain the effect of gratings height on the diffuse component of transmitted light. For un-polarized and perpendicular incident light, such functions can be used in a semi-empirical approach (Eq. 4.6) to calculate the haze parameter. This approach is based on the modification of the non-paraxial scattering theory of opaque sinusoidal gratings.

For transparent 1-D gratings that scatter light in air, rectangular shape with duty cycle equal to 50% is found to deliver the highest haze parameter. For un-polarized and perpendicular incident light, the effects of shape and duty cycle can be investigated by means of Harvey-Shack model, which removes the constraint of sinusoidal profile in the aforementioned semi-empirical approach (Eq. 4.11). In this context, studying the optical effect of deep grooves, it is found that the maximal value of the haze parameter occurs at λ_{max}, which depends on gratings height and on both incident and diffractive media.

How these scattering properties contribute altogether inside multi-layer optical structures such as thin-film silicon solar cells is not a straightforward task to handle. The optical path of scattered light surely increases with respect to the perpendicular one pass distance, allowing for the practical realization of *optically thick* and *electrically thin* absorber layers. However, due to the shape of the diffraction grating and its transfer at each internal interface, light inside the device experiences multiple angle-selective scattering steps, possibly resulting in escaping path(s). In this respect, the numerical solution of Maxwell equations seems to be the paved way for the optimization of diffraction gratings when embedded in a complete device.
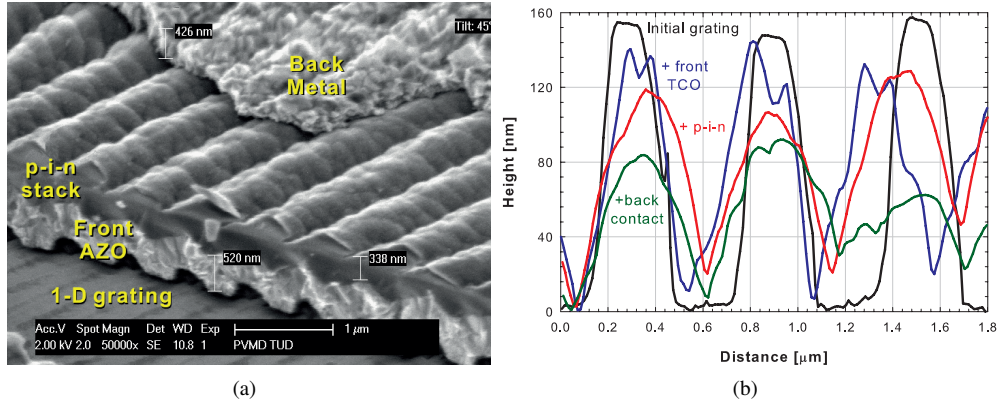
Figure 4.12: (a) Cross-sectional SEM image of a solar cell deposited on 1-D grating (P = 600 nm, h = 300 nm); (b) Cross section evolution for layers deposited on initial grating (P = 600 nm, h = 150 nm).

4.4 Solar cells on 1-D periodic gratings with Ag back re-flector

Thin-film a-Si:H *pin* single-junction solar cells were deposited by RF PE-CVD on several transparent substrates patterned with rectangular 1-D periodic gratings. RF magnetron sputtered ZnO:Al (AZO, $\sim$600 *nm* thick) was used as front TCO. For reference purposes a-Si:H *pin* single-junction solar cells were fabricated also on flat glass / ZnO:Al and Asahi-U type TCO substrates. The Asahi-U type TCO was coated with 10 *nm* thick ZnO:Al film to prevent SnO_2:F being damaged in hydrogen-rich plasma [226]. The solar cells had the following general structure: glass / TCO / nc-Si:H p-layer (10 *nm*) / a-Si:H p-layer (5 nm) / a-SiC:H buffer / a-Si:H i-layer (300 *nm*) / a-Si:H n-layer (20 *nm*) / Ag / Al. The aluminium film was merely used as protection against native oxidation of silver. In Fig. 4.12(a) the cross-sectional SEM image of a solar cell deposited on 1-D grating is depicted.

4.4.1 Evolution of surface morphology inside solar cells

The process of morphological transformation a texture endures when coated with thin-film is known as leveling effect. The change of internal surface morphology in solar cells was evaluated with AFM scans after depositing each layer. Fig. 4.12(b) reports the shape evolution of the initial bare grating in arbitrary cross-sections at different stages of solar cell fabrication, while Fig. 4.13 shows such evolution on a larger scale (3-D view). Even though the periodicity of the grating could be recognized until the last deposited layer, the height and the shape of the grating underwent subsequent changes. In Fig. 4.13(a), the morphology of the bare rectangular-like 1-D grating on glass, characterized by *P* = 600 *nm* and *h* = 150 *nm*, is depicted. After the deposition of $\sim$600 *nm* of AZO, the maximal height decreased to 145 *nm* and the shape began to change with the appearance of nano-peaks on the top part of the pattern (see Fig. 4.13(b)). After depositing the *p-i-n* stack, the height further

lowered to 130 *nm* and the shape assumed a rounder form (see Fig. 4.13(c)). Finally, after the deposition of the back contact, the height reduced to 90 *nm* and the shape did not change much from the form it assumed after *p-i-n* stack (see Fig. 4.13(d)).

Even though the leveling effect is unavoidable, this analysis on surface morphology evolution shows that the formation of nano-voids or bulb-like features can be prevented with suitable deposition conditions and moderate aspect ratios ($h/P < 0.3$).
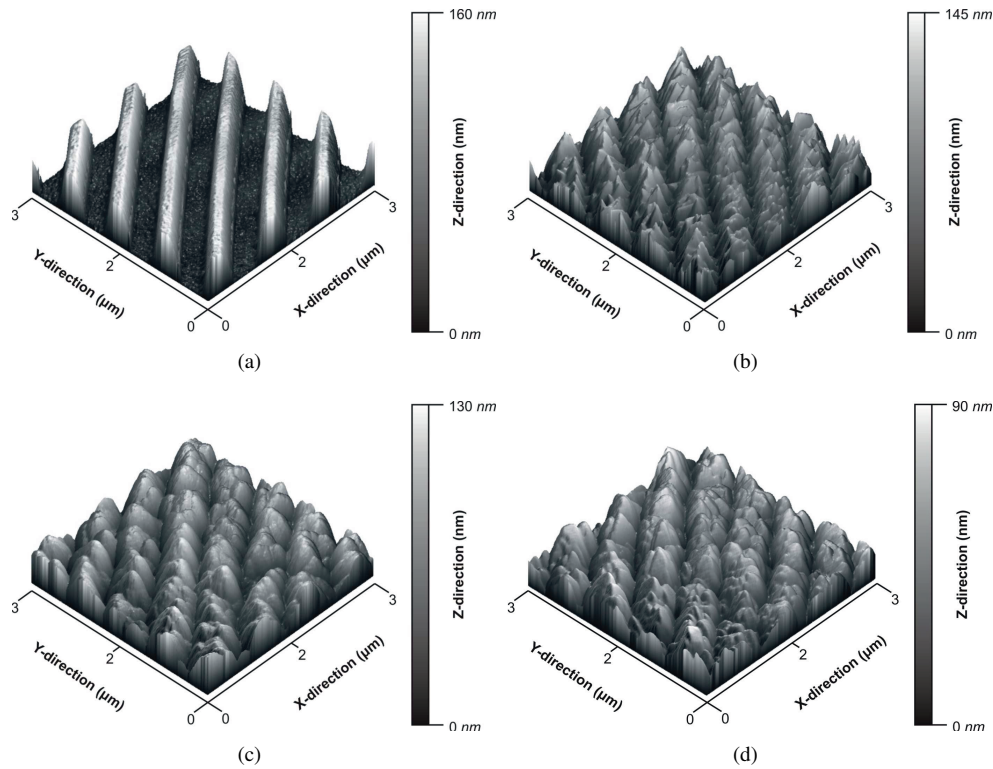
Figure 4.13: Evolution of the surface roughness: (a) bare 1-D grating (P = 600 nm, h = 300 nm), (b) grating with AZO TCO layer, (c) grating with AZO and Si layers, (d) grating with AZO, Si layers and metal back contact.

4.4.2 Solar cells results

Along with flat and randomly-textured substrates, eight transparent 1-D diffraction gratings with different combinations of period and height were processed. In Tab. 4.1 the (initial) external electrical parameters of the best measured solar cells are reported.

With the exception of the case $P = 400$ *nm* and $h = 150$ *nm*, gratings substrates presented deteriorated open circuit voltage with respect to the reference cells due to the AZO film being more structured than its flat counterpart or than Asahi-U type TCO. It was observed

Table 4.1: Initial external parameters of best measured cells fabricated on flat glass, Asahi-U type random texture, and on several 1-D diffraction gratings. Values of current density are from EQE measurements.

Substrate	Front TCO	V_{OC} [V]	J_{SC} [mA/cm^2]	FF	η [%]
Flat reference: Glass	AZO	0.847	12.65	0.620	6.64
Randomly-textured reference: Asahi-U	SnO_2:F / AZO	0.845	14.71	0.708	8.80
1-D periodic gratings reference: P [nm] x h [nm] 600 x 50	AZO	0.836	13.49	0.709	8.00
400 x 150	AZO	0.844	12.99	0.634	6.95
600 x 150	AZO	0.834	13.80	0.672	7.73
1000 x 150	AZO	0.842	13.58	0.663	7.58
500 x 300	AZO	0.829	13.50	0.682	7.63
600 x 300	AZO	0.833	14.35	0.707	8.45
750 x 300	AZO	0.832	13.69	0.611	6.96
1000 x 300	AZO	0.840	12.96	0.623	6.78

that within the set of periodic substrates, shallower groove depths and larger periods delivered slightly higher V_{OC} values. The fill factor was usually lower than Asahi-U based solar cell due to a slightly lower electrical performance of AZO TCO. As expected, the lowest current density was delivered by the cell with flat interfaces, while the highest value was obtained by the device fabricated on Asahi-U TCO. In Fig. 4.14(a) the electrical behaviour of the best solar cell deposited on the periodic grating (P = 600 *nm* and initial h = 300 *nm*) is presented together with the current density voltage characteristic of the reference cells. The two cells on textured substrates behaved similarly in virtue of their close FF and both offered a substantial gain in short-circuit current density with respect to the flat solar cell.

Looking at the spectral response of these three cells (see Fig. 4.14(b)), the *EQE* of the solar cell on grating was everywhere higher than that of the solar cell deposited on the flat substrate. This enhancement resulted from anti-reflective and scattering effects, delivered by the grating substrate. In fact, for wavelengths longer than 550 *nm*, the *EQE* of the cell on grating, showing good scattering properties, was similar to that of Asahi-U based device. On the other hand, for wavelengths shorter than 500 *nm*, both cells on AZO front contact experienced a decrease in the *EQE* due to higher absorption in UV-range of such TCO with respect to SnO_2:F.

The effect of groove depth on solar cells spectral performance is reported in Fig. 4.15(a), where two cells on gratings with the same period (P = 600 *nm*) but different height (h = 150 *nm* and h = 300 *nm*) are compared together with the flat cell. As discussed in Sec. 4.3.2, increasing the groove height resulted in an enhancement of the scattering, which led to higher *EQE* and ultimately to higher short-circuit current density. It is peculiar that most of the gain was located at short wavelengths, indicating a better light coupling due to enhanced
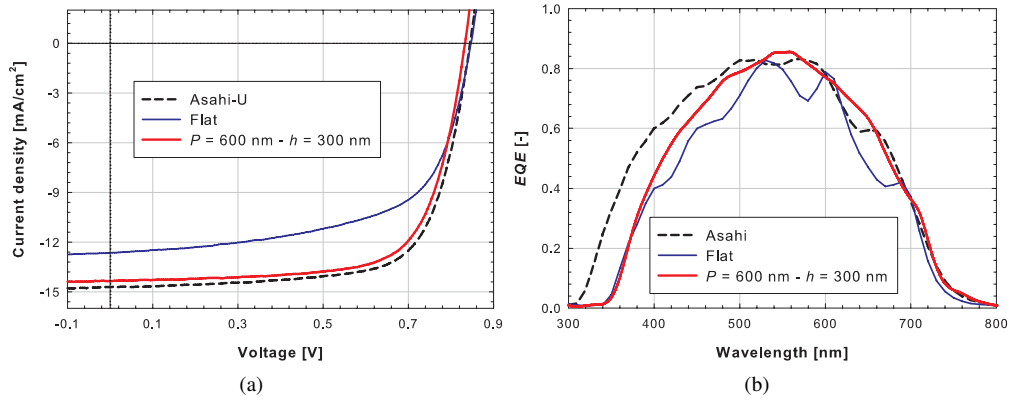
Figure 4.14: *Comparison of flat cell (blue line), Asahi-U based cell (dashed black line) and grating based cell (red line): (a) current density voltage characteristics and (b) and external quantum efficiency.*
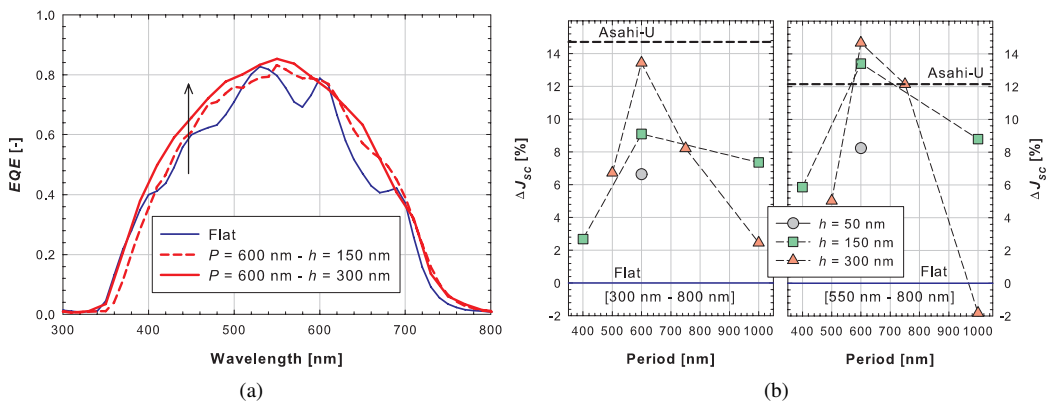
Figure 4.15: (a) The effect of height of the gratings on the EQE (blue solid line flat solar cell, solid red line h = 300 nm, dashed red line h = 150 nm); (b) Relative increase of the J_{SC} (in %) as function of period using the height as parameter: (left) integration over 300 nm 800 nm, (right) integration over 550 nm 800 nm. Solar cell deposited on flat glass substrate represents 0% level; dashed lines connecting symbols are only indication for the eyes.

anti-reflective effect of the deeper groove.

To assess the gain in J_{SC} provided by textured substrates with respect to flat glass, relative increase of short-circuit current density (ΔJ_{SC}) was calculated in two spectral zones (see Eq. 1.6): (i) the complete measurement range from 300 *nm* to 800 *nm* and (ii) the region towards weaker absorption of a-Si:H, i.e. from 550 *nm* to 800 *nm*. In Fig. 4.15(b)

these computations are shown as function of gratings period and height. Evaluat-ing the first range, although deeper groove depths and larger periods result in ΔJ_{SC} increase, the highest gain is achieved by Asahi-U based cell. However, considering the second range, that is neglecting the absorption of AZO at short wavelengths, periodic textures with P = 600 *nm* or 750 *nm* perform similarly to randomly-textured Asahi-U type. This analysis demonstrates that periodic gratings can effectively work as good scattering surfaces in thin-film silicon solar cells, but also focuses the attention on the choice of an univocal TCO to attempt any kind of comparison between different kinds of textures.

4.5 3-D modelling of thin-film silicon solar cells on periodic gratings

Reported results on solar cell performance indicate that diffraction gratings have a potential as alternative textures for light scattering. To achieve and possibly overcome the photocurrent levels obtained with best random textures the gratings have to be properly optimized. It has become clear that the analysis and optimal design of thin-film silicon solar cells on diffraction gratings require the adoption of rigorous 3-D optical models. First reported simulation studies focused primarily on the optical effects of light incident onto gratings [227, 228]. Afterwards, various optimized methods for solving numerically Maxwell equations have been used to optically simulate complete devices [173, 175, 178, 187, 229].

In this section, an effective approach of rigorous 3-D modeling based on Finite Element Method (FEM) is presented. The High Frequency Structure Simulator (HFSS) [230] was deployed to carry out simulations aimed at the modeling and optimization of *pin* a-Si:H solar cells textured with 1-D and 2-D periodic gratings on glass. Using properly the boundary conditions, it will be shown that 3-D simulations can be done in minutes or few hours with a conventional personal computer. An overview of different numerical methods for solving electromagnetic wave equations used in simulations of thin-film solar cells was presented in the previous chapter. Here, FEM is demonstrated to be a very suitable method for modelling thin-film solar cell structures with realistic optical properties of layers and interface morphologies.

The validation of 3-D modeling is evaluated by comparing simulation results with those obtained with other models. Furthermore, verification of results are shown for an a-Si:H solar cell by matching simulated and measured *EQE* of a real cell deposited on periodic grating. The optical losses and the effect of the polarization related to 1-D gratings are analyzed. Varying P and h of the gratings, the optimal combination for 1-D and 2-D gratings will be indicated. Finally, the performance analysis of the simulator will be evaluated in terms of memory usage and computational time.

4.5.1 General aspects for 3-D modelling thin-film silicon *pin* solar cells

Thin-film silicon solar cells present a special optical system with relatively thick layers (*μm* range for transparent conductive contacts or even *mm* range for the substrates) and ultra-thin layers (a few *nm* thick buffer layers or 10 *nm* thick doped layers). This implies that a variable mesh should be applied if one wants to include thick layers in simulation effectively. Additionally, according to the coherence length of solar irradiation (in the range of *μm*) one

has to consider coherent propagation of light in thin layers of the solar cell structure. In *pin* solar cells, light is propagating through thick incoherent glass layer first [231, 232]. Despite the adaptable meshing capabilities of FEM, such large thicknesses would require a lot of additional computer memory and computational time, although its optical effect is not predominant when studying the trends regarding periodic gratings in thin-film solar cells. Therefore, the followed approach was to apply the incident light from glass semiinfinite medium, neglecting (but being aware of) some effects related to front and back reflection at the first air/glass interface, which are not included in reported simulations.

4.5.2 Setting boundary conditions

Thin-film solar cells and modules have layered structure with very large transverse size. However, by setting proper boundary conditions, only small segments can be included in the analysis. In this way the volume of the design to simulate reduces to a so-called unit cell. Here the unit cell serves as the problem domain for boundary conditions extending the computational volume along the coordinate Cartesian directions *x*, *y* and *z* (see Fig. 4.16). The used boundary conditions can be divided in three groups: (i) the master-slave (M-S) boundary condition [233] acting on surfaces parallel to *xz*- or *yz*-planes, (ii) the Floquet ports (FPs) [234] acting on surfaces parallel to the *xy*-plane, and (iii) the Perfect **E** - Perfect **H** (PE-PH) conditions to handle properly symmetry cross-sectional surfaces [235].

The M-S is a boundary condition enforced between two parallel surfaces in order to mimic the periodicity along their normal direction. The components of the E-M field determined at the master surface are equalized with those at the slave surface. In general slave components are phase shifted with respect to the master ones, according to the distance between the two linked boundary surfaces (d_{M-S}). Such phase shift φ depends also on the direction of the incident field exciting the simulated structure:

$$\phi = \frac{d_{M-S}}{\lambda} sin(\theta) cos(\varphi) \tag{4.14}$$

with the polar angles θ and φ indicating the direction of the incident field propagation vector. In the reported numerical investigations, the phase difference φ has been set to zero in order to consider only the perpendicular incidence for the incident field although the scattering processes occurring inside the unit cell are rigorously taken into account.

The FPs are adopted at the top and bottom horizontal surfaces of the unit cell as efficient absorbing boundary conditions, replacing often used perfect matched layers (PML) [235]. Using FPs infinite media in which light propagates almost without reflection to infinity can be simulated. It was found that FPs are a better solution than PML-based approach since (i) smaller volume has to be meshed (i.e. faster simulations) and (ii) straightforward calculation of reflectance in the simulated structures can be carried out (see Sec. 4.5.4). The FPs approach allows the use of plane waves as source of excitation.

Symmetry conditions PE-PH are used to reduce the volume to be meshed to a half for 1-D gratings and to a quarter for 2-D gratings. This approach leads to much smaller matrix **A** (see Sec. 3.3.2) and consequently to shorter computational times and lower amount of needed random access memory (RAM). The PE (PH) symmetry boundary condition is used for **E** field perpendicular (parallel) to the symmetry surface [235].

If FPs are used only at the top and bottom horizontal surfaces of the unit cells, M-S and PE-PH boundary conditions are applied to pairs of parallel vertical surfaces. Therefore a combination of the conditions is required for simulating solar cells on 1-D or 2-D gratings. Referring to Fig. 4.16(c) and defining the parallel polarization (P-pol) with the **E** field oriented along *x*-direction and the perpendicular polarization (S-pol) with the **E** field oriented along *y*-direction, in case of solar cell on 1-D gratings investigated for S-pol, the M-S relationship is set between surfaces parallel to *yz*-plane, whereas a PE symmetry condition is applied at surfaces parallel to *xz*-planes. For the P-pol case the same M-S relationship but a PH symmetry condition is used. Regarding the structures based on 2-D gratings (see Fig. 4.16(d)), since they have two symmetry planes, two pairs of symmetry conditions are set up.
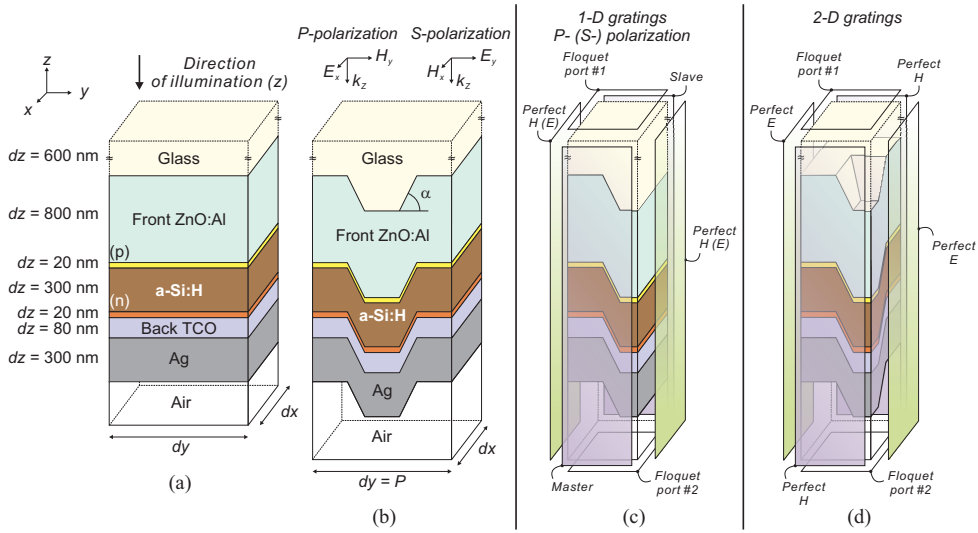

Figure 4.16: Schematic structures (unit cells) of thin-film silicon solar cells on (a) flat glass and (b) on 1-D gratings. Modelled solar cells using symmetry approach on (c) 1-D gratings (M-S, FPs, PE boundary conditions for P-pol and S-pol) and (d) 2-D gratings (FPs, PE, and PH boundary conditions). The geometrical dimensions dx, dy, and dz (layers thicknesses) define the size of the design (dimensions are not in scale). The period P, the height h, the slope α of the 1-D gratings are also reported.

4.5.3 Determination of input parameters of simulations

FEM algorithms are capable of using measured wavelength-dependent complex refractive indexes, which describe the optical properties of the layers. The real part of the refractive index (*n*) and the extinction coefficient (*k*) of the materials used in the presented simulations are shown in Fig. 4.16 and were determined by variable angle spectrometry [156, 159]: aluminum-doped zinc-oxide (ZnO:Al, also indicated as AZO), p-doped amorphous silicon-carbide (p-a-SiC:H), intrinsic amorphous silicon (a-Si:H), n-doped amorphous silicon (n-a-
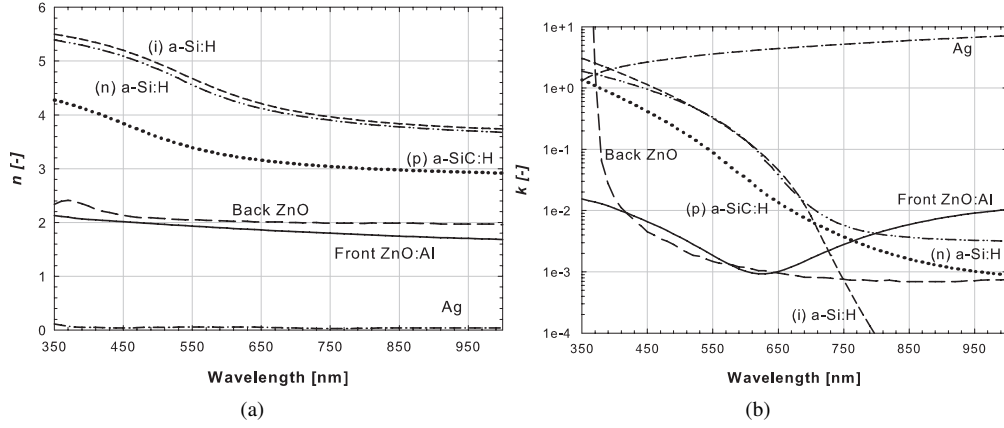
Figure 4.17: (a) Real part of the refractive index n and (b) the extinction coefficient k of all the materials used.

Si:H), undoped zinc-oxide (ZnO), and Ag layer.

In order to deal with a realistic morphology, AFM was used to characterize a 1-D diffraction grating with $P = 600$ *nm* and $h = 300$ *nm*. Since the adopted lacquer features optical properties similar to glass, it was considered as a one-layer substrate with optical properties of glass. In Fig. 4.18, the measured transverse cross-section of the 1-D grating is shown. This substrate was later deployed in a real device for verification purposes (see Sec. 4.5.5 on verification). Period, height, and duty cycle of such rectangular-like 1-D grating were 600 *nm*, 300 *nm*, and 50%, respectively. The average slope of the steep vertical segments was $81°$. In Fig. 4.18 the shape used in simulations is shown by dashed line. Such slight trapezoidal shape with the same slope $\alpha = 81°$ was used as approximation in the 3-D model.

4.5.4 Determination of output parameters from optical simulations

In this modeling approach the simulated structure is treated as a two-port high-frequency device [236]. The total reflectance, which is an output parameter of the simulation, can be straightforwardly calculated in terms of S-parameters [236] as $R = |S_{11}|^2$. For the calculation of the absorptance in the ith layer (A_i) the squared-magnitude of the electric field **E** was integrated over the volume of the film:

$$A_i = \frac{1}{2}\varepsilon_0 Im(\varepsilon_i)\omega \int_{V_i} |\mathbf{E}(x,y,z)|^2 dV \qquad (4.15)$$

where ε_0 is the dielectric constant of vacuum, $\varepsilon_i = \widetilde{n}_i^2$ is the complex relative permittivity of the ith material ($Im(\varepsilon_i) = 2n_i k_i$), and $\omega = 2\pi c/\lambda$ is the angular frequency. The transmittance T is generally numerically negligible, because of Ag at the back side of the solar cell. By convoluting the absorptance A_i with the reference photon flux $\Phi(\lambda)$ of Air Mass 1.5 [84] in the considered wavelength range (350 *nm* - 1000 *nm*), the photocurrent density or the integrated optical losses generated in the ith layer (J_{PH-i}) can be calculated using Eq. 1.6 [177].
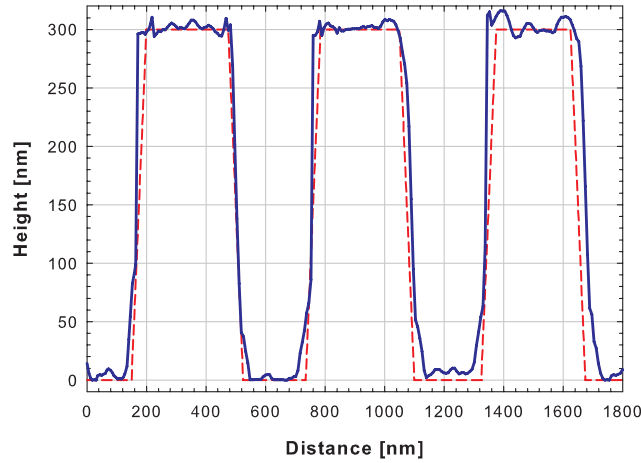
Figure 4.18: Transverse cross-section of the 1-D grating under test. The dashed red trape-
zoidal profile represents the approximation used in the model (P = 600 nm, h
= 300 nm, d_C = 50%, α = 81°).

The choice of using the wavelength range from 350 *nm* to 1000 *nm* comes from three basic reasons. Firstly, limiting the investigation to an upper bound of 800 *nm* would have prevented the probing of absorption losses at the back side of solar cell; hence the upper bound set to 1000 *nm*. Secondly, simulating wavelengths higher than 1000 *nm* would have meant prolonging the simulation to wavelengths that are ultimately not useful for amorphous silicon based single junction solar cell. Finally, starting from 300 *nm* instead from 350 *nm*, additional simulation steps should have been calculated for the partition of a mere $J_{Total-PH-300nm,340nm}$ = 0.328 *mA*/*cm*^{2} over the entire simulated structure. Furthermore, in real solar cells the *EQE* measurement from either 300 *nm* or 350 *nm* does not drop out any information, especially in case of sputtered ZnO:Al front TCO, whose transmittance usually increases around 350 *nm*.

4.5.5 Validation of the simulator

For validating the modeling approach using the HFSS software and the correctness of applied boundary conditions, a simple case of flat solar cell was studied first. Such solar cell was simulated also with 1-D simulator ASA. The simulated structure, shown in Fig. 4.16(a), comprises glass substrate, ZnO:Al in the role of front TCO, amorphous silicon layers forming the *p-i-n* junction, ZnO as back TCO, and Ag back contact. In the HFSS, the later size of unit cell was set to $dx = dy = 600$ *nm*, while the thicknesses of the layers were the same as specified in the ASA (see specifications of layer thicknesses in Fig. 4.16(a)). In case of 3-D HFSS simulation the light source (plane wave) was applied at the top border, inside glass medium, at a distance from the glass / front TCO interface of 600 *nm*. In case of ASA simulations the illumination was applied (i) at the same distance from glass / front TCO interface and taking glass as incident medium and (ii) in air, whereas glass was considered incoherent and 0.6 *mm* thick. With the example (ii) the role of front air/glass interface in the analyzed solar cell is shown.

As reported in Fig. 4.19, the reflectance (R) and absorptance in the i-layer ($A_{a-Si:H}$) carried out with the HFSS and the ASA (incident medium glass) follow each other in intensity and position of the interference fringes, thus demonstrating that the assumption of thin glass layer made within the HFSS simulations leads to a reasonably accurate modeling of propagation of light in glass medium. The average percentage difference between the spectra is limited to 0.08% for the absorptance and 0.24% for the reflectance. Results of the second simulation case with the ASA, where 0.6 *mm* glass was considered and the light applied in air medium, revealed no significant differences in R and $A_{a-Si:H}$ curves. Changes can arise when scattering is accounted for in the solar cell structure, since back scattered rays may experience total reflection at front glass/air interface. Although neglecting this interface results in a reduction of about 4% of the total reflectance (upon assuming a refraction index $n = 1.5$ for the glass layer), a minor impact is expected on the trends regarding the improvements in J_{SC} for different gratings that are analyzed in further.
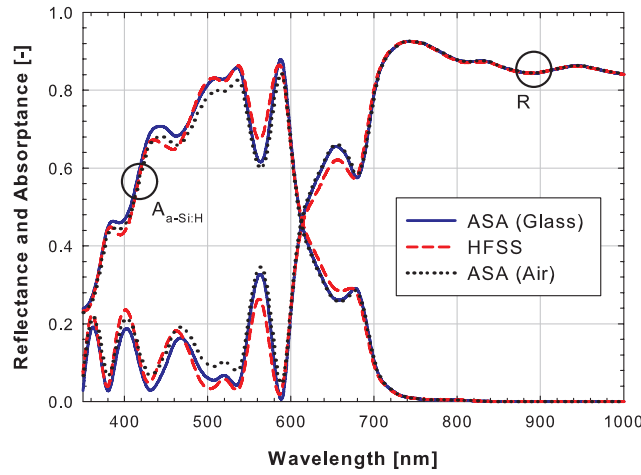

Figure 4.19: *Reflectance (R) and Absorptance ($A_{a-Si:H}$) in the i-layer for the flat solar cell calculated by the HFSS and ASA (air and glass as incident media).*

4.5.6 Simulated *pin* a-Si:H cell on 1-D gratings and verification with a realistic cell

After testing the flat solar cell, a 1-D grating textured *pin* cell was simulated in the HFSS. Layers of the cell and their thicknesses were the same as in the flat case. In the presented simulations it was assumed that the substrate texture is ideally transferred to all internal interfaces of the cell (conformal growth of layers [82]). In Fig. 4.16(b) one period of the simulated structure is shown. However, the structure with $P/2$ was taken as unit cell (see Fig. 4.16(c)), after selecting the right boundary conditions as explained in Sec. 4.5.2. The geometrical characteristics of such unit cell are $dy = P/2 = 300$ *nm*, $h = 300$ *nm*, $d_C = 50\%$, and $\alpha = 81°$. Individual simulations were done for each polarization (P- and S-pol), since 1-D gratings can excite different propagation modes [214, 237] depending on the polarization of the incident field.

Different dimensions along the *x*-direction (*dx* = 24, 60, and 600 *nm*) were checked without finding any significant difference in the simulation spectra carried out. The choice *dx* = 60 *nm* resulted to be optimal as far as memory occupancy, computational time and correctness of simulation are concerned. Furthermore, testing the same solar cell structure on 1-D gratings without taking advantage of the symmetry (*dx* = 60 *nm*, *dy* = 600 *nm*), identical results were obtained as for *dy* = 300 *nm*, corresponding to *P*/2, but within longer computational time. Fig. 4.20 shows the meshed volume of the design solved for the case of S-pol. Choosing automatic determination of the mesh, the HFSS was able to create a variable mesh, making it finer or coarser depending on the refractive index of the materials (higher *n* led to smaller tetrahedrons) with p- and n-type layers well represented by tetrahedrons generated on the steep walls. Details and restrictions of automatic meshing can be found in [235]. Although no special effort was put to get a minimal reliable meshing for the case of thin-film silicon solar cell, an additional simulation was run to prove the accuracy of the modeling choice. The edge length of mesh elements was forced to range from 2 *nm* up to 20 *nm* according to the electrical properties and geometrical characteristics of the different dielectric layers forming the solar cell. In this way, one can achieve a good numerical accuracy of the FEM-based solving procedure, while trying to keep reasonable computational times. As a matter of fact, the output spectra from such simulation were identical to those of the simulation run with automatic meshing, although resulting in solving times up to 30 times longer and memory occupancy up to 50 times higher.

For verifying the proposed optical modeling, a single junction solar cell was fabricated as an experimental reference, employing the established process for cell fabrication on periodic textures. The solar cell was deposited on 1-D gratings using RF PE-CVD deposition technique in *pin* configuration. Front and back TCO layers were deposited using RF magnetron sputtering, silver was evaporated PVD. The solar cell had the following configuration: glass / 1-D grating (see Sec. 4.5.3) / front ZnO:Al contact (600 *nm*) / (p) a-SiC:H (20 *nm*) / (i) a-Si:H (300 *nm*) / (n) a-Si:H (20 *nm*) / back ZnO (100 *nm*) / Ag contact (300 *nm*). The *EQE* was measured using un-polarized mono-chromatic light from 300 *nm* to 800 *nm*. For this reason the simulated spectra presented in this section are the average between the simulation results of P- and S-pol. The total reflectance of the solar cell was measured using the integrating sphere.

The simulated $A_{a-Si:H}$ and the measured *EQE* of the solar cell on 1-D gratings are reported together in Fig. 4.21(a). For wavelengths shorter than 560 *nm* the *EQE* of the fabricated textured *pin* solar cell is smoother than the simulated $A_{a-Si:H}$ as a consequence of the growth of sputtered ZnO:Al on 1-D gratings, which introduces nano-scale features (effect not taken into account in this model). For wavelengths larger than 560 *nm* the two curves present a similar behavior, especially for the presence of the peaks at 600 *nm* and 660 *nm*. The slight shift of the first peak in the *EQE* of the measured cell on 1-D gratings with respect to the simulated one may be due to a little difference in the thickness of the deposited i-layer on textured morphology. The lower amplitude of both peaks in the measured cell indicates that the height of the gratings was not preserved during the thin-films deposition (see Sec. 4.4.1). In Fig. 4.21(b) measured and simulated $1 - R$ and i-layer absorptance are reported. It is noticeable that also the simulated reflectance follows closely the measured one. The good agreement between measured and calculated $1 - R$ and *EQE* spectra provides basic confidence for further analysis of simulation results.
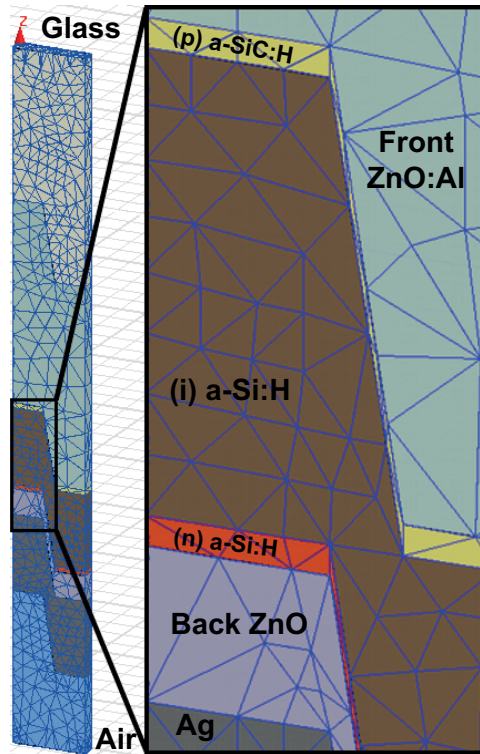
Figure 4.20: Screenshot of the meshed design for S-pol. The design here reported is dx =
600 nm, dy = 600 nm. The inset shows a detailed zoom of the pin junction.

4.5.7   Analysis of simulation results of a-Si:H cell on 1-D gratings

For short wavelengths and with respect to the absorptance of the simulated flat solar cell,
also reported in Fig. 4.21(a), the solar cell on 1-D gratings presents smoothened interference
fringes, resulting in a pronounced anti-reflective effect. For longer wavelengths the textured
cell presents much larger absorption than in the flat case, clearly showing the scattering
effect of the diffraction gratings.

In Fig. 4.22 the photocurrent densities (J_{ph}) related to absorption in i-layer (J_{SC} of the
cell) and losses due to reflected light from the structure and absorbed light in the supporting
layers are given for the two simulated cells. The anti-reflective effect given by the 1-D gra-
tings decreases the current density loss due to the reflectance (net difference of 3.98 mA/cm^2
from flat glass to 1-D gratings), but also increases the current density absorbed into the front
ZnO:Al (+32.18%), illuminated not only from its front side (scattered photons at the glass
/ front TCO interface) but also from its back side (diffuse reflectance at the front TCO / p-
layer interface). Cells in *nip* configuration, deposited on back substrate with gratings texture
suffer also from this problem [201], but in *pin* technology the front TCO is generally thicker,
thus causing higher parasitic absorption. In the *p-i-n* junction area, the p-type layer absorbs
slightly less than in flat case, due to the fact that fewer UV photons arrive in this layer, having
already been absorbed by the front TCO. Thanks to the scattering effect of the gratings and
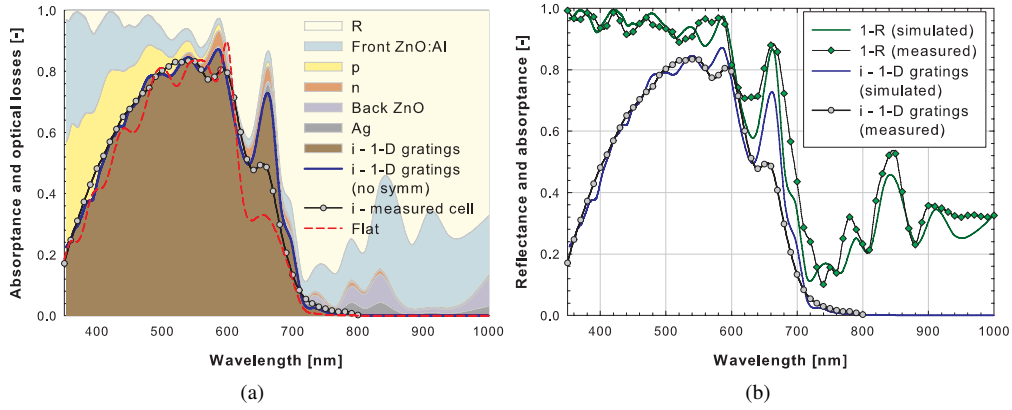
Figure 4.21: (a) Simulated i-layer absorptance and optical losses for solar cell on 1-D gra-
tings (P/2 = 300 nm, h = 300 nm); circled black line is measured EQE of
solar cell on 1-D gratings, dashed red line is the absorptance of flat cell (see
Fig. 4.19), blue line indicates modeled absorptance with no symmetry (P =
600 nm, h = 300 nm); (b) comparison between measured and simulated $1 - R$
and i-layer absorptance.

their anti-reflective action, the active i-layer delivers 15.31% more current density than in flat case. In the next section the possibility to obtain even better performance by choosing other combinations of geometrical features and/or switching from 1-D to 2-D gratings will be shown. Together with the n-type layer, the back ZnO constitutes an increased source of losses with respect to the *pin* flat cell, because of the scattering provided by the gratings. Finally, also the textured silver back contact shows parasitic absorption, which is anyhow mitigated by the presence of the back ZnO [177].

Looking at S-pol and P-pol individually offers the interpretation of the features present in the averaged spectra of the simulated *pin* cell on 1-D gratings. Fig. 4.23(a) and Fig. 4.23(b) show the reflectance and absorptances of i-layer, front and back TCO, and Ag, for S-pol and P-pol, respectively. The wavelength range is divided in three regions: (1st) from 350 *nm* to 600 *nm*, (2nd) from 600 *nm* to 700 *nm*, and (3rd) from 700 *nm* to 1000 *nm*. In Fig. 4.24 electric field magnitude spatial distributions are reported for representative wavelengths of the three regions (500 *nm*, 652 *nm*, and 700 *nm*). The results in Fig. 4.23 and Fig. 4.24 will be compared at the same time. In the first region the absorptances corresponding to S- and P-pol are very similar and only slight differences in the amplitudes can be observed, like the small oscillations in P-pol case. Also the electric field magnitude spatial distribution for both polarizations, shown in Fig. 4.24(a), confirms such trend. In the second region, the effect of the polarizations in the solar cell structure is more visible. Switching from S-pol to P-pol, the reflectance peak at 640 *nm* seems to shift towards shorter wavelengths (625 *nm*) and another one occurs at 680 *nm*. Similarly, the absorptance peak in the i-layer at 670 *nm* shifts to 660 *nm* while other two peaks appear at 690 *nm* and 740 *nm*. For the selected wavelengths, in Fig. 4.24(b) and Fig. 4.24(c) the lower intensity of the electric
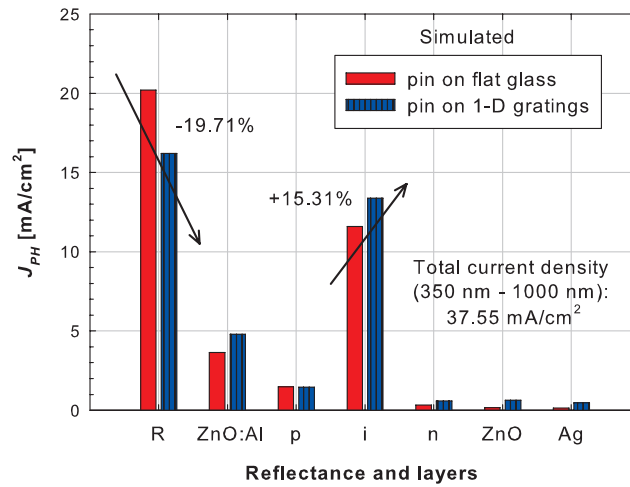
Figure 4.22: Photocurrent densities integrated over the chosen wavelength range (350 nm 1000 nm). Percentage values are calculated with respect to the flat cell.
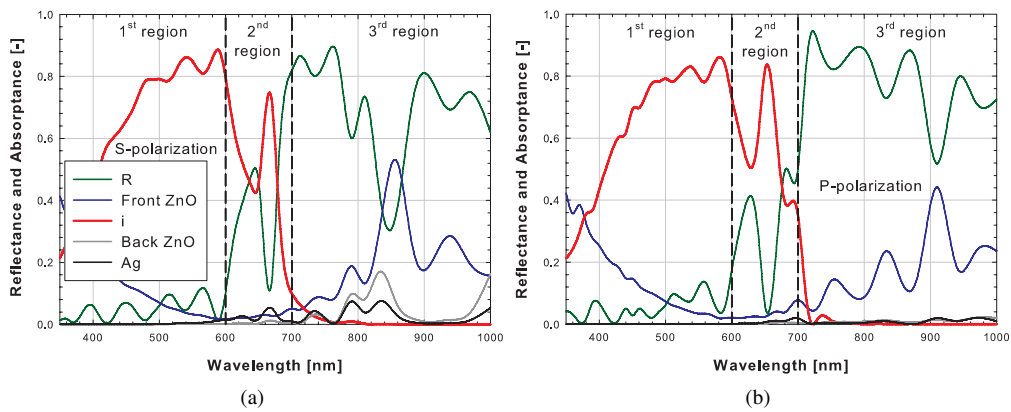

Figure 4.23: Comparison between i-layer absorptance, reflectance, and main parasitic absorptances for (a) S-pol and (b) P-pol. Vertical dashed lines delimit the discussed three regions.

field magnitude in S-pol indicates smaller absorptance and higher reflectance than the P-pol case.

The outlined physical behaviour is actually due to the enhanced excitation of propagating guided waves within the grating substrate of the solar cell under S-polarized light illumination. The wave guidance phenomenon results in a more efficient light focusing and trapping effect, and hence in superior performance in terms of external quantum efficiency (i.e., energy absorption) compared to the case of P-polarized light excitation [176, 214]. In the third region, where the extinction coefficient of the a-Si:H becomes the smallest among
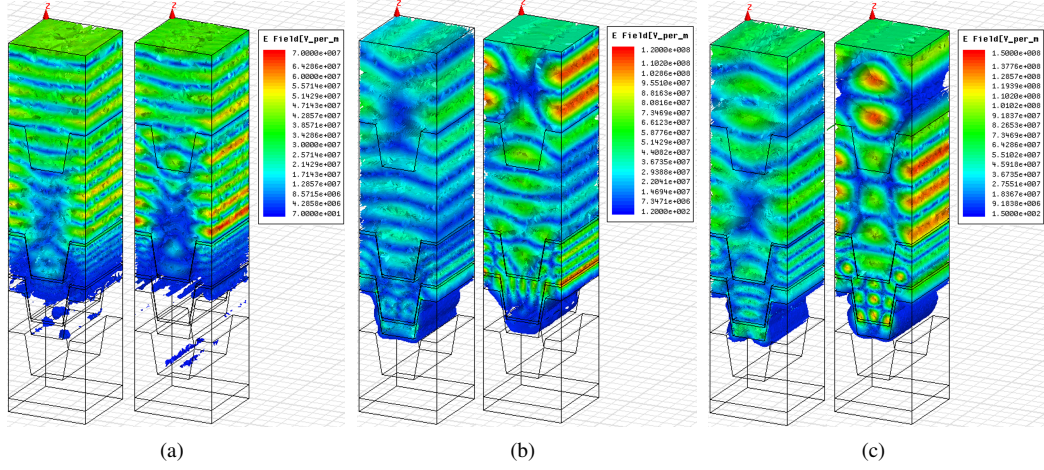
Figure 4.24: *Electric field magnitude spatial distribution at three wavelengths for S-pol (left) and P-pol (right): (a) 500 nm, (b) 652 nm, and (c) 700 nm. The pictures reported here refer to a bigger design (dx = 600 nm and dy = 600 nm) for visualization purposes.*

all the other layers (see Fig. 4.17(b)), the absorption is mainly within the silver, the front and back TCO while the reflectance constitutes the rest. However, for P-pol, the absorption in back ZnO and Ag is smaller than in S-pol case. This is due to a deep feature at 850 *nm* for the reflectance in S-pol case. In the closest range of this wavelength the optically parasitic layers resonate, thus increasing their absorptance. In Fig. 4.25 the local absorptance in the layers at 830 *nm* is shown, and, as expected from Fig. 4.23, in the S-pol case the absorption is higher than in the P-pol case. In Tab. 4.2 the J_{PH} calculated for each layer and for both polarizations are reported. In the P-pol case, the J_{PH} of the reflectance and of the absorptance of the front ZnO:Al is more pronounced than in S-pol. For all the other layers either there is no difference (p- and n-layers) between polarizations, or there is a higher response for S-pol.

4.5.8   Simulation of cells on 2-D grating textures and comparison with 1-D textures

3-D simulators, in contrast to 2-D simulators, enable to simulate structures with variations applied in both *x*- and *y*-directions. HFSS was used to simulate a *pin* a-Si:H solar cell on a 2-D grating texture. After that, a comparison of geometrical dimensions (*P* and *h*) of 1-D and 2-D gratings for optimal J_{SC} was carried out.

Referring to the structures depicted in Fig. 4.16(d), the simulation of a 2-D grating textured solar cell proceeded with boundary conditions as described in Sec. 4.5.2. Materials and thicknesses of the layers were kept identical as in case of flat and 1-D gratings textured solar cell as well as the period (*P*/2 = 300 *nm*) and the height (*h* = 300 *nm*). Since 2-D
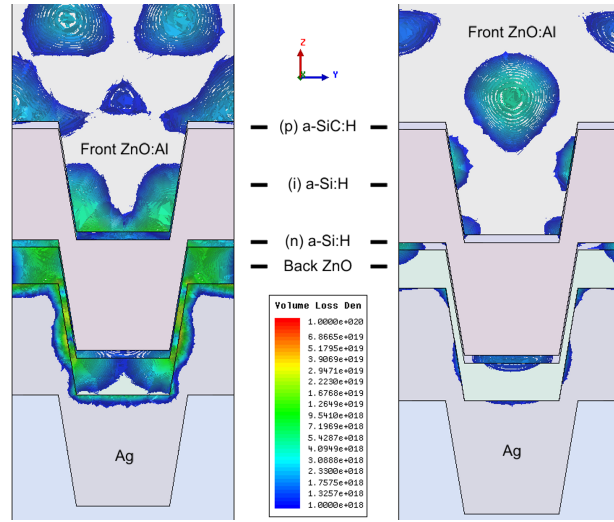
Figure 4.25: Local absorptance in the simulated structure at 830 nm for (left) S-pol and (right) P-pol simulations.

Table 4.2: J_{PH} [mA/cm^2] in each layer for flat and textured pin cells (average and polarizations).

Layers	Flat	Textured Average	S-pol	P-pol
R	20.99	15.67	14.82	16.53
ZnO:Al	2.24	4.87	4.61	5.14
p-layer	1.62	1.24	1.20	1.28
i-layer	11.54	13.80	14.08	13.52
n-layer	0.30	0.68	0.66	0.70
ZnO	0.07	0.60	1.05	0.14
Ag	0.81	0.67	1.11	0.24
Total	**37.55**	**37.55**	**37.55**	**37.55**

gratings are invariant with polarization, only one simulation was needed to determine the optical situation inside the solar cell. In Fig. 4.26(a) the absorptance in the i-layer and the optical losses related to the 2-D gratings solar cell are reported together with the $A_{i-layer}$ of flat and 1-D textured solar cells. Comparing the absorptances in the i-layer at short wavelengths, the switch from 1-D to 2-D gratings does not result in further improvements with respect to the flat cell. Actually, for this combination of period and height, the 1-D grating supplies slightly higher anti-reflective effect compared to the 2-D solution. However, for wavelengths longer than 600 *nm*, the solar cell on 2-D grating experiences a stronger scattering with the broad peak around 650 *nm* and a new one located between 700 *nm* and 750 *nm*. Due to stronger scattering effect, also the peaks related to the parasitic absorptions in the back TCO and Ag layers are more pronounced in 2-D grating case. In Fig. 4.26(b) the
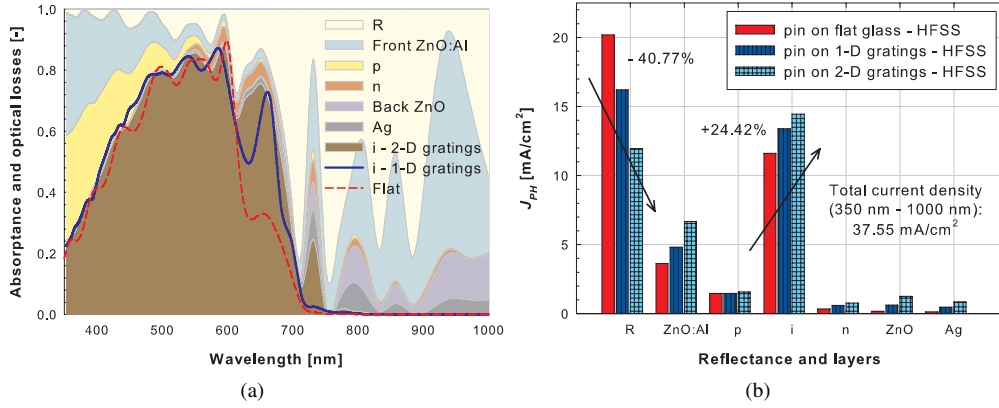
Figure 4.26: (a) Simulated absorptance in i-layer and optical losses for solar cell on 2-D gratings (P/2 = 300 nm, h = 300 nm). Blue line indicates absorptance in i-layer for solar cell on 1-D gratings (P/2 = 300 nm, h = 300 nm), dashed red line is the absorptance of flat cell (see Fig. 4.19); (b) Photocurrent densities integrated over the chosen wavelength range (350 nm 1000 nm). Percentage values are referred to the solar cell on 2-D gratings and calculated with respect to the flat cell.

photocurrent densities related to total reflectance and absorptances for the three simulated solar cells are reported. By using 2-D gratings, a further decrease of the optical losses due to the reflectance (from -19.71% of 1-D gratings to -40.77% of 2-D gratings with respect to flat cell) as well as a general increase of absorptance in all other layers are achieved. Textured with 2-D grating, the i-layer delivers 24.42% more current (+2.83 mA/cm^2) than in flat case.

After the preliminary simulation of 2-D grating textured solar cell, P and h were swept for 1-D and 2-D gratings in order to find a geometrical combination capable to deliver optimal J_{SC} for *pin* a-Si:H solar cells. The period was varied in steps from 300 *nm* to 1000 *nm*, the height from 150 *nm* to 450 *nm*, while the d_C was kept constant at 50%. The slope α was linearly varied with the period at a rate of 1.54°/100 *nm*. In this respect, for example, the simulated structures with P = 300 *nm* (1000 *nm*) have α = 85.62° (74.84°). In reported simulations, it was found that the optimal combination of P and h for 1-D and 2-D gratings does not change when varying the slope α. However, α affects the J_{SC} values. In addition, test simulations of structures on 2-D gratings with and without symmetry planes were run. Same reflectance and absorptance spectra were obtained. Results of the investigation are summarized in Fig. 4.27(left), where the J_{SC} is used as figure of merit to indicate the best combination of P and h for 1-D and 2-D gratings with respect to the flat interfaces, and in Fig. 4.27(right), where the current density related to reflectance (J_R) is used to quantify the anti-reflective effect. As previously mentioned, in case of 1-D gratings, the J_{SC} values were calculated from the averaged absorptance spectra obtained from S-pol and P-pol simulations.

The reported trends of J_{SC} for different heights are similar. Although the period 400 *nm* is the most effective for all heights, in case of $h = 450$ *nm* the influence of the P is not as significant as in the other two investigated heights. The optimal combination for this type of texture is $P = 400$ *nm* and $h = 300$ *nm*, resulting in an increase of +25.46% in J_{SC} with respect to the flat cell. Switching to the 2-D grating case, the trends of J_{SC} are again similar for the three heights, generally performing better than their 1-D grating counterparts. However, for smaller heights and large periods, the 1-D gratings work remarkably better than 2-D gratings, above all the combination $P = 1000$ *nm* and $h = 300$ *nm*. For the 2-D gratings the structure with period 500 *nm* delivers the largest J_{SC} for all the heights and the optimum is obtained for $h = 450$ *nm*. With this configuration the percentage increase in J_{SC} is found to be +32.53% with respect to the flat cell.
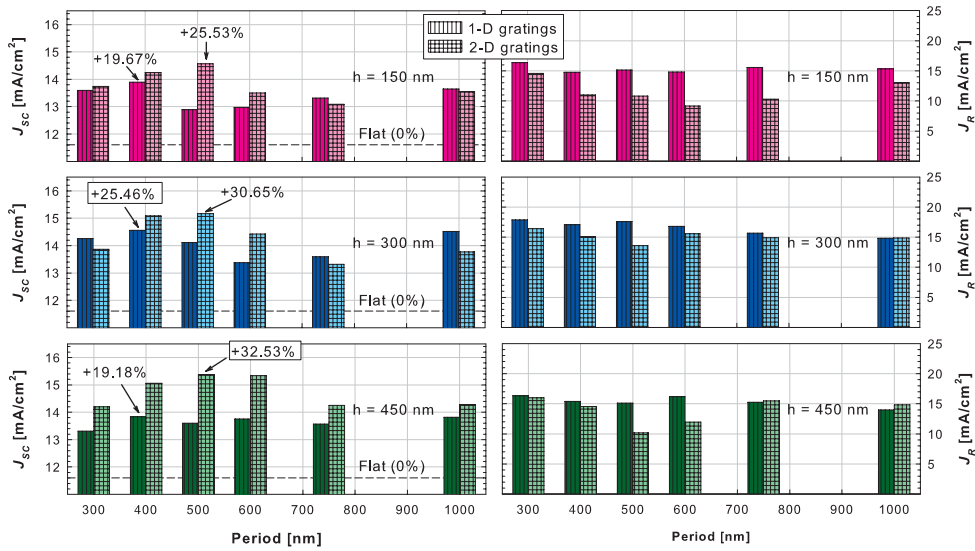

Figure 4.27: (Left) J_{SC} analysis for different periods and heights. Framed values are the highest percentage increases for 1-D and 2-D gratings with respect to the flat cell; (right) current density related to reflectance (J_R) for anti-reflective effect analysis between 1-D and 2-D gratings with respect to different periods and heights.

The values of J_R resulted from the convolution of the simulated reflectance curves with the AM1.5 photon flux over the entire wavelength range 350 *nm* 1000 *nm*. As shown in Fig. 4.27(right), all the combinations based on 2-D gratings generally exhibited better anti-reflective effect with respect to their counterparts based on 1-D gratings. In the considered wavelength range the anti-reflective effect given by the best 2-D grating is better than the one of the best 1-D grating. More in detail, the values of J_R from 1-D gratings hardly vary from 15 mA/cm^2, whereas those from 2-D gratings show dependency on period and height with minima located around the period 500 *nm* and inversely correlated with the maxima found in the J_{SC}.

Within the parameter space investigated, the textured cells performed always better than the flat one, indicating that diffraction grating textures own a realistic potential to increase

the efficiency of thin-film silicon solar cells. In Fig. 4.28 the spectral responses of the simulated flat cell and the best gratings combinations are compared. Cells on diffraction gratings outperform the flat one with important anti-reflective and scattering effects throughout the entire wavelength range. The textured solar cells, however, present different relative performance. Even though in the near infrared range the best 2-D grating results to be more efficient, the cell on the best 1-D grating shows slightly better anti-reflective effect. This is due to the fact that using a narrower wavelength range (350 *nm* 550 *nm*) the J_R is minimal around the period 400 *nm*.
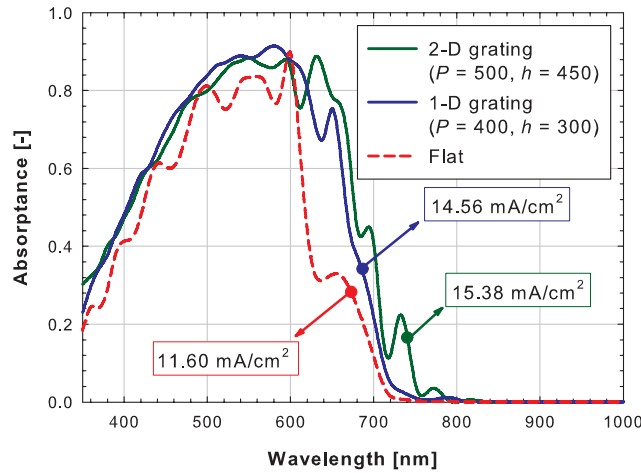

Figure 4.28: Comparison between simulated absorptances of flat solar cell and the solar cells based on best 1-D and 2-D gratings combinations; period P and height h indicated are in nm.

4.5.9 Discussion

The reliability and the efficiency of the developed 3-D model were successfully assessed in two subsequent steps: (i) validation of the HFSS behavior with respect to ASA software for a simple flat cell and (ii) verification of the simulation results with respect to real solar cell fabricated on 1-D gratings. Thus the 3-D optical model proved to be able to rigorously compare the spectral response and optical losses of thin-film silicon solar cells on diffraction gratings with respect to a flat cell.

Simulation results demonstrate that in case of 1-D gratings, polarization plays an important role with remarkable differences between S- and P-pol. Particularly, the 3-D model delivered for S-pol higher $A_{a-Si:H}$ and parasitic absorptances at the back side of the cell with respect to P-pol, finding in literature [214] an additional experimental verification. Another important aspect of this investigation is that the optimal combinations of *P* and *h* are related to a-Si:H based *pin* solar cells. As previously mentioned, changing device structure and using different absorbing material like (micro-) crystalline silicon will result in different optimal geometry [177, 202].

Looking at the efficiency of the 3-D model, in Tab. 4.3 the memory usage and the com-

Table 4.3: RAM usage, number of tetrahedrons and computational time for a selection of simulated solar cells (h = 450 nm), MB indicates Megabytes. For 1-D gratings, values of RAM and tetrahedrons are the sum of equivalent figures from S-pol and P-pol simulations. Each simulation comprised 51 data points spanning the wavelength range [350 nm - 1000 nm]. Technical details of the hardware configuration used in this work are as follows: Intel Xeon® architecture (2 x X5670, 12 cores), 24 Gigabytes DDR3-1333 RAM, Windows® 7 (64 bit) operating system.

P	1-D gratings				2-D gratings		
	RAM	Mesh	Time	Time	RAM	Mesh	Time
[nm]	[MB]	elements	(S-pol)	(S-pol)	[MB]	elements	[hr:min:s]
			[hr:min:s]	[hr:min:s]			
300	655	23453	0:36:24	0:43:39	434	20246	0:35:58
400	763	20969	0:29:38	0:50:10	628	20425	0:46:00
500	438	14331	0:25:08	0:26:24	810	16736	1:25:18
600	451	20413	0:26:16	0:32:16	597	24289	0:52:46
750	659	19590	0:38:29	0:46:19	1330	38487	1:37:25
1000	561	34263	0:38:29	0:32:42	1370	31732	1:46:25

putational times of the largest simulated solar cells on 1-D and 2-D gratings ($h = 450$ nm) are reported. The amount of used RAM rarely exceeded 1000 Megabyte: this instance occurred only for bigger designs based on 2-D gratings. The memory used for 1-D gratings is reported as the sum of RAM in both S-pol and P-pol simulations, since the two simulations were actually performed in parallel. It was noted that P-pol simulations usually took longer than S-pol ones. With average computational times of about 50 minutes, 2-D gratings textured solar cells could be simulated in a short amount of time, the lengthiest computation taking less than 2 hours.

4.6   Conclusions and outlook

In this chapter, periodic gratings were found to be suitable substrates for improved light scattering in thin-film silicon solar cells. 1-D gratings were fabricated in several combinations of period and height on glass substrates. Surface morphology and scattering properties of 1-D periodic gratings were characterized. The period and the height of the gratings showed considerable effect on angular intensity distribution, transmittance, and haze parameter. Lacking optical models devoted to the explanation of scattering from transparent rectangular gratings, the theory of opaque sinusoidal gratings and the Harvey-Shack model were modified and used to get a qualitative insight into the scattering properties of the available textures. Polarization-dependent measurements should be the first action to take for a more formal understanding of transparent gratings.

Several 1-D gratings were used as substrates for deposition of single junction a-Si:H solar cells. The evolution of surface roughness after the deposition of individual layers was determined by AFM. The periodicity of the grating was maintained while the height decreased after the deposition of silicon layers and the back contact. Best performance was

obtained on a solar cell deposited on a diffraction grating with $P = 600$ nm and $h = 300$ nm. Its quantum efficiency approached the quantum efficiency of the cell deposited on Asahi-U type TCO substrate. The short circuit current density of this solar cell based on gratings was increased by 13.4% relative to the J_{SC} of solar cell with flat interfaces. These results can be explained both by scattering and anti-reflective effects introduced by 1-D periodic diffraction gratings. Further improvements in solar cells performance are expected with the implementation of ZnO / Ag back reflector to limit losses in n-layer and Ag and increase the absorption of in the absorber layer.

An effective but rigorous 3-D optical modeling of thin-film silicon solar cells was also presented in this chapter. The HFSS software was used to simulate the optical response of *pin* thin-film silicon solar cell on 1-D and 2-D gratings. Developing fast and physically reliable method to simulate such type of solar devices is important not only for the optimization of the gratings for real-life solar cells, but also for studying the scattering processes occurring at textured interfaces.

The model was validated with the reference software ASA in case of solar cell with flat interfaces on thick glass. The 3-D model allows simulating optically thick substrates, like glass, while designing them as thin as the thin-films used in solar cells. This is an important step as the complexity of the structure can be kept low, resulting in faster calculations. The simulation of a *pin* cell on 1-D grating was also described in detail. The results were compared to a real thin-film silicon solar cell deposited on 1-D grating texture. From the comparison of the spectral responses and with the aid of the model, optical losses and polarization dependency could be addressed.

Afterwards, the model was used to carry out the simulation of solar cells on 1-D and 2-D grating textures with different periods and heights, pursuing an optimal combination for the highest J_{SC}. For 1-D (2-D) gratings such combination was found to be $P = 400$ nm (500 nm) and $h = 300$ nm (450 nm), resulting in a percentage increase of +25.5% (+32.5%) more J_{SC} than in case of flat cell. From this investigation, all gratings textured solar cells outperformed the flat one, showing that diffraction gratings can boost the efficiency of thin-film silicon solar cells.

In view of the inexpensive computer hardware used, physically reliable results could be quickly carried out: for each simulation the RAM usage was kept as low as 1500 MB and the average computational time was about 50 minutes. With such interesting technical performance, our model can be profitably used for the further optimization studies, opening a new season of 3-D FEM optical modeling in thin-film silicon solar cells.

In a future dedicated study, the presented modeling approach will be able to simulate the impact of oblique light incidence on the optical properties of realistic solar cells, as it has been already discussed in some papers [238, 239] by using FDTD-based methodologies. Another aspect that should be fixed is the implementation of a post-simulation procedure aimed to calculate the reflectance occurring at air / glass interface. In this way the effects of such interface on the optical situation inside entire structure will be properly taken into account.

Chapter 5

Modulated surface textures

In this chapter a general concept of surface texture for enhanced scattering in a broad wavelength range, namely modulated surface texture, will be introduced and analyzed. The explanation of improved scattering will be based on superposing different scattering mechanisms caused by the different geometrical features integrated in a modulated surface texture. The fabrication of such advanced textures will be reported and the application in thin-film silicon solar cells tested. Results on micromorph tandem cells were carried out in collaboration with IMT-PVLAB, Neuchâtel (Switzerland).

5.1   Introduction

Light scattering at textured interfaces leads to an increased absorption in thin absorber layers by increasing the optical light path. Especially multi-junction thin-film silicon solar cells need an efficient scattering at long wavelengths to deliver high photo-current densities. Substrates that consist of glass coated with surface-textured transparent conductive oxide (TCO) are used to introduce texture to the interfaces inside the solar cells. Notable examples are as-grown SnO_2:F [145] and ZnO:B [240] (pyramidal surface features) or wet-etched ZnO:Al [241] (crater-like surface features). TCO deposited on transparent dielectric periodical surface textures are possible alternatives to the randomly textured substrates (see Ch. 4). In Fig. 5.1 a collection of measured hazes in transmission (H_T) for such typical textures is reported, where small values are registered at long wavelengths.

For ensuring stronger light scattering in multi-junction devices, novel types of TCO have been developed. SnO_2:F and ZnO:B substrates characterized by double-texture surface morphologies or large features and by improved scattering behaviour [125, 127, 242] are capable to deliver high values of short-circuit current density when embedded in single or double junction devices. However, it has been found that the growth of high-quality nc-Si:H layers is not favoured on such novel TCOs. Large surface features are indeed responsible for voids and cracks in such absorber layers [94], limiting open-circuit voltage and fill factor of the devices. Thus smoothened versions exhibiting lower scattering have been fabricated,
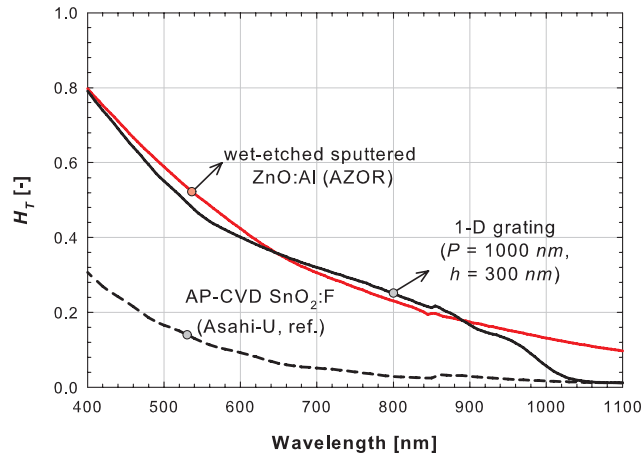
Figure 5.1: Haze in transmission of typical surface textures for single junction devices.

usually by means of dry-etching techniques[1]. In Fig. 5.2 H_T of novel TCOs is reported[2], showing how their optical behaviour can be manipulated.
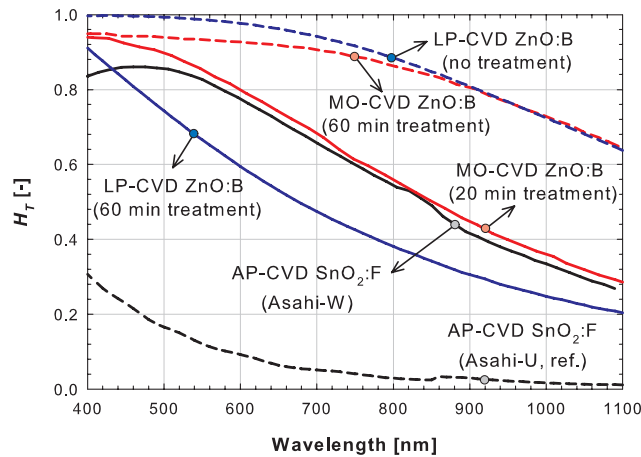

Figure 5.2: Haze in transmission of novel surface textures for single junction and multi-junction devices.

Pursuing optimal substrate for thin-film silicon solar cell is anyway not only about achieving high haze. Also TCO's low absorption and surface features angle distribution play a crucial role. Low free carrier absorption (FCA) TCOs like hydrogenated indium-oxide (In_2O_3:H) [123] or manipulated ZnO:B [243] are at the basis of recently reported

---

[1]Another approach is the implementation of amorphous or nano-crystalline silicon-oxide alloys (see Sec. 2.3.1).

[2]H_T data points of Asahi-W and MOCVD ZnO:B were digitized from referred papers, H_T data points of LPVCD ZnO:B were measured by dr. K. Jäger at TUDelft (courtesy of dr. D. Dominé, formerly at IMT-PVLAB, Neuchâtel, Switzerland). Their usage is for comparative purpose only.

high initial efficiencies for double junction solar cell [244]. From the work of Dominé *et al.* [225] to the recent contribution of Wuang *et al.* [245], the angle distribution of surface features started to be systematically studied, for which large angle distribution correlates well to high scattering and solar cells optical performance.

Surface textures for thin-film silicon solar cells can be subdivided in two classes: those introduced at TCO level (as grown and/or fabricated) and those initiated at substrate level (see Fig. 5.3). The latter case leads eventually to the depicted advanced textures, since coating textured substrates with a TCO film is unavoidable for electrical reasons. Among the techniques to texture glass, wet [246–248] or dry etching [242] can be profitably used, but also laser scribing [249] or nano-moulding [250] transparent photoresists offer a considerable degree of freedom. In this wide scenario, where different techniques, materials, and shapes can be combined together, a generalized approach is needed for designing and optimizing advanced textures. Such general approach, called modulated surface texturing (MST), is here introduced and analysed. With MST concept, existing advanced textures can be unveiled, underlying physics for high scattering can be understood, and finally new substrates can be designed.
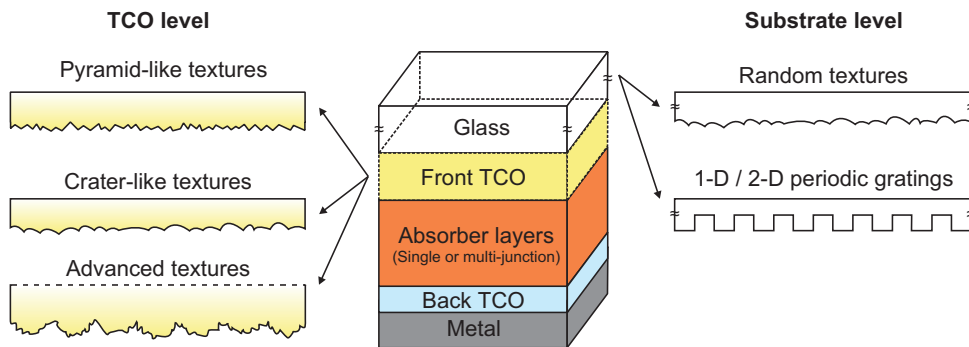

Figure 5.3: Sketch depicting different classes of surface textures introduced by TCO film in thin-film silicon solar cells.

5.2 Morphological and optical superposition

A substrate with modulated surface texture can be prepared as a stack of layers in which a different texture is introduced at individual interfaces. Provided the layers are thin enough, the textures of the individual interfaces are transferred to the subsequent interfaces. The resulting surface of the stack accommodates all the morphological components introduced at the individual interfaces. The stack may comprise layers of the same or different materials and a broad range of lateral and vertical geometrical features introduced at interfaces, as schematically shown in Fig. 5.4(a). By combining appropriate geometrical features introduced at the individual interfaces, one can take advantage of superimposing the scattering mechanisms caused by these different geometrical features and achieve higher scattering levels in a broad wavelength range in comparison to the scattering contributions from individual morphologies. An impression of the optical superposition is depicted in Fig. 5.4(b),
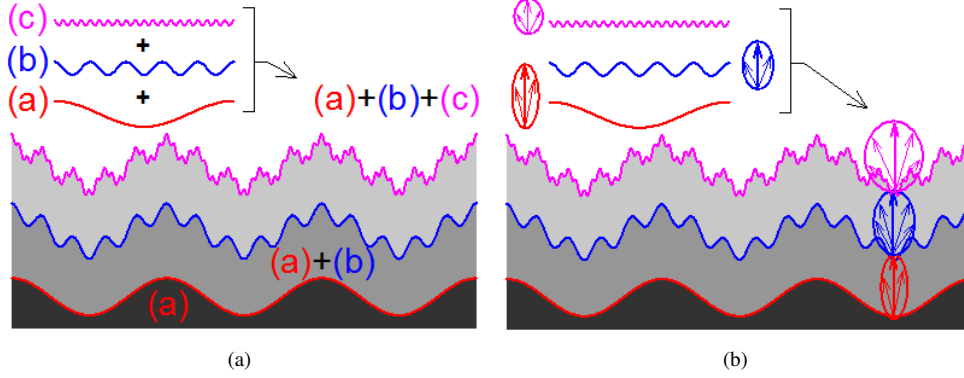
Figure 5.4: Multi-stack depicting morphologically (a) and optically (b) the MST concept.

where light entering from the bottom side, finding large features, undergoes a first scattering process called *supporting mechanism* (see Sec. 5.4), which acts especially on long wavelength photons, and then it is further scattered by encountering smaller features, which interact more efficiently with short wavelength photons.

5.3   Spatial frequency surface representation

In order to quantitatively represent and analyze the morphology of modulated surface textures the spatial frequency surface representation σ^*_{RMS}, based on the discrete Fourier transform (DFT) of the surface morphology [251], can be used.

In this frame, the surface morphology, indicated with $z(x,y)$ and containing information on surface features height, is regarded as superimposition of a set of sinusoidal profiles along lateral x- and y-directions, each characterized by particular amplitude (K_i) and period (P_i), where the subscript i indicates the ith sinusoidal profile. When applying the DFT to the surface profile, individual sinusoidal profiles are obtained. They represent the spectrum of the surface profile in a spatial frequency domain. This spectrum has discrete components located at specific spatial frequencies (f_i), defined as the inverse of the period of the single sinusoidal profile ($P_i = 1/f_i$) [251]. Considering the magnitude of the calculated spectrum and dividing it by $\sqrt{2}$, the frequency distribution of the effective root mean square (*RMS*) value of all sinusoidal profiles $\sigma^*_{RMS}(f_i)$ can be obtained.

5.3.1   Calculating the spatial frequency surface representation

The surface morphology $z(x,y)$ is scanned with AFM (see Sec. 3.2.2) over a squared area ($LxL \ \mu m^2$) to get a discrete 2-D array $z(n,m)$, whose dimension is [NxN] with N number of scan lines along x- and y-direction[3]. The spatial resolution of the scan along the two directions (τ_x and τ_y, respectively) is univocal in this case: $\tau = \tau_x = \tau_y = L/N$.

---

[3]Usually $N = 2h$ with h positive integer, because in this way discrete Fourier transform algorithm can run faster. In fact, lower bounds for the number of real multiplications and additions to perform (i.e. lower computation

The scanned image (2-D array) is then unfolded in order to get a single profile (1-D array) along x-direction, $z_U(n)$, composed by all scanned lines along y-direction for a total of N^2 elements. As it will be shown later, this choice is made to carry out a compact σ^*_{RMS}, useful for MST analysis. However, unfolding the 2-D scanned image to the 1-D profile introduces an artificial periodicity due to the scan length along the unfolding direction (in this analysis the x-direction). To handle this issue, a Tukey window filter [253] is applied to each unfolded line along y-direction, finally obtaining $z_{TU}(n)^4$.

After such filtering, the 1-D profile is transformed in spatial frequency domain by a discrete Fourier transform (DFT) algorithm over N^2 elements, getting the complex valued function $DFT[z_{TU}(n)](f)$, whose x-axis is given by N^2 points with values ranging from 0 to $N^2 - 1$. To get the spatial frequencies a proper scaling is thus necessary. The axis of the spatial frequencies goes from $f_{MIN} = 1/(NL) = 1/(N^2\tau)$ (inverse of the unfolded scan length) to $f_{MAX} = 1/(2\tau) = N/(2L)$ (inverse of twice the lateral resolution of the AFM scan, according to Nyquist-Shannon sampling theorem [251]) with constant step f_{MIN}. Consequently the total number of considered spatial frequencies is $f_{MAX}/f_{MIN} = N^2/2$, which is half of the initial set, since the DFT of a real valued function like $z_{TU}(n)$ is symmetric with respect to f_{MAX} [254]. The spatial frequency surface representation is finally obtained from the absolute value of the DFT multiplied by the FFT scaling factor $2/N^2$ and divided by $\sqrt{2}$:

$$\sigma^*_{RMS}(f_i) = \frac{2}{N^2} \frac{|DFT\,[z_{TU}(n)]\,(f_i)|}{\sqrt{2}} = \frac{K_i(f_i)}{\sqrt{2}} = \frac{K_i(1/P_i)}{\sqrt{2}}\Big|_{\forall i \in \left[0, \frac{N^2}{2}-1\right]}. \tag{5.1}$$

Eq. 5.1 represents the frequency distribution of the effective *RMS* value of all sinusoidal profiles with amplitude K_i and period P_i composing the initial morphology $z(x,y)$.

5.3.2 From spatial frequency surface representation to surface roughness

The σ_{RMS} is a statistical parameter widely used to parameterize the surface roughness of randomly-textured surfaces. It can be determined from the distribution of surface heights. In Sec. stats the σ_{RMS} was introduced as an output of AFM scan. Another approach to determine this statistical parameter is via the spatial frequency surface representation:

$$\sigma_{RMS} = \sqrt{(\sigma^*_{RMS1})^2 + ... + (\sigma^*_{RMS1})^2 + ...} = \sqrt{\sum_{i=0}^{\frac{N^2}{2}-1} \left[\sigma^*_{RMS}(f_i)\right]^2} \tag{5.2}$$

From Eq. 5.1 and Eq. 5.2 both vertical and lateral characteristics of the surface morphology can be efficiently presented using the σ^*_{RMS} distribution. In Fig. 5.5 the spatial frequency

---

complexity) are found for a DFT of power-of-two length ($N = 2h$) [252].

[4]This periodicity can be ideally modeled as a train of pulses with variable amplitude given by the difference between the value of the last point of the jth profile and the value of the first point of the j+1th profile, Δ_j. When transformed in Fourier's space, such train of impulses gives a replica of impulses scaled in amplitude by the factor $1/N$ and positioned every k/N with k integer running from $-\infty$ to $+\infty$. Applying a tapered cosine (or Tukey) window to each scan line allows forcing gradually to zero the amplitude of each scanned line. At the expenses of a little manipulation of scanned data, Δ can be made null and the unwanted train of pulses in frequency domain suppressed.

representation of the simple example of a modulated surface texture with three sinusoidal-shaped components of Fig. 5.4(a) (1-D sinusoidal-like gratings) is presented. The three vertical bars correspond to the components of spatial frequency at 0.2 μm^{-1}, 1 μm^{-1}, and 4 μm^{-1}, which have σ_{RMS}^* discrete values of 30 nm, 20 nm, and 8 nm, respectively, while periods of the sinusoids are related to spatial frequencies as $P = 1/f$.
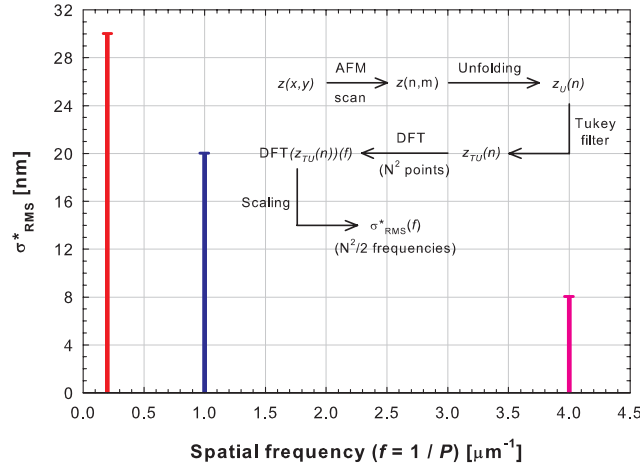

Figure 5.5: Spatial frequency surface representation of a simple modulated surface.

This way to evaluate the surface roughness has several advantages: (i) investigation of surface textures having similar σ_{RMS} but different σ_{RMS}^* distributions, (ii) indication of the fundamental discrete components that dominate the vertical and lateral surface features, (iii) simple and comprehensive representation of surface modulation, and (iv) unveiling existing advanced textures (see Fig. 5.6).
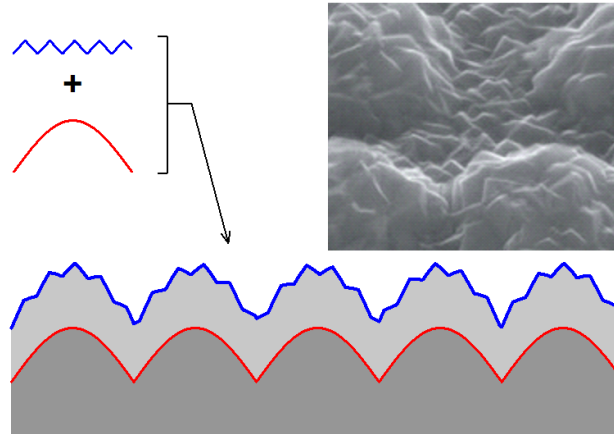

Figure 5.6: Visualization of Asahi-W (or similar MO-CVD ZnO:B) advanced surface texture in terms of simpler surface components (MST).

5.4 Scattering mechanisms

Introducing the morphological and optical superposition to define the MST, it can be pointed out that different morphologies trigger different scattering mechanisms. As the size of surface features shrinks from *μm*-scale to *nm*-scale, different optical regimes dominate and/or superpose. In this section two optical regimes are discussed as boundaries for MST applications.

When the geometrical dimensions of the rough surface are larger than the wavelength of light, the scattering with strongly directional and weakly wavelength-dependent characteristics can be enhanced. This scattering behaviour can be well described by the Mie solution of Maxwell equations [255]. It is possible to represent such surface-textured morphology as a distribution of spherical particles [206], so that the diffuse transmittance, T_D, can be expressed as:

$$T_D = \frac{\pi a^2}{L_C^2} Q_{sca} \tag{5.3}$$

where πa^2 is the geometrical cross-section of the modelled distribution-averaged spherical particle of radius a, which is defined as half of the peak-to-peak height of the surface texture; L_C is the correlation length of the surface texture; and Q_{sca} is the scattering efficiency [257], that has a weak wavelength dependency [258]. The peak-to-peak height and the correlation length are directly calculated from AFM-scanned surface height distribution. Also surface features, approximated to *grained spheroids* and characterized by a random distribution of diameters, is obtained from AFM. Such distribution can be used as input for the computation of Q_{sca} extended to statistical case in software like MiePlot citetwohundredfiftynine. Thus the Eq. 5.3 expresses a mixed model, which uses a random distribution of surface spheres for characterizing the scattering and an ordered arrangement of surface spheres for correcting the intensity of such scattering (see Fig. 5.7).
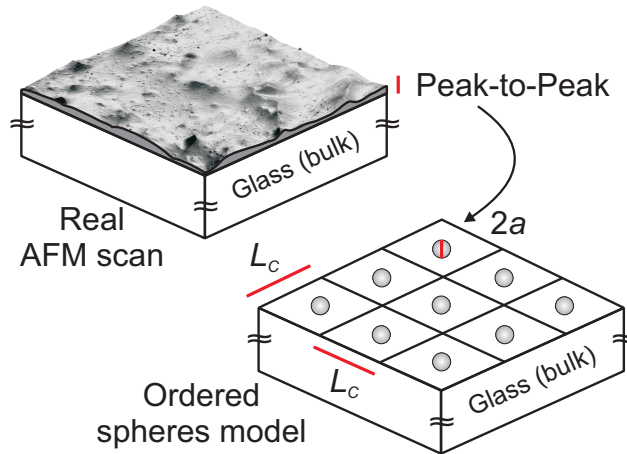

Figure 5.7: Schematic sketch of the ordered spheres model for the special case of etched glass.

When the vertical dimensions of the surface roughness become comparable to the wavelength of light, another scattering mechanism becomes dominant. This type of surface exhibits a more diffuse (i.e. less directional) scattering and a significant wavelength dependency. Scalar scattering theory [221] can be used to approximate this scattering behaviour. In this case the T_D can be described as:

$$T_D = T_T \left\{ 1 - exp \left[- \left(\frac{2\pi\sigma_{RMS}|n_0 - n_1|}{\lambda} \right)^\gamma \right] \right\} \tag{5.4}$$

where T_T is the total (diffuse + specular) transmittance of a rough interface, σ_{RMS} is the surface *RMS* roughness, n_0 and n_1 are the refractive indices of the materials forming the interface, λ is the wavelength, and γ is the exponent which ranges from ~ 1.5 to 3 depending on the height distribution function of the surface morphology [127, 167, 260]. This scattering mechanism is characterized by a pronounced exponential decay in T_D with increasing wavelength, which is typical for the commonly used randomly surface-textured substrates for thin-film solar cells.

For all combinations between these two boundaries a superposition of the two effects is expected, with one dominating the other according to the geometrical size of the background texture. Particularly, the minimal value to which the haze saturates (*supporting mechanism*) is strongly determined by the background texture as sketched in Fig. 5.4(b) and highlighted in Fig. 5.8 for some existing advanced TCO substrates. This effect can be manipulated by changing the correlation length and the peak-to-peak height of features of the background texture, as it will be shown in Sec. 5.7.
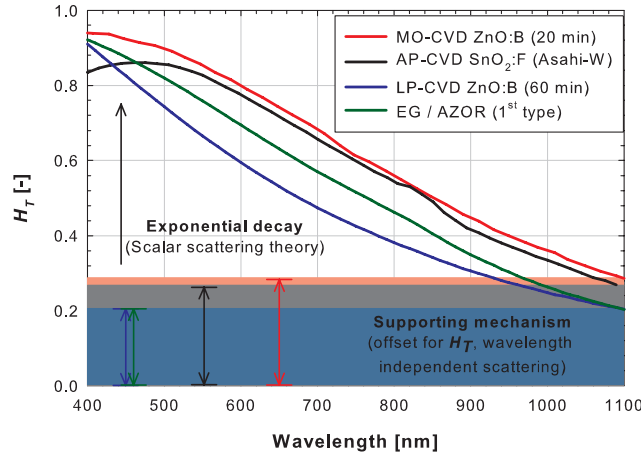

Figure 5.8: Supporting mechanism highlighted in some of the existing advanced textures.

5.5   MST on first type of etched glass

Morphological and scattering properties for an example of designed TCO substrate with a modulated surface texture are presented and analyzed. This advanced substrate formed by

etched glass and wet-etched TCO was tested in *pin* single junction thin-film silicon solar cells.

5.5.1   Samples fabrication

The MST sample was fabricated by chemically-etching a flat Corning Eagle 2000^{TM} glass substrate in a compound solution composed by HF and H_3PO_4 for 35 minutes at room temperature (etched glass, EG). Such etching resulted in a surface morphology with large feature sizes. Following this, a 1 *μm* thick ZnO:Al TCO layer was deposited using RF magnetron sputtering (normal ZnO:Al, AZON) and chemically wet-etched in 0.5% diluted HCl for 40 seconds (rough ZnO:Al, AZOR) to add smaller texture features to the surface roughness [261]. AFM was used to determine the morphology and the spatial frequency surface representation of the investigated textures.

5.5.2   Morphological and optical analysis

In Fig. 5.9, AFM scans are shown for the surfaces of etched glass (texture (a) - large features), etched TCO deposited on a flat glass as a reference (texture (b) - small features), and etched TCO on etched glass (the modulated texture (c)). In Fig. 5.10, the σ^*_{RMS} distributions for the three morphologies are shown. In contrast to Fig. 5.5, Fig. 5.10 shows that the analyzed textures evolve in a dense distribution of discrete σ^*_{RMS} components. Only the tops of the bars are drawn in the Fig. 5.10, which results in step-wise σ^*_{RMS} curves.
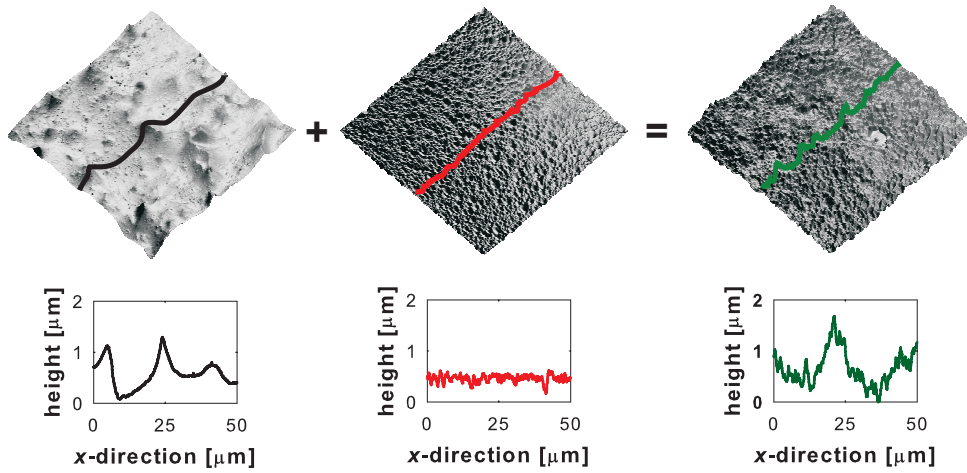

Figure 5.9: The AFM scans (50x50 μm^2 area) and cross sections along x-direction of three different textures: (a) - larger texture (EG, σ_{RMS} = 200 nm), (b) - smaller texture (flat glass / AZOR, σ_{RMS} = 82 nm), and (c) the resulting modulated texture (EG / AZOR, σ_{RMS} = 252 nm).

The σ^*_{RMS} of the texture (a) (large features) is characterized by a distinct peak at low frequencies, which corresponds to features with large lateral and vertical dimensions (zone 1). This is followed by a decay (zone 2) and then saturation (zone 3). The σ^*_{RMS} curve of the
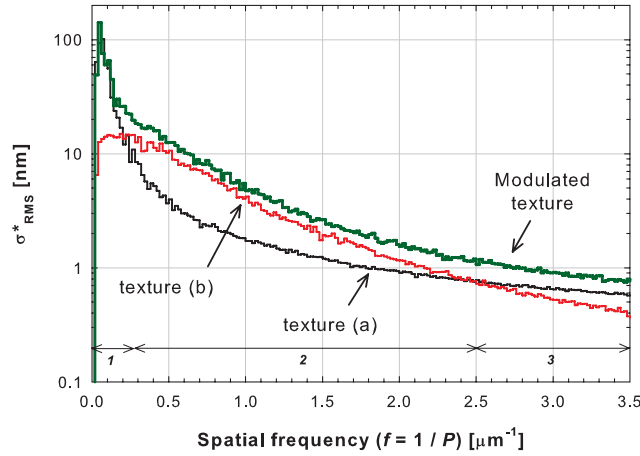
*Figure 5.10: Spatial frequency surface representation (log scale) of texture (a) large fea-
tures, texture (b) small features and the modulated texture.*

texture (b) (small features) does not feature a distinct peak at low frequencies, but instead
exhibits a broader distribution of higher values of σ^*_{RMS} in zone 2 with respect to the texture
(a). The sample with a modulated texture shows a high peak in the σ^*_{RMS} values at low
spatial frequencies due to the contribution of the etched glass, and also higher σ^*_{RMS} values
over the rest of the spatial frequency spectrum due to the contribution of the etched TCO.

The light scattering properties of the textured substrates were measured using integrat-
ing sphere and variable angle spectrometry techniques as mentioned earlier in Sec. 3.2.6.
The diffuse transmittance (T_D) of the different surface textures are presented in Fig. 5.11.
Texture (a) exhibits an almost constant T_D over a broad range of wavelengths. This be-
haviour was modelled using Eq. 5.3 with $a = 0.85\ \mu m$, $L_C = 5.7\ \mu m$, and Q_{sca} calculated
from the surface grains distribution (see Fig. 5.12), proving that this scattering can be well
described by the Mie scattering. The texture (b) exhibits an exponential decay in T_D, which
can be modelled using Eq. 5.4 based on the scalar scattering theory with $\sigma_{RMS} = 82\ nm$,
$\gamma = 1.5$, and T_T as determined for the structure. The T_D of texture (b) decreases at the shorter
wavelengths due to absorption in the TCO layer at these wavelengths. The modulated sur-
face texture exhibits the highest T_D across the entire wavelength range. One can observe
that the T_D of the modulated surface texture combines the optical behaviour of the individ-
ual textures (a) and (b), thus confirming that both scattering mechanisms are present and
active.

In Fig. 5.13, the angular intensity distribution of transmitted light (AID_T), measured in
the plane normal to the scattering interface, is shown. The AID_T corresponding to the modu-
lated surface texture has the lowest specular component and the highest diffuse component
for almost all scattering angles. The high scattering level results from a combination of the
low specular component that originates from the presence of large surface textures, and the
broad angular distribution function that comes from scattering at the small surface textures.
Therefore two scattering mechanisms, described by Eq. 5.3 and Eq. 5.4, are present in
the resulting AID_T. The first one contributes to a high scattering level nearby the specular
direction and the second one assures more efficient scattering at larger scattering angles. It
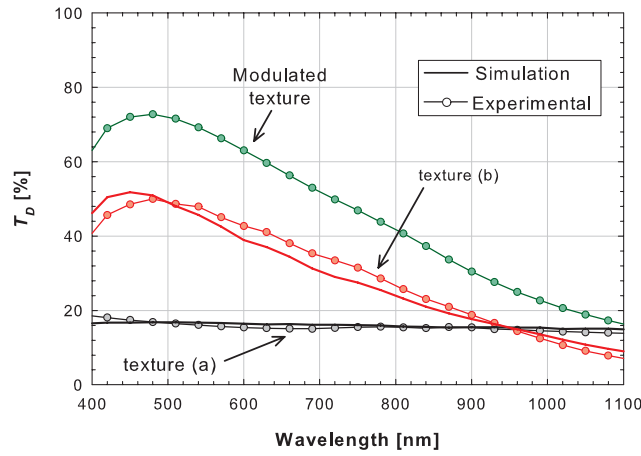
Figure 5.11: Symbols: measured T_D of the texture (a) large features, texture (b) small features and the modulated texture; solid lines: calculated T_D.
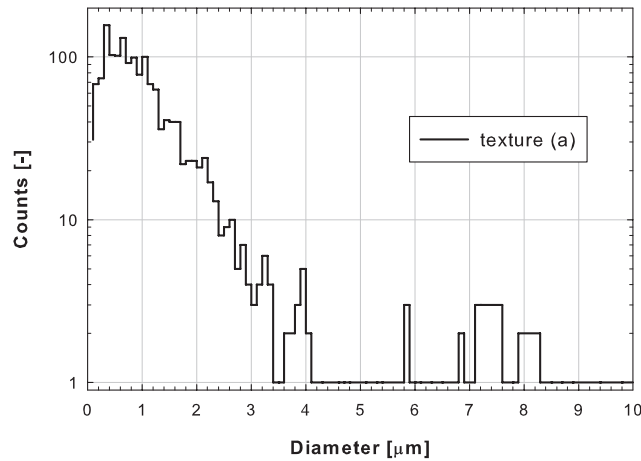

Figure 5.12: Distribution of grains diameter evaluated on the surface of texture (a). The scale of counts is logarithmic and the width of bins is 0.1 μm.

is this superimposed scattering behaviour that is essential for the efficient light trapping in thin-film silicon solar cells. It may be achieved and tailored by surface texture modulation, which can activate several scattering mechanisms.

In this section the scattering properties of a modulated surface texture for application in thin-film silicon solar cells were analyzed. Enhanced scattering levels were achieved by superimposing different scattering mechanisms. It was demonstrated that such mechanisms were activated by the different geometrical features integrated in the modulated surface texture. This example of modulated surface-textured TCO substrate exhibited an increased scattering level across a broad wavelength range up to 1100 *nm*, and also scattered into large angles. Both of these scattering properties are required for efficient light trapping in
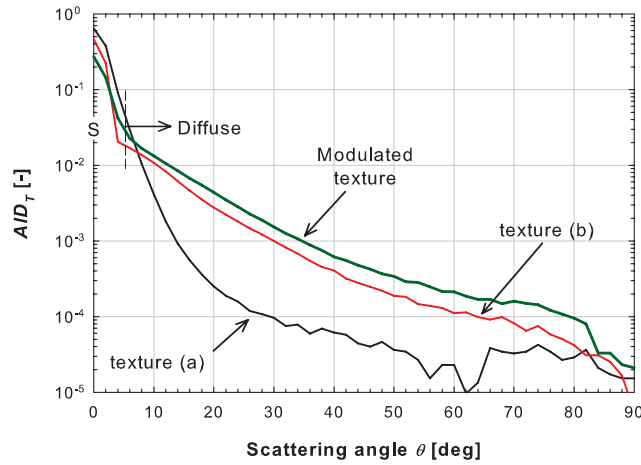
Figure 5.13: AID_T of texture (a) large features, texture (b) small features, and modulated texture at $\lambda = 633$ nm. Letter S indicates the specular component.

multi-junction thin-film silicon solar cells. The scattering behaviour of the substrate can be understood by a combination of Mie scattering for larger features, superimposed with the exponential decay of scattered light from smaller features, which can be described by scalar scattering theory.

5.5.3   Single junction solar cells

Three a-Si:H *pin* single-junction solar cells were deposited by RF PE-CVD on flat glass / AZOR (reference), EG / AZON, and EG / AZOR (MST) TCO substrates. Solar cells structure is as follows: glass (0.6 *mm*) / front ZnO:Al (600 *nm*) / nc-Si:H p-layer (10 *nm*) / a-Si:H p-layer (5 *nm*) / a-SiC:H buffer / a-Si:H i-layer (300 *nm*) / a-Si:H n-layer (20 *nm*) / back ZnO:Al (80 *nm*) / Ag 100 *nm*. AZOR thickness was obtained after the etching process described in Sec. 5.5.1, while AZON thickness was as-deposited 600 *nm* thick. Initial external electrical parameters of the best dots are reported in Tab. 5.1, while the relative current density-voltage characteristics and *EQE* are reported, respectively, in Fig. 5.14(a) and 5.14(b). The analysis of external parameters reveals that V_{OC} and FF of both cells on AZOR are slightly worse than the cell on AZON, even being deposited on etched glass. This indicates that the quality of *pin* a-Si:H junction depends mainly on nano-scale roughness. Looking at solar cells spectral response allows to correctly understand J_{SC} values. Even having different surface textures, the solar cells deposited on flat glass / AZOR or on EG / AZON behave similarly at short wavelengths. At long wavelengths the reference cell outperforms the one on flat glass / AZON, since this cell, as it will be shown in Sec. 5.7, behaves as being optically flat. For both short and long wavelengths the spectral response of the solar cell based on MST is improved. The enhancement results from anti-reflecting effect, assured by combination of small craters on top of large features, and from efficient scattering, given by the modulated surface-textured TCO with broader AID_T and higher haze.

Table 5.1: Initial external parameters of best measured cells on three TCO substrates. Values of current density are from EQE measurements.

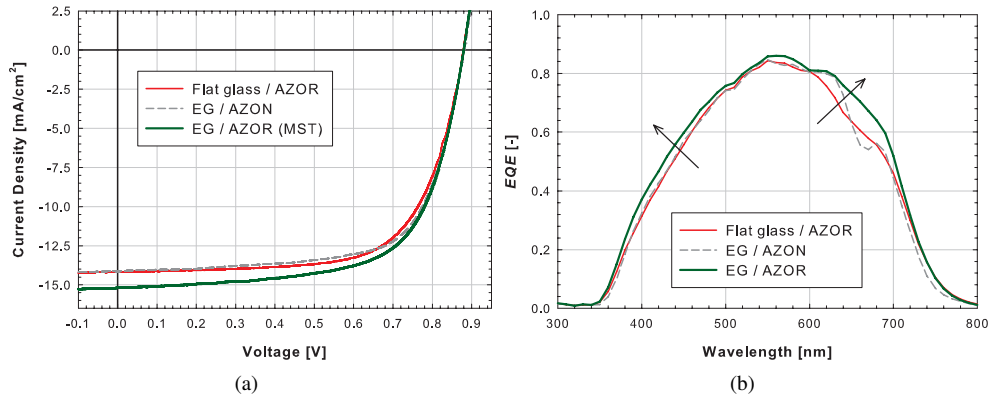| TCO substrate	V_{OC} [V]	J_{SC} [mA/cm^2]	FF	η [%]
Flat glass / AZOR (ref.)	0.878	14.18	0.670	8.34
EG / AZON	0.882	14.13	0.686	8.55
EG / AZOR	0.880	15.20	0.661	8.84

Figure 5.14: Current density-voltage characteristics (a) and external quantum efficiency (b) of the three solar cells reported in Tab. 5.1.

5.6 MST on 1-D gratings

Another application of modulated surface texturing can be based on transparent 1-D gratings underneath wet-etched ZnO:Al, combining the angle-selective behaviour of the gratings with the random scattering of small features. Also this advanced substrate was tested in *pin* single junction thin-film silicon solar cells.

5.6.1 Morphological analysis

On top of a lacquer-based laser-scribed 1-D grating ($P = 1000$ *nm*, $h = 150$ *nm*), 1 *μm* thick ZnO:Al was sputtered as a front contact. The surface morphology of the ZnO:Al layer, which resembled the underlying periodic texture, was additionally textured as indicated in previous section, thus obtaining another type of MST. In Fig. 5.15 three AFM pictures (left column) and the corresponding scan-line profiles taken in the horizontal direction (right column) are presented. The top row shows the surface morphology of the patterned lacquer, the middle row shows the surface morphology after ZnO:Al deposition and the bottom row presents the surface morphology after etching of the ZnO:Al layer. The scan area in this case was set to 20x20 *μm²* with lateral resolution 39 *nm*. Measured period and height of the grating were 1 *μm* and 150 *nm*, respectively. After ZnO:Al deposition the initial morphology was smoothened as ZnO:Al flattened the surface roughness. Finally, after the etching step,

typical holes and craters of the rough ZnO:Al were observed resulting in a higher value of σ_{RMS}.

$$\sigma_{RMS} = 55.6 \text{ nm}$$

$$\sigma_{RMS} = 34.9 \text{ nm}$$
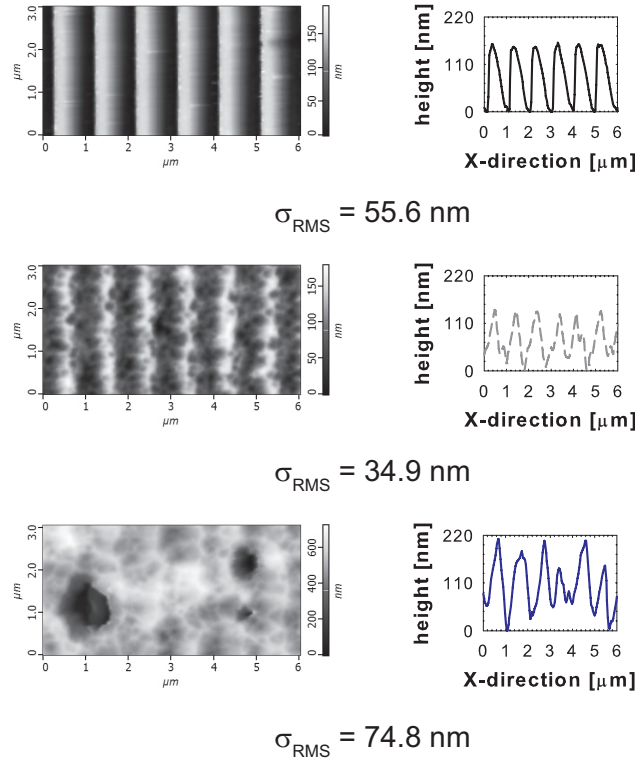

$$\sigma_{RMS} = 74.8 \text{ nm}$$

Figure 5.15: Surface morphology development (left column) and selected scan-line profiles (right column) for a MST based on 1-D gratings: from bare grating (P = 1 μm, h = 150 nm) (top row), though ZnO:Al coating (middle row), to final MST (bottom row).

In Fig. 5.16 σ_{RMS}^* spectra are presented for bare grating (patterned lacquer), wet-etched zinc-oxide (AZOR), and grating covered with ZnO:Al layer before etching and after etching. In the case of the bare grating specific, a discrete σ_{RMS}^* component is located at the fundamental spatial frequency 1 μm^{-1}, which corresponds to the grating period of 1 μm. At higher frequencies additional components are observed due to the not perfect sinusoidal shape of the periodic texture. In the AZOR spectrum, a strong peak located at low frequencies can be related to the deep holes created by the etching. The less deep crater-like features, having different lateral sizes, are spread over the rest of the frequency spectrum. By covering the grating with ZnO:Al the smoothening of the surface can be recognized. The main peak of the 1-D grating is still present and aligned with the one of the bare grating (i.e. preservation of the periodicity), although it is less intense. The high frequency components are also lowered because the steep walls of the gratings are now covered by ZnO:Al with small surface nano-structures. It can be observed in the σ_{RMS}^* distribution of the modulated texture that the additional etching does not affect the periodicity of the gratings, although

the intensity of the gratings main peak is further decreased. Moreover, the etching step resulted in the appearance of the low frequency components due to the holes in the surface and the high frequency components due to craters. Finally, due to the decrease of the ZnO:Al thickness in the acidic bath, the second peak of the grating spectrum was detected again.
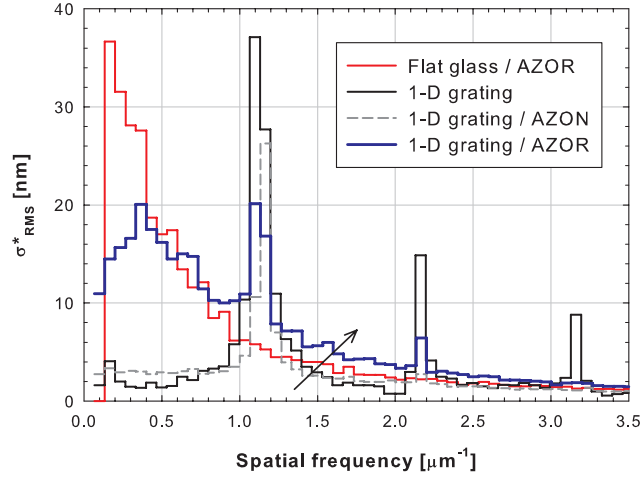

Figure 5.16: σ^*_{RMS} distributions for the textures constituting the MST on 1-D gratings.

5.6.2 Scattering properties

The AID_T and the haze in transmission (H_T) of the modulated surface texture on the 1-D grating are shown in Fig. 5.17 and Fig. 5.18, respectively. The initial periodic texture exhibits low scattering level, but characterized by diffraction modes (the first order is located around 40° at $\lambda = 633\ nm$), which are prevented to propagate for wavelengths larger than the period. Limited haze values are due to the low height of the grating as previously shown in Ch. 4. The patterned surface coated with the ZnO:Al film shows slightly worse behaviour than the bare surfaces because of the decreased height of the as-grown periodic texture, but still featuring the scattering mode around 40°. This is another proof of periodicity conservation after the coating. Finally, as for the modulated texture, the AID_T is greatly improved with the superposition of the broad angular scattering of small rough features. For wavelength larger than 640 nm, this results in haze values slightly higher than those of AZOR reference. On the other hand, for shorter wavelengths, AZOR exhibits higher haze due to better interaction between light and small random textures with respect to the periodic grating used in this experiment [157, 206].

5.6.3 Single junction solar cells

The substrates with and without modulated surface texture were applied in a-Si:H solar cells. The structure is as reported in Sec. 5.5.3. A summary of the initial external parameters of the best dots is reported in Table 5.2. The *EQE* of solar cells is shown in Fig. 5.19. Passing from flat glass / AZOR substrate to the MST, the V_{OC} remains almost unchanged, while a better
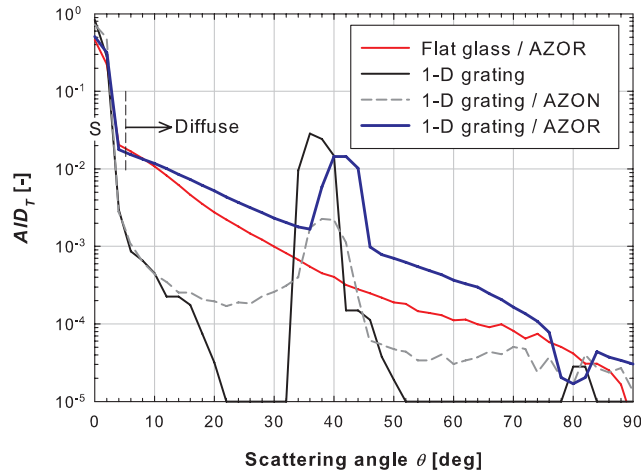
Figure 5.17: AID$_T$ of the substrates constituting the 1-D grating-based MST at λ = 633 nm. Letter S indicates the specular component or the 0th order for 1-D gratings.
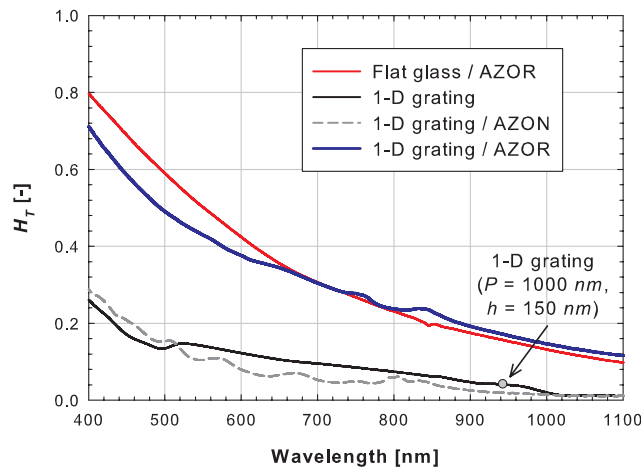

Figure 5.18: Haze parameter in transmission of the substrates based on 1-D gratings.

FF is noticeable for both 1-D grating-based substrates. This difference might be related to inter-batch opto-electrical performance variation of sputtered ZnO:Al. The slight gain in J_{SC} from the reference texture to MST can be analyzed with the *EQE*. For short wavelengths the spectral response of the solar cells based on the modulated textures is improved with respect to the solar cells deposited either on AZOR or on 1-D grating / AZON textures. This enhancement results partly from the AR effect given by the periodic background and partly from different TCO thickness before and after etching, due to not perfect etching uniformity in case of periodic substrate. For long wavelengths, the roughness of modulated texture, smaller than that of AZOR ($\sigma_{RMS-AZOR}$ = 87 *nm*), and the difference in thickness of ZnO:Al shift the interference fringes related to both scattering and AR effects.

Table 5.2: Initial external parameters of best measured cells on three TCO substrates. Values of current density are from EQE measurements.

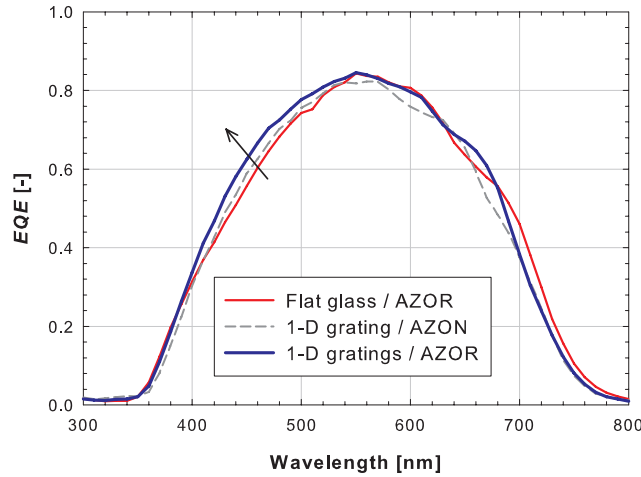| TCO substrate	V_{OC} [V]	J_{SC} [mA/cm^2]	FF	η [%]
Flat glass / AZOR (ref.)	0.878	14.18	0.670	8.34
1-D grating / AZON	0.876	13.78	0.709	8.56
1-D grating / AZOR	0.870	14.33	0.707	8.81

Figure 5.19: EQE of the three solar cells reported in Tab. 5.2.

5.7 MST on second type of etched glass

In order to control the etching of glass substrate and therefore fabricate a variety of modulated surface textures, an additional step in the etching procedure was introduced. Prior to the etching, on flat glass a conductive sacrificial layer was deposited, whose thickness allowed for tuning the resulting surface morphology. Thanks to such layer, five sets of etched glasses with increasing optical properties could be fabricated and a more systematic study on the surface modulation could be carried out.

5.7.1 Samples fabrication

Five sets of textured substrates were fabricated, each comprising three samples: (i) etched glass (EG), (ii) etched glass coated with non-treated ZnO:Al (EG / AZON), and (iii) etched glass coated with surface wet-etched ZnO:Al (EG / AZOR, MST). The etched glasses were prepared by depositing five increasing thicknesses of a conductive sacrificial layer on Corning Eagle XG$^\circledR$ glass sheets subsequently wet-etched in a mix of HF and H_2O_2, obtaining EG1 - EG5. The ZnO:Al layers were RF magnetron sputtered. AZON layers were as-deposited 1.2 *μm* thick; AZOR layers were initially 1.6 *μm* thick and then etched to 1.2 *μm* thick by the acidic bath in HCl. An AZOR layer was also fabricated on flat glass substrate as a reference. In Fig. 5.20 the explained flow-chart is reported.
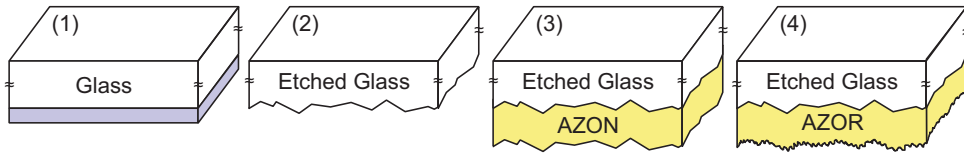
Figure 5.20: Schematic flow-chart for fabricating the second type of modulated surface textures: (1) sacrificial layer deposition, (2) etching in HF + H_2O_2, (3) TCO RF-magnetron sputtering, and (4) TCO wet-etching.

5.7.2   Morphological analysis

SEM images of the fabricated samples are presented in Fig. 5.21. The EG substrates show large microscopic carved features. AZON layers coat the EG background, smoothing the surface features, because of different ZnO:Al growth orientations at the glass ridges. Finally, AZOR layers with their typical small craters cover the big carved features of EG forming the MST. It is noticeable that the wet-etching of ZnO:Al affected the ridges differently than the rest of the morphology resulting in further horizontal widening of the craters. For each fabricated sample, AFM scans were performed in five different spots. In Fig. 5.22 the averaged L_C and σ_{RMS} with relative error bars are reported for all MST substrates. It was found that increasing the thickness of the sacrificial layer resulted in a strong roughening of the glass surface morphology in both horizontal and vertical directions. However, EG5-based MST demonstrated a decrease in statistical surface parameters. Similar trend was found also for the substrates EG and EG / AZON. The angle distribution of surface facets was evaluated with respect to the direction perpendicular to an ideal flat surface ($0°$), as explained earlier in Sec. 3.2.3. For this set of textured substrates, the average angle ranged from $13°$ to $17°$. Despite the increasing roughness of the glass surface with the increased thickness of the sacrificial layer, such small angle deviation indicates that the features become large and wider without changing shape. To demonstrate the surface modulation of the etched glass substrates, the spatial frequency surface representation of the EG1-based and EG4-based substrates is presented in Fig. 5.23 along with the reference flat glass / AZOR substrate. In the first case, the surface modulation is clearly the envelope between the background (EG1) and the reference AZOR. In the second case, the EG4 representation is always higher than the reference AZOR, nevertheless the MST representation is shifted up by the reference AZOR spectral components, thus demonstrating the surface modulation of the etched glass background.

5.7.3   Optical analysis

The total transmittance (T_T) and reflectance (R_T) of the EG substrates was compared with a flat glass. As presented in Fig. 5.24 the etched glass substrates have similar R_T and T_T as their flat counterpart and exhibit a slight anti-reflective effect in the visible range. The haze of transmitted light (H_T) was measured for both EG and MST substrates and compared to the reference flat glass / AZOR substrate (see Fig. 5.25). Even the least rough MST of the series (EG1 / AZOR) has H_T higher than the reference wet-etched ZnO:Al, taking advantage of the offset effect of its background (EG1). The same effect is also reported
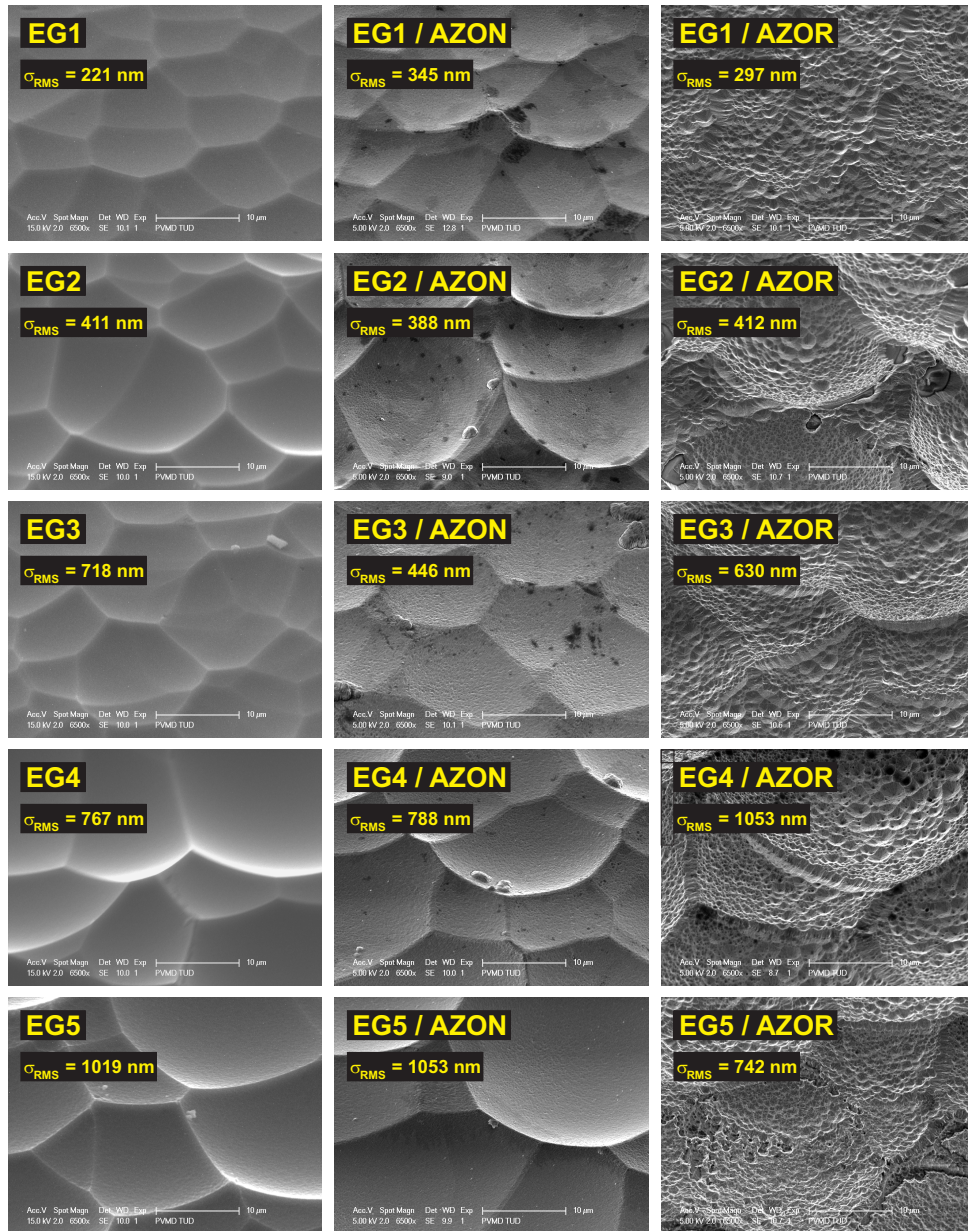
Figure 5.21: SEM images of EG1-5 (left column), EG1-5 / AZON (central column), and EG1-5/AZOR (right column). Surface features increase from top to bottom as the sacrificial layer thickness increases. Scale bars denote 10 μm.

for EG3-based substrates showing a stronger offset ($H_T >\sim 0.65$). In accordance with the statistical analysis, the EG4 / AZOR substrate presented the highest haze (average $H_T =$ 0.89), while the H_T of EG5 / AZOR decreased following the observed statistical trend.

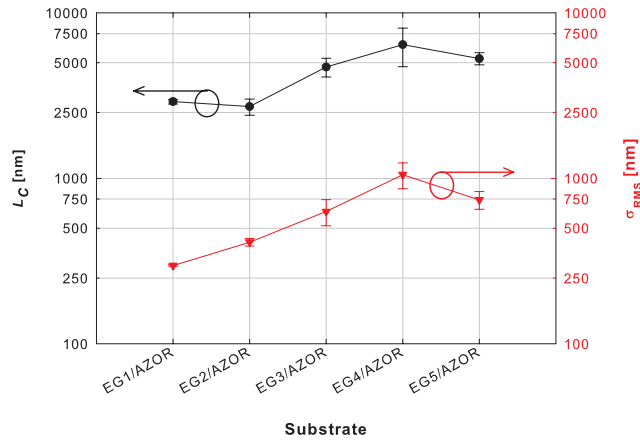*Figure 5.22: Correlation length L_C and surface roughness σ_{RMS} of the second type of MST substrates.*
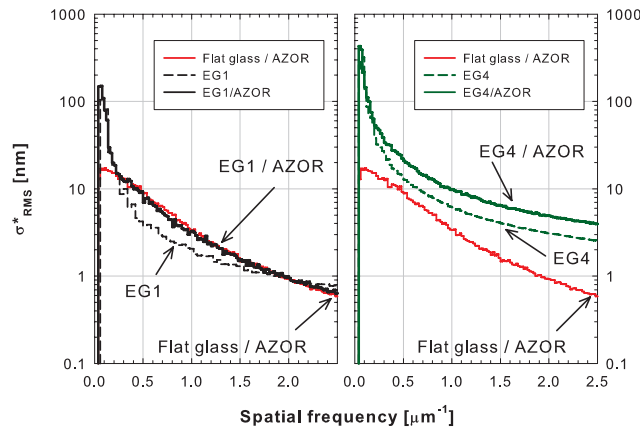

Figure 5.23: Spatial frequency surface representation of EG1-based and EG4-based substrates. All y-axes are in logarithmic scale.

In contrast to the reference textured TCO, the AID_T of the advanced textured substrate exhibited a very weak dependency on wavelengths. In Fig. 5.26 the measurements at 700 *nm* are reported. Increasing the roughness of the MST substrates resulted in a decreased specular component of transmitted light and broader AID_T than that of the reference TCO. For better understanding of the EG-based AID_T, two phenomenological interpretations are proposed: one related to the measured AID_T only, another connected to the nature of MST.

The AID_T of MST substrates can be regarded as the composition of an exponential decaying part for small scattering angles and a cosine (*Lambertian*) part for large scattering angles (mixed fitting):
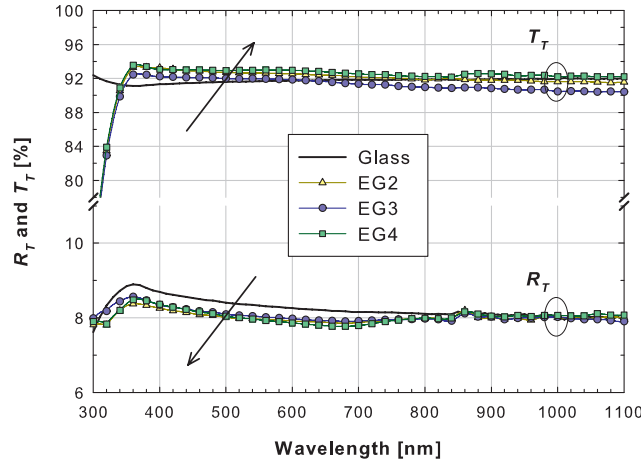
Figure 5.24: T_T and R_T of different etched glass carriers compared to flat glass substrate.
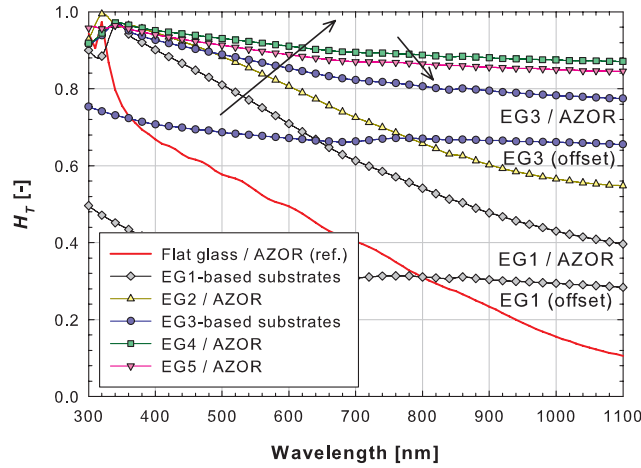
Figure 5.25: H_T of second type modulated surface textured substrates compared to reference textured TCO.

$$AID_T = \begin{cases} A \cdot e^{-B\theta}; \theta_{specular} < \theta < \theta_{exp} \\ A \cdot e^{-B\theta_{exp}} + C \cdot cos(\theta); \theta > \theta_{exp} \end{cases} \qquad (5.5)$$

where A, B, and C are angle-independent fitting parameters, $\theta_{specular}$ is the scattering angle at which the exponential decay starts, and θ_{exp} is the scattering angle at which the Lambertian component becomes dominant. These parameters are all determined from experimental results and vary for different MST substrates (see Tab. 5.3).

As an example, the mixed fitting of the AID_T in case of EG5 / AZOR substrate is reported in Fig. 5.27. Measuring the AID_T of the EG substrates, we found that such type

Figure 5.26: AID$_T$ of different MST compared to reference textured TCO. Dashed lines refer to the mixed fitting of EG5 / AZOR MST substrate (reported trends are for λ_{air} = 700 nm).

Table 5.3: Fitting parameters for second type MST.

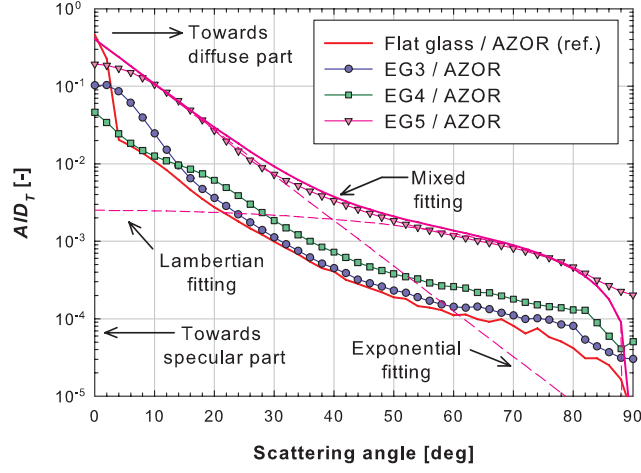| MST substrate	A	B	C	$\theta_{specular}$	θ_{exp}	f_{AID}
EG1 / AZOR	0.029	0.097	0.0003	12	46	1.25
EG2 / AZOR	0.036	0.092	0.0007	20	42	1
EG3 / AZOR	0.037	0.011	0.0004	20	38	1.25
EG4 / AZOR	0.047	0.1	0.00045	20	38	2
EG5 / AZOR	0.14	0.15	0.00055	10	30	7

of mixed fitting could be applied also to etched glass substrates. Indeed, the AID_T of the reference textured TCO simply followed an exponential decay with scattering angles. Combining the AID_T of EG and AZOR substrates, it was found that the AID_T of the MST can be also expressed as follows:

$$AID^*_{MST} = AID^*_{EG} + f_{AID} \cdot AID^*_{AZOR} \qquad (5.6)$$

where the asterisks refer to sine-weighted AID_T and f_{AID} is a fitting parameter depending on the different MST (see Tab. 5.3). Fig. 5.27 demonstrates how much the AID_T of EG5 / AZOR substrate benefits from the AID_T of its background (EG5) (offset effect) with respect to the reference textured TCO. A good agreement between the measured and fitted AID_T of the EG5 / AZOR substrate is also shown using Eq. 5.6.

5.7.4 Single junction solar cells

The second type MST were used as substrates in a-Si:H *pin* single junction solar cells. Their structure was the same as in Sec. 5.5.3 with TCO thickness as described in Sec. 5.7.1. Dealing with highly textured morphologies, the yield for each substrate was calculated con-
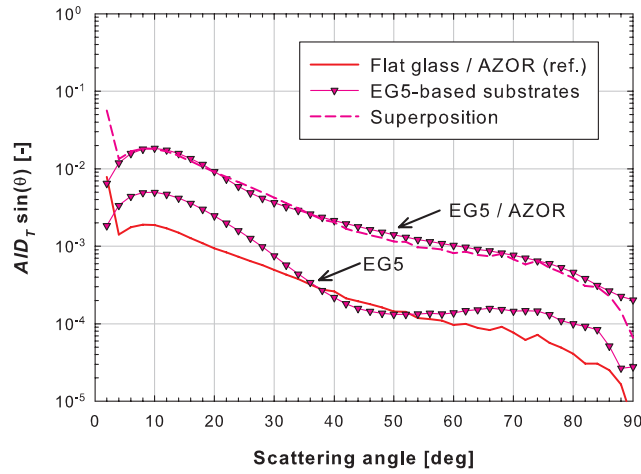
Figure 5.27: Sine-weighted AID$_T$ of reference textured TCO, and EG5-based substrates. The dashed curve represents the superposition of different scattering mechanisms according to Eq. 5.5.

sidering the number of cells with an efficiency higher than or equal to 90% of the best one (Y_{90}). The solar cells deposited on EG / AZON substrates less well than the reference flat glass / AZOR, because in this case the $p-i-n$ junction was locally flat. In Fig. 5.28 selected SEM images of a solar cell deposited on EG4 / AZON represent such situation. On the contrary, solar cells on MST substrate delivered performance in line with or better than the reference. In Fig. 5.29, top view of rear metallic contact and cross section of a solar cell deposited on EG4 / AZOR are shown, where the modulation of large background features with small features of etched TCO is clearly visible.
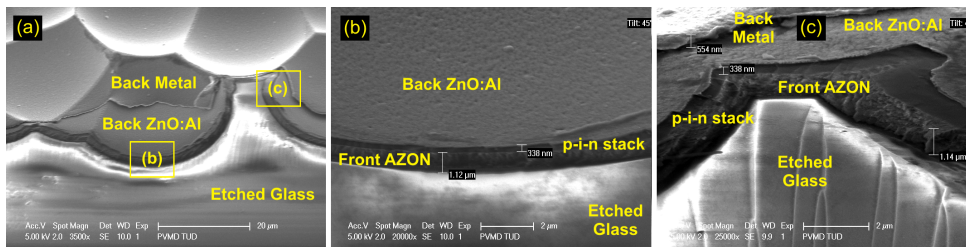
Figure 5.28: Cross-sectional SEM images of a solar cell on EG4 / AZON at different levels of zoom.

The overview of measured efficiencies is shown in Fig. 5.30 with the enhancement of short-circuit current density (ΔJ_{SC}) expressed in percentage and calculated with respect to the reference cell. The efficiency increase follows the roughening of surface morphology. Only the EG4-based substrates did not follow such trend because of too large roughness and/or problems during the deposition of the cells, as confirmed by low yield. It is evident from *EQE* measurements (e. g. EG1 / AZON curve in Fig. 5.31) that the solar cells on non-

(a)   (b)
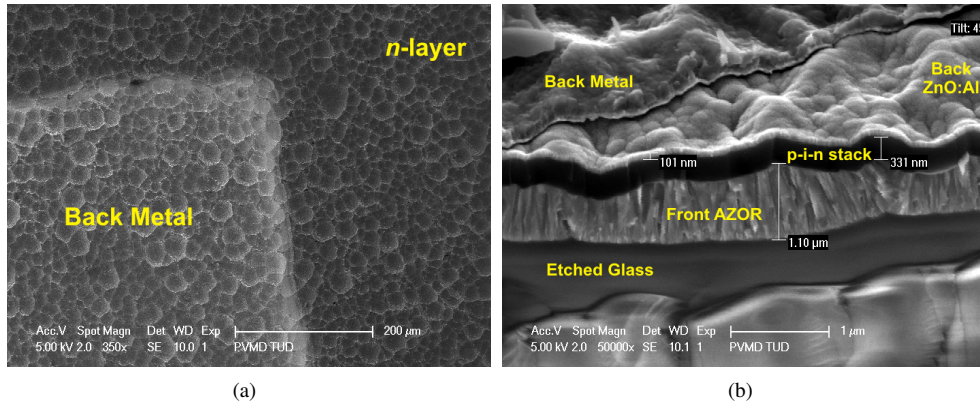
Figure 5.29: Top view of rear metallic contact and n-layer (a) and cross-sectional SEM image (b) of a single junction solar cell on EG4 / AZOR advanced substrate.

treated front ZnO:Al on etched glass behave like flat cells. The only gain of these solar cells with respect to the reference is observed in the range 400 *nm* 550 *nm* that confirms the AR effect. The solar cells deposited on EG / AZOR substrates demonstrated efficiencies equal to or higher than the reference with peak performance using EG5 / AZOR substrate. Such enhancement depends on the increased lateral and vertical features of the MST substrates resulting in the high HT and the broad AID_T as reported in previous section. Among the *EQEs* reported in Fig. 5.31, one can observe the performance of the cell on EG5 / AZOR presenting widened AR effect (up to 600 *nm*) and additional scattering, triggered by the superposition of large and small features. Initial external parameters of the best dots are reported in Tab. 5.4.

Figure 5.30: Initial efficiency of the solar cells deposited on advanced textured substrates. Numbers on bars are ΔJ_{SC} with respect to the reference, framed numbers are Y_{90} for each substrate.

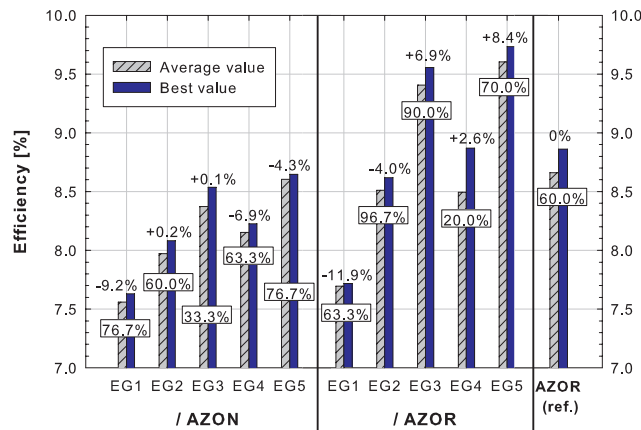*Table 5.4: Initial external parameters of best measured cells on three TCO substrates. Values of current density are from EQE measurements.*

TCO substrate	V_{OC} [V]	J_{SC} [mA/cm^2]	FF	η [%]
Flat glass / AZOR (ref.)	0.900	13.83	0.696	8.66
EG1 / AZON	0.891	12.55	0.683	7.63
EG2 / AZON	0.844	13.86	0.691	8.08
EG3 / AZON	0.898	13.85	0.686	8.53
EG4 / AZON	0.895	12.87	0.714	8.22
EG5 / AZON	0.897	13.27	0.729	8.65
EG1 / AZOR	0.895	12.18	0.708	7.72
EG2 / AZOR	0.896	13.27	0.725	8.62
EG3 / AZOR	0.902	14.78	0.717	9.56
EG4 / AZOR	0.892	14.19	0.701	8.87
EG5 / AZOR	0.901	14.99	0.721	9.74
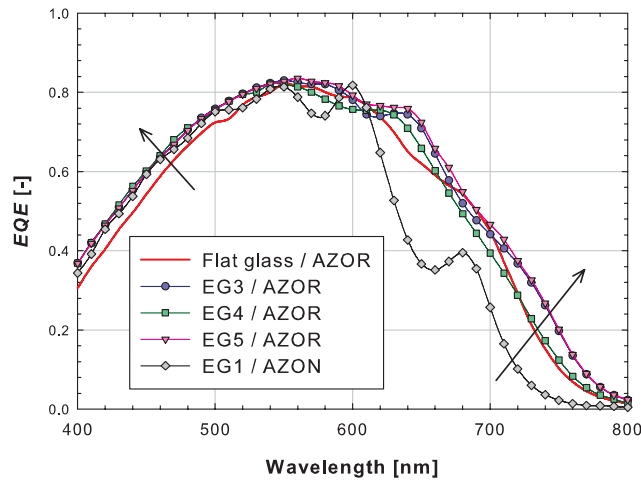
Figure 5.31: EQE of the best dots on advanced textured substrates compared to the reference substrate flat glass / AZOR.

5.7.5 Double junction solar cells

The best performing etched glass carrier (EG5) was chosen for application in tandem micromorph cell fabricated at IMT-PVLAB[5]. The substrate EG5 was coated with 1 *μm* thick ZnO:B (BZO) layer exhibiting σ_{RMS} = 49 *nm* and L_C = 120 *nm*. For reference purposes the same TCO layer and a thicker ZnO:B layer were also deposited on flat glass. The thickness of i-layers in micromorph cells were 250 *nm* and 1.1 *μm* for top a-Si:H and bottom nc-Si:H i-layers, respectively.

In Fig. 5.32 the cross-sectional SEM image of the tandem micromorph cell shows a modulated surface-textured substrate formed by the large features of etched glass with superposed small pyramids of the 1 μm thick BZO. In Fig. 5.33 the *EQE* of two tandem micromorph solar cells are reported: (i) reference micromorph cell on flat glass and ZnO:B and (ii) micromorph cell on the MST. From 350 *nm* until the onset of the bottom cell absorption, the top cells performed similarly since the small pyramidal texture of LP-CVD BZO efficiently suppresses reflection losses. After that threshold, a current redistribution is noticeable between top and bottom cells: the top cell exhibited $\Delta J_{PH-top} = -2.86\%$ with respect to its reference, while the bottom cell presented higher absorption than the reference bottom cell ($\Delta J_{PH-bottom} = +8.73\%$) all over the rest of measurement range. Considering the total photo-current density ($J_{PHtotal} = J_{PHtop} + J_{PH-bottom}$), which is not the real current flowing in the device but a measure to quantify the absorption in both top and bottom cells, the tandem micromorph on advanced texture delivered $\Delta J_{PH-total} = +2.24\%$. Such enhancement depends on the increased lateral and vertical features of the advanced substrate, which exhibits broadband high haze and broader angular intensity distribution recognizable in higher red-response.
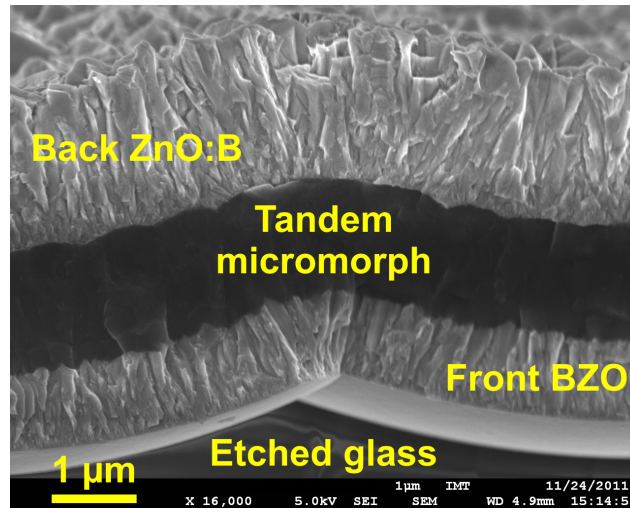
Figure 5.32: Cross-sectional SEM image of the tandem micromorph cell on EG5 / BZO MST.

The electrical performance of tandem micromorph cells reported in Tab. 5.5 was measured using a mask with 0.25 cm^2 area and adding the back reflector. The presence of two different BZO thicknesses as reference on flat glass was aimed to demonstrate the potential of MST exhibiting high current comparable with state-of-the-art thick BZO without deteriorating electrical performance. The V_{OC} of the cells with 1 μm thick BZO is almost identical. On the other hand, the FF is lower for the cell on MST, because of better matching between top and bottom cell currents, but still higher than the matched cell on thick BZO. In case of etched glass substrate the open-circuit voltage is higher than the cell on 2.5 μm thick BZO, due to the surface morphology more favorable for high quality nc-Si:H bottom cell.

Figure 5.33: EQE of tandem micromorph solar cells: reference flat glass / ZnO:B (dashed line) and advanced substrate etched glass / ZnO:B (solid line).

Table 5.5: Initial external parameters of the best tandem micromorph pin devices. Values of current density are from EQE measurements.

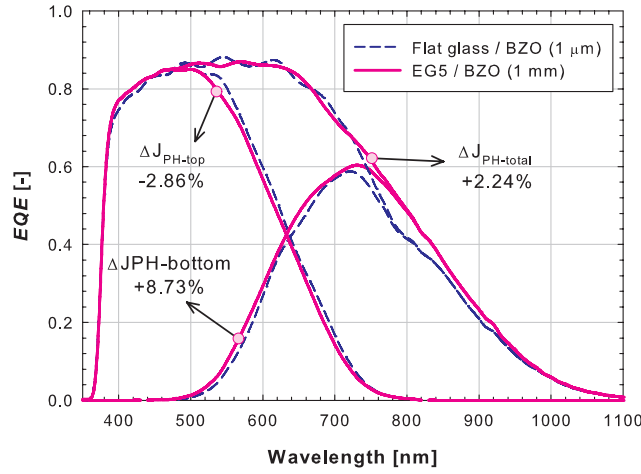| TCO substrate	V_{OC} [V]	J_{SC-top} [mA/cm^2]	$J_{SC-bottom}$ [mA/cm^2]	FF	η [%]
Flat glass / BZO (2.5 μm, ref.)	1.381	12.60	12.00	0.717	11.88
Flat glass / BZO (1 μm)	1.408	12.90	10.10	0.785	11.16
EG5 / BZO (1 μm)	1.403	12.50	11.00	0.754	11.64

5.8   Other ideas for modulated surface texturization

State-of-the-art optical performance in thin-film silicon solar cells results not only from optimized angle intensity distribution and haze but also from proper angle distribution of surface features facets. High haze values, originating from the (partial) suppression of specular component of transmitted or reflected light, may not lead to remarkable increase in i-layer(s) absorption if photons are not efficiently scattered into angles larger than the critical angle of the material. Thus, an efficiently textured surface morphology not only scatters light into angles away from the specular direction, but it is also characterized by features whose inclination helps coupling light in thin absorber layers.

Referring to the first and second type of etched glass-based MST, in Fig. 5.34 a selection of angle distributions describing features inclination (see Sec. 3.2.3) normalized with respect to the etched glass substrates is reported. The first type of etched glass has its mean slope $S_M = 3.3°$, which shifts to $3.9°$ when coated with AZOR film. Although resulting in higher scattering level with respect to the flat glass / AZOR reference, as shown in Sec. 5.6.1, the angle distribution of the first type MST should be further shifted towards larger values in order to achieve higher absorption, especially at long wavelengths [225]. In case of second type etched glass, considering for example EG5, the mean slope moves from

17.4° for the bare substrate to 15.1° for the MST EG5 / AZOR. This small backward shift could be put in relation with horizontal widening of the craters after etching ZnO:Al film as reported in Sec. 5.7.2 (see Fig. 5.21, right column). Such larger average angle with respect to the previous case constitutes a more favourable situation for efficient light scattering. In fact, considering the *EQE* of single junction solar cells related to these substrates, despite the device fabricated on first type etched glass (see Fig. 5.14 and Tab. 5.1) develops higher photo-current than the one on second type etched glass (see Tab. 5.4), the latter exhibits higher absorption for wavelengths larger than 700 *nm* (see Fig. 5.31).
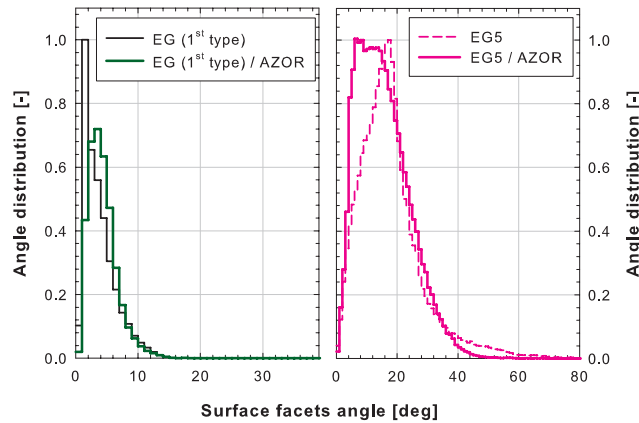

Figure 5.34: Angle distributions of selected first (left) and second (right) type etched glass-based MST. Angle bins are 1° wide.

For realizing larger angle distributions, three other advanced substrates suitable for modulated surface textures were developed: (i) third type etched glass, (ii) etched multi-crystalline silicon wafer (EW), and (iii) etched multi-crystalline silicon wafer coated with self-ordered aluminium dimples (EW / AD). The last two are opaque, thus not directly suitable for *pin* sequenced solar cells. However, with the concept of nano-moulding, such textures can be replicated with high fidelity on transparent photoresist / glass and thus made compatible with *pin* processes. It will be shown that substrates (i) and (iii) constitute per se MST, while substrate (ii) needs to be combined with another smaller texture to feature a MST. For application in solar cells all of them require anyway a coating of TCO (for *pin*) or Ag / TCO (for *nip*). Based on the procedure described in Sec. 3.2.3 for post-processing AFM digital data, the statistical analysis of such advanced substrates is reported in Tab. 5.6, while a comparison of the angle distributions is reported in Fig. 5.35. Next sections will deal with the three introduced substrates.

5.8.1 MST on third type etched glass

The third type of etched glass was achieved with a two-step process based on sacrificial layer approach. Tuning the thickness of sacrificial layers determined a MST already on glass substrate. After the first thick film of sacrificial layer (400 *nm*) and the subsequent etching forming the substrate EG5, another 320 *nm* thick film of the same material was deposited.

Table 5.6: Main statistical parameters of five advanced substrates for MST development.

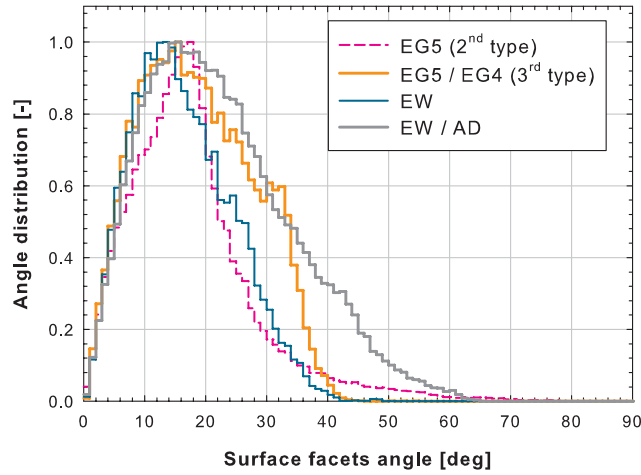| Statistical parameters	1st type EG	2nd type EG5	3rd type EG5 / EG4	EW	EW / AD
$P2P$ [μm]	1.69	5.52	3.24	5.25	2.56
σ_{RMS} [μm]	0.20	1.02	0.40	0.66	0.36
L_C [μm]	5.70	6.20	4.00	2.90	1.02
$Aspect_R$	0.04	0.16	0.10	0.23	0.35
S_M [deg]	3.33	17.41	18.23	15.85	21.97
$Area_R$ [%]	2.03	9.33	5.64	5.64	26.97
D_M [μm]	1.17	3.55	2.75	3.52	0.74

Figure 5.35: Angle distributions of the three advanced substrates for MST applications compared to the best second type etched glass (EG5, dashed line). Angle bins are 1° wide.

From the second etching step fractal morphology resulted with small carved features embedded on similar bigger ones (EG5 / EG4) (see Fig. 5.36). Thanks to such combination, the angle distribution broadened with respect to the distribution of EG5 substrate and the average angle reached 18.23° (see Fig. 5.35).

From optical point of view (see Fig. 5.37), the total transmittance of EG5 / EG4 was slightly higher than the substrate EG5. This effect can be related to the additional anti-reflection offered by smaller features embedded in the morphology. As for the haze in transmission, because of the smaller mean grain diameter (see Eq. 5.3) and the lower surface roughness (see Eq. 5.4) of the third type etched glass, the combination of supporting mechanism and exponential decay resulted to be lower than the case of second type etched glass.

Micromorph tandem solar cells were deposited at IMT-PVLAB also on this advanced MST. Cells were sized 1 cm^2 and measured with mask and back reflector. The i-layers of top and bottom cell were 250 nm and 2 μm thick, respectively. With respect to the previ-
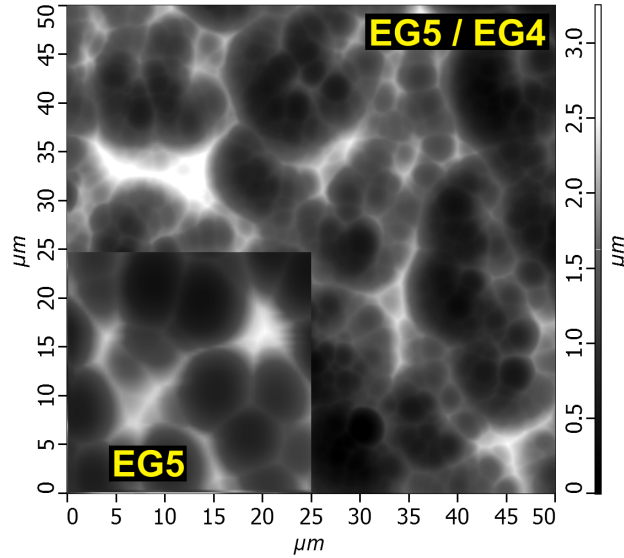
Figure 5.36: AFM scan of the third type etched glass (EG5 / EG4). Scan of EG5 substrate is superposed in bottom left corner for comparison purposes.
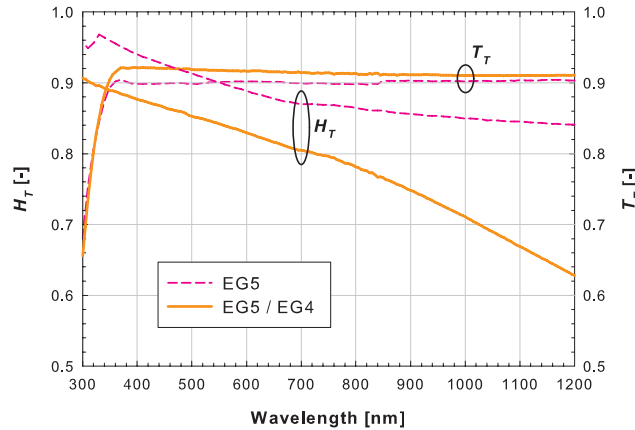
Figure 5.37: Haze in transmission and total transmittance of two etched glass types: EG5 (second type) and EG5 / EG4 (third type).

ous micromorph cells (see Sec. 5.7.5), the front TCO used here was a stack of In_2O_3:H (IOH, 140 *nm*) plus 1 *μm* non-intentionally doped ZnO (Z1). Adding the In_2O_3:H allowed to avoid doping the ZnO, thus reducing the parasitic absorption in the bottom cell. For comparison, also a flat glass substrate with the same TCO stack was processed. In Fig. 5.38 cross sectional SEM images of the micromorph tandem cells on second and third type etched glass-based MST are shown. Spectral response results were in line with the previous experiment (see Fig. 5.39). With respect to the flat substrate, the top cell on MST absorbed slightly less ($\Delta J_{PH-top} = -2.37\%$), while the bottom cell exhibited higher response

($\Delta J_{PH-bottom} = +3.81\%$, corresponding to 0.52 mA/cm^2). The micromorph solar cell on third type etched glass-based MST showed $\Delta J_{PH-total} = +1.07\%$, which is less pronounced than the previous case for thinner bottom cells.
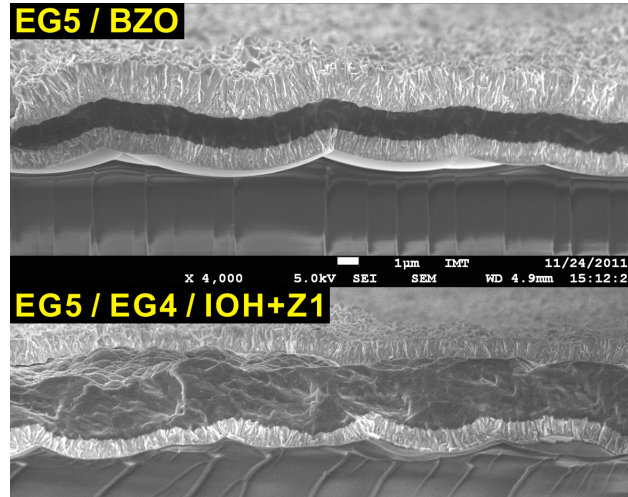
Figure 5.38: Cross-sectional SEM images comparing micromorph tandem cells on second (top) and third (bottom) type etched glass-based MST.
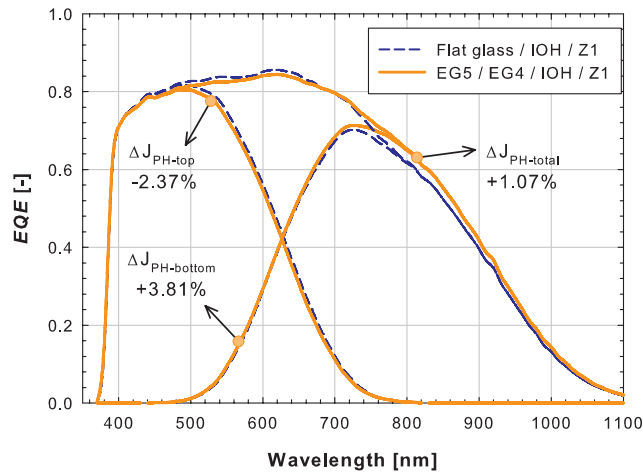
Figure 5.39: EQE of tandem micromorph solar cells on reference flat glass substrate (dashed line) and on third type etched glass-based substrate (solid line).

5.8.2 Etched wafer-based MST

Crystalline and multi-crystalline silicon used as absorber material in wafer-based solar cells is typically etched in order to minimize reflectance losses. Because of resulting morpholo-
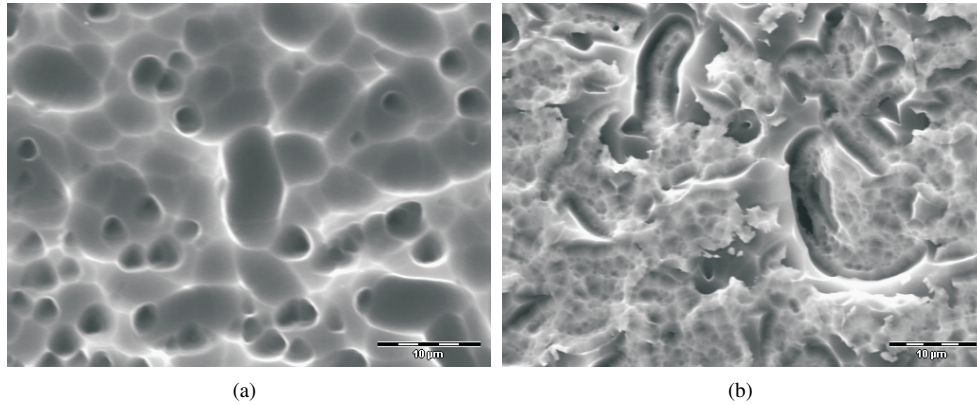
Figure 5.40: SEM top view of a wet-etched multi-crystalline silicon wafer (a) and of the MST obtained with AZOR film coating (b). Scale bar is 10 μm.

gies are characterized by large features, etched wafers (EW) could be used in thin-film silicon solar cell technology as supporting mechanism in MST development. Furthermore, the usage of silicon wafer in place of glass sheet allows the application of a wider amount of etching / patterning techniques borrowed from integrated circuits field.

Multi-crystalline silicon wafers were etched at Solland Solar Cells B.V. with an aqueous acidic solution (HNO_3:HF:H_2O). The result was a morphology characterized by large carved bean-like features and rounded deep holes, as shown in Fig. 5.40(a). The peak-to-peak height, the mean grain diameter, and the surface facets angle distribution of this morphology are comparable with those of the second type etched glass (see Tab. 5.6 and Fig. 5.35), with the average angle equal to $15.9°$. The deposition of AZOR film (1.2 *μm* thick after wet-etching, as mentioned in Sec. 5.7.1) led to the formation of a MST. In Fig. 5.40(b) such morphology is reported. Despite having controlled the thickness of ZnO:Al, over-etching around surface features ridges is evident. This suggests the need for ZnO:Al over-deposition to get complete coverage of the wafer and to keep on using the same etching time for the TCO film (i.e. similar crater-like features with respect to the MST on second type etched glass).

Another MST based on etched wafer was conceived by patterning the surface morphology of textured wafers with self-ordered aluminium dimples (EW / AD). A 2 *mum* thick aluminium film was deposited on etched wafer, anodized and etched in a two step process (see Tab. 5.7), which resulted in the inclusion of hexagonal latticed aluminium dimples (250 *nm* average diameter) in the big carved features of the etched wafer (see Fig. 5.41). Anodized aluminium oxide template with bigger pore diameter in the range between 500 *nm* and 900 *nm* would be actually the optimum for application in thin film solar cells [262]. In order to achieve such target, an optimization of the experimental set up is mandatory with higher stable power supply and a better cooling system. Anyway, the obtained angle distribution of surface facets is the broadest among the presented advanced substrates with an average angle ~$22°$. Furthermore, the aspect ratio is the highest and the surface morphology is warped enough to be almost 30% larger than the projected flat area.

Table 5.7: Aluminum dimples preparation in two-step anodization.

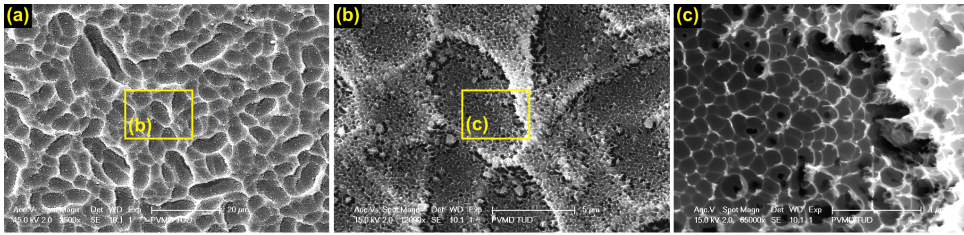|	1st step	2nd step
Anodization voltahe [V]	40	100
Anodization time [min]	10	10
Temperature [$^{\circ}C$]	20	5
Electrolyte	Oxalic acid	Phosphoric acid
Etchant	Phosphoric acid	Phosphoric acid
Etching time [min]	30	180

Figure 5.41: SEM top view of wet-etched multi-crystalline silicon wafer with superposed aluminium dimples (EW / AD); (a), (b), and (c) images denote three different levels of zoom with 20 μm, 5 μm, and 1 μm scale bar, respectively.

Both discussed morphologies (EW / AZOR and EW / AD) would be suitable for *nip* applications after being coated with an appropriate Ag / TCO back electrode and reflector, or for *pin* applications after being replicated onto glassy transparent substrate and coated with a thin and less absorptive film of TCO (e.g. IOH). Particularly, with its high statistical parameters, EW / AD MST constitutes a very interesting morphology for thin-film silicon solar cells applications.

5.9 Discussion and conclusions

The concept of modulated surface texture was achieved by combining either large random surface textures (1st type etched glass) or 1-D periodic grating with additional finer random surface features (etched ZnO:Al). The morphological analysis demonstrated the development of the modulated textures. In particular, the spatial frequency surface representation of the final surface and of the constituting elements was used to take both lateral and vertical features into account when investigating the surface roughness-scattering relation. The optical analysis revealed enhanced light scattering for MST with respect to the starting textures. Such behaviour could be modelled by superposing independent scattering mechanisms active for different feature sizes. Solar cells deposited on modulated surface-textured exhibited higher *EQE* with respect to conventionally textured cells due to improved anti-reflective and scattering properties.

After the proof of concept, a second type of etched glass was developed by using a sacrificial layer removal approach for etching glass sheets. AFM analysis demonstrated the controlled manipulation of the etched glass and the modulated surface texturing. The deve-

loped MST showed broad AID_T and very high H_T due to strong and controllable supporting mechanism of the background texture of the etched glass. An AR effect was observed for the etched glass substrates. Such substrates were tested in single and double junction solar cells. Etched glass substrates coated with AZON films did not result in efficient solar cell devices since the a-Si:H $p - i - n$ junctions were found to be locally flat on a micro-scale. The best performance was found on a-Si:H single junction devices deposited on EG5 / AZOR substrate. Also solar cells on the EG3 / AZOR substrate performed well with a very high Y_{90}. On the EG5 substrate thin tandem micromorph cells in combination with BZO were fabricated at IMT-PVLAB, Neuchâtel (Switzerland). In spite of a slight performance decrease of the top cell with respect to the flat glass reference coated with 2.5 μm thick BZO, the bottom cell showed a broadband increase in the (red) spectral response, underlining the potential of the modulated surface textures for thin-film silicon solar cells applications. In addition, high V_{OC} and FF were preserved.

Together with broad angular intensity distribution and haze values, large angle distribution of surface facets was recognized to have an important role for enhancing the optical performance of thin-film solar cells. For this reason, three additional advanced substrates were developed to feature large angle distribution of surface facets. Third type etched glass and etched multi-crystalline silicon wafers modulated with AZOR film or self-ordered aluminium dimples were developed. The first micromorph tandem cell on a three-level MST (third type etched glass substrate coated with a combination of IOH and ZnO), also fabricated IMT-PVLAB, showed interesting potential for bottom cell current enhancement, although further tuning of bottom cell thickness is necessary to meet proper current matching constituting sub-cells.

In conclusion, advanced modulated surface-textured TCO substrates, lately also called multi-scale substrates, have found prominent application in industrial R&D products [50] and lab-scale record tandem micromorph cells [263]. Further developments should head towards both *nip* and *pin* technologies. The application MST concept in multi-junction *nip* cells can lead to the fabrication of thinner devices thanks to enhanced light scattering at long wavelengths. The replication of a MST on flat glass coated with low absorption front TCO in multi-junction *pin* cells can be a supplementary strategy with respect to the so-called multi-scale TCO.

Chapter 6

Distributed Bragg reflectors as dielectric mirrors

Distributed Bragg reflectors formed by pairs of dielectric materials will be investigated in this chapter. Motivation for their usage in single and multi-junction thin-film silicon solar cells will be given. Following the theory of DBR, optical properties and design rules for *wavelength-selective* high reflectance will be presented. Fabricated DBR at low temperature will be studied with respect to polarized light, embedding materials and substrates. Finally the application in single junction solar cells in both *pin* and *nip* configuration will be presented.

6.1 Introduction

The rear side of thin-film silicon solar cells accomplishes two tasks: (i) ensuring the extraction of electrons to the external circuit and (ii) providing the absorber layer with efficient back reflectance. Because of the typical front side texturization for light scattering, reflection at the textured back contact is a critical issue. In fact, conventional metal reflectors (Ag, Al), even coated with back TCO, suffer from undesired plasmon absorption, limiting the long wavelength response of the solar cell [128, 222]. Optically speaking, an ideal back reflector should assure high reflectance (R close to unity) in a wide wavelength range and broad angular domain. A practical example fitting such requirements is the stack formed by back TCO and white paint currently used in state-of-the-art double junction solar cells [50, 129, 130]. In this case, like in any other application of dielectric back reflector, thickness and opto-electrical behaviour of the back TCO play a crucial role since it replaces the metal contact (see Sec. 6.5).

Also, the intermediate reflector in multi junction applications is an important part of the cell. While it electrically connects the sub-cells in series, it allows the passage of long wavelength photons to the bottom cell while enhancing the absorption in top sub-cell(s) by offering higher reflectance at short wavelengths. Thus the high reflectance requirement for such reflector is more stringent from wavelength range point of view. Furthermore the optical loss related to the intermediate reflector should be negligible or at least minimized

in order to take full advantage of incident light spectral filtering.

Recently, novel structures for wavelength-selective manipulation of the reflectance (R) and transmittance (T) at particular interface inside a solar cell have been investigated. They are formed by two materials characterized by a refractive index mismatch and arranged in a certain spatial periodicity. 1-D multi-layered structures in the role of a distributed Bragg reflector (DBR) [264–266], or 2-D and 3-D Photonic Crystals (PC) [267] feature a photonic band gap (*PBG*), which prevents photons having energy in the gap to go through, thus implying the high reflectance. If the *PBG* is conserved for different polarizations and different angles of incidence, the structure is said omni-directional. Although some authors define DBRs as 1-D PCs because of their 1-D structure and photonic band gap, in this chapter the classical nomenclature (DBR) will be used [268].

DBR, 2-D and 3-D PC can be used as wavelength-selective optical filters in various parts of the solar cell, affecting reflectance of transmittance. Provided the choice of materials not absorbing in the wavelength range of interest, the design wavelength depends on the application (intermediate layer or back reflector for single or multi-junction cells). For example, a DBR formed by pairs of SiO_2/Ta_2O_5 and used as anti-reflective coating on glass substrate provides spectral and directional selective R and T [269]. As intermediate reflector in multi junction silicon solar cells, n-type a-Si:H / ZnO:Al DBR or inverted opal ZnO 3-D PC have been introduced, showing enhanced absorption in the top cell [99, 100, 102]. Finally, DBR, 2-D and 3-D PC have been also applied at the rear side of amorphous and crystalline silicon solar cells. Chirped porous silicon reflectors [133], a-Si:H / a-SiN$_x$:H DBR [270], and combinations of DBR with 2-D periodic gratings [131, 271, 272] are noteworthy examples of dielectric back reflectors used in c-Si solar cells. So-called modulated DBR for a wider wavelength range of high reflectance [273], or the Flattened Light-Scattering Substrate (FLiSS) [134], which offers improved long wavelength diffused reflectance and flat surface for favourable growth of high quality nc-Si:H (see Ch. 7), have been proposed for thin-film silicon solar cells technology.

This chapter is focused on the DBR for application as dielectric back reflector in thin-film silicon solar cells. DBR with the desired wavelength-selective behaviour were studied and designed by optical simulators. Specifically, the ASA program was used to tune the thickness of layers, the number of alternating pairs, and the combination of refractive indexes [200], whereas the HFSS software was deployed for investigating the optical response for different angles of incidence and polarizations. Different DBR based on alternating layers of a-Si:H and a-SiN$_x$:H were fabricated, optically tested, and finally applied at the rear side of *pin* and *nip* single junction solar cells.

6.2 Validation of the simulators

To describe in detail the properties of DBRs and the design rules useful for their fabrication, computer programs like ASA and HFSS were used to simulate a number of DBRs involving several different pairs of materials. It is clear that assessing the validity of the used optical simulators was of primary importance. The validation consisted in matching with simulations the reflectance of a real DBR on glass measured at perpendicular incidence in two configurations: (i) air / DBR / glass and (ii) air / glass / DBR.

The DBR fabricated for validation purposes was formed by four pairs of a-Si:H / a-
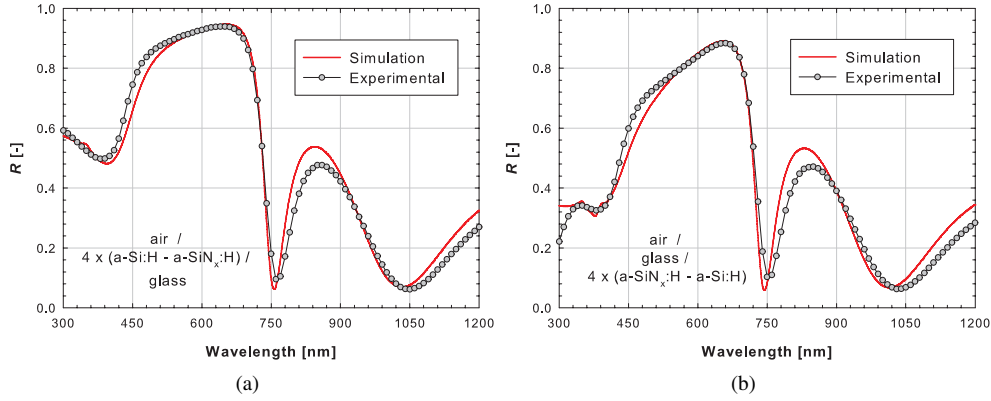
Figure 6.1: Measured (grey circles) and simulated reflectance (solid red lines) of (a) air /
DBR / glass and (b) air / glass / DBR optical systems. Simulated curves in the
two plots are representative of both ASA and HFSS outputs. Note the deposition
sequence of single layers forming the DBR.

SiN$_x$:H deposited on glass and designed to deliver high reflectance around 600 *nm* (see
Sec. 6.3.1). Such DBR was then modelled in both optical simulators. Specifically, layers
thickness was determined from deposition rate, real optical constants for both materials
were used, and both measurement configurations were considered. As for the thick glass
substrate, it was modelled as an incoherent layer in ASA, whereas it was simulated as a 200
nm thick layer in HFSS. In a processing stage subsequent HFSS simulation, the reflectance
at air / thick glass interface was properly taken into account by using an approach based on
Fresnel coefficients.

In Fig. 6.1(a) and (b) validation results are reported. In both cases, the outcome of
the simulators is exactly the same (red curve in both plots), that is the reflectance curves
cannot be distinguished as long as the same wavelength step is chosen in both simulators.
When comparing the simulated reflectance spectra with the measured ones a nearly perfect
matching is achieved. As it will be shown in the next section, in order to achieve higher
reflectance strong refractive index contrast is necessary not only between the constituting
materials of the DBR but also between the incident medium and the first layer of the DBR.
This explains why for the same fabricated / simulated DBR the reflectance is higher when
a-Si:H is the placed as first layer in front of light in air environment (see Fig. 6.1(a)). The
presented results validate the use of ASA and HFSS for describing, studying, and designing
dielectric DBRs.

6.3 Properties of DBR and design rules

The DBR is a 1-D multilayer structure in which two layers with different optical properties
(refractive indexes) are periodically alternated with period $P = d_L + d_H$, where d_L and d_H
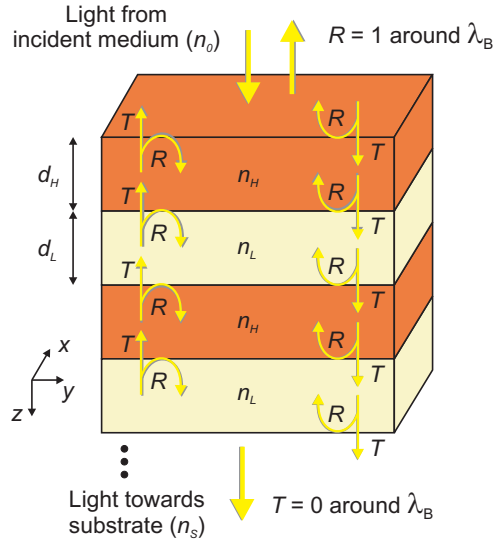are the thicknesses of low and high refractive indexes media, respectively (see Fig. 6.2).

Figure 6.2: Sketch of the DBR. Light from incident medium undergoes constructive and destructive interferences resulting in suppressed T around λ_B.

When light propagates through the DBR, constructive and destructive interferences arise. Looking at Fig. 6.3, where the measured reflectance of six pairs a-Si:H / a-SiN$_x$:H DBR on glass is shown, high reflectance can be achieved for a wide range of wavelengths around the so-called Bragg wavelength (λ_B). Such range is the aforementioned *PBG* ($\Delta\lambda = \lambda_R - \lambda_L$, see sec. refphotonicbg), in which the transmittance is almost completely suppressed.

Analyzing the properties of DBRs, a set of empirical rules can be suggested for designing efficient dielectric DBR for application in thin-film silicon solar cells. In the following text, two adjectives - realistic or synthetic define the constituting materials of a DBR. The first indicates the wavelength dependency of the complex refractive indexes, the second refers to lossless complex refractive indexes ($k = 0 \,\forall\lambda$).

6.3.1   Bragg wavelength and maximal reflectance

If the thickness of constituting layers of a DBR respects the $\lambda/4$ rule (see Sec. 2.3.2), reflected waves from each layer are all exactly in phase at the mid gap wavelength $\lambda = \lambda_B$ [266]. Therefore, the Bragg wavelength can be calculated as follows:

$$\lambda_B = 4d_L n_L(\lambda_B) = 4d_H n_H(\lambda_B) \tag{6.1}$$

where n_H and n_L are the high/low refractive indexes of the alternating layers, respectively, evaluated at λ_B. Design rule descending from Eq. 6.1 is that *the choice of Bragg wavelength for a certain application depends only on the used materials.* Thicknesses d_L and d_H are thus *derived per application.*

From the calculation of reflection coefficient of a multi-layer structure [274], the maximal reflectance achievable by a DBR at Bragg wavelength $R(\lambda_B)$ can be expressed as:
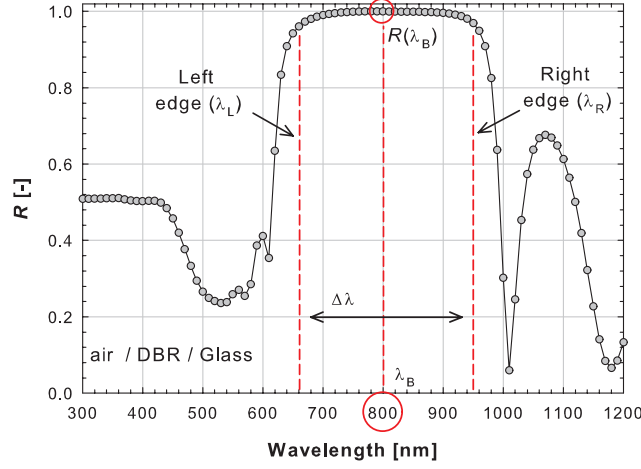
Figure 6.3: Measured reflectance of a 6 pairs a-Si:H / a-SiN$_x$:H DBR; optical system is air / DBR / glass. The region of high reflectance is indicated with $\Delta\lambda$.

$$R(\lambda_B) = \left(\frac{n_0 n_L^{2M} - n_S n_H^{2M}}{n_0 n_L^{2M} + n_S n_H^{2M}} \right)^2 \tag{6.2}$$

where n_0 and n_s are the refractive indexes of the incident medium and of the substrate, respectively (see Fig. 6.2), M is the number of stacked pairs and the dependency on λ_B of all the refractive indexes is omitted for brevity. For $M = 0$, the difference in refractive index between the incident medium and the substrate ($\Delta_{0S} = n_0 - n_S$) evidences the reflectance at their interface, since no DBR is present. Such reflectance is more pronounced for higher Δ_{0S} and constitutes an offset value for the reflectance offered by inserting the DBR in the optical system (n_0 / DBR / n_S). On the other hand, for $M \neq 0$, also the difference in refractive index between the materials constituting the dielectric mirror ($\Delta_{HL} = n_H - n_L$) becomes important. The higher is Δ_{HL}, the smaller is the number of pairs needed to get the maximal reflectance, $R(\lambda_B) = 1$. Both cases are recognizable in Fig. 6.4 where the reflectance at Bragg wavelength is plotted as function of number of pairs for air/air and air/a-Si:H embedding media and for different index mismatches. In this case the wavelength dependency of n_0, n_S, n_L and n_H is simply not taken into account to focus only on parameters M, Δ_{0S}, and Δ_{HL}. Design rule descending from Eq. 6.2 is that *for an efficient (high R) and easy to fabricate (M small) DBR, Δ_{0S} and Δ_{HL} should be large around λ_B.*

Fig. 6.5 shows simulated reflectance spectra of a realistic a-Si:H / a-SiN$_x$:H DBR embedded in air / a-Si:H, designed at $\lambda_B = 800$ *nm* and for different number of pairs M. Even though the wavelength dependency of n_L and n_H is now taken into account, the highest reflectance increases with M as predicted by Eq. 6.2. In fact, if the DBR is designed for a wavelength region where absorption in constituting materials is negligible or absent the highest reflectance coincides with the result of Eq. 6.2. In case such hypothesis does not hold, a relevant difference arises between measured or simulated highest reflectance and the value calculated from Eq. 6.2. For example, in Fig. 6.6 simulated reflectance spectra of a DBR made up of six pairs of *realistic* In$_2$O$_3$:Sn / a-Si:H is reported for three Bragg
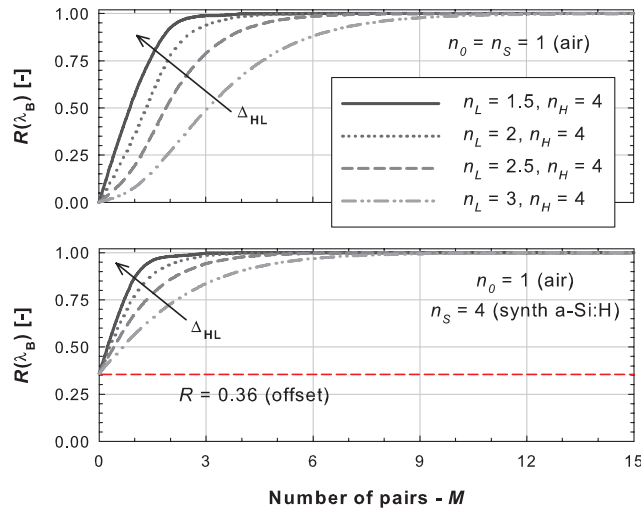
Figure 6.4: *Reflectance at* λ_B *as function of DBR pairs for air/air (top panel) and air/synthetic a-Si:H em-bedding media and for different index mismatches (bottom panel).*
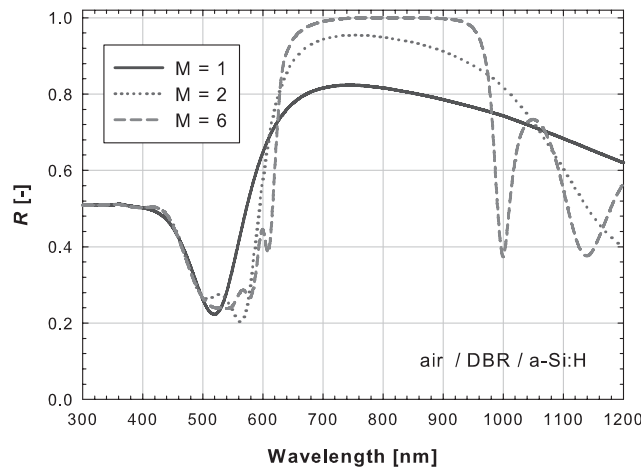
Figure 6.5: *Simulated reflectance of* realistic *a-Si:H / a-SiN$_x$:H DBR for different number of pairs M; optical system is air / DBR / a-Si:H.*

wavelength designs (600, 700, and 800 *nm*). Despite the occurrence of a region of high reflectance for all three designs, the deviation from theoretical maximal reflectance for λB is noticeable, because one or both materials significantly absorb around the design wavelengths.

Depending on deposition uniformity of the equipment used to fabricate the DBR, a deviation in layers thickness could be introduced and performance of the DBR decreased. This effect can be studied by simulating a DBR and a set of its clones with thicknesses

Figure 6.6: Simulated reflectance of six pairs of realistic In$_2$O$_3$:Sn / a-Si:H DBR designed *at 600, 700, and 800 nm; optical system is air / DBR / glass. Grey dots indicate theoretical reflectance at given* λ_B.

randomly deviating from designed values. In Fig. 6.7 the simulated optical response of previous DBR (six pairs of *realistic* In$_2$O$_3$:Sn / a-Si:H) designed at 800 *nm* is compared with the averaged reflectance of ten similar DBRs with layers thickness varie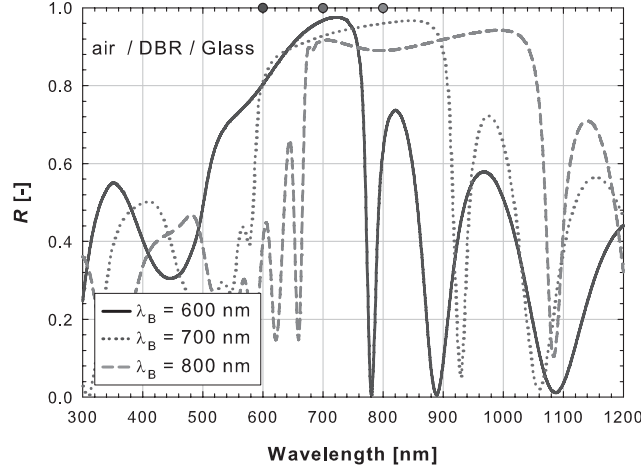d according normal distribution within ±5% of the original thickness. The random deviation has more impact on the wavelengths outside the band edges, while it has no significant influence on the region of high reflectance. A DBR design can be considered rugged within state-of-the-art industrial uniformity after passing this kind of test.

   Another important aspect is the angle of incidence θ_0 of light at the interface n_0 / DBR. The issue is hidden in Eq. 6.2, arranged for the typical case of perpendicular incidence of light (propagation vector k of the E-M field parallel to the normal of DBR surface, $\mathbf{k} = \mathbf{k_z} \Rightarrow |\mathbf{k}| = k_z$). Actually, in a more general treatment using propagation matrices formalism [275], the DBR structure is seen as a sequence of multiple dielectric slabs whose reflection coefficient can be carried out from generalized Fresnel equations. The *effective* refractive index ($\bar{n}$) for the i$_{th}$ layer inside the DBR is defined as:

$$\bar{n} = \begin{cases} n_i \cdot cos(\theta_i); \text{S} - \text{polarization} \\ \\ \frac{n_i}{cos(\theta_i)}; \text{P} - \text{polarization} \end{cases} \tag{6.3}$$

where n_i is the refractive index and θ_i is the propagation angle of light inside the ith layer. Angles of propagation inside each layer of the DBR with high or low refractive index can be computed from Snell law [276]:

$$n_0 sin(\theta_0) = n_L sin(\theta_L) = n_H sin(\theta_H). \tag{6.4}$$

Substituting in Eq. 6.2 the refractive indexes with their effective counterparts, evaluated at λ_B, allows calculating $R(\lambda_B)$ for angles of incidence different than 0° and for different
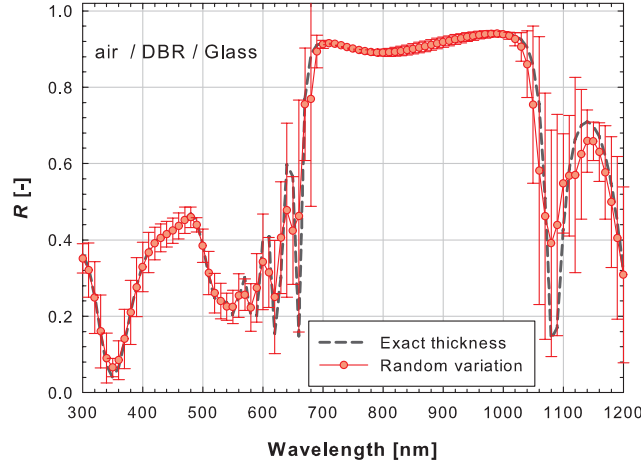
Figure 6.7: Simulated reflectance of six pairs of realistic In$_2$O$_3$:Sn / a-Si:H DBR designed at 800 nm with exact thicknesses (dashed line) and averaged curve from ten reflectance spectra (red line and error bars) given by random variation of layers thickness in the DBR.

polarizations.

6.3.2 Photonic band gap, dispersion relation and field penetration

The *PBG* of a DBR, that is the wavelength range of high reflectance $\Delta\lambda$, is given by the difference between the right and left wavelengths (λ_R and λ_L, respectively) enclosing the gap, also known as band edges [277]:

$$\begin{cases} \lambda_L = \frac{\pi(d_L n_L + d_H n_H)}{cos^{-1}(-\rho)} \\[2ex] \lambda_R = \frac{\pi(d_L n_L + d_H n_H)}{cos^{-1}(\rho)} \end{cases} \tag{6.5}$$

where ρ is the reflection coefficient at the interface between high and low refractive index media. Such coefficient can be written for S- or P-polarization in a compact form using the *effective* refractive indexes:

$$\rho_{(\cdot)} = \frac{\bar{n}_H - \bar{n}_L}{\bar{n}_H + \bar{n}_L} \tag{6.6}$$

with $(\cdot)$ indicating S- or P-polarization. The *PBG* can be therefore expressed as follows:

$$\Delta\lambda = \lambda_R - \lambda_T = \frac{4}{\pi}\lambda_B sin^{-1}\left[\rho_{(\cdot)}\right]. \tag{6.7}$$

In Fig. 6.8 the *PBG* calculated for perpendicular incidence is plotted against the Bragg wavelength and for different pairs of refractive index. Design rule descending from Eq. 6.7 is that *to obtain a DBR with large PBG, it is necessary not only to set λ_B at long wavelengths, but also to choose the pair of materials to deploy such that Δ_{HL} is large around λ_B.* In

addition, for *realistic* materials, the imaginary part of the complex refractive indexes should not be too high at least in the wavelength range of interest to avoid deviations from Eq. 6.2 and Eq. 6.7.
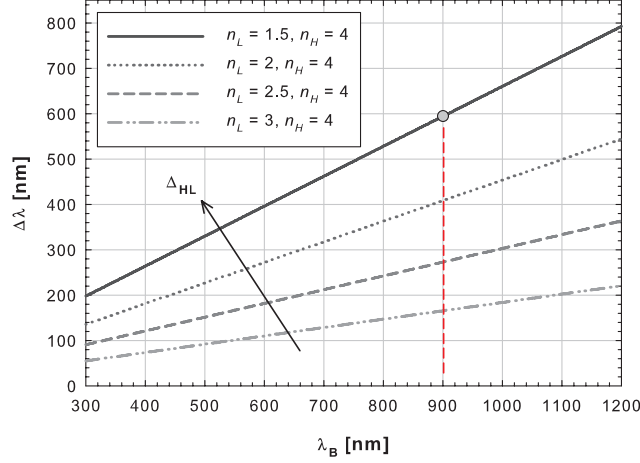

Figure 6.8: PBG as function of λ_B for different Δ_{HL} values. The grey spot indicates the PBG amplitude for a DBR with $n_L = 1.5$ and $n_H = 4$ designed at $\lambda_B = 900$ nm (see Fig. 6.9.

Combining Maxwell equations with Bloch theorem for 1-D periodic structure, the dispersion relation of an ideal DBR formed by infinite number of pairs along the axis of the multilayer (*z*-direction) and for perpendicular incidence can be expressed as follows [278]:

$$cos(k_z P) = cos(k_z P)cos(k_H d_H) - \frac{1}{2}\left(\frac{n_L}{n_H} + \frac{n_H}{n_L}\right)sin(k_L d_L)sin(k_H d_H) \qquad (6.8)$$

where k_z is the amplitude of Bloch vector along *z*-direction, $k_{L(H)} = n_{L(H)} \cdot \omega/c$ is the wave vector in low (high) refractive index layer and $\omega = 2\pi c/\lambda$ is the angular frequency.

Let an ideal DBR formed by infinite pairs of a-SiO$_x$:H / a-Si:H, designed at $\lambda_B = 900$ *nm* and characterized by wavelength independent refractive indexes $n_L = 1.5$ and $n_H = 4$. In Fig. 6.9, the photonic band dispersion relation of such ideal DBR (left panel) is related to the simulated reflectance of the same ideal DBR but truncated at $M = 5$ (right panel). The dispersion relation is plotted for normalized Bloch vector ($k_z P/2\pi$), such that parts of the curve with abscissa $k_z P/2\pi < 0$ or $k_z P/2\pi > 0.5$ folds back, basically populating the first Brillouin zone of the DBR. In this frame, the photonic band gap defines (i) region of high reflectance and (ii) folding region of the dispersion relation. On the other hand, a so-called *pseudo photonic band gap* individuates only a folding point of the dispersion relation. In the reported example, two photonic band gaps and one pseudo photonic band gap can be recognized: the fundamental gap located around the Bragg wavelength (E_B 1.38 *eV*), the second one (E_{2B}) situated at energies higher than 4.13 *eV*, and the pseudo photonic band gap situated around 2.75 *eV*.

The fundamental photonic band gap ($\Delta\lambda$)of the designed DBR divides the photonic states in the dielectric structure (dielectric band) from the photonic states extended in the
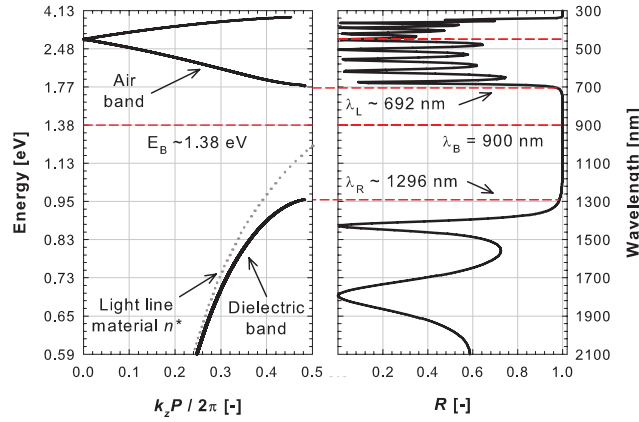
Figure 6.9: Photonic band dispersion (left) and simulated reflectance (right) of a-SiO$_x$:H / a-Si:H DBR designed at λ_B = 900 nm. Grey dotted curve in the left panel is the light line of material n*.

incident medium (air band). For low energies, the dielectric band is approximated by the light line of a synthetic material, whose refractive index n^* is the weighted average of the indexes n_L and n_H with respect to the considered thicknesses:

$$n^* = \frac{d_L n_L + d_H n_H}{d_L + d_H}.\qquad(6.9)$$

This is because the E-M field at long wavelengths is not able to resolve anymore the passage from one material to the other, thus it sees the periodicity of refractive indexes inside the mirror as an effective medium [266]. In the right panel of Fig. 6.9, the reflectance spectrum is plotted with a perfect correspondence of the *PBG* with the region of the reflectance. Note that the bandwidth $\Delta\lambda$ represents the asymptotic width of the reflecting band for M approaching infinity. In such extreme condition the region of high reflectance would have a squared shape. The second photonic band gap is barely visible in the considered energy range, although its onset is clear when looking at the reflectance spectrum around 300 *nm*. Finally, at the pseudo photonic band gap energy a folding of the dispersion relation occurs.

The wavelength range between the two indicated photonic band gaps is dwelled by a number of smaller peaks, rendered more visible zooming Fig. 6.9 between 300 *nm* and 800 *nm* (see Fig. 6.10). They can be grouped in two sets: below the pseudo photonic band gap at $2E_B$ 2.75 *eV* (second folding point of Brillouin zone) and above it. These peaks represent the excitation of discretized photonic modes in the energy range between the gaps. The number of peaks in each group corresponds to the number of DBR pairs minus one $(M-1)$ [279].

Looking at the optical situation inside the DBR under test, it is interesting to see that, despite the high reflectance achievable, there is a partial penetration of the electric field around the design wavelength (see Fig. 6.10). The penetration depth L_{DBR} depends on both angles and polarization, but for perpendicular incidence it can be simply written as follows [280]:
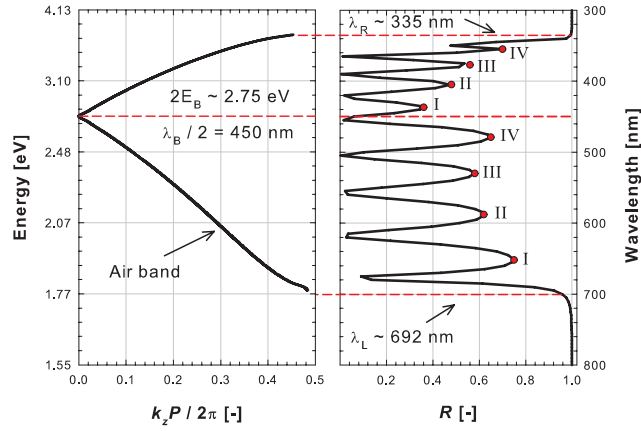
Figure 6.10: Zoomed at high energies of photonic band dispersion (left) and simulated reflectance (right) of a-SiO$_x$:H / a-Si:H DBR designed at λ_B = 900 nm. Roman numbers enumerate the smaller peaks.

$$L_{DBR} = \frac{2}{n_H^2 - n_L^2} \left(d_L n_L^2 + d_H n_H^2 \right). \qquad (6.10)$$

In the DBR under test the penetration depth is 180 *nm*, which is equal to the thickness of the first a-SiO$_x$:H layer (d_L = 150 *nm*) plus around the half of the first a-Si:H layer thickness (d_H = 56.25 *nm*). This result explains why $R(\lambda_B) = 1$ can be hardly achieved with a DBR formed by only one pair (see Eq. 6.2).
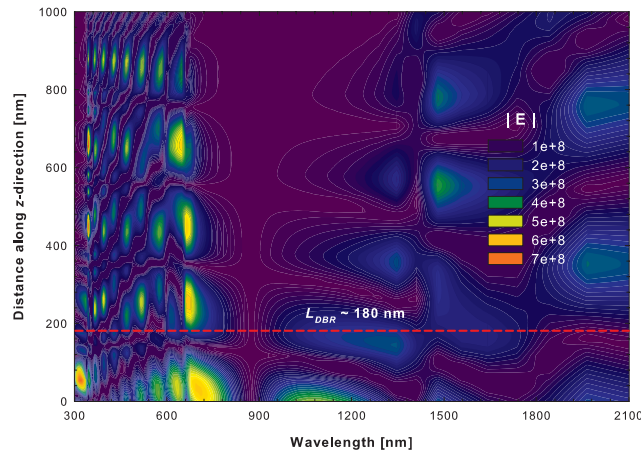
Figure 6.11: Penetration of electric field in the DBR for perpendicular incidence. Illumination side is the bottom of the plot; horizontal dashed line indicates the penetration depth L_{DBR}.

6.3.3 Omni-directionality

The usage of dielectric DBR in place of metallic back reflectors in solar cells is especially appealing for high reflectance with negligible loss at infrared wavelengths. However, not all kinds of DBR exhibit the omni-directional reflectance typical of metallic reflectors. This is an important issue to tackle when designing the DBR, since most of the solar cell technologies make use of light scattering for improving the EQE. Under two specific conditions dielectric mirrors can actually exhibit an omni-directional behavior, which means a unique PGB for all angles of incidence and polarizations [281, 282].
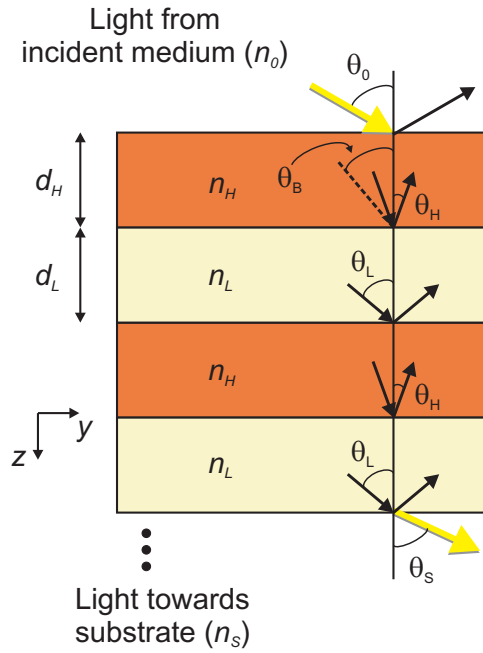

Figure 6.12: *Angles development from the incident medium (θ_0) through the DBR (theta$_H$ and theta$_L$) until the substrate (theta$_S$). Notice the Brewster angle at the first internal interface of the DBR (theta$_B$).*

The first condition deals with the development of angles inside the dielectric mirror (see Fig. 6.12). *The maximal refraction angle at the interface incident medium / DBR (θ_{Hmax}) should not exceed the Brewster angle (θ_B) at the internal interface of the first DBR pair.* If this does not apply, the E-M field is partly transmitted throughout the structure and the DBR ceases to act as such. This condition can be mathematically expressed as $\theta_{Hmax} < \theta_B$, which is equivalent to $sin(theta_{Hmax}) < sin(\theta B)$ or to the following relation [275]:

$$\begin{cases} sin(\theta_{Hmax}) = \frac{n_0}{n_H} sin(\theta_0)_{|\theta_0 = \frac{\pi}{2}}; \text{Snell law} \\ \wedge \\ sin(\theta_B) = \frac{n_L}{\sqrt{n_L^2 + n_H^2}}; \text{Brewster anlge} \end{cases} \Leftrightarrow n_0 < \frac{n_L \cdot n_H}{\sqrt{n_L^2 + n_H^2}} = n_0'. \qquad (6.11)$$

In Fig. 6.13 the first omni-directionality condition is shown as function of n_L and n_H.

For design purposes, *it is possible to enter the plot at desired incident medium refractive index and choose the refractive indexes of materials that will constitute the DBR in such a way that $n_0 < n_0'$.* As long as n_H and n_L are inverted in both Snell law and Brewster angle relationships, Eq. 6.11 applies also when a material with low refractive index begins the DBR. Considering air as incident medium and refractive indexes $n_L = 1.5$ and $n_H = 4$, the first omni-directionality condition is verified for the ideal DBR presented in previous section.
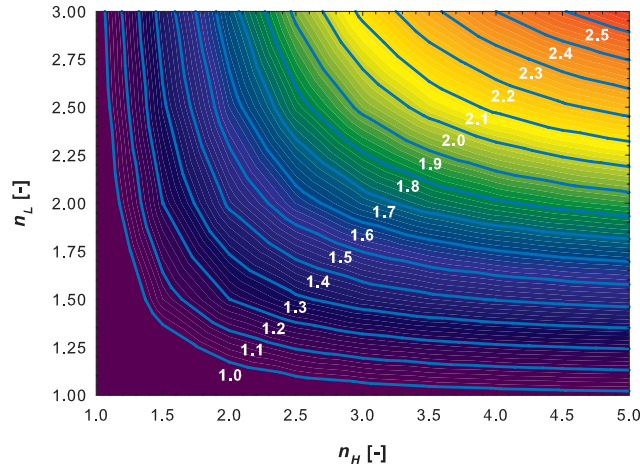

Figure 6.13: First omni-directionality condition as function of n_L and n_H. Labels on contour lines indicate different values of the refractive index n_0'.

The second condition states that *the DBR should exhibit a region of high reflectance in common for all angles of incidence and for both polarizations* [275]. To accomplish this, one should analyze the angular behavior of band edges for different polarizations and eventually recognize an overlap among the *PBGs*. After calculating the reflection coefficient (Eq. 6.6) for different angles and polarizations, Eq. 6.5 and 6.7 determine the influence of the angle of incidence θ_0 on the photonic band gap edges and thus on the *PBG* amplitude. Also, the Bragg wavelength changes in correspondence of incident angles and polarizations. In fact, combining Eq. 6.1 and Eq. 6.5, λ_B can be equivalently expressed in term of left or right band edge:

$$\lambda_B = \begin{cases} \dfrac{2\lambda_L cos^{-1}\left[-\rho_{(\cdot)}\right]}{\pi} \\[2em] \dfrac{2\lambda_R cos^{-1}\left[-\rho_{(\cdot)}\right]}{\pi} \end{cases} . \tag{6.12}$$

If the difference between the right photonic band edge for broad angles in P-polarization (upper bound) and the left photonic band edge at perpendicular incidence (lower bound) determines a common region of high reflectance, then the second condition for omni-directionality is fulfilled. The role of these two bounds is going to be clarified.

In Fig. 6.14, simulated reflectance spectra of the aforementioned ideal a-SiO^x:H / a-Si:H DBR ($M = 5$) are reported for angles of incidence ranging from $0°$ to $90°$ and for S- and P-

polarizations. Superposed to the graphs, calculated angle-dependent band edges and Bragg wavelengths show a perfect matching with simulations for S-polarization and a reasonable approximation for P-polarization until $50°$. For wider angles, the region of high reflectance quenches. This happens because the P-polarized reflection coefficient is null at the Brewster angle ($\lambda_B \sim 70°$ for the DBR under test). On the other hand, for S-polarization, $\Delta\lambda$ tends to increase with the Bragg wavelength shifting towards higher energies for large incident angles. Therefore, the difference between the discussed upper and lower bounds effectively constitute the maximal achievable omni-directional photonic band gap for a generic DBR. For the analyzed DBR, an overlap of high reflectance for different polarizations and ranging for all angles of incidence exists. Thus also the second discussed condition holds, making such DBR omni-directional. However in practice, considering the wavelength dependency of optical constants, the achievement of omni-directionality becomes more difficult.
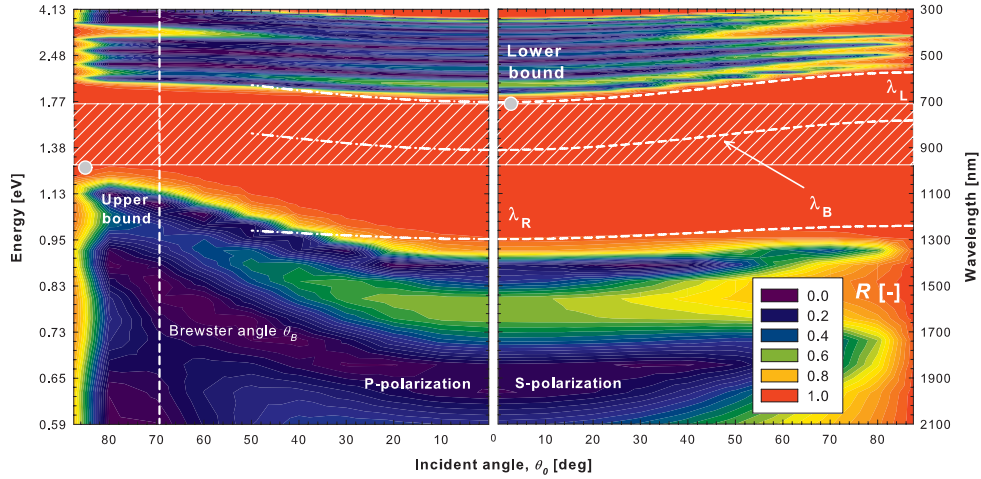
Figure 6.14: Simulated reflectance spectra for different angle of incidence and for P-polarization (left) and S-polarization (right). White shaded area represents the omni-directional PGB, dashed and dash-dotted white curves are the angle dependent photonic band edges and Bragg wavelengths, and vertical dashed white line locates the Brewster angle. Color from violet to red represent increasing values of reflectance.

6.3.4 Modulation

The last property of DBR discussed in this section is the so-called modulation. Two or more DBR designed at different Bragg wavelengths can be combined together in order to enlarge the resulting region of high reflectance. The schematic sketch of a modulated DBR is reported in Fig. 6.14. The term modulation refers to the appropriate choice of design wavelengths (i.e. thicknesses involved) for the specific application [273]. This concept is especially interesting for extending the spectral capabilities of a dielectric mirror without changing materials and therefore without changing production processes.

In Fig. 6.16, simulated reflectance of a modulated DBR in air / c-Si embedding materials

Figure 6.15: Schematic sketch of a modulated dielectric mirror. The constituting DBR$_1$ and DBR$_2$ must be designed with $\lambda_{B1} < \lambda_{B2}$.

is presented together with the reflectance of its constituting elements. Such elements are two simpler dielectric reflectors (named DBR$_1$ and DBR$_2$) both made up of 5 pairs of realistic a-Si:H / a-SiN$_x$:H but with thicknesses of layers aimed at two differen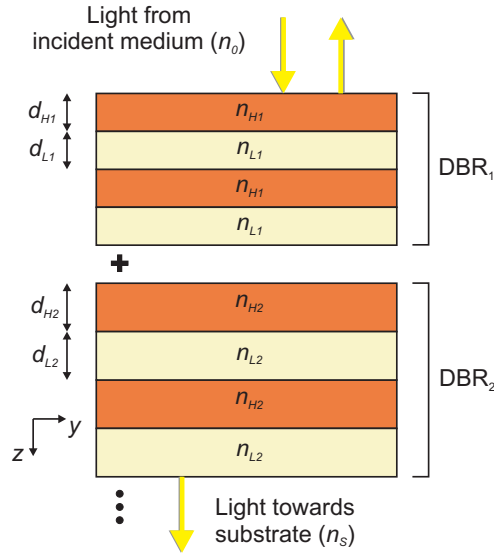t design wavelengths ($\lambda_{B1} = 650$ *nm* and $\lambda_{B2} = 800$ *nm*, respectively). Individually the simple DBRs behave as described so far with noticeable regions of high reflectance around Bragg wavelengths and with the optical window of DBR$_1$ slightly skewed because of the absorption in a-Si:H at short wavelengths (dashed lines in the figure). When combining sequentially DBR$_1$ and DBR$_2$ in a modulated dielectric mirror, the region of high reflectance is equal to the union of the two separated ones. In this case, two dips in the reflectance spectrum, located at 860 *nm* and 980 *nm*, correspond to local minima in DBR$_1$ reflectance.

6.4 Fabrication of DBR at low temperature

For the application of a DBR in the role of dielectric mirror in thin-film silicon solar cells, the constituting materials must be developed at temperature compatible with the *pin* junction(s) (¡ 200 °*C*). Furthermore, in order to use the same deposition system for a continuous process, a-Si:H and a-SiN$_x$:H were chosen as suitable materials to form the dielectric mirror. In this section, a simple DBR is optically characterized at perpendicular and tilted incidence in order to demonstrate the validity of developed low temperature process with continuous glow discharge plasma.

The analyzed DBR was fabricated by RF PE-CVD at 172 °*C*, formed by three pairs of a-Si:H / a-SiN$_x$:H layers, and designed around $\lambda_B = 800$ *nm*. In Fig. 6.17 reflectance of such structure is reported, while in Fig. 6.18 the effect of the incidence angle θ_0 for P-polarization is shown. Measurements were taken according the optical system air / DBR / glass. In both
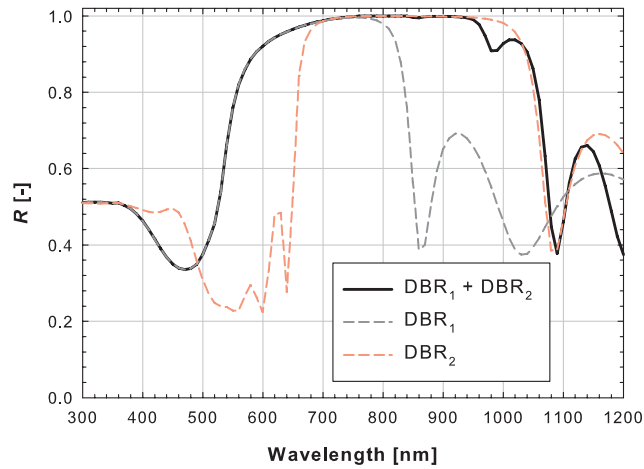
Figure 6.16: Simulated reflectance of a modulated DBR (solid black line) with its realistic constitutive elements (dashed lines).

figures the experimental curves are closely matched by simulated spectra that were carried out using realistic optical constants. These simulations further validate the trustworthiness of the used optical models and highlight the precision achieved in the deposition process when switching from one material to the other. It is possible to notice that amorphous layers suitable for highly reflective DBR can be fabricated even at low deposition temperature. In addition, the quenching of high reflectance region for P-polarization towards higher energies (see Fig. 6.14 left panel) finds practical confirmation when looking at the optical response for tilted illumination.
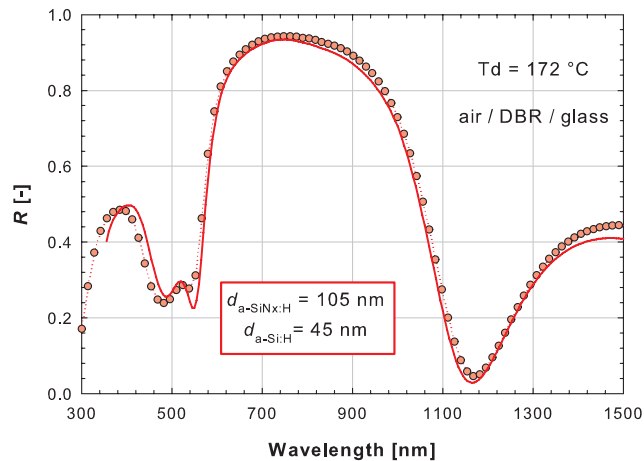
Figure 6.17: Reflectance of three pairs a-Si:H / a-SiN$_x$:H DBR deposited at low temperature. Solid curve is simulation, symbol-dotted curve is measurements.
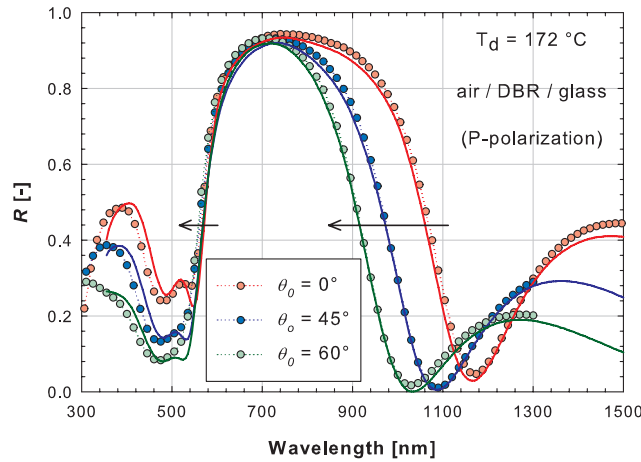
Figure 6.18: Tilted illumination effect on three pairs a-Si:H / a-SiN$_x$:H DBR. Solid curves are simulations, circle-dotted curves are measurements.

6.5 Application of DBR in single junction solar cells

A DBR formed by four pairs of a-Si:H / a-SiN$_x$:H layers is finally used as the back reflector in single junction thin-film silicon solar cells. The DBR was designed to perform in a broad wavelength range with the peak reflectance at 600 *nm*. Fabricated at low substrate temperature, it was applied at the rear side of flat and textured amorphous silicon single-junction solar cells in both superstrate (*pin*) and substrate (*nip*) configurations. The spectral response and electrical characteristics were measured. Solar cells with optimized DBR exhibit enhanced external quantum efficiency in the long wavelength range and the electrical performance is comparable to solar cells having conventional Ag back reflector.

After choosing the materials for the back reflector (TCO and DBR), different combinations of λ_B and number of pairs *M* were investigated in optical simulations in order to achieve the highest short-circuit current density (J_{SC}). Afterwards, *pin* and *nip* single junction thin-film silicon solar cells with the dielectric DBR were fabricated on both flat and textured substrates (see Fig. 6.19). In case of *pin* configuration two photolithographic methods were developed in order to precisely define the rear contact area. Spectral response and current-voltage characteristics of the fabricated devices were measured. The influence of the back contact design on the electrical properties of TFSSC is discussed and demonstrates the feasibility of using the TCO-DBR stack as the back contact/reflector.

6.5.1 Optical simulations

An optimal dielectric DBR for single-junction a-Si:H solar cells was designed using the ASA software. Hydrogenated amorphous silicon and silicon nitride films were selected for the alternating pairs. Simulations of flat solar cells with the rear contact/reflector formed by the back ZnO:Al (BAZO) and DBR were carried out. In the simulations the number of pairs of the DBR (from 1 to 10) and the λ_B (from 500 *nm* to 800 *nm*) were varied. The 1-D PC structure was tested in two arrangements: (i) a-Si:H or (ii) a-SiN$_x$:H as the first layer

Table 6.1: Simulated structures of single junction thin-film silicon solar cells. ITO indicates
Indium-Tin-Oxide.

Structure	*pin*	*nip*
Substrate	glass (0.6 *mm*)	–
Front TCO	ITO (400 *nm*)	ITO (80 *nm*)
p-layer	a-SiC:H (15 *nm*)	
i-layer	a-Si:H (300 *nm*)	
n-layer	a-Si:H (20 *nm*)	
Back TCO	AZO (500 *nm*)	
Back reflector	DBR or Ag (300 *nm*) or Al (300 *nm*)	

on the BAZO layer. The absorptance in the i-layer was used to calculate the implied short-circuit current density (J_{SC}) in the wavelength range between 300 *nm* and 850 *nm*. Solar cells with metal Ag and Al back reflectors were also simulated. Through a comparison of the simulated J_{SC}, the optimal DBR was selected. Simulated structures of single junction thin-film silicon solar cells are reported in Tab. 6.1. The thickness of the BAZO layer is a compromise between sufficient conductivity and transparency, while the thickness of the individual layers in the DBR is calculated on a quarter-wavelength basis for each simulated λ_B (see Eq. 6.1).

Using the optimal DBR, the internal reflectance was calculated at the n-layer / BAZO interface for Ag, Al, and DBR back reflectors. Furthermore, the reflectance at the air / DBR interface for glass and Ag substrates was also simulated and measured to verify the experimental results obtained at the device level.
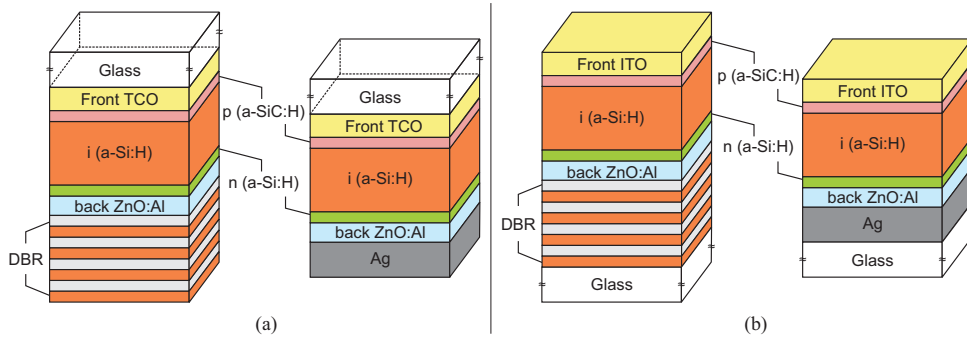
Figure 6.19: Schematic sketch of flat (a) pin and (b) nip single junction solar cells on DBR
or Ag back reflectors. Textured counterparts are not reported for simplicity.

6.5.2 Samples fabrication

Glass substrates were used for flat devices, while SnO$_2$:F (FTO) on glass (Asahi-U type TCO) was deployed as a textured counterpart (front TCO in *pin* configuration, textured substrate in *nip* configuration). ITO and BAZO films were deposited using RF magnetron sputtering while PVD was used for the Ag and Al films. The $p-i-n$ junctions and the

optimal DBR were fabricated at 180 °C and 172 °C, respectively, using RF PE-CVD. The optimal DBR was also deposited on glass and glass / Ag substrates for reflectance measurements. Solar cells in *pin* configuration were tested with three different back reflectors (optimal DBR, Ag, and Al) that were applied at the rear side of the BAZO layer. In *nip* configuration Al was not used.

For *pin* devices with dielectric DBR, two different methods were developed to precisely define the back contact area (see Fig. 6.20). In both methods, *dots displaced* (*DD*) and *vertical vias* (*VV*), a RIE step consisting of 10 minutes of plasma etching from a CF_4-SF_6-O_2 gaseous mixture was used to define the individual DBR pads. The BAZO layers were wet-etched in a 0.5% HCl solution. Back metal (Ag) pads were evaporated only to improve the electrical contact between the BAZO layers and measurement probes. For *nip* solar cells the front ITO deposited through a mask defined the device front contact area.

6.5.3 Morphological and electrical characterization

The complex refractive indices of the simulated materials were characterized using the technique described in Ch. 3 or multi-angle incidence and double-polarization. The spectrophotometer with the integrating sphere was used to measure the reflectance of the optimal DBR in air deposited either on glass or on Ag-coated glass. The four probes setup was used to measure the sheet resistance (R_{Sheet}) of the TCOs. The ITO films exhibited $R_{Sheet} < 10$ $\Omega/\square$ and the BAZO films had $R_{Sheet} \sim 20$ $\Omega/\square$. In both *pin* and *nip* devices the BAZO films were the only electrical contact at the rear side when combined with the DBR. The thicknesses of all layers presented in Tab. 6.1 were confirmed with cross-sectional SEM analysis (see Fig. 6.21). The *EQE* and the $J-V$ characteristic of the fabricated devices were measured with the spectral response and the solar simulator, respectively. All $J-V$ measurements were performed with a mask having area size of 3x3 mm^2.

6.5.4 Optical characterization and simulation results

The increase in *JSC* (ΔJ_{SC}) with respect to the *JSC* of the reference solar cell with the BAZO / Al back contact was used as the figure of merit for optimizing the number of pairs *M* and the $\lambda_B B$ of the dielectric DBR in the simulations with ASA. The results obtained for both *pin* and *nip* configurations were essentially the same (see Fig. 6.22): (i) the arrangement with a-SiN$_x$:H as the first DBR layer performed better than the arrangement with a-Si:H as the first layer, (ii) the optimal λ_B was 600 *nm*, and (iii) no difference in performance was found when the number of pairs was increased from four to ten. In these optimal conditions the ΔJ_{SC} for solar cells with dielectric DBR was 1.57% (*pin*) or 1.62% (*nip*). Solar cells with Ag reflector slightly outperformed the ones with the DBR by +1.85% for the *pin* configuration and +1.87% for the *nip* configuration with respect to the Al back reflector. The thicknesses of the layers forming the optimal DBR were 87 *nm* for a-SiN$_x$:H and 34 *nm* for a-Si:H.

In Fig. 6.23(a) the simulated internal reflectance at the interface between the n-layer and the BAZO for Ag, Al, and the optimal DBR is shown. The optimal DBR demonstrates a higher reflectance than both metals around $\lambda_B = 600$ *nm* and performs generally better than Al between 560 and 800 *nm*. Fig. 6.23(b) presents a close matching between the simulated and measured reflectance of the optimal DBR at the air / a-SiN$_x$:H interface. Furthermore the reflectance in air of the optimal DBR is not influenced by the Ag film for wavelengths

Method #1: *dots displaced*   Method #2: *vertical vias*
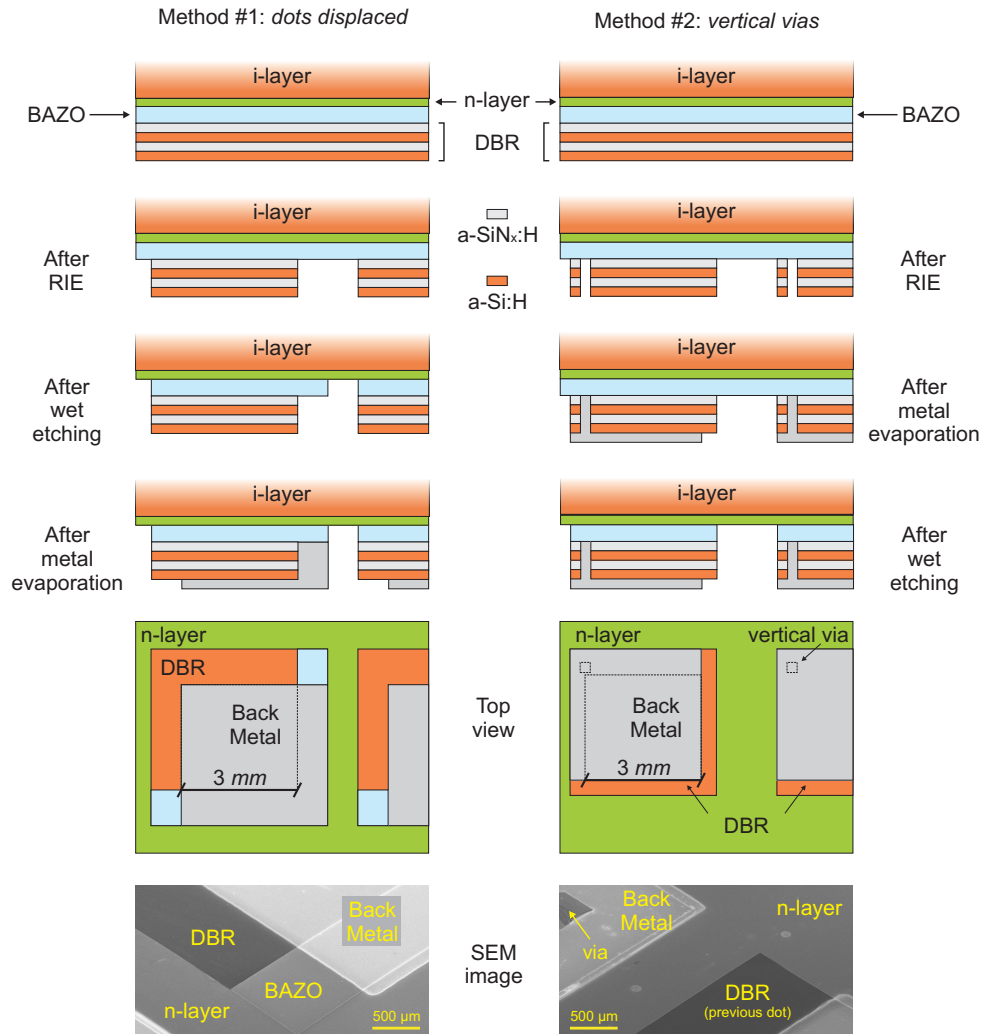
*Figure 6.20: Flow charts for fabricating the two different back contacts for flat and textured
            pin cells with dielectric DBR and relative 45° tilted SEM images: (left column)
            method #1 is called dots displaced (DD), (right column) method #2 is called
            vertical vias (VV).*

below 800 *nm*. Such test verified that the back metal pads did not affect the performance of
DD and *VV* solar cells. The dips located at 760 *nm* and 1010 *nm* for the DBR / Ag stack are
resonances of Ag mediated by the dielectric DBR. The reflectance of DBR using a synthetic
lossless a-Si:H was simulated to practically show that the use of realistic a-Si:H limits the
design of the dielectric DBR in its weakly-absorptive wavelength range. In case of solar
cells with textured interfaces, the reflectance of DBR is expected to be slightly lower than
on flat substrate with shrinkage of the region of high reflectance due to the disturbance of
the alternating thicknesses of different materials.
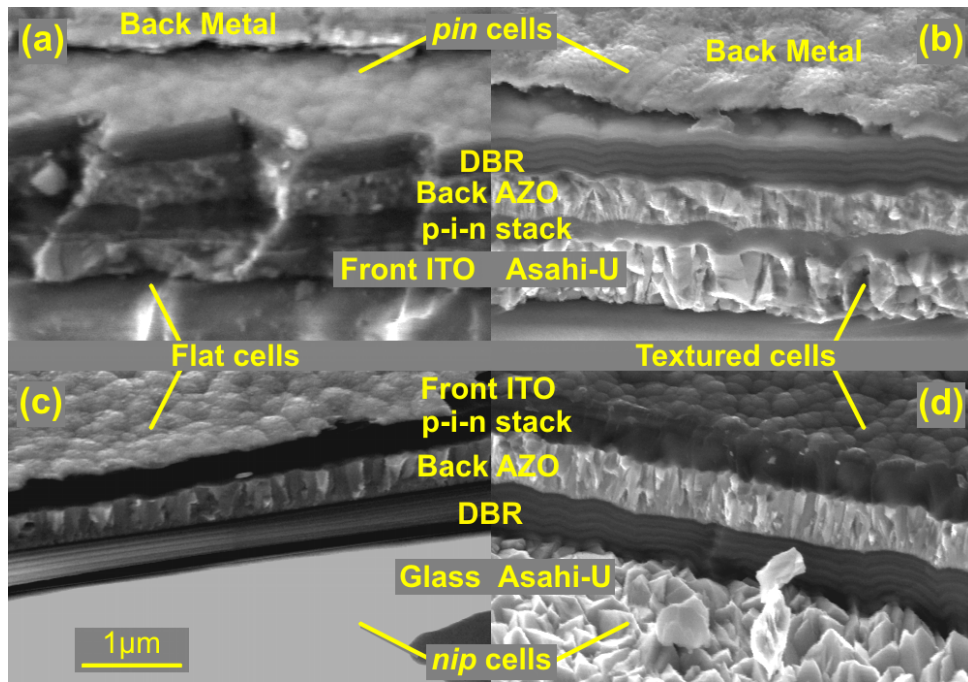
Figure 6.21: Cross-sectional SEM images of flat and textured pin (ab) and nip (cd) devices with dielectric DBR (tilt angle = 45°). Brighter layers of the 1-D PC stacks are made of a-SiN$_x$:H.

Figure 6.22: Optical simulations results of (a) pin and (b) nip flat cells with BAZO / DBR back reflector for different Bragg wavelength designs and number of pairs. Grey areas indicate the ΔJ_{SC} for BAZO / Al (ref. 0%) and BAZO / Ag metallic back reflectors.

*Figure 6.23: (a) Internal reflectance at the interface between the n-layer and the BAZO
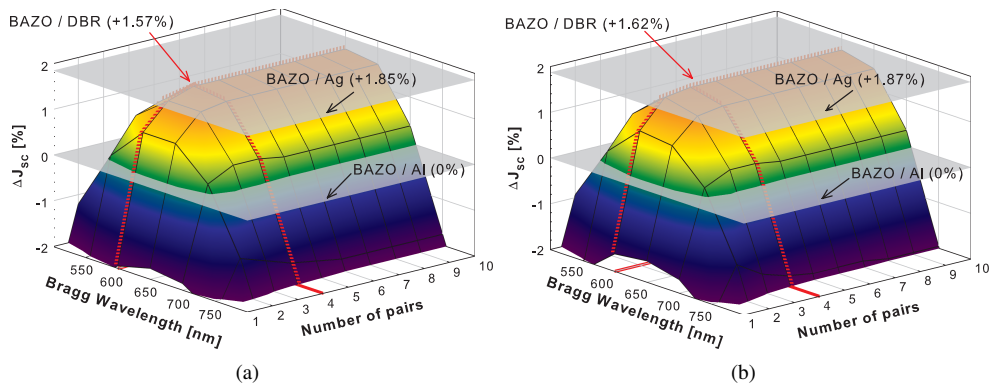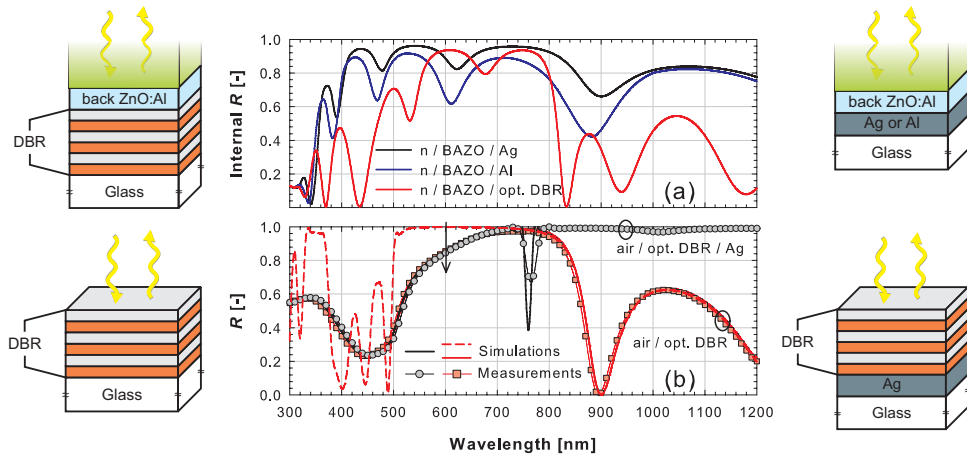for Ag, Al, and optimal DBR back reflectors; (b) measured and simulated re-
flectance of the optimal DBR in air. Dashed line indicates the simulated re-
flectance of the optimal DBR using a synthetic non-absorptive a-Si:H. Sketches
on both sides define the optical systems.*

Considering the refractive indexes of materials constituting the optimal DBR around
600 *nm* and analyzing the internal reflectance at the interface between the n-layer and the
BAZO / optimal DBR for different angles of incidence and different polarizations, it is clear
that in this case the conditions for omni-directionality are not verified, especially for the
quenching of high reflectance around the Brewster angle (see Fig. 6.23). However it is
possible to recognize a valid optical behaviour of the dielectric mirror with respect to the
BAZO / Ag reflector at least until 800 *nm*.

6.5.5 Solar cells results

The initial external parameters of all the fabricated cells are reported in Tab. 6.2. The
reported values are averaged over at least 30 solar cells. Devices with the dielectric DBR
in the *pin* and *nip* configurations showed electrical performance in line with both flat and
textured reference cells. For the *pin* cells with the dielectric DBR, the back contact design
influenced the external parameters. In comparison to the dots displaced cells, both flat and
textured vertical vias cells exhibited worse V_{OC}, J_{SC}, and FF, although the performance of
the textured cells might have been influenced by fabrication issues. On the other hand, the
dots displaced cells did not suffer from a performance loss due to photolithographic steps
and performed as good as the solar cells with the conventional Ag back reflector. The FF
of the *nip* cells with the dielectric DBR was not better with respect to the reference cells.
However, it is remarkable that the V_{OC} of the flat cells with the DBR was better than the V_{OC}
of the reference cell.

The measured EQE of the fabricated flat and textured *pin* solar cells is shown in Fig.
6.25. The EQE behaviour of the devices with dielectric DBR is similar to those with Ag
and Al reflectors. Particularly in case of the textured cells, the anti-reflective and scattering
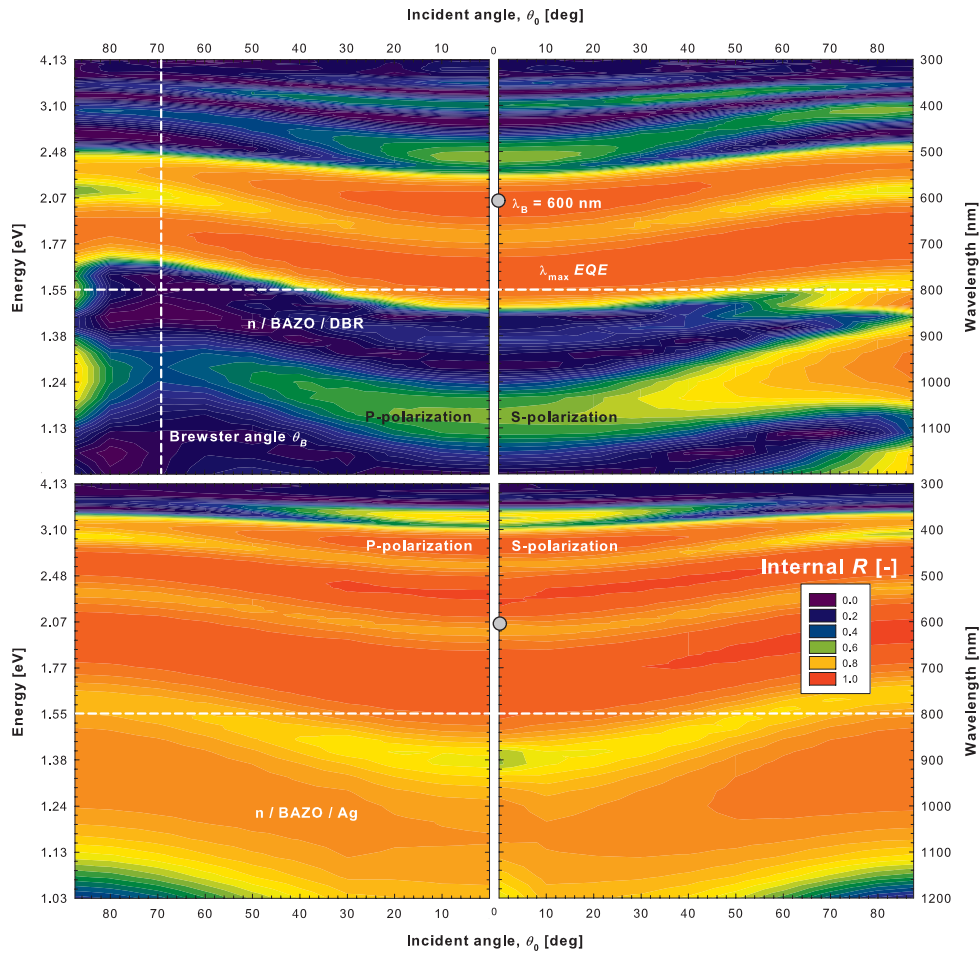
Figure 6.24: Internal reflectance for different angle of incidence and different polarizations at the interface between the n-layer and the BAZO for optimal DBR (top panels) and Ag (bottom panels).

effects due to the use of FTO were confirmed also in the cells with the dielectric DBR. For wavelengths shorter than 550 *nm*, the solar cells with metal reflectors exhibited a slightly higher response. For wavelengths larger than 550 *nm* the interference fringes (more pronounced in the flat case) are related to the internal optical situation depicted in Fig. 6.23(a). As predicted by the simulations, the use of dielectric DBR results in better EQE performance around 620 and 740 *nm* than Ag and Al.

The measured *EQE* of the best flat and textured *nip* solar cells are reported instead in Fig. 6.26. Comparing the flat devices, the two EQE curves are nearly identical in the 300-550 *nm* range. For larger wavelengths the trend is similar to the one observed for the flat *pin* cells, where the spectral response in case of the dielectric DBR around 620 and 740 *nm* peaks is higher than in case of Ag. The effect of introducing the texture is directly visible in the *nip* configuration, because both flat and textured devices have the same front TCO.

Table 6.2: Averaged initial external parameters of the fabricated devices. All cells comprise a 500 nm thick BAZO layer. DD and VV indicate, respectively, dots displaced and vertical vias.

Reflector	V_{OC} [V]	J_{SC} [mA/cm^2]	FF	η [%]
pin flat devices				
DBR (*DD*)	0.864 ± 0.008	11.27 ± 0.026	0.69 ± 0.03	6.76 ± 0.32
DBR (*VV*)	0.855 ± 0.007	10.80 ± 0.028	0.61 ± 0.04	5.67 ± 0.46
Al (ref.)	0.850 ± 0.004	11.19 ± 0.017	0.62 ± 0.01	5.92 ± 0.06
Ag (ref.)	0.854 ± 0.003	11.47 ± 0.017	0.69 ± 0.04	6.76 ± 0.41
pin textured devices				
DBR (*DD*)	0.836 ± 0.010	15.10 ± 0.33	0.69 ± 0.04	8.56 ± 0.62
DBR (*VV*)	0.766 ± 0.078	14.61 ± 0.69	0.63 ± 0.07	6.89 ± 0.93
Al (ref.)	0.831 ± 0.014	15.27 ± 0.24	0.65 ± 0.01	8.22 ± 0.06
Ag (ref.)	0.831 ± 0.016	15.56 ± 0.75	0.68 ± 0.04	8.47 ± 0.33
nip devices				
Flat glass / DBR	0.851 ± 0.009	13.38 ± 0.50	0.59 ± 0.02	6.78 ± 0.42
Flat glass / Ag (ref.)	0.816 ± 0.012	13.66 ± 0.44	0.67 ± 0.01	7.51 ± 0.25
Asahi-U / DBR	0.759 ± 0.006	13.48 ± 0.16	0.60 ± 0.03	6.14 ± 0.35

In the cell with the textured dielectric DBR a higher *EQE* can be observed for $\lambda < 550$ *nm* due to the anti-reflective effect and for $\lambda > 550$ *nm* due to the scattering effect.
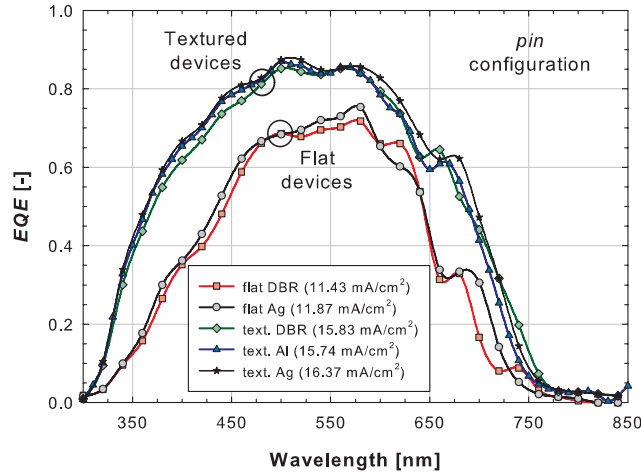

Figure 6.25: Measured EQE of the best flat and textured pin devices with dielectric DBR and metallic back reflectors. Bracketed J_{SC} values are calculated from the EQE.
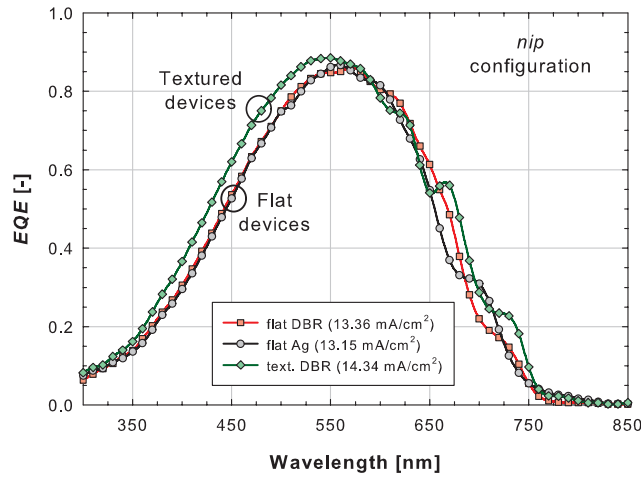
Figure 6.26: Measured EQE of the best flat and textured nip devices with the dielectric DBR and Ag back reflectors. Bracketed J_{SC} values are calculated from the EQE.

6.6 Conclusions

Distributed Bragg reflectors in the role of dielectric rear mirror for thin-film silicon solar cells were investigated. Physical properties and practical rules for appropriate design were discussed by means of 1-D and 3-D simulations and measured spectra of fabricated DBRs. It was found that choosing the Bragg wavelength suitable for a certain optical application depends only on the used materials with respect to the embedding media. In fact, if Δ_{0S} and Δ_{HL} are large around such λ_B, the number of pairs to achieve the highest reflectance is minimized and the *PBG* maximized. In addition, a DBR can be designed omni-directional if (i) the maximal refraction angle at the interface incident medium / DBR does not exceed the Brewster angle (θ_B) at the internal interface of the first DBR pair and (ii) a region of high reflectance in common for all angles of incidence and for both polarizations exists. Finally, when combining sequentially two constitutive DBRs in a modulated dielectric mirror, the region of high reflectance is equal to the union of the two separated ones. Of course, when dealing with realistic optical constants, simulated or measured spectra may deviate from the value of highest reflectance $R(\lambda_B)$ and the ideal photonic band gap. In that respect, computer simulations can offer a valuable help in designing and optimizing DBR for solar cells applications.

The omni-directionality can be indicated as one of the most appealing properties of such optical structures. With a wise choice of materials, it could be possible to realize a dielectric DBR capable to compete over a very large range of wavelengths with metallic reflectors or white paints. For example, considering that up-to-date thin-film silicon solar cells are often terminated with n-type SiO_x:H layers, a viable solution might be a DBR formed by pairs of n-type a-Si:H/ZnO. Also the concept of modulation offers a number of application scenarios worth to be investigated, especially for double and triple junction solar cells.

A continuous plasma glow discharge deposition process was demonstrated. Using such

approach a DBR was fabricated at low temperature. From the optical analysis such dielectric mirror behaved in accordance with theoretical expectations, validating the process, especially in the continuous switch between one layer and another.

The design and application of the dielectric DBR in single junction thin-film silicon solar cells was also reported. Optical simulations showed that flat cells with an optimal dielectric DBR, centred at 600 *nm* and formed by four pairs of a-SiN$_x$:H / a-Si:H layers, outperform flat devices with Al reflector. The optimal DBR was deposited at the rear side of the BAZO layer in *pin* and *nip* flat and textured solar cells. Two photolithographic methods were developed in order to define the contact area in *pin* configuration. From the *EQE* and $J-V$ measurements, solar cells with the DBR performed as well as the reference cells with Ag reflector.

Chapter 7

Flattened Light Scattering Substrate: optical optimization and electrical simulation

The Flattened Light-Scattering Substrate[1] (FLiSS) is formed by a combination of two materials with a high refractive-index mismatch and it has a flat surface. A specific realization of this concept is a flattened two-dimensional (2-D) grating that can be used as efficient back reflector substrate in *nip* solar cells. In this chapter the 3-D optical optimization of *nip* single and multi-junction solar cells based on FLiSS will be reported. Afterwards, using the spectral generation rate as input for ASA, the electrical simulation of highly efficient solar devices will be presented. Results here presented were carried out in collaboration with National Institute of Advanced Industrial Science and Technology, Tsukuba (Japan).

7.1   Introduction

Three light management techniques are commonly deployed in todays solar cells: antireflection for reducing total reflectance of the device, multi-junction approach for an effective use of the solar spectrum, and light trapping for increasing absorption in the absorber layers. The last technique is accomplished by scattering of light at randomly textured interfaces and application of a back reflector. For highly efficient double- or triple-junction thin-film silicon solar cells the following requirements have to be fulfilled: (i) thin top (and middle) cell to limit the light induced degradation [81], (ii) high quality bottom cell absorber, and (iii) current matching of the stacked cells. In particular, special attention must be paid to the second requirement. When grown on textured surfaces with large and deep morphological features to promote light scattering, the electronic quality of nano-crystalline silicon (nc-Si:H) can deteriorate resulting in a reduction of the open-circuit voltage of the bottom cell [94]. Therefore, it is crucial to optimize the substrate surface features with respect to an effective light scattering and nc-Si:H material quality.

---

[1]The FLiSS was conceived and realized by dr. H. Sai at the National Institute of Advanced Industrial Science and Technology, Tsukuba, Japan.

The concept of Flattened Light-Scattering Substrate (FLiSS) has been recently develo-
ped for *nip* thin-film silicon solar cells to deal with this trade-off [134]. A realization of
FLiSS is a two-dimensional (2-D) grating formed by two materials with a large refractive
index contrast. It delivers a high diffused reflectance at long wavelengths without sacrific-
ing the growth of high-quality nc-Si:H. The choice to use a FLiSS structure was aimed to
completely decouple the electrical from the optical performance. In this way, the flatness
of the substrate assures state-of-the-art V_{OC} and FF, while all gained J_{SC} with respect to a
flat conventional back reflector can be related exclusively to the optical configuration of the
substrate. In Fig. 7.1 the *original* FLiSS design is sketched, where gallium-doped zinc oxi-
de (ZnO:Ga) rods forming the 2-D grating (material B, refractive index n_B) are immersed
in n-type a-Si:H (dead layer) (material A, refractive index n_A). The FLiSS is generally fab-
ricated on a flat reflector formed by Ag and ZnO:Ga, which acts also as rear electrode (see
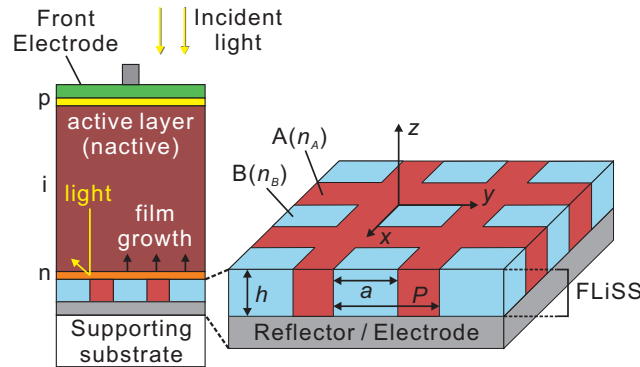Sec. 7.3.1).

*Figure 7.1: Schematic sketch of a nip single junction thin-film silicon solar cell on an orig-
inal FLiSS design (reproduced from [134], courtesy of dr. H. Sai). P, h, and
a/P refer to period, height, and duty cycle, respectively.*

To assess the potential of FLiSS as back reflector, total and diffuse reflectance measured
in air were compared with that of two different back reflectors: a 2-D grating formed by
ZnO:Ga vertical rods ($P = 1000$ *nm* and $h = 300$ *nm*) and coated with Ag / ZnO:Ga back
electrode and a randomly-textured Asahi-U / Ag / ZnO:Al (160 *nm*) (see Fig. 7.2). With
respect to the 2-D grating, the FLiSS exhibits lower reflectance spectra. This is due to optical
losses in the dead material surrounding the ZnO:Ga rods. In fact, the n-type a-Si:H dummy
layer absorbs light either directly at short wavelengths or by scattering at long wavelengths.
With respect to the considered randomly-textured back reflector, the FLiSS shows a similar
trend at long wavelengths ($\lambda > 700$ *nm*). However, peaks in diffuse reflectance makes FLiSS
an interesting back reflector for solar cells based on nc-Si:H. The flatness of this novel
substrate, that results in augmented electrical behaviour when embedded in solar devices,
counterbalances the reported optical performance [134]. In order to design a FLiSS with
increased reflective and scattering capabilities, an optimization study is here reported.
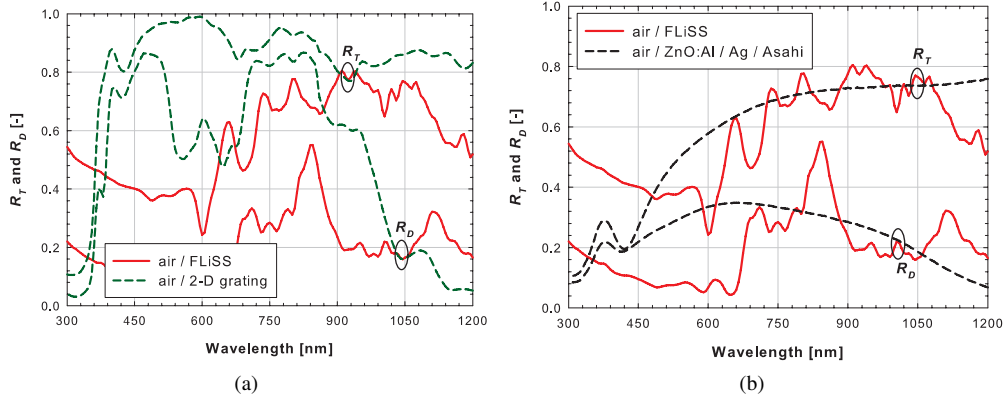
Figure 7.2: Total and diffuse reflectance of FLiSS (courtesy of H. Sai, AIST, unpublished) compared with that of other two back reflectors: (a) ZnO:Ga rods (2-D grating) / ZnO:Ga / Ag or (b) ZnO:Al (160 nm) / Ag / Asahi-U substrate (courtesy of G. Yang, TUDelft). All spectra were measured in air.

7.2 Modelling approach

The FLiSS is an object intrinsically three-dimensional (3-D). Therefore a full-wave analysis of the electromagnetic field is necessary for the correct modelling of FLiSS-based solar cells. The modelling was based on two subsequent stages: (i) 3-D optical modelling of solar cells solving Maxwell equations with FEM and (ii) calculation of solar cells electrical behaviour using a semiconductor equations solver. The two stages were coupled since one of the outputs from optical simulations, the spectral absorption rate $a(r,\lambda)$ introduced in Ch. 2, was used as input in electrical simulations.

Simulated structures were *nip* thin-film silicon solar cells. From optical point of view, they could be conceptually reduced to a unit cell with its length, width, and depth down to *x*-, *y*-, and *z*-directions, respectively. The case of a single junction cell with boundary conditions is shown in Fig. 7.3. The unit cell describes the entire structure if replicated in an infinite two-dimensional array along *x*- and *y*-directions. Excitations and boundary conditions are then arranged to complete the set of information needed for simulation. Plane waves travelling along z-direction excited the structure, while master-slave (M-S) and Floquet ports (FP) were the used boundary conditions (see Sec. 4.5.2).

The verification of optical part of the modeling was carried out by matching simulated and measured spectral responses of *nip* single junction solar cells on the original FLiSS design and on the standard flat back reflector (ZnO:Ga / Ag). After that, single junction *nip* nc-Si:H solar cells on the FLiSS with three different shapes of gratings were simulated as function of the ZnO:Ga volume fraction in the substrate. The best potential design was determined by comparing i-layer implied photo-currents (J_{PH}). The FLiSS was further optimized by replacing materials constituting the substrate and the front transparent conductive oxide (TCO) with ones that absorb less in red and infrared wavelength range. Finally, period
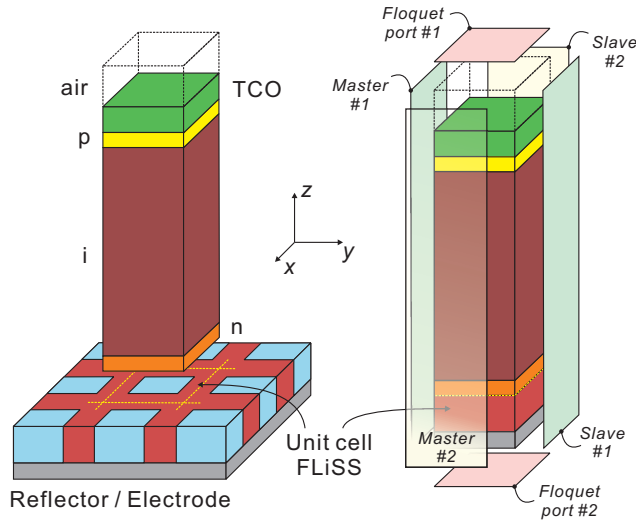
Figure 7.3: Definition of FLiSS unit cell (left) and example of application of M-S and FP boundary conditions on nip *single junction solar cell based on FLiSS (right).*

and height of the optimized FLiSS were varied to study the variation of i-layer absorptance with respect to the optical losses in supporting layers and the total reflectance of the cell. The application of FLiSS in thin double- and triple-junction *nip* solar cells was also investigated. Using optimal materials and optimal FLiSS design, current-matched multi-junction devices could be simulated exhibiting state-of-the-art optical performance.

From electrical point of view, simulated nip solar cells were modelled in ASA as flat multi-layer stacks that comprised only the materials forming the *p-i-n* junction(s). The inclusion of front TCO and back reflector (FLiSS + rear electrode) was not necessary, since the spectral absorption rate was imported from optical simulations. Anyway, the electrical effect of front and rear electrodes was taken into account (see Sec. 7.3.9) and used as boundary condition for solving the semiconductor equations.

The verification of electrical part of the modeling was carried out by matching simulated and measured current density-voltage characteristics of *nip* single junction solar cells on the original FLiSS design and on the standard flat back reflector. Current-voltage characteristics of the optically optimized *nip* single and multi-junction solar cells on the FLiSS were simulated. Thin *nip* solar cells showed potential initial efficiencies in line or beyond up-to-date thicker *nip* solar cells based on textured back reflectors [48, 83, 283].

7.3   Results

7.3.1   Input parameters for 3-D modeling of FLiSS-based *nip* solar cell

The 3-D modelling was initiated by considering the structure and the thickness of layers in two fabricated solar cell. Referring to Fig. 7.1 (from bottom to top), the first cell was constituted by reflector/electrode of Ag (200 *nm*) and ZnO:Ga (50 *nm* pad) sputtered on sup-

porting c-Si wafer substrate, original FLiSS formed by ZnO:Ga and dead n-type a-Si:H[2], a n (30 *nm*) - i (∼1 *μm*) - p (10 *nm*) nc-Si:H single junction fabricated using plasma glow discharge, and a front electrode realized with 70 *nm* of sputtered In_2O_3:Sn (ITO). The second cell, used as flat reference, was the same as previous device but without FLiSS. In this study the metal front grid was not considered, even though an estimation of its shadowing effect will be given in Sec. 7.4.

To measure the geometrical parameters of original FLiSS and individuate a suitable unit cell for 3-D simulations, two scanning electron microscopy (SEM) images were inspected. In Fig. 7.4(a), the fabricated 2-D grating made up of ZnO:Ga cylindrical rods with height 300 *nm* and period 1000 *nm* is shown, while in Fig. 7.4(b) the unit cell (1x1 μm^2) on flattened surface filled with dead (n) a-Si:H is highlighted.

When simulating a nc-Si:H solar cell, proper handling of its native surface morphology is necessary, since it is responsible of a not negligible anti-reflective (AR) effect (see Sec. 7.3.3). AFM scan was executed on the surface of 1 *μm* thick intrinsic nc-Si:H layer grown on flat glass coated with Ag and ZnO:Ga. From the resulting image, reported in Fig. 7.5, average height and correlation length, equal to 26.4 *nm* and 95.6 *nm*, respectively, were calculated. These parameters were used to define a truncated pyramidal shape (see inset of Fig. 7.5). Such elementary volume was chosen to model in a ordered 2-D array the native surface morphology of intrinsic nc-Si:H layer. In Fig. 7.6 a sketch of the two solar cells considered for validating the optical model is shown. It should be noted that a cubic ZnO:Ga rod is present in the modelled FLiSS unit cell. Verifications were done and no differences with cylindrical rod were found in simulations.
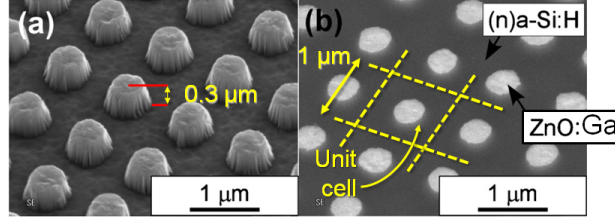
Figure 7.4: SEM of (a) surface-relief structure of the 2-D grating made up of cylindrical ZnO:Ga rods in squared lattice and (b) flattened surface filled with n-type a-Si:H (FLiSS) with highlighted squared unit cell for 3-D simulations (reproduced from [134], courtesy of dr. H. Sai).

Last input parameters were the optical properties of materials involved in simulated structures. Measured optical data were deployed for all aforementioned layers. Refractive indexes (*n*) and extinction coefficients (*k*) of materials suitable for three specialized purposes are reported in Fig. 7.7: (i) front TCO, (ii) dead layer, and (iii) back TCO. As front TCO materials, ITO [121] and In_2O_3:H [123] are compared. IOH presents a sensibly smaller extinction coefficient than ITO due to its lower free carrier absorption (FCA). As dead layer, n-type a-Si:H and nc-Si:H are considered. For simplifying calculations, the same

---

[2]Fabrication details are as follows [134]: the 2-D grating of ZnO:Ga was fabricated using photolithography and chloride gas-based dry etching (see Fig. 7.4(a)). Trenches of the ZnO:Ga grating were afterwards filled by n-type a-Si:H deposited by PE-CVD. Finally, the substrate surface was flattened by chemical mechanical polishing and the ZnO:Ga parts exposed as in Fig. 7.4(b).

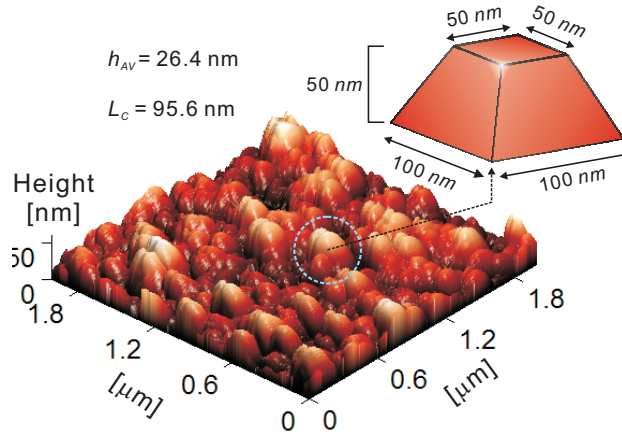*Figure 7.5: AFM scan of the morphology natively present on the surface of 1 μm thick nc-Si:H layer (left) and truncated pyramid modeling a single feature (dashed circle) of the scanned surface (right). Surface average height (h_{AV}) and correlation length (L_C) are also reported.*

optical properties for both n-type and intrinsic nc-Si:H layers were used as data sets of both materials were really similar. Finally as back TCO, two types of ZnO:Ga (GZOa and GZOc) are taken into account. Particularly GZOa is provided with a lower FCA with respect to GZOc. Such nomenclature for ZnO:Ga types is taken from [121]. Materials involved in the validation structures were ITO, n-type a-Si:H, and GZOc, while the usage of their counterparts will be presented in Sec. 7.3.5. For sake of clarity, in all presented simulations the back TCO pad and the TCO in FLiSS were always constituted by the same material.

7.3.2   Determination of output parameters from optical simulations

As described in Sec. 4.5.4, the total reflectance R was computed from the S-parameters, the absorptance in the jth layer (A_j) was calculated as in Eq. 4.15, the transmittance T was found to be numerically negligible because of Ag at the rear side and the conservation of energy at each wavelength was assured by verifying that $R + \sum_j A_j + T = 1$. The implied photo-current density of the i-layer (J_{PH-i}) and the integrated optical losses generated in the supporting layers were calculated using Eq. 1.6 and considering a wavelength range from 300 *nm* to 1200 *nm*. Supposing that each photon absorbed in the absorber layer creates an electron-hole pair and such pair is collected at the electrodes (i.e. neglecting recombination loss mechanisms), J_{PH-i} can be equalized to the short-circuit current density of the solar cell.

Multiplying the unit cell area (A_{UC}) for the squared-magnitude of the electric field **E** projected on a straight vertical line, applied at certain coordinates (x_0, y_0, z_0) and long $d = z_{max} - z_{min}$, the spectral absorption rate along z-direction is defined as follows:

$$a(x_0, y_0, z, \lambda) = A_{UC} \cdot \frac{1}{2} \cdot \varepsilon_0 Im(\varepsilon(z)) \omega |\mathbf{E}(x_0, y_0, z, \lambda)|^2 = \left[\frac{W}{m} \right] \tag{7.1}$$
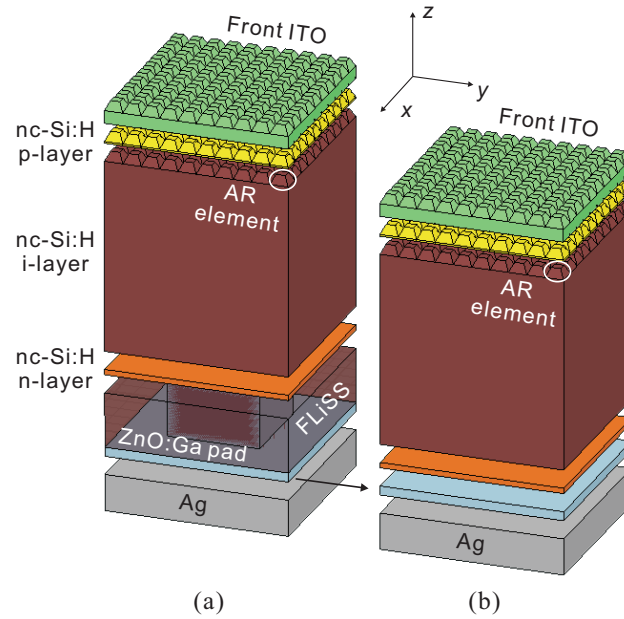
Figure 7.6: Sketch of the original FLiSS-based solar cell (a) and of the flat reference cell (b). Notice the 2-D arrays of small truncated pyramids used as AR elements.
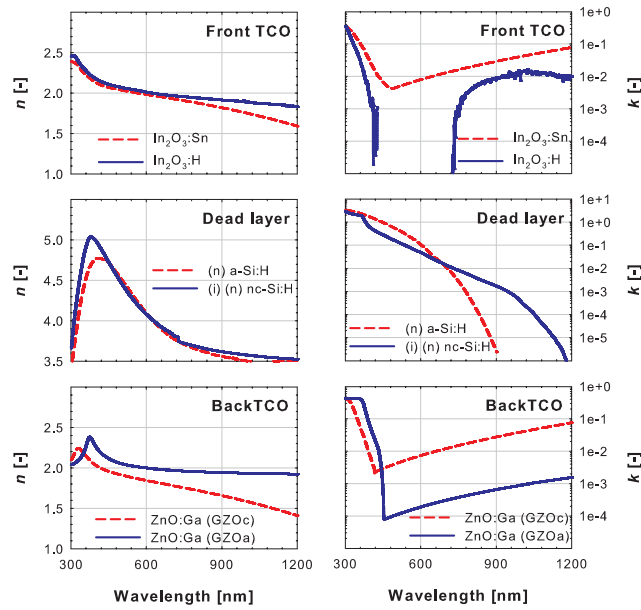

Figure 7.7: Refractive indexes (left) and extinction coefficients (right) for different front TCOs, dead layers, and back TCOs.

where $\varepsilon(z)$ denotes the wavelength dependent complex relative permittivity of the structure at different heights (i.e. in different materials). Considering a relevant number of vertical lines, evenly distributed over the xy-area of the simulated unit cell, parallel to each other, and with the same application height (z_0) and length (d), it is possible to calculate an averaged spectral absorption rate which is 1-D and resembles the optical situation inside the simulated structure:

$$a(z, \lambda) = \frac{1}{N} \sum_{j=1}^{N} a_j(x_j, y_j, z, \lambda) \tag{7.2}$$

where N is the number of considered vertical lines. For the application of this compression technique is not necessary to consider the entire depth of the device, but only the distance from the top of p-layer ($z_{min} = 0$ nm) to the bottom of n-layer (z_{max}), since ASA looks only at the electronic layers for the solution of semiconductor equations. Both Eq. 7.1 and Eq. 7.2 must be normalized to the incident power carried by injected plane waves, which is 1 W in the reported simulations. In Sec. 7.4 a detailed explanation of the numeric compression from 3-D to 1-D spectral absorption rate will be given.

7.3.3   Verification of the optical model with real flat and FLiSS-based solar cells

Verification of the optical model was accomplished by comparing simulated absorptance and measured EQE of the two aforementioned nip single junction solar cells (see Fig. 7.6 for simulated structures and Fig. 7.8 for results). The optical model was capable to describe almost perfectly the spectral behavior of both flat and FLiSS-based cells.

From short wavelengths to almost 700 nm, measured and simulated curves are matched. For wavelengths longer than 700 nm amplitudes of the peaks noticeable in measurements are slightly different but still located at right positions. These results were achieved by considering a bulk thickness of nc-Si:H i-layer equal to 1050 nm plus the height of the 2-D array of small truncated pyramids (50 nm). An additional simulation was run using the original FLiSS-based structure, but maintaining flat all interfaces and considering the thickness of nc-Si:H i-layer equal to 1050 nm (dotted curve in Fig. 7.8). For long wavelengths the resulting spectral behavior is similar to the previous case. However the absence of native roughness on top of the i-layer and subsequently the flatness of top p-layer and front ITO resulted in red shift of the peak previously located at 500 nm. This implies that the 2-D array of small truncated pyramids can properly model properly the AR effect furnished by native nc-Si:H surface.

The inclusion in the simulated structures of all the materials used in real cell allows for quantifying and localizing the optical losses occurring in supporting layers. In Fig. 7.9 an area plot showing the balance between reflectance, absorptance in supporting layers, and absorptance in i-layer of the FLiSS-based cell is reported. Aside reflectance losses (equivalent to 14.10 mA/cm^2), major parasitic losses are located at the front ITO (3.85 mA/cm^2) and in the FLiSS where back GZOc and dead n-type a-Si:H absorb together the corresponding of 6.93 mA/cm^2. Losses minimization and the need for enhanced scattering at long wavelengths demand an optimization of FLiSS design.
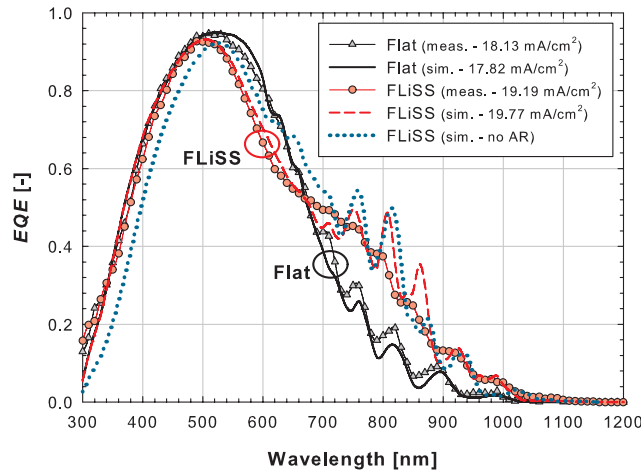
Figure 7.8: Measured EQE of flat (triangles) and FLiSS-based (circles) nip single junction nc-Si:H solar cells compared to the simulated absorptance in the i-layer of flat cell (solid black line) and FLiSS-based cell (dashed thick red line), respectively. Dotted cyan line refers to the simulated FLiSS-based structure without AR-elements on top surface of the nc-Si:H i-layer.
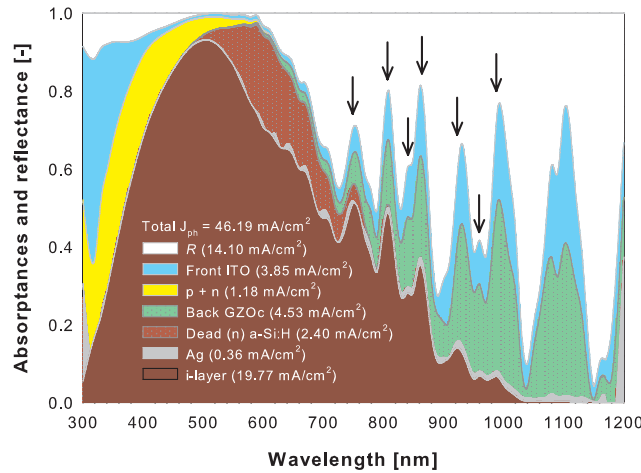
Figure 7.9: Area plot of reflectance, absorptance in supporting layers, and absorptance in i-layer of the original FLiSS-based cell. Implied photo-current densities are mentioned together with the maximal photo-current density available in the wavelength range of interest (Shockley-Queisser limit: 46.19 mA/cm^2) [26]. Black arrows point to i-layer ripples at long wavelengths.

For electrical simulation of the two validating structures (see Sec. 7.3.9), also the spectral generation rate was carried out. The averaged spectral generation rate related to the original FLiSS-based structure is presented in Fig. 10. The position of ripples at long wave-

lengths in the measured *EQE* is compatible with the location of resonances in the spectral absorption rate (from 750 *nm* to 1000 *nm*), which spread narrowly and continuously throughout the entire i-layer thickness.
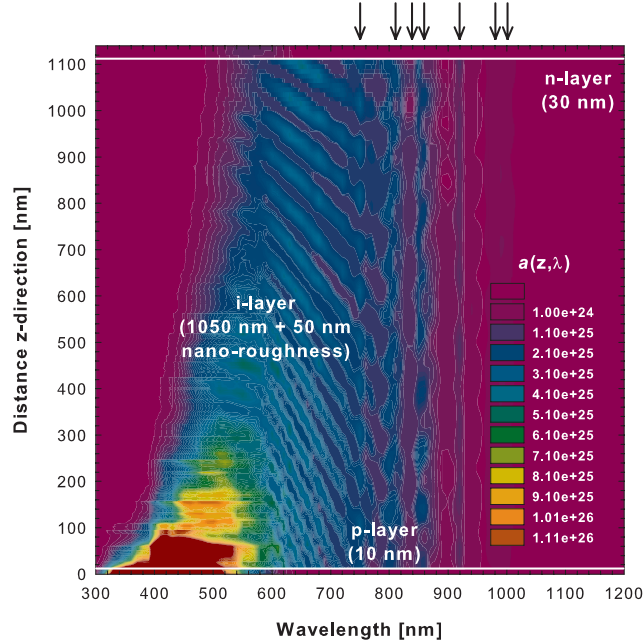
Figure 7.10: Averaged spectral absorption rate $a(z,\lambda)$ of the FLiSS-based cell. Black arrows indicate the correlation with ripples highlighted in Fig. 7.9.

7.3.4   Optimization of FLiSS shape

Assessed the trustworthiness of the optical model, the first step of the optimization study was to investigate different FLiSS shapes. All simulated cells in the optimization study had nc-Si:H i-layer thickness equal to 950 *nm* plus the height of the AR elements (50 *nm*). Three shapes were varied, using as sweeping parameter the GZOc to FLiSS volume ratio (V_R). The shapes are sketched in Fig. 7.11 with an impression of their dynamic change: (a) GZOc cubes in dead n-type a-Si:H (original FLiSS shape), (b) dead n-type a-Si:H cubes in GZOc, and (c) dead n-type a-Si:H inverted pyramids in GZOc. All three sweeps share the same starting and final points, $V_R = 0\%$ and $V_R = 100\%$. They are equivalent, respectively, to a 300 *nm* thick dead n-type a-Si:H layer or a 300 *nm* thick GZOc layer both on top the reflector/electrode (GZOc pad / Ag). The first sweep makes bigger cubic GZOc rods placed in the middle of unit cell with fixed height 300 *nm*. The second sweep shrinks the initial dead n-type a-Si:H block towards the center of unit cell. The third sweep also squeezes the initial dead n-type a-Si:H volume but passing through three phases: truncated pyramids at full height (steps 2, 3, and 4 with $h = 300$ *nm*), inverted pyramid at full height (step 5, $h = 300$ *nm*), and inverted pyramids at reduced heights (steps 6, 7, and 8 with $h < 300$ *nm*).

   Figure of merit to determine the best potential design among swept shapes was the
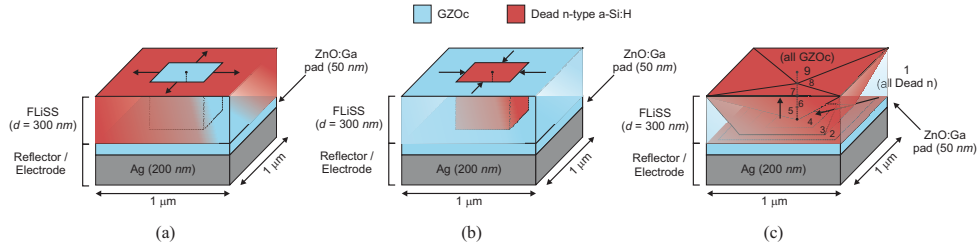
Figure 7.11: Three FLiSS shapes investigated: (a) GZOc cubes in dead n-type a-Si:H, (b) dead n-type a-Si:H cubes in GZOc, and (c) dead n-type a-Si:H inverted pyramids in GZOc. Arrows indicate the direction of change in shape. Numbers in (c) link FLiSS structure with photo-current density values in Fig. 7.12.

implied photo-current density of the nc-Si:H i-layer. In Fig. 7.12 $J_{PH-i-layer}$ as function of V_R for the investigated shapes is reported. For all three shapes the V_R range assuring performance higher than original FLiSS is between 25% and 75%. Shape (a) shows the least performance increase. In FLiSS shape (b) performance are generally higher than in the previous case, although at $V_R = 75\%$ both they perform similarly. The series of shape (c) exhibits the best performance throughout the complete sweep of V_R.

Single junction *nip* nc-Si:H solar cell on FLiSS formed by dead n-type a-Si:H inverted pyramid at full height (step 5, $V_R = 66.6\%$) in GZOc delivers an implied photo-current density of 22.43 mA/cm^2. This corresponds to +13.45% gain with respect to $J_{PH-i-layer}$ of the original FLiSS design. This solar cell structure was called #1.
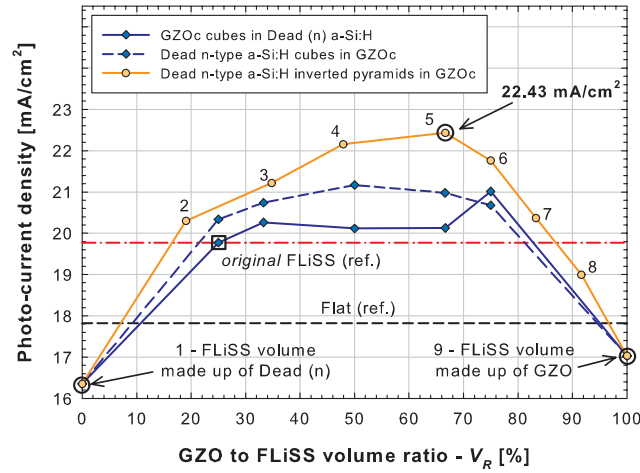
Figure 7.12: Implied photo-current density as function of V_R for the three investigated shapes. Reference dashed lines are simulation values from Fig. 7.8, numbers close to inverted pyramid series refer to Fig. 7.11(c), and the squared-marked spot is the modelled original FLiSS design ($V_R = 25\%$).

7.3.5   FLiSS-based cells with less absorptive materials

The second step of the optimization study was focused on replacing the original materials used for front TCO, dead layer, and back TCO with ones less absorptive leaving unchanged all the rest. The best potential design previously discussed (1x1 μm^2 unit cell, h = 300 nm, dead n-type a-Si:H inverted pyramid at full height in GZOc) was used in this stage. The front ITO was changed with front IOH, dead n-type a-Si:H with n-type nc-Si:H, and GZOc with GZOa. A total of eight combinations were tested. Results are divided per front TCO and summarized in Fig. 7.13.
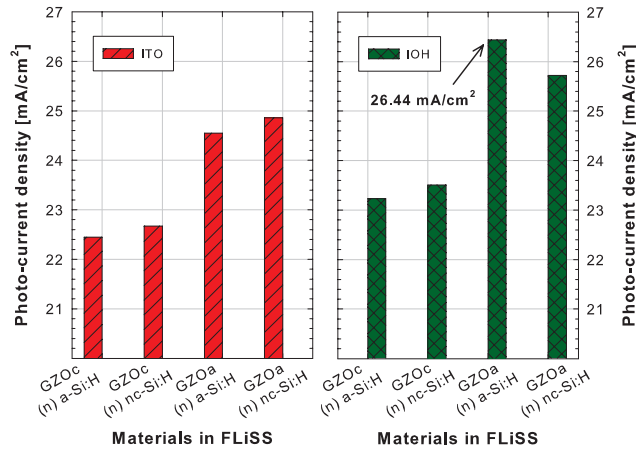
Figure 7.13: Implied photo-current density in nc-Si:H i-layer as function of materials in FLiSS and for different front ITO (left) or IOH (right).

Independently from front TCO and dead material used to form the FLiSS, it appears that the performance of cells with GZOa is better than with GZOc. Similarly, independently from the materials forming the FLiSS, the performance of cells endowed with IOH is better than with ITO as front TCO. These results occur since both IOH and GZOa are TCO with very low FCA in red and infrared range. As for the dead layer, the performance of cells with n-type nc-Si:H is generally better than with n-type a-Si:H, but not in combination with front IOH and back GZOa, whereas the usage n-type a-Si:H results in better performance. Differently than previous cases, such effect cannot be interpreted independently from front and back TCOs. In fact, one should observe that (i) the two types of dead layers absorb in different wavelength ranges (500 nm 800 nm for n-type a-Si:H and 500 nm 1100 nm for n-type nc-Si:H) and (ii) when using simultaneously IOH and GZOa less optical losses occur at long wavelengths causing a potential increase of i-layer absorptance. If selected dead layer is nano-crystalline, the nc-Si:H i-layer will share such potential gain with the dead layer, since they behave optically in similar way. On the other hand, if the used dead layer is a-Si:H, the absorptance of nc-Si:H i-layer will increase undisturbed as the absorption of n-type a-Si:H is negligible at long wavelengths. To support such arguments, the aforementioned eight combinations with the same FLiSS shape but for h = 450 nm were simulated. The same trend as in Fig. 7.13 was found.

Single junction *nip* nc-Si:H solar cell on FLiSS formed by dead n-type a-Si:H inverted

pyramid at full height (h = 300 nm) in GZOa and in combination with front IOH delivers an implied photo-current density of 26.44 mA/cm^2. This is equal to +33.74% gain with respect to $J_{PH-i-layer}$ of the original FLiSS design. This solar cell structure was called #2.

7.3.6 Period-height variation of optimized FLiSS: losses analysis and absorptance limit

In the third and final step of the optimization study FLiSS geometrical parameters were manipulated. Using optimized FLiSS design and proper materials as presented in previous sections, a wide range of periods (from 500 nm to 3000 nm) and heights (from 200 nm to 850 nm) was investigated leaving all the rest unchanged. The implied photo-current density in i-layer ($J_{PH-i-layer}$), the integrated reflectance loss (J_{PH-R}), and the integrated optical losses ($J_{PH-Losses}$) were considered as figures of merit. Particularly, $J_{PH-Losses}$ was defined as the sum of integrated losses of all the supporting layers. In Fig. 7.14 three contour plots are shown, reporting the influence of FLiSS geometrical parameters variation on implied photo-current densities.

From the variation of periods and heights a wide range of $J_{PH-i-layer}$ values were carried out. In Fig. 7.14(a) the least performance, close to the original FLiSS design, was found for the smallest period and the biggest heights, while for the smallest height the performance started to increase, (almost) independently from the period. Local maxima were found for periods between 1250 nm and 2000 nm and h = 450 nm or for P = 3000 nm and h = 650 nm. The inverse situation is represented in Fig. 7.14(b) where J_{PH-R} shows opposite behavior with respect to $J_{PH-i-layer}$. In Fig. 7.14(c) the optical losses increase with increasing period and height, since the FLiSS gets bigger. The absolute maximum in photo-current density is obtained for P = 2000 nm and h = 450 nm, where the sum of J_{PH-R} and $J_{PH-Losses}$ is minimized.

Single junction *nip* nc-Si:H solar cell on FLiSS formed by 2x2 μm^2 unit cell, dead n-type a-Si:H inverted pyramid at full height (h = 450 nm) in GZOa and in combination with front IOH delivers an implied photo-current density of 27.43 mA/cm^2. This represents +38.75% gain with respect to $J_{PH-i-layer}$ of the original FLiSS design. This solar cell structure was called #3.

The optical performance of such single junction *nip* nc-Si:H solar cell on optimized FLiSS was compared with theoretical lower (A_{LL}) and upper (A_{UL}) limits for light absorption and with the more realistic Deckman-Wronski (A_D) limit (see Ch. 2). The three limits were calculated for a nc-Si:H absorber layer 1 μm thick. In particular, the A_D limit was carried out by taking into account the reflectance at air / IOH interface and the absorptances of front IOH and p-layer. These wavelength dependent quantities were elaborated as prefactors ($1 - R$, $1 - A_{IOH}$, and $1 - A_p$) to properly scale the enhancement factor F^{enh} (see Eq. 2.3 and Eq. 2.4). The three limits together with the i-layer absorptance ($A_{i-layer}$) of the optimized cell are reported in Fig. 7.15.

A_D limit was overcome for wavelengths longer than 750 nm. For wavelengths longer than 800 nm $A_{i-layer}$ followed closely the A_{UL} exponential decay even resulting higher than such limit at some specific wavelengths. This result is due to the fact that in A_{UL} limit and in the optimized structure two different diffraction regimes take place. The A_{UL} limit is based on ray optics where both absorber film thickness and random (or periodic) scattering elements are much larger than the wavelength range of interest. In the case under study, on
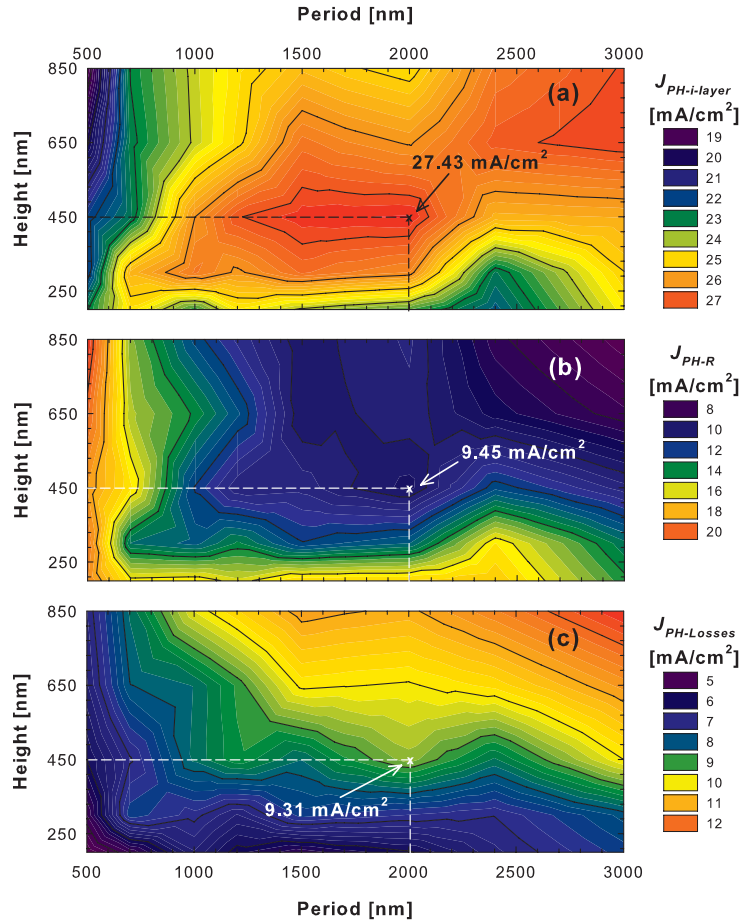
Figure 7.14: Contour plots of the geometrical parameters optimization: (a) implied photo-current density in i-layer, (b) integrated reflectance loss, and (c) integrated absorption losses vs FLiSS period and height.

the contrary, wave optics regime applies as i-layer thickness and dimensions of scattering elements are comparable with the wavelength range of interest [213]. This comparison indicates that (i) the optimized solar cell has very little to gain at short wavelengths ($\lambda <$ 500 *nm*); (ii) the absorptance of dead n-type a-Si:H limits the performance in the wavelength range between 500 *nm* and 750 *nm*; (iii) the simulated light trapping scheme (AR-elements at front side and FLiSS at rear side) is suitable for implementation in highly efficient multi-junction thin-film silicon solar cells.

7.3.7 FLiSS-based thin double junction solar cells

Four simplified design rules can be used to design a current-matched multi-junction solar cell: (i) thin absorber layers for improved stability and high production throughput; (ii) state-of-the-art photo-current density delivered by sub-cells $> 12 \; mA/cm^2$ ($> 9 \; mA/cm^2$)
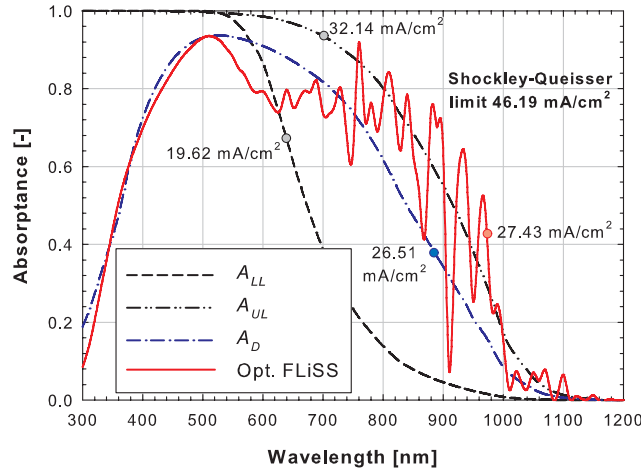
Figure 7.15: Comparison of optical limits (A_{LL}, A_{UL} and A_D) with the i-layer absorptance of the single junction nip nc-Si:H solar cells on optimized FLiSS. Numbers in the graph indicate the implied photo-current density of each reported plot.

for double (triple) junction cells; (iii) suitable light trapping scheme; (iv) enhanced absorption for bottom cell able to deliver alone the total targeted photo-current density. It is clear that fulfilling the last requirement, the thickness of the top cell(s) can be tuned in order to meet requirement (i). These design rules were deployed to demonstrate state-of-the-art optical performance in very thin absorber layers using FLiSS approach.

From previous section, optimized FLiSS with $P = 1000$ nm or 1500 nm and $h = 450$ nm can be regarded as promising candidates to meet not only requirement (iv) (26 mA/cm^2 and 27.33 mA/cm^2, respectively, for 1 μm thick nc-Si:H absorber layer) but also requirement (i). In addition, the choice of suitable material for dead layer should be further tested in double junction structures, because, as seen in Sec. 7.3.5, the absorption in dead layer depends on the absorptance of other layers. For this reasons, four very thin double junction *nip* solar cells were simulated. The thicknesses of absorber layers were fixed to 200 nm for the top a-Si:H i-layer and 550+50 nm for the bottom nc-Si:H i-layer. The two chosen FLiSS designs were characterized by 1x1 μm^2 or 1.5x1.5 μm^2 unit cell area with both $h = 450$ nm and dead n-type a-Si:H or nc-Si:H inverted pyramids ($V_R = 66.6\%$) in GZOa. All four tested structures comprised low FCA front IOH and were characterized by the usual 2-D array of AR elements which made corrugated the top cell and the front electrode. Even being aware that the native surface roughness of nc-Si:H layer depends on its thickness, we did not change the modeling of AR elements, since no large roughness difference is expected for 1 μm or 550 nm thick nc-Si:H layer.

In Fig. 7.16 current matching analysis in simulated double junction *nip* solar cells is reported. It is clearly visible that, aside the absolute values of implied photo-current density, the choice of dead n-type a-Si:H or nc-Si:H determines if the tandem is top or bottom limited. In both geometrical arrangements, the solar cells are top limited when using n-type a-Si:H or bottom limited when using n-type nc-Si:H. This behaviour follows the argument earlier discussed for which the absorber layer shares a potential absorptance gain with the
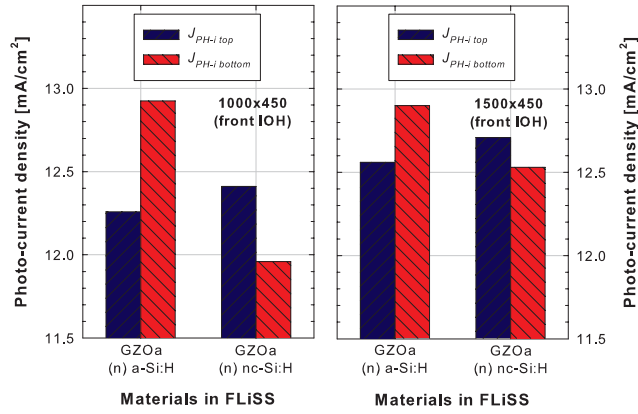
Figure 7.16: Current matching analysis in double junction nip solar cells for different combinations of materials in FLiSS.

dead layer. If n-type a-Si:H is used, it will claim part of such potential gain from the top cell, since they are both optically active in the similar spectral region. Same applies when using nc-Si:H with respect to the bottom cell.

Analyzing the simulated double junction cells and considering the highest among the limited implied photo-current densities, the best double junction *nip* solar cell resulted to be the one on FLiSS with $P = 1500$ *nm*, $h = 450$ *nm* and materials pair GZOa / n-type a-Si:H. In Fig. 7.17 the area plot of such tandem cell is reported, showing how much reflectance and optical losses from supporting layers are lowered with respect to Fig. 7.9. In this configuration the top cell delivers 12.56 mA/cm^2 and the bottom cell 12.90 mA/cm^2 for a total implied photo-current density of 25.46 mA/cm^2.

Figure 7.17: Area plot of reflectance, absorptance in supporting layers, and absorptance in top and bottom i-layers of the best FLiSS-based double junction nip solar cell. Implied photo-current densities are mentioned.

7.3.8   FLiSS-based triple junction solar cells

Following the same rules for current matching in multi-junction thin-film silicon solar cells, a triple junction a-Si:H/a-SiGe:H/nc-Si:H *nip* solar cell based on FLiSS concept was designed. The schematic 3-D sketch of such device is reported in Fig. 7.18, where the GZOa of optimized FLiSS is volumetrically united with the typical 50 *nm* thick GZOa pad. As in double junction case, top and middle cells were corrugated according to the 2-D array of AR elements on the top surface of bottom nc-Si:H i-layer.
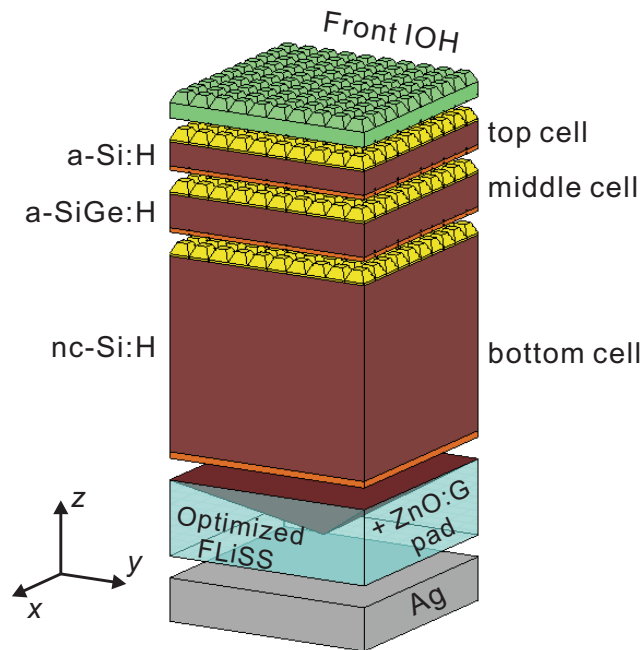
Figure 7.18: Schematic 3-D sketch of triple junction nip solar cell on optimized FLiSS (dead n-type nc-Si:H inverted pyramid in GZOa, V_R = 66.6%) with P = 1000 nm and h = 300 nm.

After a preliminary study on the thickness of absorber layers and on the choice of suitable dead layer material, it was found that using n-type a-Si:H as dead layer in triple junction structure is slightly detrimental for middle cell optical performance. Therefore, the following structure was picked for further optimization: front IOH, a-Si:H top i-layer 110 *nm* thick, a-SiGe:H middle i-layer 155 *nm* thick, nc-Si:H bottom i-layer 900+50 *nm* thick, and optimized FLiSS, constituted by dead n-type nc-Si:H inverted pyramid in GZOa (V_R = 66.6%, P = 1000 *nm* and h = 300 *nm*).

For pursuing current matching two FLiSS heights (300 *nm* and 450 *nm*) and four periods (1000 *nm*, 1200 *nm*, 1500 *nm* and 2000 *nm*) were tested, basically spanning one of the local maxima in Fig. 7.19(a), according to requirement (iv) in Sec. 7.3.7. Results of such test are reported in Fig. 7.19, where implied photo-current densities of top, middle and bottom cells are evaluated as function of FLiSS period and height.

For the case h = 300 *nm*, top cell performance slightly increases by increasing FLiSS
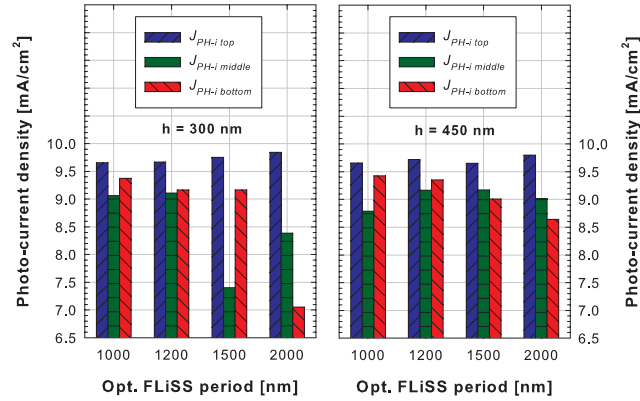
Figure 7.19: Top, middle, and bottom cell implied photo-current densities as function of FLiSS period for h = 300 nm (left) and h = 450 nm (right).

period, while both middle and bottom cells performance decrease. For the case $h = 450\ nm$, the photo-current density related to middle and bottom cells ameliorates with top cell photo-current density mostly unaffected by the period variation. The geometrical combination with the minimal difference between sub-cells photo-current densities is found to be $P = 1200\ nm$ and $h = 450\ nm$. After tuning the top cell i-layer thickness from $110\ nm$ to $105\ nm$, an almost perfect current matching was achieved. The triple junction in such configuration could deliver a total implied photo-current density of $28.24\ mA/cm^2$ ($9.41\ mA/cm^2$ for the top cell, $9.37\ mA/cm^2$ for the middle cell, and $9.46\ mA/cm^2$ for the bottom cell). In Fig. 7.20 the area plot of such tandem cell is reported, showing very limited optical losses at long wavelengths in front TCO, dead layer, and back TCO.
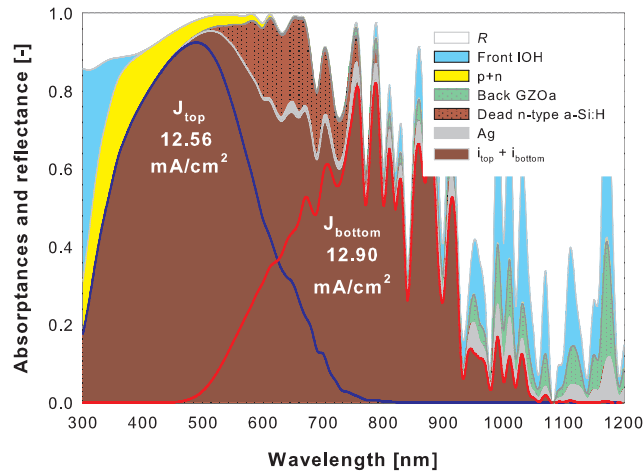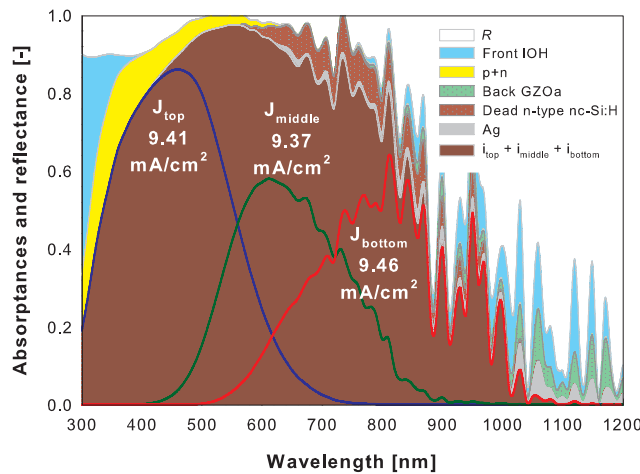

Figure 7.20: Area plot of reflectance, absorptance in supporting layers, and absorptance in top, middle, and bottom i-layers of the best FLiSS-based triple junction nip solar cell. Implied photo-current densities are mentioned.

7.3.9 Electrical simulation of FLiSS-based single, double and triple junction solar cells

For all presented 3-D optical simulations the averaged spectral absorption rate $a(z, \lambda)$ was exported from HFSS and used as input in 1-D electrical simulations carried out with ASA program (see diagram in Fig. 7.21). The electrical model was preliminary developed for single junction *nip* nc-Si:H solar cells and then extended to double and triple junction *nip* solar cells.
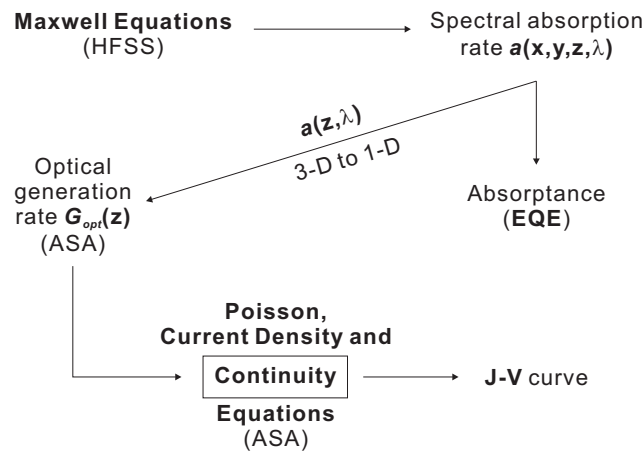
Figure 7.21: Sequence of actions binding HFSS and ASA program. 3-D spectral absorption rate from HFSS is compressed to 1-D averaged spectral absorption rate. Using Eq. 2.8, which runs inside ASA, the optical generation rate is obtained and plugged in the Continuity equation.

If ASA is used just for electronic modeling, only junction(s), boundary conditions, and external circuit settings need to be defined. Electronic parameters for a-Si:H or a-SiGe:H sub-cells were taken from [284, 285] and [286, 287], respectively, while electronic parameters of nc-Si:H sub-cells came from [197]. Density of states in a-Si:H layer and its intrinsic/doped alloys was modeled with standard parabolic conduction and valence bands, respectively followed by exponentially decaying conduction and valence band tails. In addition, two Gaussian distributions of states around the mid gap, separated from each other by correlation energy, represented defects in amorphous network. Capture cross section of electrons-holes and correlation energy in the density of states played a major role in calibrating the electrical model. The mobility gap (E_{mob}) was used to describe the band gap of involved layers, whereas in optical simulations materials were characterized by n and k data set and corresponding Tauc gap. As boundary conditions, Schottky barriers were set at both front and rear side of the junction(s) to describe the electronic behaviour of front TCO / p-layer and rear n-layer / FLiSS interfaces. Finally, realistic values of series and parallel resistances were implemented to closely fit the FF of measured solar cells. In Tab. 7.1 a description of material, thickness and E_{mob} of each layer used in modeled single, double, and triple junction *nip* solar cells is reported. A mobility gap of 1.86 eV was used for intrinsic a-Si:H, which resulted in V_{OC} around 1 V for both double and triple junction applications

Table 7.1: Description of material, thickness, and mobility gap (E_{mob}) of each layer used in modeled single, double, and triple junction solar cells.

Layer type	Material	Thickness [nm]	E_{mob} [eV]
Single junction			
p-layer	(p) nc-Si:H	10	1.2
i-layer	nc-Si:H	950+50	1.2
n-layer	(n) nc-Si:H	30	1.2
Double junction			
p-layer	(p) a-SiC:H	10	1.97
i-layer	a-Si:H	200	1.86
n-layer	(n) nc-Si:H	20	1.85
p-layer	(p) nc-Si:H	10	1.2
i-layer	nc-Si:H	550+50	1.2
n-layer	(n) nc-Si:H	30	1.2
Triple junction			
p-layer	(p) a-SiC:H	10	1.97
i-layer	a-Si:H	110	1.86
n-layer	(n) nc-Si:H	20	1.85
p-layer	(p) a-SiC:H	10	1.97
i-layer	a-SiGe:H	155	1.55
n-layer	(n) nc-Si:H	20	1.2
p-layer	(p) nc-Si:H	10	1.2
i-layer	nc-Si:H	900+50	1.2
n-layer	(n) nc-Si:H	30	1.2

[83]. This value of mobility gap, corresponding to a material which has an optical Tauc gap of 1.82 *eV* based on measured absorption, is compatible with measurements reported in [288]. Finally, to keep simple the electronic structure of the triple junction, the middle cell was simulated without the support of band gap grading technique [286].

In addition to the two solar cells simulated for validating the electrical part of the model, other three single junction devices resulting from the optimization steps were considered. Results of the electrical modeling on single junction *nip* nc-si:H solar cells are summarized in Fig. 7.22 (current density-voltage characteristics, $J-V$) and in Tab. 7.2 and 7.3 (external parameters). The short-circuit current density is basically provided by the optical generation rate (i.e. by the optical simulation), while the remaining external parameters result from electrical simulation.

Simulated flat reference and original FLiSS-based cells match very closely the measured $J-V$ curves. This result calibrated the electronic parameters describing the fabricated nc-Si:H $p-i-n$ junctions. The other three curves show that for the predicted increase of J_{SC} with respect to the original FLiSS-based cell an increase in open-circuit voltage (V_{OC}) occurs. Such trend is compatible with the following equation [91]:
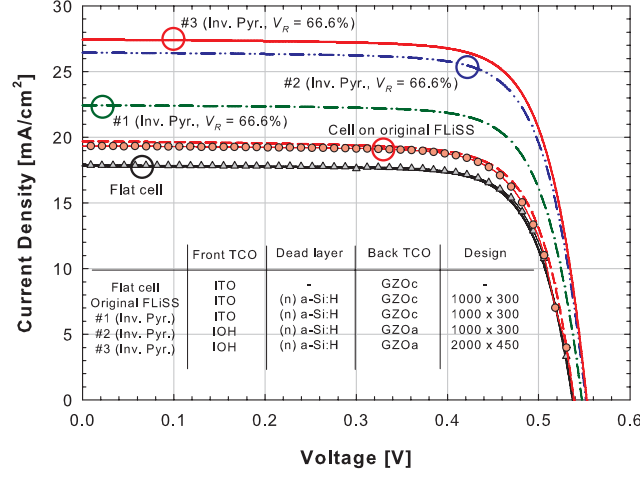
Figure 7.22: $J-V$ characteristics of five single junction nc-Si:H solar cells simulated with the coupled opto-electrical modelling. Measured $J-V$ of flat (triangles) and original FLiSS-based (circles) nip single junction nc-Si:H solar cells are compared to the simulated $J-V$ of flat cell (solid black line) and FLiSS-based cell (dashed thick red line), respectively. $J-V$ curves labeled with #1, #2, and #3 are referenced in the inset, where materials and designs of the simulated cells are reported. Inv. Pyr. text stands for inverted pyramid.

Table 7.2: External parameters of the two single junction nip nc-Si:H solar cells simulated for validation purposes.

	Flat		Original FLiSS	
	Measured	Simulated	Measured	Simulated
V_{OC} [V]	0.538	0.537	0.539	0.539
J_{SC} [mA/cm^2]	17.8	17.82	19.3	19.77
FF	0.764	0.764	0.757	0.756
η [%]	7.32	7.32	7.87	8.06

$$qV_{OC} = E_g + i_f k_B T ln\left(\frac{J_{PH}}{J_{00}}\right) \tag{7.3}$$

where i_f is the junction ideality factor ($i_f = 2$ for nc-Si:H $p-i-n$ junction [289]), k_B is the Boltzmann constant, T is the absolute temperature, J_{PH} is the photo-current density in the i-layer (with $J_{PH} = J_{SC}$), and J_{00} is an empirical pre-factor used to model the reverse saturation current density of $p-n$ [114] or $p-i-n$ junctions [289]. Considering in Tab. Tab. 7.2 and 7.3 V_{OC} and J_{SC} of the original FLiSS-based solar cell and using Eq. 7.3, J_{00} was found to be equal to 1190 mA/cm^2. Plotting V_{OC} as function of simulated J_{SC} of the four cells on FLiSS design, a reasonably good agreement between theory and simulations was found (see Fig. 7.23). Plausible values of FF were also carried out, actually slightly lower than the up-to-date record single junction *nip* nc-Si:H solar cell ($FF_{record} = 0.768$) [48].

Table 7.3: External parameters of the three optimized single junction nip nc-Si:H solar cells (#1, #2, #3).

	#1 simulated	#2 Simulated	#3 Simulated
V_{OC} [V]	0.547	0.552	0.553
J_{SC} [mA/cm^2]	22.43	26.44	27.43
FF	0.762	0.760	0.762
η [%]	9.35	11.09	11.56
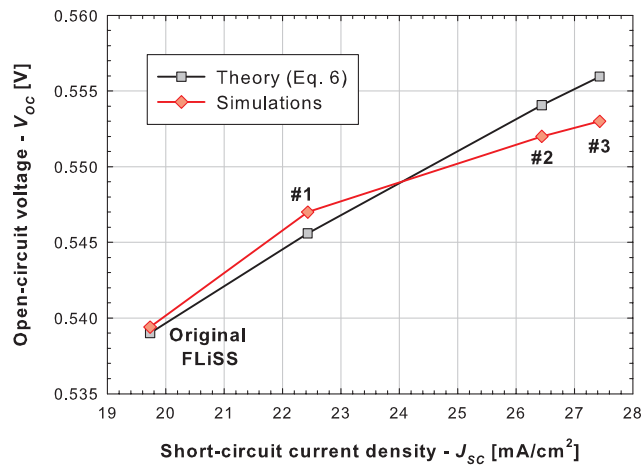
Figure 7.23: V_{OC} vs J_{SC} for the four simulated single junction nip nc-si:H solar cells on FLiSS designs.

Thanks to the increased optical performance of optimized FLiSS design and to the current-driven V_{OC} increase, a potential conversion efficiency of 11.56% for a single junction *nip* nc-Si:H (1 *μm* thick i-layer) is reported.

After modeling single junction nc-Si:H solar cells, double and triple junctions were simulated. Following the approach proposed in [197], to avoid eventual numerical instability by using the tunneling recombination junction approach [284], the sub-cells in tandem structures were simulated independently. $J-V$ characteristics of tandem cells and relative external parameters were afterwards collected by summing the current-dependent voltages of the sub-cells. Importantly, the set of electronic parameters was left untouched. Tandem devices simulated are the current-matched double and triple junction structures discussed in Sec. 7.3.7 and 7.3.8, respectively. In Tab. 7.4 and 7.5 the external parameters of tandems and of their constituting sub-cells are reported.

In both simulated tandems, sub-cells V_{OC} depends on i-layers thickness. From double to triple junction, the V_{OC} of a-Si:H top cell increases as the thickness passes from 200 *nm* to 105 *nm*. A similar effect is also noticeable from 1 *μm* thick nc-Si:H i-layer in single junctions to 600 *nm* thick nc-Si:H bottom i-layer in double junction structure. Then the V_{OC} of nc-Si:H bottom i-layer in the triple junction decreases again for 950 *nm* thickness.

Table 7.4: External parameters of the simulated double junction nip solar cell and its constituting sub-cells

	Top cell	Bottom cell	Double junction
V_{OC} [V]	0.946	0.545	1.490
J_{SC} [mA/cm^2]	12.56	12.91	12.56
FF	0.746	0.766	0.760
η [%]	8.86	5.45	14.23

Table 7.5: External parameters of the simulated triple junction nip solar cell and its constituting sub-cells

	Top cell	Middle cell	Bottom cell	Double junction
V_{OC} [V]	1.005	0.727	0.539	2.271
J_{SC} [mA/cm^2]	9.41	9.37	9.46	9.37
FF	0.749	0.751	0.766	0.753
η [%]	7.08	5.11	3.90	16.03

FF of the sub-cells inversely correlates with their band gap: for higher band gap lower *FF* is obtained. Simulated tandems express not only state-of-the-art J_{SC} but also a slightly lower *FF* with respect to maximal *FF* among relative sub-cells. This highlights, also from electrical point of the view, the current-matching achieved through the preliminary optical study. To summarize the results of the opto-electrical modeling of *nip* thin-film silicon solar cells, $J-V$ characteristics of the best single, double, and triple junction solar cells on FLiSS concept together with their potential initial conversion efficiency are presented in Fig. 24.
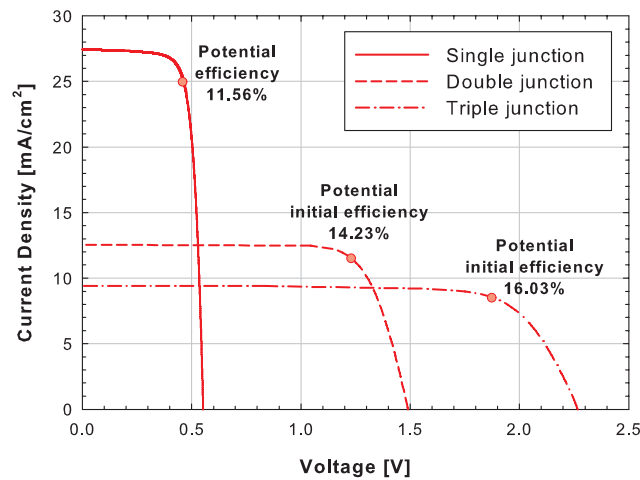

Figure 7.24: $J-V$ characteristics of the best designed thin-film silicon single, double, and triple junction nip solar cells on FLiSS concept together with their potential initial conversion efficiency.

7.4 Discussion

The transformation of 3-D spectral generation rate into 1-D dataset plays an im-portant role to obtain reliable simulations. In particular, the number of lines N (see Eq. 7.2) has to be evaluated per case. In the optimization study on FLiSS concept, it was found that N scales with the period of FLiSS (i.e. with the size of the simulated unit cell). For instance, N should be at least equal to 25 for the structure based on the original FLiSS. In fact, for N less than 25 and depending on the application coordinates of the lines, the optical absorption might be under- or over-estimated. This drawback can be avoided by choosing an even disposition of the vertical lines (i.e. no clusters of lines) and/or taking advantage of an eventual symmetry of the structure.

The application of the averaging procedure of spectral absorption rate prior to ASA simulation is well justified. Considering the original FLiSS design, a verification was done in two steps in order to check the linearity of the averaging operator. In the first step, 25 different vertical lines were evenly distributed in the simulated structure. The 25 resulting spectral absorption rates were then averaged using Eq. 7.2 and the result (the averaged 1-D spectral absorption rate) served as input to ASA to calculate a current-voltage characteristic. In the second step, 25 spectral absorption rates from the same simulated structure were exported using Eq. 7.1 and singularly used in ASA to obtain 25 corresponding current-voltage characteristics. These were afterwards averaged and the resulting single current-voltage characteristic was compared with the current-voltage characteristic obtained in the first step. An excellent matching between the two approaches was achieved.

In Fig. 7.25 one-quarter cut of double junction structure is reported. In that sketch, provided only for visualization purposes, the internal disposition of vertical lines used for calculating the averaged spectral absorption rate $a(z,\lambda)$ is depicted. All vertical lines depart from the top surface of p-layer to the bottom surface of n-layer. This is because ASA engine needs optical information only about the electronic layers involved in the structure in order to solve semiconductor equations. The length d for all vertical lines is constant, since the texturization introduced by nc-Si:H i-layer was modeled with a regular 2-D pattern of truncated pyramids. Note, however, that changing the solar cell structure (single, double, or triple junction) also the length d changes, as it is the sum of the thicknesses of all electrical layers.

The vertical lines are 100 nm apart from each other in both x- and y-directions, since this is the distance between central points of truncated pyramids flat surfaces (see Fig. 7.5). Each vertical line, containing absorption rate information for all wavelength steps, was exported from HFSS with a step of 1 nm along z-direction in order to ensure a fine sampling of the optical situation inside the solar cell. For each wavelength step, the averaging process in Eq. 7.2 averages values of spectral absorption from all the vertical lines at the same height proceeding nanometer-by-nanometer (see Fig. 7.26). The result $a(z,\lambda)$ is thus a matrix constituted by $(d+1)x91$ elements, where 91 is the number of wavelength steps used in reported simulations (from 300 nm to 1200 nm each 10 nm).

In Fig. 7.10, where the averaged spectral absorption rate is reported, narrow resonances developing throughout the i-layer were related to ripples at specific wavelengths in the si-mulated absorptance or in the measured EQE of the original FLiSS-based solar cell. In this study, devoted to the optimization of the FLiSS design, the analysis of wave-guided modes inside FLiSS-based solar cells is not done. In a future investigation, the variation of FLiSS
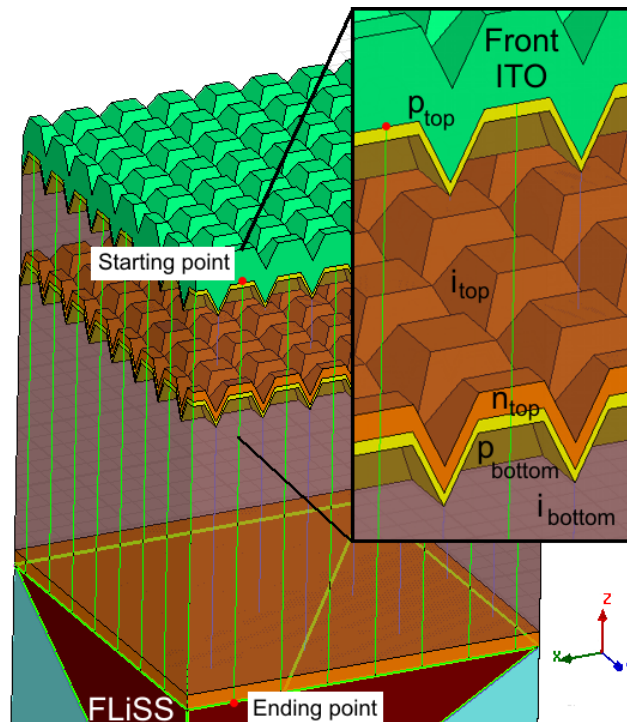
Figure 7.25: One-quarter cut of double junction structure revealing the internal disposition of vertical lines used for calculating the averaged spectral absorption rate $a(z, \lambda)$. This cut structure was not used in simulations.
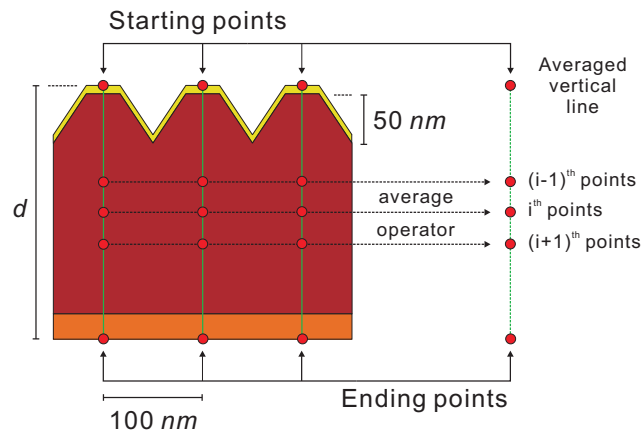
Figure 7.26: Schematic of the compression technique applied to a single junction solar cell structure. Note that vertical lines are distributed in a 3-D space like in Fig. 7.25. Here, for simplicity of representation, a simple 2-D cross section is sketched.

duty cycle, the break of symmetry in the unit cell in novel asymmetric FLiSS designs, and/or tilted external illumination can bring important insights in this attractive subject [290, 291].

In Sec. 7.3.4, the inverse version of shape (c), equivalent to GZOc inverted pyramids in dead n-type a-Si:H was not tested. The reason is that the GZOc inverted pyramids would efficiently scatter light inside the dead layer. This case would severely increase the absorption in the dead layer and reduce the internal reflectance potentially obtained by the FLiSS. With respect to the absorption in the dead layer, it was demonstrated that an unambiguous choice of materials for the FLiSS that is optimal for all different types of solar cell structures cannot be done. Depending on whether one deals with a single or multi-junction solar cell structure, the optical performance of dead layer material has to be carried out. The presented opto-electrical model is especially suitable for such optimization task, also in view of different suitable dead layer materials. For example, it has been lately shown that losses in the dead layer can be minimized by using intrinsic a-Si:H, a-SiN:H or a-SiC:H [292, 293].

The electrical simulations with the ASA program were carried out on simple flat-based solar cell structures in order to calibrate the set of electronic parameters describing the materials involved in our structures. Therefore, the insertion of intrinsic a-SiC:H buffer layer at p/i interface in the top cell or the band gap grading applied to the middle cell i-layer were not taken into account. Another aspect that was not investigated in this study was the application of doped silicon-oxide (SiO_x:H) layers [83]. Due to presence of flat interfaces in solar cells when using the FLiSS, an excellent quality of nc-Si:H layers is expected. Therefore there is no compelling need to use SiO^x:H layers to improve the resilience of nc-Si:H material against cracks and voids [97]. However, as lately shown by K. Söderström et al. [294], the implementation of SiO_x:H layers in the role of intermediate reflectors in multi-junction solar cell structures in combination with FLiSS concept could open new possibilities for performance improvement worth to be analyzed and optimized.

Finally, the reported J_{SC} values of simulated nip solar cells structures do not take into account the shadowing effect given by an eventual front grid or dead area resulting from laser scribing. Considering up-to-date industrial processes based on laser scribing for series connection, the dead area accounts for less than 5% of the total area. It depends, in fact, on the width of the cell stripe (usually 1 cm) and on the width of optimized scribing levels (generally less than 500 μm). In this respect, indicated values of short circuit current densities should be roughly decreased by 5% as well.

7.5   Conclusions

Recently developed FLiSS concept demonstrated that effective light scattering can be achieved without sacrificing nc-Si:H material quality. This investigation was aimed at finding an optimized FLiSS design, which could further improve the light scattering and minimize optical losses occurring in the back TCO and in the dead layer. Furthermore, the potential of FLiSS concept was studied when embedded in multi-junction solar cell structures not only from optical, but also from electrical point of view, assuming the high quality of nc-Si:H material grown on flattened substrate. These two goals were accomplished by means of a full-wave opto-electrical modeling that coupled FEM-based 3-D optical simulations with electrical simulations using a 1-D device solver. The optimization strategy consisted of two subsequent phases. In the first phase, the HFSS software was used to optically

study and optimize FLiSS-based single, double, and triple-junction *nip* solar cells. In the second phase, the ASA program was deployed to simulate the initial conversion efficiency of optimized FLiSS-based solar cells. Coupling between these two phases was executed by transforming the 3-D spectral absorption rate obtained from the HFSS program into 1-D average spectral generation rate that served as input for the ASA program.

In the first phase, the suitability of the optical model was demonstrated by matching the measured EQE and simulated absorptance of two solar cells, one on a flat reference substrate and one using the original FLiSS. After such verification, different shapes, materials, and geometrical parameters of the FLiSS were studied. An optimized FLiSS has the following features: 2x2 μm^2 unit cell, $h = 450$ *nm*, dead n-type a-Si:H inverted pyramid in GZOa, and $V_R = 66.6\%$. A single junction *nip* nc-Si:H solar cell with 1 μm thick (950 *nm* bulk + 50 *nm* AR element) absorber layer on the optimized FLiSS combined with low FCA front IOH resulted in an implied photo-current density of 27.4 mA/cm^2. In addition, based on optimized FLiSS shape and materials, current-matched double and triple junction solar cells were simulated with 12.6 mA/cm^2 and 9.4 mA/cm^2 implied matched photo-current density, respectively. The absorber layers of simulated multi-junction solar cells were very thin: 200 *nm* top a-Si:H / 600 *nm* bottom nc-Si:H for double junction and 105 *nm* top a-Si:H / 155 *nm* middle a-SiGe:H / 950 *nm* bottom nc-Si:H for triple junction solar cell.

After the numerical transformation of 3-D spectral absorption rate profiles into 1-D profile, the electrical model was verified by matching the measured and simulated $J - V$ characteristics of the two aforementioned reference solar cells. Then single, double, and triple junction solar cells on optimized FLiSS were simulated and the effects of enhanced current-density or absorbers thickness on open-circuit voltage were analyzed. A potential initial conversion efficiency of 11.6%, 14.2%, and 16.0% for single, double, and triple junction solar cells on the optimized FLiSS, respectively, was reported. Considering the reduced thickness of amorphous absorber layers and the expected high quality growth of nc-Si:H layer on FLiSS, these efficiencies represent a promising starting point for highly stable multi-junction thin-film silicon solar cells.

Chapter 8

General conclusions and outlook

The aim of this doctoral thesis was to investigate and deploy novel light management techniques in thin-film silicon solar cells. In this class of solar devices light absorption in the absorber layers must be enhanced to maximize the current density while the absorber layers need to be kept thin to minimize the light induced degradation effect. Such *optically thick electrically thin* trade-off for the absorber layers can be treated by implementing an efficient light trapping scheme. This is enabled by light scattering at textured interfaces together with the reflection of light at the rear side of the solar cell. In this thesis, periodic diffraction gratings and modulated surface textures were introduced as alternative ways to efficiently scatter light in single and double junction *pin* solar cells; dielectric distributed Bragg reflectors were studied as effective metal-free back reflectors in single junction flat and textured *pin* and *nip* solar cells; conductive two-dimensional flattened periodic gratings were optimized for enhanced light scattering and internal reflectance towards highly efficient single and multi-junction *nip* solar cells.

8.1 1-D periodic diffraction gratings

Transparent rectangular-like 1-D periodic gratings were used as angle-selective scattering substrates in *pin* solar cells. Fabricated in several combinations of period and height on glass sheets, these gratings were characterized from both morphological and optical perspectives. From the theory of opaque sinusoidal gratings and the Harvey-Shack scattering model for un-polarized illumination, it was found that the geometrical parameters and the shape of such gratings play a considerable role on light scattering. Recalling n_1 and n_2 as the incident and diffractive medium, respectively, the product $n_2 \cdot P$ defines the maximal wavelength for which scattering occurs; the product $2h \cdot |n_1 - n_2|$ closely approximates the wavelength at which the haze in transmission is maximized; h directly influences the intensity of light scattering; rectangular shape develops the highest haze in air; and finally $d_C = 50\%$ promotes the highest haze.

The 1-D gratings previously characterized were for the first time deployed in the fabrication of single junction a-Si:H solar cells. From SEM and AFM imaging, it was found that the subsequent deposition of front TCO, *p-i-n* junction and metallic back contact resulted in unaltered periodicity but levelling of the initial shape with features generally smoothened.

Even though grooves became shallower during the fabrication, it was demonstrated that scattering and anti-reflective effects were introduced in the absorber layer and could be made stronger by choosing deeper initial gratings. Among the fabricated devices, the best solar cell on a diffraction grating ($P = 600$ nm and $h = 300$ nm) delivered +13.4% J_{SC} with respect to the solar cell with flat interfaces and exhibited, for wavelengths longer than 550 nm, EQE slightly higher than the solar cell deposited on the reference randomly-textured substrate.

In order to optimize period and height of rectangular-like 1-D gratings and to explore the potential of 2-D gratings, a rigorous but fast 3-D optical model based on FEM was proposed. Specialized boundary conditions allowed the simulation of thin glass substrates, thus reducing drastically the simulation time to a matter of few hours. The model was validated with the reference software ASA in case of solar cell with flat interfaces on thick glass and with the measured EQE of a pin solar cell deposited on 1-D gratings and endowed with ZnO / Ag back reflector. From the latter comparison optical losses and polarization dependency could be addressed. Finally, solar cell structures on 1-D (2-D) grating textures with different periods and heights were simulated. The combination leading to the highest J_{SC} was $P = 400$ nm (500 nm) and $h = 300$ nm (450 nm), resulting in a percentage increase of +25.5% (+32.5%) more J_{SC} than in case of flat cell.

The wave guiding approach paves the way for future studies dedicated to these transparent periodic textures. Specifically, polarization-dependent and tilted incidence characterization should be carried out for a sounder understanding of light scattering performance. In this respect computer modelling can quickly provide additional data for not available textures or for newly designed gratings. From fabrication point of view, it is of key importance to reduce parasitic losses in TCO and back reflector in order to deliver state-of-the-art solar cells.

8.2   Modulated surface textures

Efficient light scattering at long wavelengths for multi-junction applications justified the study of modulated surface texturing (MST). This concept regards the combination of two or more classes of textures on the same substrate, which is capable to deliver increased broad band light scattering. By combining large surface textures with additional finer random surface features, several modulated surface textures were fabricated, characterized, modelled and used as substrates for single and double junction pin solar cells.

The development of surface modulation was demonstrated by using the spatial frequency surface representation, where the spectral content of final surface resulted to be a superposition of the constituting elements. Similarly, the improved light scattering of MSTs was modelled by superposing independent scattering mechanisms active for different feature sizes. Solar cells deposited on modulated surface-textured exhibited higher EQE with respect to conventionally textured cells due to improved anti-reflective and scattering properties.

Aside the successful realization of a MST based on 1-D gratings, other MST based on etched glass sheets or etched multi-crystalline silicon wafers, characterized by deep and large surface features, were fabricated.

MST on etched glass reported in this doctoral thesis can be classified in three types. The

first generation served as a proof of concept and to properly model the weakly wavelength dependent supporting mechanism. The second type, developed by using a sacrificial layer removal approach, showed the possibility to manipulate the surface texturing and the optical performance with sacrificial layer thickness. Such substrates were tested in single *pin* junction solar cells, which exhibited very good yield despite severe surface roughness and initial efficiency up to 9.74%. The best etched glass substrate (EG5) was afterwards applied in tandem *pin* micromorph cells in combination with 1 *μm* thick front BZO. Because of the large background textures featured by the etched glass, with respect to the flat glass / BZO (also 1 *μm* thick) based reference cell, a redistribution of light absorption between top and bottom cell occurred with a broadband increase in the (red) spectral response. Furthermore, having used thinner front TCO with respect to the flat glass / BZO (2.5 *μm* thick) second reference cell resulted in 22 *mV* higher V_{OC}. The third type, realized with a two-steps etching process, was developed to enlarge the surface facets angle distribution, recognized to have an important role in the enhancement of optical performance. The first tandem *pin* micromorph cell fabricated on a three-level MST (third generation etched glass substrate coated with a combination of IO:H and ZnO) showed bottom cell current enhancement, whereas a finer tuning of sub-cells thickness would be needed to achieve current-matching condition.

Regarding the etched multi-crystalline silicon wafers, two MST were carried out, one modulated with etched AZO and the other with self-ordered aluminium dimples. These were characterized only from morphological point of view and served as development ideas for future MSTs. Especially the one on self-ordered aluminium dimples holds an interesting potential for *nip* applications because of its surface facets angle distribution, which is the broadest among all the fabricated MSTs.

Advanced textured TCO substrates based on MST approach have recently found applications in industrial R&D products and lab-scale record tandem *pin* micromorph cells. Further developments should head towards both *nip* and *pin* technologies. The application MST concept in multi-junction *nip* cells can lead to the fabrication of thinner devices thanks to enhanced light scattering at long wavelengths. The replication of a MST on flat glass coated with low absorption front TCO in multi-junction *pin* cells can be a supplementary strategy with respect to the so-called multi-scale TCO.

8.3 Distributed Bragg reflectors

Distributed Bragg reflectors (DBR) were investigated as dielectric rear mirrors in thin-film silicon solar cells. 1-D and 3-D simulations together with measured spectra of fabricated DBRs were deployed to discuss DBRs physical properties and define practical rules for appropriate design. Main conclusion is that the choice of Bragg wavelength (λ_B) suitable for certain optical application depends only on the used materials with respect to the embedding media. If Δ_{0S} and Δ_{HL} are large around such λ_B, the number of pairs to achieve the highest reflectance is minimized and the PBG maximized. In addition, the conditions to design an omni-directional DBR or a modulated DBR were examined, being of primary importance for the fabrication of effective metal-free back reflectors. When dealing with realistic optical constants, simulated or measured reflectance spectra may deviate from the value of highest reflectance $R(\lambda_B)$ and the ideal photonic band gap. In that respect, computer simulations offer a valuable help in characterizing, designing, and optimizing DBRs

for solar cells applications.

Using a continuous RF PE-CVD process at low temperature, a DBR based on pairs of a-SiN^x:H / a-Si:H was fabricated and optically characterized. This dielectric mirror behaved in accordance with theoretical expectations thus validating the process, especially the continuous switch between one layer and another. Afterwards, the optimized design and application of such dielectric DBR in single junction thin-film silicon solar cells was also reported. Optical simulations showed that flat cells with dielectric DBR, centred at 600 nm and formed by four pairs of a-SiN^x:H / a-Si:H layers, could outperform flat devices with Al reflector. The optimal DBR was then deposited at the rear side of the BAZO layer in pin and nip flat and textured solar cells. Two photolithographic methods were developed in order to define the contact area in pin configuration. From the EQE and J-V measurements, solar cells with the DBR performed as well as the reference cells with Ag reflector.

In a future study, the omni-directionality property should be properly exploited. With a wise choice of materials, it could be possible to realize a dielectric DBR capable to compete over a very large range of wavelengths with metallic reflectors or white paints. Considering, for example, that up-to-date thin-film silicon solar cells are often terminated with n-type SiO$_x$:H layers, a viable solution might be a DBR formed by pairs of n-type a-Si:H/ZnO (see Eq. 6.11). Also the concept of modulation should be further deepened and applied in real devices, especially looking at multi-junction solar cells.

8.4 Flattened Light Scattering Substrates

The recently developed Flattened Light Scattering Substrates (FLiSS) for nip solar cells is a specialized back reflector that effectively scatters light at long wavelengths and allows depositing high quality nc-Si:H material. The FLiSS is therefore a valuable mean to decouple the electrical performance from the spectral behaviour of the cell. In its initial configuration, however, FLiSS-based solar cells do not overcome, from current density point of view, the performance of solar cells deposited on state-of-the-art back reflectors. For this reason an opto-electrical model was presented to design optimized FLiSS-based nip solar cells.

The proposed model coupled the 3-D FEM optical model previously used in Ch. 4 with the 1-D electrical model accomplished with ASA software. Key point of such coupling was the development of an algorithm that allowed transforming the 3-D spectral absorption rate from the optical simulator in a 1-D averaged spectral absorption rate to the electrical simulator. Such hybrid model was verified by matching the measured EQE and J-V curves of two single junction nip nc-Si:H real cells, one deposited on FLiSS and the other on flat GZOc / Ag back reflector.

Assessed the reliability of the model, the optimization strategy regarded mainly the study of shape, constitutive materials, and geometrical parameters of the FLiSS from optical point of view. It was found that an optimized FLiSS-based nip cell in combination with low free carrier absorption front IOH with features such as 2x2 μm^2 unit cell, $h = 450$ nm, dead n-type a-Si:H inverted pyramid in GZOa, and $V_R = 66.6\%$ exhibited an implied photo-current density of 27.4 mA/cm^2 for a 1 μm thick nc-Si:H absorber layer. Analyzing the spectral performance of such solar cell, the absorption in the i-layer for wavelengths longer than 750 nm resulted to be higher than the classical $4n^2$ limit [87] in several points. This was a remarkable achievement, given the flatness of the nc-Si:H absorber layer.

Afterwards, using the optimized FLiSS shape and materials, double and triple junction solar cells were simulated. The absorber layers were very thin: 200 *nm* top a-Si:H / 600 *nm* bottom nc-Si:H for double junction and 105 *nm* top a-Si:H / 155 *nm* middle a-SiGe:H / 950 *nm* bottom nc-Si:H for triple junction solar cell. Nevertheless, these multi-junction devices showed state-of-the-art implied photo-current densities in current-matching conditions: 12.6 mA/cm^2 and 9.4 mA/cm^2 for double and triple junction, respectively.

Using the averaged spectral absorption rates as input in the ASA program, the electrical model simulated the *J-V* characteristics of optimized devices. A potential initial conversion efficiency of 11.6%, 14.2%, and 16.0% for single, double, and triple junction solar cells on the optimized FLiSS, respectively, was reported. Considering the reduced thickness of amorphous absorber layers and the expected high quality growth of nc-Si:H layer on FLiSS, these efficiencies represent a promising starting point for highly stable multi-junction thin-film silicon solar cells.

From optical point of view, three aspects should be taken into account in a future investigation of FLiSS. Firstly, the study of FLiSS duty cycle variation, the break of symmetry in novel asymmetric FLiSS designs, and tilted external illumination can bring important insights in the analysis of wave-guided modes inside FLiSS-based solar cells. Secondly, different dead layer materials like intrinsic a-Si:H should be tested to further minimize optical losses. Finally, the implementation of (doped) SiO_x:H layers in the role of intermediate reflectors in multi-junction solar cell structures based on FLiSS should lead to improved performance and to the design of thinner devices. From electrical point of view, the insertion of intrinsic a-SiC:H buffer layer at *p/i* interface in the top and middle cells or the band gap grading applied to the middle cell i-layer should be included to model more realistic *p-i-n* top and middle junctions.

8.5 General outlook

Up-to-date record single, double and triple junction thin-film silicon solar cells have largely benefitted from both improved processing and light management techniques. In this respect, high performance TCOs, multi-junctions, intermediate reflectors, scattering at textured interfaces and efficient back reflectors are instrumental components. To further enhance the conversion efficiency of thin-film silicon solar cells, the strategy to follow is the development of a quadruple junction device [295]. This will possible only if the following challenges will be tackled in near future:

- Reduce losses in TCOs, doped layers and back reflector for further increasing the absorption in absorber layers;

- Re-think the device structure to directly expose absorber layers to the incoming light;

- Unveil the mechanisms of light induced degradation in amorphous silicon alloys for stable devices;

- Develop materials delivering high V_{OC} or exhibiting quantum effects for custom spectral use;

- Design and implement textures with *mixed* features comprising both randomness and periodicity for efficient light in-coupling and light scattering;

- Improve further deposition techniques for device quality materials and high through-put.

Bibliography

[1] W. M. Adams, *The Future of Sustainability: Re-thinking Environment and Development in the Twenty-first Century*, Report of the IUCN Renowned Thinkers Meeting, 2931 January 2006 (http://www.corriere.it).

[2] *State of the World 2009*, Worldwatch Institute, 2009 (http://www.worldwatch.org/node/5984).

[3] *2011 Global Energy Statistical Yearbook*, Enerdata, 2011 (http://www.enerdata.net/enerdatauk/press-and-publication/publications).

[4] *Worlds Worst Pollution Problems Report 2010*, Blacksmith Institute and Green Cross, 2010 (http://www.worstpolluted.org).

[5] *CO_2 Emissions from Fuel Combustion*, International Energy Agency, 2012 (http://www.iea.org/co2highlights/co2highlights.pdf).

[6] *Has the World Already Passed Peak Oil?*, National Geographic News, 9 November 2010 (http://news.nationalgeographic.com/news/energy/2010/11/101109-peak-oil-iea-world-energy-outlook/).

[7] International energy statistics webpage of U.S. Energy Information Administration (http://www.eia.gov/cfapps/ipdbproject/IEDIndex3.cfm).

[8] J. Chaves, *Introduction to Nonimaging Optics*, CRC Press, 2008 (ISBN: 978-1-420-05429-3).

[9] J. Perlin, *The Silicon Solar Cell Turns 50*, National Renewable Energy Laboratory, 2004 (http://www.nrel.gov/docs/fy04osti/33947.pdf).

[10] *Solar industry celebrates grid parity*, ABC News, 7 September 2011 (http://www.abc.net.au/news/2011-09-07/solar-industry-celebrates-grid-parity/2875592/?site=sydney).

[11] *Solar PV edging towards grid parity in Europe*, Environmental Finance, 6 September 2011 (http://www.environmental-finance.com/news/view/1959).

[12] *Creating (Not Overly) Disruptive Changes in Solar Manufacturing*, RenewableEnergy-World.com, 14 July 2009 (http://www.renewableenergyworld.com/rea/blog/post/2009/07/

creating-not-overly-disruptive-changes-in-solar-manufacturing?
cmpid=WNL-Friday-July17-2009).

[13] Abengoa Solar, 2008 (http://www.abengoasolar.com).

[14] *The Outlook for Energy: A View to 2030*, ExxonMobil Corporation, 2009 (http://www.exxonmobil.com/corporate/files/news_pub_eo_2009.pdf).

[15] *Total primary power density supply from sunlight*, Matthias Loster's website (http://www.ez2c.de/ml/solar_land_area/index.html).

[16] A. E. Becquerel, *Mmoire sur les effets lectriques produits sous l'influence des rayons solaires*, Comptes Rendus des Sances Hebdomadaires, vol. **9**, pp. 561-567, 1839.

[17] W. G. Adams and R. E. Day, *The Action of Light on Selenium*, Proceedings of the Royal Society, vol. **A25**, p. 113, 1877.

[18] C. E. Fritts, *On a New Form of Selenium Photocell*, American Journal of Science, Vol. **26**, p. 465, 1883.

[19] L. O. Grondahl, *The Copper-Cuprous-Oxide Rectifier and Photoelectric Cell*, Review of Modern Physics, vol. **5**, p. 141, 1933.

[20] L. Bergmann, *Uber eine neue Selen- Sperrschicht Photozelle*, Physikalische Zeitschrift, vol. **32**, p. 286, 1931.

[21] F. C. Nix and A. W. Treptwo, *A Thallous Sulphide Photo EMF Cell*, Journal Opt. Society of America, vol. **29**, p. 457, 1939.

[22] J. Czochralski, *Ein neues Verfahren zur Messung der Kristallisationsgeschwindigkeit der Metalle*, Zeitschrift fur Physikalische Chemie, vol. **92**, p. 219, 1917.

[23] D. C. Brock, *Useless No More: Gordon K. Teal, Germanium, and Single-Crystal Transistors*, Chemical Heritage Newsmagazine (Chemical Heritage Foundation) **24**, 1, Spring 2006.

[24] D. M. Chapin, C. S. Fuller and G. L. Pearson, *New Silicon p-n Junction Photocell for Converting Solar Radiation into Electrical Power*, Journal of Applied Physics, vol. **25**, 676, May 1954 (DOI:10.1063/1.1721711).

[25] D. C. Reynolds, G. Leies, L. L. Antes and R. E. Marburger, *Photovoltaic Effect in Cadmium Sulfide*, Physical Review, vol. **96**, p. 533, 1954.

[26] W. Shockley and H. J. Queisser, *Detailed Balance Limit of Efficiency of pn Junction Solar Cells*, Journal of Applied Physics, vol. **32**, 510, 1961 (DOI: 10.1063/1.1736034).

[27] Z. I. Alferov, V. M. Andreev, M. B. Kagan, I. I. Protasov and V. G. Trofim, *Solar-energy converters based on p-n $Al_xGa_{1-x}As - GaAs$ heterojunctions*, Soviet physics: Semiconductors, vol. **4**, p. 2047, 1971.

[28] http://www.nobelprize.org/nobel_prizes/physics/laureates/2000/alferov-lecture.pdf

[29] D. E. Carlson and C. R. wronski, *Amorphous silicon solar cell*, Applied Physics Letters, vol. **28**, p. 671, 1976 (DOI: 10.1063/1.88617).

[30] W. E. Spear and P. G. Le Comber, *Substitutional doping of amorphous silicon*, Solid State Communications, vol. **17**, Issue 9, p. 1193, 1 November 1975 (DOI: 10.1016/0038-1098(75)90284-7).

[31] A. De Vos, *Detailed balance limit of the efficiency of tandem solar cells*, Journal of Physics D: Applied Physics, vol. **13**, p. 839, 1980 (DOI: 10.1088/0022-3727/13/5/018).

[32] R. B. Hall, R. W. Birkmire, J. E. Phillips and J. D. Meakin, *Thin-film polycrystalline CdZn/S/Cu$_2$S solar cells of 10% conversion efficiency*, Photovoltaic Solar Energy Conference; Proceedings of the Third International Conference, Cannes, France, 27-31 October, 1980.

[33] A. W. Blakers and M. A. Green, *20% Efficient Silicon Solar Cell*, Applied Physics Letters, vol. **48**, p. 215, 1986 (DOI: 10.1063/1.96799).

[34] J. Yang, A. Banerjee and S. Guha, *Triple-junction amorphous silicon alloy solar cell with 14.6% initial and 13.0% stable conversion efficiencies*, Applied Physics Letters, vol. **70**, p. 2975, 1997 (DOI: 10.1063/1.118761).

[35] K. Yamamoto, M. Yoshimi, Y. Tawada, Y. Okamoto and A. Nakajima, *Thin film Si solar cell fabricated at low temperature*, Journal of Non-Crystalline Solids, vol. **266–269**, p. 1082, 2000 (DOI: 10.1016/S0022-3093(99)00907-2).

[36] J. Meier, S. Dubail, D. Fischer, J. A. Anna Selvan, N. Pellaton Vaucher, R. Platz, C. Hof, R. Flückiger, U. Kroll, N. Wÿrsch, P. Torres, H. Keppner, A. Shah and K.-D. Ufert, *The 'Micromorph' Solar Cells: a New Way to High Efficiency Thin Film Silicon Solar Cells*, Proceedings of the 13rd EC Photovoltaic Solar Energy Conference, p. 1445, Nice, France, October 1995.

[37] B. O'Regan and M Grätzel, *A low-cost, high-efficiency solar cell based on dye-sensitized colloidal TiO$_2$ films*, Nature, vol. **353**, p. 737, 24 October 1991 (DOI: 10.1038/353737a0).

[38] Renewables Global Status Report 2011 (http://www.ren21.net/Portals/97/documents/GSR/GSR2011_Master18.pdf).

[39] Web of Knowledge http://apps.webofknowledge.com (Keywords: solar cells, photovoltaic, solar energy).

[40] http://www.wipo.int/patentscope/search/en/result.jsf?topic=solar_power_materials.

[41] J. Zhao, A. Wang, M. A. Green and F. Ferrazza, *Novel 19.8% efficient honeycomb textured multicrystalline and 24.4% monocrystalline silicon solar cells*, Applied Physics Letters, vol. **73**, p. 1991, 1998 (DOI: 10.1063/1.122345).

[42] T. Kinoshita, D. Fujishima, A. Yano, A. Ogane, S. Tohoda, K. Matsuyama, Y. Nakamura, N. Tokuoka, H. Kanno, H. Sakata, M. Taguchi and E. Maruyama, *The Approaches for High Efficiency HIT^{TM} Solar Cell with Very Thin (<100 µm) Silicon Wafer over 23%*, 26th European Photovoltaic Solar Energy Conference and Exhibition, p. 871, Hamburg, Germany, September 2011 (DOI: 10.4229/26thEUPVSEC2011-2AO.2.6).

[43] O. Schultz, S. W. Glunz and G. P. Willeke, *Multicrystalline silicon solar cells exceeding 20% efficiency*, Progress in Photovoltaics: Research and Applications, vol. **12**, p. 553, 2004 (DOI: 10.1002/pip.583).

[44] C. J. Keavney, V. E. Haven and S. M. Vernon, *Emitter structures in MOCVD InP solar cells*, 21st IEEE Photovoltaic Specialists Conference, vol. **1**, p. 141, Kissimimee, U.S.A., May 1990 (DOI: 10.1109/PVSC.1990.111606).

[45] B. M. Kayes, H. Nie, R. Twist, S. G. Spruytte, F. Reinhardt, I. C. Kizilyalli and G. S. Higashi, *27.6% Conversion Efficiency, a New Record for Single-Junction Solar Cells Under 1 Sun Illumination*, 37th IEEE Photovoltaic Specialist Conference, p. 4, Seattle, U.S.A., June 2011 (DOI: 10.1109/PVSC.2011.6185831).

[46] P. Jackson, D. Hariskos, E. Lotter, S. Paetel, R. Wuerz, R. Menner, W. Wischmann, M. Powalla, *New world record efficiency for $Cu(In,Ga)Se_2$ thin-film solar cells beyond 20%*, Progress In Photovoltaics: Research and Applications, vol. **19**, p. 894, 2011 (DOI: 10.1002/pip.1078).

[47] S. Benagli, D. Borrello, E. Vallat-Sauvain, J. Meier, U. Kroll, J. Hötzel, J. Spitznagel, J. Steinhauser, L. Castens and Y. Djeridane, *High-efficiency amorphous silicon devices on LPCVD-ZnO TCO prepared in industrial KAI-M R&D reactor*, 24th European Photovoltaic Solar Energy Conference and Exhibition, p. 2293, Hamburg, Germany, September 2009 (DOI: 10.4229/24thEUPVSEC2009-3BO.9.3).

[48] K. Yamamoto, M. Yoshimi, Y. Tawada, T. Okamoto, A. Nakajima and S. Igari, *Thin film poly-Si solar cell on glass substrate fabricated at low temperature*, Applied Physics A, vol. **69**, p. 179, 1999 (DOI: 10.1007/s003390050988).

[49] http://www.kaneka-solar.com

[50] U. Kroll, J. Meier, L. Fesquet, J. Steinhauser, S. Benagli, J. B. Orhan, B. Wolf, D. Borrello, L. Castens, Y. Djeridane, X. Multone, G. Choong, D. Dominé, J.-F. Boucher, P.-A. Madliger, M. Marmelo, G. Monteduro, B. Dehbozorgi, D. Romang, E. Omnes, M. Chevalley, G. Charitat, A. Pomey, E. Vallat-Sauvain, S. Marjanovic, G. Kohnke, K. Koch, J. Liu, R. Modavis, D. Thelen, S. Vallon, A. Zakharian and D. Weidman, *Recent Developments of High-Efficiency Micromorph Tandem Solar Cells in KAI-M Plasmabox PECVD Reactors*, 26th European Photovoltaic Solar Energy Conference and Exhibition, p. 2340, Hamburg, Germany, September 2011 (DOI: 10.4229/26thEUPVSEC2011-3BO.2.6).

[51] A. Banerjee, T. Su, D. Beglau, G. Pietka, F. Liu, G. DeMaggio, S. Almutawalli, B. Yan, G. Yue, J. Yang and S. Guha, *High efficiency, multi-junction nc-Si:H based solar*

cells at high deposition rate, 37th IEEE Photovoltaic Specialist Conference, vol. **2**, p. 99, Seattle, U.S.A., June 2011(DOI: 10.1109/JPHOTOV.2011.2180892).

[52] H.-M. Lee, S.-W. Ahn, S.-E. Lee and J.-H. Choi, *Silicon thin film technology applications for low cost and high efficiency photovoltaics*, 21st International Photovoltaic Science and Engineering Conference November, 4A-2I-01, Fukuoka, Japan, December 2011.

[53] N. Koide, R. Yamanaka and H. Katayama, *Recent advances of dye-sensitized solar cells and integrated modules at SHARP*, MRS Proceedings, vol. **1211**, 2009 (DOI: 10.1557/PROC-1211-R12-02).

[54] http://www.konarka.com

[55] www.sj-solar.com

[56] *Spire pushes solar cell record to 42.3%*, Optics.org, October 2010 (http://www.spirecorp.com).

[57] J. Tang, K. W. Kemp, S. Hoogland, K. S. Jeong, H. Liu, L. Levina, M. Furukawa, X. Wang, R. Debnath, D. Cha, K. Wei Chou, A. Fischer, A. Amassian, J. B. Asbury and E. H. Sargent, *Colloidal-quantum-dot photovoltaics using atomic-ligand passivation*, Nature Materials, vol. **10**, p. 765, 2011 (DOI: 10.1038/nmat3118).

[58] A. Shalav, B. S. Richards, K. W. Krämer and H. U. Güdel, *Application of $NaYF_4$: Er^{3+} up-converting phosphors for enhanced near-infrared silicon solar cell response*, Applied Physics Letters, vol. **86**, 013505, 2005 (DOI: 10.1063/1.1844592).

[59] A. Shalav, B. S. Richards, K. W. Krämer and G. Güdel, *Improvements of an up-conversion $NaYF_4$: Er^{3+} phosphor/silicon solar cell system for an enhanced response in the near-infrared*, 31st IEEE Photovoltaic Specialist Conference, p. 114, Lake Buena Vista, U.S.A., January 2005 (DOI: 10.1109/PVSC.2005.1488082).

[60] B.S. Richard and A. Shalav, *The role of polymers in the luminescence conversion of sunlight for enhanced solar cell performance*, Synthetic Metals, vol. **154**, p. 61, 2005 (DOI: 10.1016/j.synthmet.2005.07.021).

[61] S. De Rycke, *Aliphatic polyurethane frame for solar modules*, 4th World Conference on Photovoltaic Energy Conversion, vol. **2**, p. 2172, May 2006, (DOI: 10.1109/WCPEC.2006.279936).

[62] F. Wang, R. Deng, J. Wang, Q. Wang, Y. Han, H. Zhu, X. Che and X. Liu, *Tuning upconversion through energy migration in coreshell nanoparticles*, Nature Materials, vol. **10**, p. 968, 2011 (DOI: 10.1038/nmat3149).

[63] H. A. Atwater and A. Polman, *Plasmonics for improved photovoltaic devices*, Nature Materials, vol. **9**, p. 205, 2010 (DOI: 10.1038/nmat2629).

[64] PV Status Report 2011 (http://publications.jrc.ec.europa.eu/repository/handle/111111111/22468).

[65] PV Status Report 2012 (http://www.emis.vito.be/sites/default/files/articles/1125/2012/PVReport-2012.pdf).

[66] http://pubs.usgs.gov/fs/2002/fs087-02/

[67] http://www.renewableenergyworld.com/rea/blog/post/2011/11/solar-pv-how-does-pv-work

[68] http://gigaom.com/cleantech/how-cigs-solar-thin-film-can-become-mainstream/

[69] *Nomination of Cadmium Telluride to the National Toxicology Program*, United States Department of Health and Human Services, April 2003 (http://ntp.niehs.nih.gov/ntp/htdocs/Chem_Background/ExSumPdf/CdTe.pdf).

[70] G. B. Haxel, J. B. Hedrick and G. J. Orris, *Rare Earth ElementsCritical Resources for High Technology*, U. S. Geological Survey Fact Sheet 087-02, 2002 (http://pubs.usgs.gov/fs/2002/fs087-02/).

[71] First Solar Financial Report for Quarter 3, 2011 (http://investor.firstsolar.com/financials.cfm).

[72] http://meroli.web.cern.ch/meroli/Lecture_silicon_floatzone_czochralski.html

[73] M. Zeman, *Advanced Amorphous Silicon Solar Cell Technology in Thin Film Solar Cells: Fabrication, Characterization and Applications*, eds. J. Poortmans and V. Archipov, p. 173, Wiley, Chichester, U.K., 2006 (ISBN: 978-0-470-09126-5).

[74] A. H. M. Smets and M. C. M. van de Sanden, *Relation of the Si:H stretching frequency to the nanostructural Si:H bulk environment*, Physical Review B, vol. **76**, 073202, 2007 (DOI: 10.1103/PhysRevB.76.073202).

[75] A. Morimoto, T. Kataoka and T. Shimizu, *Annealing studies on hydrogenated amorphous silicon-tin films*, Japanese Journal of Applied Physics, vol. **24**, p. 1122, 1985 (DOI: 10.1143/JJAP.24.1122).

[76] P. Buehlmann, J. Bailat, D. Dominé, A. Billet, F. Meillaud, A. Feltrin and C. Ballif, *In situ silicon oxide based intermediate reflector for thin-film silicon micromorph solar cells*, Applied Physics Letters, vol. **91**, 143505, 2007 (DOI: 10.1063/1.2794423).

[77] T. Chen, D. Yang, R. Carius and F. Finger, *Highly Conductive p-type Silicon Carbon Alloys Deposited by Hot-Wire Chemical Vapor Deposition*, Japanese Journal of Applied Physics, vol. **49**, 041303, 2010 (DOI: 10.1143/JJAP.49.041303).

[78] A. V. Shah, H. Schade, M. Vaněček, J. Meier, E. Vallat-Sauvain, N. Wÿrsch, U. Kroll, C. Droz and J. Bailat, *Thin-film silicon solar cells technology*, Progress In Photovoltaics: Research and Applications, vol. **12**, p. 113, 2004 (DOI: 10.1002/pip.533).

[79] D. L. Staebler and C. R. Wronski, *Optically induced conductivity changes in discharge produced hydrogenated amorphous silicon*, Journal of Applied Physics, vol. **51**, 3262, 1980 (DOI: 10.1063/1.328084).

[80] C. Wronski, J. Deng, X. Niu and A. H. M. Smets, *Dependence of recombination in protocrystalline a-Si:H films and cells on their different light induced gap states*, 35th IEEE Photovoltaic Specialist Conference, p. 146, Honolulu, U.S.A., June 2010 (DOI: 10.1109/PVSC.2010.5615895).

[81] H. Kakinuma, S. Nishikawa and T. Watanabe, *Thickness dependence of Staebler-Wronski effect in a-Si:H*, Journal of Non-Crystalline Solids, vol. **59-60**, p. 421, December 1983 (DOI: 10.1016/0022-3093(83)90610-5).

[82] T. Söderström, F.-J. Haug, X. Niquille, V. Terrazzoni and C. Ballif, *Asymmetric intermediate reflector for tandem Micromorph thin film silicon solar cells*, Applied Physics Letters, vol. **94**: 063501, 2009 (DOI: 10.1063/1.3079414).

[83] B. Yan, Y. Guozhen, L. Sivec, J. Yang, S. Guha and C.-S. Jiang, *Innovative dual function nc-SiOx:H layer leading to a > 16% efficient multi-junction thin-film silicon solar cell*, Applied Physics Letters, vol. **99**, 113512, 2011 (DOI: 10.1063/1.3638068).

[84] http://rredc.nrel.gov/solar/spectra/am1.5/

[85] M. A. Green, K. E, Y. Hishikawa, W. Warta and E. D. Dunlop, *Solar cell efficiency tables (Version 38)*, Progress In Photovoltaics: Research and Applications, vol. **19**, p. 565, 2011 (DOI: 10.1002/pip.1150).

[86] E. Yablonovitch and G. D. Cody, *Intensity Enhancement in Textured Optical Sheets for Solar Cells*, IEEE Transactions on Electron Devices, vol. **29**, p. 300, 1982 (DOI: 10.1109/T-ED.1982.20700).

[87] T. Tiedje, E. Yablonovitch, G. Cody and B. Brooks, *Limiting efficiency of silicon solar cells*, IEEE Transactions on Electron Devices, vol. **31**, p. 711, 1984 (DOI: 10.1109/T-ED.1984.21594).

[88] H. W. Deckmann, C. R. Wronski, H. Witzke and E. Yablonovitch, *Optically enhanced amorphous silicon solar cells*, Applied Physics Letters, vol. **42**, 968, 1983 (DOI: 10.1063/1.93817).

[89] M. Berginski, J. Hüpkes, A. Gordijn, W. Reetz, T. Wätjen, B. Rech and M. Wuttig, *Experimental studies and limitations of the light trapping and optical losses in microcrystalline silicon solar cells*, Solar Energy Materials & Solar Cells, vol. **92**, p. 1037, 2008 (DOI: 10.1016/j.solmat.2008.03.005).

[90] T. Matsui, H. Jia, M. Kondo, K. Mizuno, S. Tsuruga, S. Sakai and Y. Takeuchi, *Application of microcrystalline $Si_{1x}Ge_x$ infrared absorbers in triple junction solar cells*, 35th IEEE Photovoltaic Specialist Conference, p. 146, Honolulu, U.S.A., June 2010 (DOI: 10.1109/PVSC.2010.5615904).

[91] A. V. Shah, M. Vaněček, J. Meier, F. Meillaud, J. Guillet, D. Fischer, C. Droz, X. Niquille, S. Faÿ, E. Vallat-Sauvain, V. Terrazzoni-Daudrix and J. Bailat, *Basic efficiency limits, recent experimental results and novel light-trapping schemes in a-Si:H, μc-Si:H and micromorph tandem solar cells*, Journal of Non-Crystalline Solids, vol. **338-340**, p. 639, 2004 (DOI: 10.1016/j.jnoncrysol.2004.03.074).

[92] J. J. Hanak, *Monolithic solar cell panel of amorphous silicon*, Solar Energy, vol. **23**, p. 145, 1979 (DOI: 10.1016/0038-092X(79)90115-4).

[93] C. Battaglia, J. Escarré, K. Söderström, L. Erni, L. Ding, G. Bugnon, A. Billet, M. Boccard, L. Barraud, S. De Wolf, F.-J. Haug, M. Despeisse and C. Ballif, *Nanoimprint Lithography for High-Efficiency Thin-Film Silicon Solar Cells*, Nano Letters, vol. **11**, p. 661, 2011 (DOI: 10.1021/nl1037787).

[94] M. Python, E. Vallat-Sauvain, J. Bailat, D. Dominé, L. Fesquet, A. Shah and C. Ballif, *Relation between substrate surface morphology and microcrystalline silicon solar cell performance*, Journal of Non-Crystalline Solids, vol. **354**, p. 2258, 2008 (DOI: 10.1016/j.jnoncrysol.2007.09.084).

[95] J. Krč, F. Smole and M. Topič, *Optical simulation of the role of reflecting interlayers in tandem micromorph silicon solar cells*, Solar Energy Materials & Solar Cells, vol. **86**, p. 537, 2005 (DOI: 10.1016/j.solmat.2004.09.005).

[96] M. Ichikawa, T. Meguro, T. Suezaki, T. Kuchiyama, K. Yoshikawa and K. Yamamoto, Technical Digest of the International PVSEC-17, Fukuoka, Japan, December 2007.

[97] P. Cuony, D. T. L. Alexander, I. Perez-Wurfl, M. Despeisse, G. Bugnon, M. Boccard, T. Söderström, A. Hessler-Wyser, C. Hébert and C. Ballif, *Silicon filaments in silicon oxide for next-generation photovoltaics*, Advanced Materials, vol. **24**, p. 1182, 2012 (DOI: 10.1002/adma.201104578).

[98] O. Isabella, S. Solntsev, D. Caratelli and M. Zeman, *3-D optical modeling of single and multi-junction thin-film silicon solar cells on gratings*, MRS Proceedings, vol. **1426**, 2012 (DOI: 10.1557/opl.2012.897).

[99] A. Bielawny, J. Üpping, P. T. Miclea, R. B. Wehrspohn, C. Rockstuhl, F. Lederer, M. Peters, L. Steidl, R. Zentel, S.-M. Lee, M. Knez, A. Lambertz and R. Carius, *3D photonic crystal intermediate reflector for micromorph thin-film tandem solar cell*, Physica Status Solidi (a), vol. **205**, p. 2796, 2008 (DOI: 10.1002/pssa.200880455).

[100] M. Zeman, O. Isabella, P. Babal, A. H. M. Smets, J. Krč, *Design and integration of 1-D photonic crystals in thin-film silicon solar cells*, MRS Fall meeting, Symposium J, Boston, U.S.A., November 2011.

[101] *Thin-film photoelectric conversion device*, Kaneka patent, WO/2009/057698.

[102] A. Bielawny, C. Rockstuhl, F. Lederer and R. B. Wehrspohn, *Intermediate reflectors for enhanced top cell performance in photovoltaic thin-film tandem cells*, Optics Express, vol. **17**, p. 8439, 2009 (DOI: 10.1364/OE.17.008439).

[103] A. Barnett, D. Kirkpatrick, C. Honsberg, D. Moore, M. Wanlass, K. Emery, R. Schwartz, D. Carlson, S. Bowden, D. Aiken, A. Gray, S. Kurtz, L. Kazmerski, M. Steiner, J. Gray, T. Davenport, R. Buelow, L. Takacs, N. Shatz, J. Bortz, O. Jani, K. Goossen, F. Kiamilev, A. Doolittle, I. Ferguson, B. Unger, G. Schmidt, E. Christensen and D. Salzman, *Very High Efciency Solar Cell Modules*, Progress In Photovoltaics: Research and Applications, vol. **17**, p. 75, 2009 (DOI: 10.1002/pip.852)

[104] D. Ginley, M. A. Green and R. Collins, *Solar Energy Conversion Toward 1 Terawatt*, MRS Bulletin, vol. **33**, p. 355, 2008 (DOI: 10.1557/mrs2008.71).

[105] S. Ivanova, F. Pellé, R. Esteban, M. Laroche, J. J. Greffet, S. Collin, J. L. Pelouard and J. F. Guillemoles, *Thin Film Concepts for Photon Addition Materials*, 23rd European Photovoltaic Solar Energy Conference and Exhibition, p. 734, Valencia, Spain, September 2008 (DOI: 10.4229/23rdEUPVSEC2008-1DV.2.56).

[106] P. Löper, J.C. Goldschmidt, S. Fischer, M. Peters, A. Meijerink, D. Biner, K. Krämer, O. Schultz-Wittmann, S.W. Glunz and J. Luther, *Upconversion for Silicon Solar Cells: Material and System Characterization*, 23rd European Photovoltaic Solar Energy Conference and Exhibition, p. 173, Valencia, Spain, September 2008 (DOI: 10.4229/23rdEUPVSEC2008-1CO.3.1).

[107] G. Conibeer, R. Patterson, L. Huang, J.-F. Guillemoles, D. König, S. Shrestha and M. A. Green, *Modelling of hot carrier solar cell absorbers*, Solar Energy Materials & Solar Cells, vol. **94**, p. 1516, 2012 (DOI: 10.1016/j.solmat.2010.01.018).

[108] A. Luque, A. Martí and A. J. Nozik, *Solar cells based on quantum dots: multiple exciton generation and intermediate bands*, MRS Bulletin, vol. **32**, p. 236, 2007 (DOI: 10.1557/mrs2007.28).

[109] J. Zhu, Z. Yu, G. F. Burkhard, C.-M. Hsu, S. T. Connor, Y. Xu, Q. Wang, M. McGehee, S. Fan and Y. Cui, *Optical Absorption Enhancement in Amorphous Silicon Nanowire and Nanocone Arrays*, Nano Letters, vol. **9**, p. 279, 2009 (DOI: 10.1021/nl802886y).

[110] R. Tena-Zaera, J. Elias and C. Lévy–Clément, *ZnO nanowire arrays: Optical scattering and sensitization to solar light*, Applied Physics Letters, vol. **93**, 233119, 2008 (DOI: 10.1063/1.3040054).

[111] Z. Fan, R. Kapadia, P. W. Leu, X. Zhang, Y.-L. Chueh, K. Takei, K. Yu, A. Jamshidi, A. A. Rathore, D. J. Ruebusch, M. Wu and A. Javey, *Ordered Arrays of Dual-Diameter Nanopillars for Maximized Optical Absorption*, Nano Letters, vol. **10**, p. 3823, 2010 (DOI: 10.1021/nl1010788).

[112] M. J. Naughton, K. Kempa, Z. F. Ren, Y. Gao, J. Rybczynski, N. Argenti, W. Gao, Y. Wang, Y. Peng, J. R. Naughton, G. McMahon, T. Paudel, Y. C. Lan, M. J. Burns, A. Shepard, M. Clary, C. Ballif, F.-J. Haug, T. Söderström, O. Cubero and C. Eminian, *Efficient nanocoax-based solar cells*, Physica Status Solidi RRL, vol. **4**, p. 181, 2010 (DOI: 10.1002/pssr.201004154).

[113] M. Vaněček, O. Babchenko, A. Purkrt, J. Holovsky, N. Neykova, A. Poruba, Z. Remes, J. Meier and U. Kroll, emphNanostructured three-dimensional thin film silicon solar cells with very high efficiency potential, Applied Physics Letters, vol. **98**, 163503, 2011 (DOI: 10.1063/1.3583377).

[114] M. A. Green, *Solar Cells: Operating Principles, Technology, and System Applications*, Prentice Hall, Englewood Cliffs, U.S.A., 1981 (ISBN: 978-0-138-22270-3).

[115] J. Krč, F. Smole and M. Topič, *Advanced optical design of tandem micromorph silicon solar cells*, Journal of Non-Crystalline Solids, vol. **352**, p. 1892, 2006 (DOI: 10.1016/j.jnoncrysol.2005.12.040).

[116] T. Fujibayashi, T. Matsui and M. Kondo, *Improvement in quantum efficiency of thin film Si solar cells due to the suppression of optical reflectance at transparent conducting oxide/Si interface by TiO$_2$/ZnO antireflection coating*, Applied Physics Letters, vol. **88**, 183508, 2006 (DOI: 10.1063/1.220074).

[117] S. A. Boden and D. M. Bagnall, *Optimization of moth-eye antireflection schemes for silicon solar cells*. Progress In Photovoltaics: Research and Applications, vol. **18**, p. 195, 2010 (DOI: 10.1002/pip.951).

[118] M.-Y. Chiu, C.-H. Chang, M.-A. Tsai, F.-Y. Chang and P. Yu, *Improved optical transmission and current matching of a triple junction solar cell utilizing subwavelength antireflective structures*, Optics Express, vol. **18**, p. A308, 2010 (DOI: 10.1364/OE.18.00A308).

[119] R. Bouffaron, L. Escoubas, V. Brissonneau, J. J. Simon, G. Bergine, P. Torchio, F. Flory and P. Masclet, *Spherically shaped micro-structured antireflective surfaces*, Optics Express, vol. **17**, p. 21590, 2009 (DOI: 10.1364/OE.17.021590).

[120] J. Escarré, K. Söderström, M. Despeisse, S. Nicolay, C. Battaglia, G.Bugnon, L. Ding, F. Meillaud, F.-J. Haug and C. Ballif, *Geometric Light Trapping for High Efficiency Thin Film Silicon Solar Cells*, Solar Energy Materials & Solar Cells, vol. **98**, p. 185, 2012 (DOI: 10.1016/j.solmat.2011.10.031).

[121] H. Fujiwara and M. Kondo, *Effects of carrier concentration on the dieletric function of ZnO:Ga and In$_2$O$_3$:Sn studied by spectroscopic ellipsometry: Analysis of free-carrier and band-edge absorption*, Physical Review B, vol. **71**, 075109, 2005 (DOI: 10.1103/PhysRevB.71.075109).

[122] S. Faÿ, J. Steinhauser, N. Oliveira, E. Vallat-Sauvain and C. Ballif, *Opto-Electronic Properties of Rough LP-CVD ZnO:B for Use as TCO in Thin-Film Solar Cells*, Thin Solid Films, vol. **515**, p. 8558, 2007 (DOI: 10.1016/j.tsf.2007.03.130).

[123] T. Koida, H. Fujiwara and M. Kondo, *Hydrogen-Doped In$_2$O$_3$ as High-Mobility Transparent Conductive Oxide*, Japanese Journal of Applied Physics, vol. **46**, p. L685, 2007.

[124] M. Berginski, J. Hüpkes, W. Reetz, B. Rech and M. Wuttig, *Recent development on surface-textured ZnO:Al films prepared by sputtering for thin-film solar cell application*, Thin Solid Films, vol. **516**, p. 5836, 2008 (DOI: 10.1016/j.tsf.2007.10.029).

[125] M. Kambe, A. Takahashi, N. Taneda, K. Masumo, T. Oyama and K. Sato, *Fabrication of a-Si:H solar cells on high haze SnO$_2$:F thin films*, 33rd IEEE Photovoltaic Specialist Conference, p. 1, San Diego, U.S.A., May 2008 (DOI: 10.1109/PVSC.2008.4922507).

[126] C. Das, A. Lambertz, J. Hüpkes, W. Reetz and F. Finger, *A constructive combination of antireflection and intermediate-reflector layers for a-Si/µc-Si thin film solar cells*, Applied Physics Letters, vol. **92**, 053509, 2008 (DOI: 10.1063/1.2841824).

[127] D. Dominé P. Buehlmann, J. Bailat, A. Billet, A. Feltrin and C. Ballif, *Optical management in high-efficiency thin-film silicon micromorph solar cells with a silicon oxide based intermediate reflector*, Physica Status Solidi RRL, vol. **2**, p. 163, 2008 (DOI: 10.1002/pssr.200802118).

[128] J. Springer, A. Poruba, L. Mullerova, M. Vaněček, O. Kluth and B. Rech, *Absorption loss at nanorough silver back reflector of thin-film silicon solar cells*, Journal of Applied Physics, vol. **95**, 1427, 2004 (DOI: 10.1063/1.1633652).

[129] B. Lipovšek, J. Krč, O. Isabella, M. Zeman and M. Topič, *Modeling and optimization of white paint back reflectors for thin-film silicon solar cells*, Journal of Applied Physics, vol. **108**, 103115, 2010 (DOI: 10.1063/1.3512907).

[130] J. Meier, U. Kroll, J. Spitznagel, S. Benagli, T. Roschek, G. Pfanner, C. Ellert, G. Androutsopoulos, A. Hugli, M. Nagel, C. Bucher, L. Feitknecht, G. Buchel and A. Buchel, *Progress in up-scaling of thin film silicon solar cells by large-area PECVD KAI systems*, 31st IEEE Photovoltaic Specialist Conference, p. 1464, Lake Buena Vista, U.S.A., January 2005 (DOI: 10.1109/PVSC.2005.1488418).

[131] L. Zeng, P. Bermel, Y. Yi, B. A. Alamariu, K. A. Broderick, J. Liu, C. Hong, X. Duan, J. Joannopoulos and L. C. Kimerling, *Demonstration of enhanced absorption in thin film Si solar cells with textured photonic crystal back reflector*, Applied Physics Letters, vol. 93, 221105, 2008 (DOI: 10.1063/1.3039787).

[132] O. Isabella, B. Lipovšek, J. Krč and M. Zeman, *Photonic crystals back reflectors in thin-film silicon solar cells*, MRS Proceedings, vol. **1153**, 2009 (DOI: 10.1557/PROC-1153-A03-05).

[133] I. J. Kuzma-Filipek, F. Duerinckx, E. Van Kerschaver, K. Van Nieuwenhuysen, G. Beaucarne and J. Poortmans, *Chirped porous silicon reflectors for thin-film epitaxial silicon solar cells*, Journal of Applied Physics, vol. **104**, 073529, 2008 (DOI: 10.1063/1.2993753).

[134] H. Sai, Y. Kanamori and M. Kondo, *Flattened light-scattering substrate in thin film silicon solar cells for improved infrared response*, Applied Physics Letters, vol. **98**, 113502, 2011 (DOI: 10.1063/1.3565249).

[135] M. Zeman, O. Isabella, K. Jäger, R. Santbergen, R. Liang, S. Solntsev and J. Krč, *Advanced Light Trapping in Thin-film Silicon Solar Cells*, MRS Proceedings, vol. **1245**, 2010 (DOI: 10.1557/PROC-1245-A03-03).

[136] K. R. Catchpole and A. Polman, *Design principles for particle plasmon enhanced solar cells*, Applied Physics Letters, vol. **93**, 191113, 2008 (DOI: 10.1063/1.3021072).

[137] S. Fahr, C. Rockstuhl and F. Lederer, *Metallic nanoparticles as intermediate reflectors in tandem solar cells*, Applied Physics Letters, vol. 95, 121105, 2009 (DOI: 10.1063/1.3232230).

[138] T. L. Temple, G. D. K. Mahanama, H. S. Reehal and D. M. Bagnall, *Influence of localized surface plasmon excitation in silver nanoparticles on the performance of silicon solar cells*, Solar Energy Materials & Solar Cells, vol. **93**, p. 1978, 2009 (DOI: 10.1016/j.solmat.2009.07.014).

[139] Y. A. Akimov, W. S. Koh, S. Y. Sian and S. Ren, *Nanoparticle-enhanced thin film solar cells: Metallic or dielectric nanoparticles?*, Applied Physics Letters, vol. **96**, 073111, 2010 (DOI: 10.1063/1.3315942).

[140] E. Moulin, J. Sukmanowski, M. Schulte, A. Gordijn, F. X. Royer and Stiebig H, *Thin-film silicon solar cells with integrated silver nanoparticles*, Thin Solid Films, vol. **516**, p. 6813, 2008 (DOI: 10.1016/j.tsf.2007.12.018).

[141] V. E. Ferry, M. A. Verschuuren, H. B. T. Li, R. E. I. Schropp, H. A. Atwater and A. Polman, *Improved red-response in thin film a-Si:H solar cells with soft-imprinted plasmonic back reflectors*, Applied Physics Letters, vol. **95**, 183503, 2009 (DOI: 10.1063/1.3256187).

[142] R. Santbergen, R. Liang and M. Zeman, *A-Si:H solar cells with embedded silver nanoparticles*, 35th IEEE Photovoltaic Specialist Conference, p. 748, Honolulu, U.S.A., June 2010 (DOI: 10.1109/PVSC.2010.5617095).

[143] C. Eminian, F.-J. Haug, O. Cubero, X. Niquille and C. Ballif, *Photocurrent enhancement in thin film amorphous silicon solar cells with silver nanoparticles*, Progress in Photovoltaics: Research and Applications, vol. **19**, p. 260, 2010 (DOI: 10.1002/pip.1015).

[144] H. Tan, R. Santbergen, A. H. M. Smets and M. Zeman, *Plasmonic Light Trapping in Thin-film Silicon Solar Cells with Improved Self-Assembled Silver Nanoparticles*, Nano Letters, vol. **12**, p. 4070, 2012 (DOI: 10.1021/nl301521z).

[145] K. Sato, Y. Gotoh, Y. Wakayama, Y. Hayashi, K. Adachi and H. Nishimura, *Highly textured SnO$_2$:F TCO films for a-Si solar cells*, Reports Research Laboratory Asahi Glass, vol. **42**, p. 129, 1992.

[146] M. Berginski, J. Hüpkes, M. Schulte, G. Schöpe, H. Stiebig, B. Rech and M. Wuttig, *The effect of front ZnO:Al surface texture and optical transparency on efficient light trapping in silicon thin-film solar cells*, Journal of Applied Physics, vol. 101, 074903, 2007 (DOI: 10.1063/1.2715554).

[147] K. Wasa and S. Hayakawa, *Handbook of Sputter Deposition Technology: Principles, Technology and Applications*, Noyes Publications, Park Ridge, U.S.A., 1992 (ISBN: 978-0-815-51280-6).

[148] K. Carl, H. Schmitt and I. Friedrich, *Optimization of sputtered ITO films with respect to the oxygen partial pressure and substrate temperature*, Thin Solid Films, vol. **295**, p. 151, 1997 (DOI: 10.1016/S0040-6090(96)09167-5).

[149] J. A. Thornton, *Magnetron sputtering: basic physics and application to cylindrical magnetrons*, Journal of Vacuum Science & Technology, vol. **15**, 171, 1978 (DOI: 10.1116/1.569448).

[150] O. Kluth, G. Schöpe, J. Hüpkes, C. Agashe, J. Müller and B. Rech, *Modified Thorn-ton model for magnetron sputtered zinc oxide: film structure and etching behaviour*, Thin Solid Films, vol. **442**, p. 80, 2003 (DOI: 10.1016/S0040-6090(03)00949-0).

[151] G. van Elzakker, *Hydrogenated amorphous silicon solar cells deposited from silane diluted with hydrogen*, PhD thesis, Delft University of Technology, 2010 (ISBN: 978-90-9025532-3).

[152] S. M. Sze, *Semiconductor Devices: Physics and Technology*, John Wiley & Sons Incorporated, 2001 (ISBN: 978-0-471-33372-2)

[153] K. Jäger, M. Fischer, R. A. C. M. M. van Swaaij and M. Zeman, *A scattering model for nano-textured interfaces and its applications in opto-electrical simulations of thin-film silicon solar cells*, Journal of Applied Physics, vol. **111**, 083108, 2012 (DOI: 10.1063/1.4704372).

[154] K. Söderström, J. Escarré, O. Cubero, F.-J. Haug, S. Perregaux and C. Ballif, *UV-nano-imprint lithography technique for the replication of back reflectors for n-i-p thin film silicon solar cells*, Progress in Photovoltaics: Research and Applications, vol. **19**, p. 202, 2011 (DOI: 10.1002/pip.1003).

[155] http://gwyddion.net/documentation/

[156] P. A. van Nijnatten, *An automated directional reflectance/transmittance analyser for coating analysis*, Thin Solid Films, vol. **442**, p. 74, 2003 (DOI: 10.1016/S0040-6090(03)00947-7).

[157] K. Jäger, O. Isabella, L. Zhao and M. Zeman, *Light scattering properties of sur-face textured substrates*, Physica Status Solidi C, vol. **7**, p. 945, 2010 (DOI: 10.1002/pssc.200982695).

[158] K. Jäger, O. Isabella, R. A. C. M. M. van Swaaij and M. Zeman, *Angular resolved scattering measurements of nano-textured substrates in a broad wavelength range*, Measurement Science and Technology, vol. **22**, 105601, 2011 (DOI: 10.1088/0957-0233/22/10/105601).

[159] J. A. Sap, O. Isabella, K. Jäger and M. Zeman, *Extraction of optical properties of flat and surface-textured transparent condictive oxide films in a broad wavelength range*, Thin Solid Films, vol. **520**, p. 1096, 2011 (DOI: 10.1016/j.tsf.2011.08.023).

[160] W. Theiss, *Hard and Software for Optical Spectroscopy*, Dr.-Bernhard-Klein-Str.110, D-52078 Aachen, Germany, 2002 (http://www.wtheiss.com).

[161] S. K. O' Leary, S. R. Johnson and P. K. Lim, *The relationship between the distribution of electronic states and the optical absorption spectrum of an amorphous semicon-ductor: An empirical analysis*, Journal of Applied Physics, vol. **82**, 3334, 1997 (DOI: 10.1063/1.365643).

[162] R. Brendel and D. Bormann, *An infrared dielectric function model for amorphous solids*, Journal of Applied Physics, vol. **71**, 1, 1992 (DOI: 10.1063/1.350737).

[163] D. A. G. Bruggeman, *Berechnung verschiedener physikalischer Konstanten von heterogenen Substanzen. I. Dielektrizitätskonstanten und Leitfähigkeiten der Mischkörper aus isotropen Substanzen*, Annalen der Physik, vol. **416**, p. 636, 1935 (DOI: 10.1002/andp.19354160705).

[164] P. Drude, *Zur Elektronentheorie der Metalle*, Annalen der Physik, vol. **306**, p. 566, 1900 (DOI:: 10.1002/andp.19003060312).

[165] P. Drude, *Zur Elektronentheorie der Metalle; II. Teil. Galvanomagnetische und thermomagnetische Effecte*, Annalen der Physik, vol. **308**, p. 369, 1900 (DOI: 10.1002/andp.19003081102).

[166] H. E. Bennett and J. O. Porteus, *Relation Between Surface Roughness and Specular Reflectance at Normal Incidence*, Journal of the Optical Society of America, vol. **51**, p. 123, 1961 (DOI: 10.1364/JOSA.51.000123).

[167] C. K. Carniglia, *Scalar scattering theory for multilayer optical coatings*, Optical Engineering, vol. **18**, p. 104, 1979.

[168] N. Ehrmann and R. Reineke-Koch, *Ellipsometric studies on ZnO:Al thin films: Refinement of dispersion theories*, Thin Solid Films, vol. 519, p. 1475, 2010 (DOI: 10.1016/j.tsf.2010.09.057).

[169] A. Taflove and S. C. Hagness, *Computational Electrodynamics: The Finite Difference Time Domain Method*, 3rd ed. Artech House, Norwood, U.S.A., 2005 (ISBN: 978-1-58053-832-9).

[170] C. Haase and H. Stiebig, *Optical properties of thin-film silicon solar cells with grating couplers*, Progress in Photovoltaics: Research and Applications, vol. **14**; p. 629, 2006 (DOI: 10.1002/pip.694).

[171] R. J. Luebbers and F. Hunsberger, *FDTD for Nth-order dispersive media*, Antennas and Propagation, IEEE Transactions on, vol. **40**, p. 1297, 1992 (DOI: 10.1109/8.202707).

[172] S. Solntsev and M. Zeman, *Optical modeling of thin-film silicon solar cells with submicron periodic gratings and nonconformal layers*, Energy Procedia, vol. **10**, p. 308, 2011 (DOI: 10.1016/j.egypro.2011.10.196).

[173] T. Weiland, *A discretization model for the solution of Maxwell's equations for six-component fields*, Archiv für Elektronik und Üebertragungstechnik, vol. **31**, p. 116, 1977.

[174] S. Solntsev, O. Isabella, D. Caratelli, M. Kyriakou, O. Yarovyi and M. Zeman, *Advanced Optical Modeling of Thin-film Silicon Solar Cells with 1-D Periodic Gratings*, MRS Proceedings, vol. **1322**, 2011 (DOI: 10.1557/opl.2011.1298).

[175] M. G. Moharam and T. K. Gaylord, *Rigorous coupled-wave analysis of planar-grating diffraction*, Journal of the Optical Society of America, vol. **71**, p. 811, 1981 (DOI: 10.1364/JOSA.71.000811).

[176] A. Naqavi, K. Söderström, F.-J. Haug, V. Paeder, T. Scharf, H. P. Herzig and C. Ballif, *Understanding of photocurrent enhancement in real thin film solar cells: towards optimal one-dimensional gratings*, Optics Express, vol. **19**, p. 128, 2011 (DOI: 10.1364/OE.19.000128).

[177] M. Peters, M. Rüdiger, H. Hauser, M. Hermle and B. Bläsi, *Diffractive gratings for crystalline silicon solar cells optimum parameters and loss mechanisms*, Progress in Photovoltaics: Research and Applications, vol. **20**, p. 862, 2012 (DOI: 10.1002/pip.1151).

[178] W. C. Gibson, *The Method of Moments in Electromagnetics*, Chapman and Hall/CRC, Boca Raton, U.S.A., 2008 (ISBN: 978-1-4200-6145-1).

[179] M. Tomisawa and M. Tokuda, *Induction characteristics of a solar cell to radiated electromagnetic disturbances*, Asia-Pacific and 19th International Zurich Symposium on Electromagnetic Compatibility, p. 538, Singapore, May 2008 (DOI: 10.1109/APEMC.2008.4559931).

[180] J. A. Stratton, *Electromagnetic Theory*, IEEE Press, Piscataway, U.S.A., 2007 (ISBN: 978-0-470-13153-4).

[181] W. Ritz, *Über eine neue Methode zur Lösung gewisser Variationsprobleme der mathemati-schen Physik*, Journal für reine und angewandte Mathematik, vol. **135**; p. 1, 1909 (DOI: 10.1515/crll.1909.135.1).

[182] J. L. Volakis, A. Chatterjee and L. C. Kempel, *Finite Element Method for Electromagnetics: Antennas, Microwave Circuits, and Scattering Applications*, IEEE Press, Piscataway, U.S.A., 1998 (ISBN: 0-7803-3425-6).

[183] J. J. H. Wang, *Generalized Moment Methods in Electromagnetics*, John Wiley & Sons Incorporated, New York, U.S.A., 1991 (ISBN: 978-0471-51443-5).

[184] C. D. Meyer, *Matrix Analysis and Applied Linear Algebra*, SIAM, Philadelphia, U.S.A., 2000 (ISBN: 0-89871-454-0).

[185] Y. Saad, *Iterative Methods for Sparse Linear Systems*, 2nd ed. SIAM, Philadelphia, U.S.A., 2003 (ISBN: 978-0-898715-34-7).

[186] S. Nagakura, S. Noguchi, H. Yamashita and V. Cingoski, *Automatic hexahedral mesh generation for FEM using shape recognition technique and tree method*, IEEE Transactions on Magnetics, vol. **38**, p. 417, 2002 (DOI: 10.1109/20.996111).

[187] K. Yee, *Numerical solution of initial boundary value problems involving Maxwells equations*, IEEE Transactions on Antennas Propagation, vol. **14**, p. 302, 1966 (DOI: 10.1109/TAP.1966.1138693).

[188] D. B. Davidson, *Computational Electromagnetics for RF and Microwave Engineering*, Cambridge University Press, Cambridge, U.K., 2005 (ISBN: 978-0-521-51891-8).

[189] COMSOL official website: http://www.comsol.com/products/multiphysics/

[190] J. C. C. Fan, *Theoretical temperature dependence of solar cell parameters*, Solar Cells, vol. **17**; p. 309, 1986 (DOI: 10.1016/0379-6787(86)90020-7).

[191] B. Lipovšek, M. Cvek, A. Čampa, J. Krč and M. Topič, *Analysis and Optimisation of Periodic Interface Textures in Thin-Film Silicon Solar Cells*, 25th European Photovoltaic Solar Energy Conference and Exhibition, p. 3120, Valencia, Spain, September 2010 (DOI: 10.4229/25thEUPVSEC2010-3AV.1.81).

[192] White papers in Ansys HFSS official website (http://www.ansoft.com/products/hf/ hfss/)

[193] G. Gentile, R. Dekker, P. de Graaf, M. Spirito, M. J. Pelk, L. C. N. de Vreede and B. Rejaei Salmassi, *Silicon Filled Integrated Waveguides*, IEEE Microwave and Wireless Components Letters, vol. **20**, p. 536, 2010 (DOI: 10.1109/LMWC.2010.2063420).

[194] A. M. K. Dagamseh, B. Vet, P. Šutta and M. Zeman, *Modelling and optimization of a-Si:H solar cells with ZnO:Al back reflector*, Solar Energy Materials & Solar Cells, vol. **94**, p. 2119, 2010 (DOI: 10.1016/j.solmat.2010.06.039).

[195] B. E. Pieters, H. Stiebig, M. Zeman, and R. A. C. M. M. van Swaaij, *Determination of the mobility gap of intrinsic μc-Si:H in p-i-n solar cells*, Journal of Applied Physics, vol. **105**, 044502, 2009 (DOI: 10.1063/1.3078044).

[196] M. Zeman, O. Isabella, K. Jäger, P. Babal, S. Solntsev, R. Santbergen, *Modeling of Advanced Light Trapping Approaches in Thin-Film Silicon Solar Cells*, MRS Proceedings, vol. **1321**, 2011 (DOI: 10.1557/opl.2011.955).

[197] K. Ding, T. Kirchartz, B. E. Pieters, C. Ulbrich, A. M. Ermes, S. Schicho, A. Lambertz, R. Carius and U. Rau, *Characterization and simulation of a-Si:H/μc-Si:H tandem solar cells*, Solar Energy Materials & Solar Cells, vol. **95**, p. 3318, 2011 (DOI: 10.1016/j.solmat.2011.07.023).

[198] S. Selberherr, *Analysis and Simulation of Semiconductor Devices*, Springer-Verlag, Vienna, Austria, 1984 (ISBN: 3-211-81800-6).

[199] H. K. Gummel, *A self-consistent iterative scheme for one-dimensional steady state transistor calculations*, IEEE Transaction on Electron Devices, vol. **11**, p. 455, 1964 (DOI: 10.1109/T-ED.1964.15364).

[200] J. Krč, M. Zeman, A. Čampa, F. Smole and M. Topič, *Novel approaches of light management in thin-film silicon solar cells*, MRS Proceedings, vol. **910**, 2006 (DOI: /10.1557/PROC-0910-A25-01).

[201] A. Čampa, O. Isabella, R. van Erven, P. Peeters, H. Borg, J. Krč, M. Topič and M. Zeman, *Optimal design of periodic surface texture for thin-film a-Si:H solar cells*, Progress in Photovoltaics: Research and Applications, vol. **18**, p. 160, 2010 (DOI: 10.1002/pip.940).

[202] A. Čampa, J. Krč and M. Topič, *Analysis and optimisation of microcrystalline silicon solar cells with periodic sinusoidal textured interfaces by two-dimensional optical simulations*, Journal of Applied Physics, vol. **105**, 083107, 2009 (DOI: 10.1063/1.3115408).

[203] S. Solntsev, O. Isabella, D. Caratelli and M. Zeman, *Thin-film silicon solar cells on 1-D periodic gratings with non-conformal layers: optical analysis*, IEEE Journal of Photovoltaics, vol. **3**, p. 46, 2012 (DOI: 10.1109/JPHOTOV.2012.2220123).

[204] H. Stiebig, C. Haase, C. Zahren, B. Rech and N. Senoussaoui, *Thin-film silicon solar cells with grating couplers An experimental and numerical study*, Journal of Non-Crystalline Solids, vol. **352**, p. 1949, 2006 (DOI: 10.1016/j.jnoncrysol.2006.01.072).

[205] O. Isabella, A. Čampa, M. Heijna, W. J. Soppe, R. van Erven, R. H. Franken, H. Borg and M. Zeman, *Diffraction gratings for light trapping in thin-film silicon solar cells*, 23rd European Photovoltaic Solar Energy Conference and Exhibition, p. 2320, Valencia, Spain, September 2008 (DOI: 10.4229/23rdEUPVSEC2008-3AV.1.48).

[206] C. Battaglia, C.-M. Hsu, K. Söderström, J. Escarré, F.-J. Haug, M. Charriere, M. Boccard, M. Despeisse, D. T. L. Alexander, M. Cantoni, Y. Cui and C. Ballif, *Light Trapping in Solar Cells: Can Periodic Beat Random*?, ACS Nano, vol. **6**, p. 2790, 2012 (DOI: 10.1021/nn300287j).

[207] A. J. M. van Erven, M. Steltenpool, J. Rutten, G. van der Hofstad, H. de Groot, J. de Ruijter, M. Bos, B. Titulaer and G. Rajeswaran, *Periodically textured glass for 20% bottom cell current increase in a-Si:H/μc-Si:H tandem solar cells*, 37th IEEE Photovoltaic Specialist Conference, p. 686, Seattle, U.S.A., June 2011 (DOI: 10.1109/PVSC.2011.6186046).

[208] T. Söderström, F.-J. Haug, X. Niquille and C. Ballif, *TCOs for Nip Thin Film Silicon Solar Cells*, Progress in Photovoltaics: Research and Applications, vol. **17**, p. 165, 2009 (DOI: 10.1002/pip.869).

[209] R. Biswas and C. Xu, *Nano-crystalline silicon solar cell architecture with absorption at the classical $4n^2$ limit*, Optics Express, vol. **19**, p. A664, 2011 (DOI: 10.1364/OE.19.00A664).

[210] T. Söderström, F.-J. Haug, V. Terrazzoni-Daudrix and C. Ballif, *Flexible micromorph tandem a-Si/μc-Si solar cells*, Journal of Applied Physics, vol. **107**, 014507, 2010 (DOI: 10.1063/1.3275860).

[211] F.-J. Haug, T. Söderström, O. Cubero, V. Terrazzoni-Daudrix and C. Ballif, *Influence of the ZnO buffer on the guided mode structure in Si/ZnO/Ag multilayers*, Journal of Applied Physics, vol. **106**, 044502, 2009 (DOI: 10.1063/1.3203937).

[212] F.-J. Haug, K. Söderström, A. Naqvi and C. Ballif, *Excitation of guided-mode resonances in thin film silicon solar cells*, MRS Proceedings, vol. **1321**, 2011 (DOI: 10.1557/opl.2011.946).

[213] Z. Yu, A. Raman and S. Fan, *Fundamental limit of light trapping in grating structures*, Optics Express, vol. **18**, p. A366, 2010 (DOI: 10.1364/OE.18.00A366).

[214] K. Söderström, F.-J. Haug, J. Escarré, O. Cubero and C. Ballif, *Photocurrent increase in n-i-p thin film silicon solar cells by guided mode excitation via grating coupler*, Applied Physics Letters, vol. **96**, 213508, 2010 (DOI: 10.1063/1.3435481).

[215] F.-J. Haug, K. Söderström, A. Naqavi and C. Ballif, *Resonances and absorption enhancement in thin film silicon solar cells with periodic interface texture*, Journal of Applied Physics, vol. **109**, 084516, 2011 (DOI: 10.1063/1.3569689).

[216] K. Söderström, F.-J. Haug, C. Pahud, R. Biron, J. Escarré, M. Duchamp, R. Dunin-Borkowski and C. Ballif, *Reflectance Improvement by Thermal Annealing of Sputtered Ag/ZnO Back Reflectors in a-Si:H Thin Film Silicon Solar Cells*, MRS Proceedings, vol. **1321**, 2011 (DOI: 10.1557/opl.2011.812).

[217] J. Bhattacharya, N. Chakravarty, S. Pattnaik, W. D. Slafer, R. Biswas and V. Dalal, *Comparison of optical properties of periodic photonicplasmonic and randomly textured back reflectors for nc-Si solar cells*, Journal of Non-Crystalline Solids, vol. **358**, p. 2313, 2012 (DOI: 10.1016/j.jnoncrysol.2011.12.108).

[218] K. Jäger, M. Fischer, R. A. C. M. M. van Swaaij and M. Zeman, *An Algorithm for Finding Optimized Interface Morphologies in Thin Film Silicon Solar Cells*, MRS Proceedings, vol. **1426**, 2012 (DOI: 10.1557/opl.2012.886).

[219] F.-J. Haug, K. Söderström, A. Naqavi, C. Battaglia and C. Ballif, *Excitation of plasmon and guided-mode resonances in thin film silicon solar cells*, MRS Proceedings, vol. **1391**, 2012 (DOI: 10.1557/opl.2012.494.)

[220] http://www.blu-raydisc.com/Assets/Downloadablefile/
BD-ROMwhitepaper20070308-15270.pdf

[221] P. Beckmann and A. Spizzichino, *The Scattering of Electromagnetic Waves from Rough Surfaces*, Artech House, Norwood, U.S.A., 1987 (ISBN: 978-0-890-06238-8).

[222] F.-J. Haug, T. Söderström, O. Cubero, V. Terrazzoni-Daudrix, X. Niquille, S. Perregaux and C. Ballif, *Periodic textures for enhanced current in thin film silicon solar cells*, MRS proceedings, vol. **1101**, 2008 (DOI: 10.1557/PROC-1101-KK13-01).

[223] J. E. Harvey and A. Krywonos, *A Global View of Diffraction: Revisited*, Proceedings SPIE, AM100-26, 2004 (http://imaging.creol.ucf.edu/publications/102%20SPIE%20AM100-26.pdf).

[224] F.-J. Haug, A. Naqavi and C. Ballif, *Diffraction and absorption enhancement from textured back reflectors of thin film solar cells*, Journal of Applied Physics, vol. **112**, 024516, 2012 (DOI: 10.1063/1.4737606).

[225] D. Dominé, F.-J. Haug, C. Battaglia and C. Ballif, *Modeling of light scattering from micro- and nanotextured surfaces*, Journal of Applied Physics, vol. **107**, 044504, 2010 (DOI: 10.1063/1.3295902).

[226] M. Kubon, E. Boehmer, F. Siebke, B. Rech, C. Beneking and H. Wagner, *Solution of the ZnO/p contact problem in a-Si:H solar cells*, Solar Energy Materials & Solar Cells, vol. **41–42**, p. 485, 1996 (DOI: 10.1016/0927-0248(95)00126-3).

[227] C. Heine and R. H. Morf, *Submicrometer gratings for solar energy applications*, Applied Optics, vol. **34**, p. 2476, 1995 (DOI: 10.1364/AO.34.002476).

[228] R. H. Morf, *Exponentially convergent numerically efficient solution of Maxwell's equations for lamellar gratings*, Journal of the Optical Society of America A, vol. **12**, p. 1043, 1995 (DOI: 10.1364/JOSAA.12.001043).

[229] J.-M. Jin, *The Finite Element Method in Electromagnetics*, 2nd ed. John Wiley & Sons Incorporated, New York, U.S.A., 2002 (ISBN: 978-0-471-43818-2).

[230] Ansys HFSS official website: http://www.ansoft.com/products/hf/hfss/

[231] P. W. Milonni and J. H. Eberly, *Lasers*, John Wiley & Sons Incorporated, New York, U.S.A., 1988 (ISBN: 978-047162-731-90.

[232] L. Ley, *Photoemission and Optical Properties*, in *The Physics of Hydrogenated Amorphous Silicon II*, Topics in Applied Physics, Springer-Verlag, Vienna, Austria, 1984 (DOI: 978-3-540-12808-3).

[233] I. Bardi, R. Remski, D. Perry and Z. Cendes, *Plane wave scattering from frequency-selective surfaces by the finite-element method*, IEEE Transactions on Magnetics, vol. **38**, p. 641, 2002 (DOI: 10.1109/20.996167).

[234] D. Kröner, *Absorbing boundary conditions for the linearized Euler equations in 2-d*, Mathematics of Computation, vol. **57**, p. 153, 1991 (DOI: 10.1090/S0025-5718-1991-1079023-0).

[235] Ansys HFSS 12, HFSS online help, Technical notes.

[236] G. Gonzalez, *Microwave transistor amplifiers analysis and design*, 2nd ed. Prentice Hall, Upper Saddle River, U.S.A., 1997 (ISBN: 978-13581-646-2).

[237] V. E. Ferry, M. A. Verschuuren, H. B. T. Li, E. Verhagen, R. J. Walters, R. E. I. Schropp, H. A. Atwater and A. Polman, *Light trapping in ultrathin plasmonic solar cells*, Optics Express, vol. **18**, p. A237, 2010 (DOI: 10.1364/OE.18.00A237).

[238] C. Pflaum, C. Haase, H. Stiebig and C. Jandl, *Simulation of Light In-Coupling at Oblique Angles in Thin-Film Silicon Solar Cells*, 24th European Photovoltaic Solar Energy Conference and Exhibition, p. 2310, Hamburg, Germany, September 2009 (DOI: 10.4229/24thEUPVSEC2009-3BO.9.6).

[239] C. Jandl, K. Hertel, C. Pflaum and Helmut Stiebig, *Simulation of silicon thin-film solar cells for oblique incident waves*, Proceedings SPIE 8065, 2011 (DOI: 10.1117/12.882860).

[240] S. Faÿ, S. Dubail, U. Kroll, J. Meier, Y. Ziegler and A. Shah, 16th European Photovoltaic Solar Energy Conference and Exhibition, p. 361, Glasgow, September 2000.

[241] O. Kluth, B. Rech, L. Houben, S. Wieder, G. Schöpe, C. Beneking, H. Wagner, A. Löffl and H. W. Schock, *Texture etched ZnO:Al coated glass substrates for silicon based thin film solar cells*, Thin Solid Films, vol. **351**, p. 247, 1999 (DOI: 10.1016/S0040-6090(99)00085-1).

[242] A. Hongsingthong, T. Krajangsang, I. A. Yunaz, S. Miyajima and M. Konagai, *ZnO Films with Very High Haze Value for Use as Front Transparent Conductive Oxide Films in Thin-Film Silicon Solar Cells*, Applied Physics Express, vol. **3**, 51102, 2010 (DOI: 10.1143/APEX.3.051102).

[243] S. Faÿ, J. Steinhauser, S. Nicolay and C. Ballif, *Polycrystalline ZnO:B grown by LPCVD as TCO for thin film silicon solar cells*, Thin Solid Films, vol. **518**, p. 2961, 2010 (DOI: 10.1016/j.tsf.2009.09.189).

[244] C. Battaglia, L. Erni, M. Boccard, L. Barraud, J. Escarré, K. Söderström, G. Bugnon, A. Billet, L. Ding, M. Despeisse, F.-J. Haug, S. De Wolf and Christophe Ballif, *Micromorph thin-film silicon solar cells with transparent high-mobility hydrogenated indium oxide front electrodes*, Journal of Applied Physics, vol. **109**, 114501, 2011 (DOI: 10.1063/1.3592885).

[245] J. Wang, S. Venkataraj, P. Vayalakkara and A. G. Aberle, *Analysis of optical and structural properties of AIT (Aluminum Induced Texture) glass*, 21st International Photovoltaic Science and Engineering Conference November, 4A-2O-11, Fukuoka, Japan, December 2011.

[246] O. Isabella, P. Liu, B. Bolman, J. Krč, A. H. M. Smets and M. Zeman, *Modulated surface-textured substrates with high haze: From concept to application in thin-film silicon solar cells*, 37th IEEE Photovoltaic Specialist Conference, p. 616, Seattle, U.S.A., June 2011 (DOI: 10.1109/PVSC.2011.6186029).

[247] P. I. Widenborg and Armin G. Aberle, *Polycrystalline Silicon Thin-Film Solar Cells on AIT-Textured Glass Superstrates*, Advances in OptoElectronics, vol. **2007**, 24584, 2007 (DOI: 10.1155/2007/24584).

[248] *Photovoltaic cell front face substrate and use of a substrate for a photovoltaic cell front face*, Saint-Gobain Glass France patent, WO/2009/019401A2.

[249] R. van Erven, R.H. Franken, J. de Ruijter, P. Peeters, W. Vugts, O. Isabella, M. Zeman, C. Haase, U. Rau and H. Borg, *Controlled Texturing of Thin Film Silicon Solar Cell Substrates*, 23rd European Photovoltaic Solar Energy Conference and Exhibition, p. 2096, Valencia, Spain, September 2008 (DOI:10.4229/23rdEUPVSEC2008-3CO.9.4).

[250] C. Battaglia, J. Escarré, K. Söderström, M. Charriére, M. Despeisse, F.-J. Haug and C. Ballif, *Nanomoulding of transparent zinc oxide electrodes for efficient light trapping in solar cells*, Nature Photonics, vol. **5**, p. 535, 2011 (DOI: 10.1038/nphoton.2011.198).

[251] J. M. Bennett and L. Mattson, *Introduction to Surface Roughness and Scattering*, Optical Society of America, Washington D.C., U.S.A., 1989 (ISBN: 978-1-557-52108-8).

[252] S. Winograd, *On computing the Discrete Fourier Transform*, Mathematics of Computation, vol. **32**, p. 175, 1978 (DOI: 10.1090/S0025-5718-1978-0468306-4).

[253] J. W. Tukey, *An introduction to the calculations of numerical spectrum analysis* in *Spectral Analysis of Time Series*, Wiley, New York, U.S.A., 1967.

[254] A. V. Oppenheimer and R. W. Shaffer, *Digital Signal Processing*, Prentice-Hall, Englewood Cliffs, U.S.A., 1975 (ISBN: 978-0-132-14635-7).

[255] G. Mie, *Beiträge zur Optik trüber Medien, speziell kolloidaler Metallösungen*, Annalen der Physik, vol. **330**, p. 377, 1908 (DOI: 10.1002/andp.19083300302).

[256] J. O' Dowd, *A model for light scattering by rough tin oxide*, Solar Energy Materials, vol. **16**, p. 383, 1987 (DOI: 10.1016/0165-1633(87)90032-3).

[257] H. Schade and Z. E. Smith, *Mie scattering and rough surfaces*, Applied Optics, vol. **24**, p. 3221, 1985 (DOI: 10.1364/AO.24.003221).

[258] C. F. Bohren and D. R. Huffmann, *Absorption and scattering of light by small particles*, Wiley-Interscience, New York, 1983 (ISBN: 978-0-471-29340-8).

[259] P. Laven, *Simulation of rainbows, coronas, and glories by use of Mie theory*, Applied Optics, vol. **42**, p. 436, 2003 (DOI: 10.1364/AO.42.000436)

[260] J. Krč, M. Zeman, O. Kluth, F. Smole and M. Topič, *Effect of surface roughness of ZnO:Al films on light scattering in hydrogenated amorphous silicon solar cells*, Thin Solid Films, vol. **426**, p. 296, 2003 (DOI: 10.1016/S0040-6090(03)00006-3).

[261] O. Kluth, A. Loffl, S. Wieder, C. Beneking, W. Appenzeller, L. Houben, B. Rech, H. Wagner, S. Hoffmann, R. Waser, J. A. Anna Selvan and H. Keppnet, *Texture etched Al-doped ZnO: a new material for enhanced light trapping in thin film solar cells*, 26th IEEE Photovoltaic Specialist Conference, p. 715, Anaheim, U.S.A., October 1997 (DOI: 10.1109/PVSC.1997.654189).

[262] H. Sai, H. Fujiwara and M. Kondo, *Back surface reflectors with periodic textures fabricated by self-ordering process for light trapping in thin-film microcrystalline silicon solar cells*, Solar Energy Materials & Solar Cells, vol. **93**, p. 1087, 2009 (DOI: 10.1016/j.solmat.2008.12.030).

[263] M. Boccard, C. Battaglia, S. Hänni, K. Söderström, J. Escarré, S. Nicolay, F. Meillaud, M. Despeisse and C. Ballif, *Multiscale Transparent Electrode Architecture for Efficient Light Management and Carrier Collection in Solar Cells*, Nano Letters, vol. **12**, p. 1344, 2012 (DOI: 10.1021/nl203909u).

[264] J. W. Strutt, *On the maintenance of vibrations by forces of double frequency, and on the propagation of waves through a medium endowed with a periodic structure*, Philosophical Magazine, vol. **24**, p. 1, 1887 (DOI: 10.1017/CBO9780511703980).

[265] J. W. Strutt, *On the remarkable phenomenon of crystalline reflexion described by Prof. Stokes*, Philosophical Magazine, vol. **26**, p. 256, 1888 (DOI: 10.1017/CBO9780511703980.010).

[266] J. D. Joannopoulos, S. G. Johnson, J. N. Winn and R. D. Meade, *Photonic Crystals: Molding the Flow of Light*, 2nd edition, Princeton University Press, Princeton, U.S.A., 2008 (ISBN: 978-0-691-12456-8).

[267] E. Yablonovitch and T.J. Gmitter, *Photonic band structure: The face-centered-cubic case*, Physical Review Letters, vol. **63**, p. 1950, 1989 (DOI: 10.1103/Phys-RevLett.63.1950).

[268] E. Yablonovitch, *Photonic Crystals: What's in a name?*, Optics and Photonics, March 2007 (http://www.osa-opn.org/home/articles/volume_18/issue_3/departments/light_touch/photonic_crystals_what%E2%80%99s_in_a_name/#.UOhYjW9X3HQ).

[269] C. Ulbrich, M. Peters, B. Bläsi, T. Kirchartz, A. Gerber and Uwe Rau, *Enhanced light trapping in thin-film solar cells by a directionally selective filter*, Optics Express, vol. **18**, p. A133, 2010 (DOI: 10.1364/OE.18.00A133).

[270] M. Tucci, L. Serenelli, E. Salza, L. Pirozzi, G. De Cesare, D. Caputo and M. Ceccarelli, *Bragg reflector and laser fired back contact in a-Si:H/c-Si heterostructure solar cell*, Materials Science and Engineering B, vol. **159-160**, p. 48, 2009 (DOI: 10.1016/j.mseb.2008.09.026).

[271] P. Bermel, C. Luo, L. Zeng, L. C. Kimerling and J. D. Joannopoulos, *Improving thin-film crystalline silicon solar cell efficiencies with photonic crystals*, Optics Express, vol. **15**, p. 16986, 2007 (DOI: 10.1364/OE.15.016986).

[272] L. Zeng, Y. Yi, C. Hong, J. Liu, N. Feng, X. Duan, L. C. Kimerling and B. A. Alamariu, *Efficiency enhancement in Si solar cells by textured photonic crystal back reflector*, Applied Physics Letters, vol. **89**, 111111, 2006 (DOI: 10.1063/1.2349845).

[273] J. Krč, M. Zeman, S. Luxembourg and M. Topič, *Modulated photonic-crystal structures as broadband back reflectors in thin-film solar cells*, Applied Physics Letters, vol. 94, 153501, 2009 (DOI: 10.1063/1.3109781).

[274] C. J. R. Sheppard, *Approximate calculation of the reflection coefficient from a stratified medium*, Pure and Applied Optics, vol. **4**, p. 665, 1995 (DOI: 10.1088/0963-9659/4/5/018).

[275] S. J. Orfanidis, *Electromagnetic Waves and Antennas*, Rutgers University, New Brunswick, U.S.A., 2010 (www.ece.rutgers.edu/~orfanidi/ewa).

[276] W. H. Southwell, *Omnidirectional mirror design with quarter-wave dielectric stacks*, Applied Optics, vol. **38**, p. 5464, 1999 (DOI: 10.1364/AO.38.005464).

[277] C.-J. Wu, B.-H. Chu, M.-T. Weng and H.-L. Lee, *Enhancement of Bandwidth in a Chirped Quarter-Wave Dielectric Mirror*, Journal of Electromagnetic Waves and Applications, vol. **23**, p. 437, 2009 (DOI: 10.1163/156939309787612365).

[278] A. Yariv and P. Yeh, *Photonics: Optical Electronics in Modern Communications (The Oxford Series in Electrical and Computer Engineering)*, 6th edition, Oxford University Press, U.S.A., 2006 (ISBN: 978-0-195-17946-0).

[279] M. Patrini, M. Galli, M. Belotti, L. C. Andreani, G. Guizzetti, G. Pucker, A. Lui, P. Bellutti and L. Pavesi, *Optical response of one-dimensional* $(Si/SiO_2)_m$ *photonic crystals*, Journal of Applied Physics, vol. **92**, 1816, 2002 (DOI: 10.1063/1.1492866).

[280] G. Panzarini, L. C. Andreani, A. Armitage, D. Baxter, M. S. Skolnick, V. N. Astratov, J. S. Roberts, A. V. Kavokin, M. R. Vladimirova and M. A. Kaliteevski, *Exciton-light coupling in single and coupled semiconductor cavities: polariton dispersion and polarization splitting*, Physics of the Solid State, vol. **41**, p. 1223, 1999 (DOI: 10.1134/1.1130973).

[281] Y. Fink, J. N. Winn, S. Fan, C. Chen, J. Michel, J. D. Joannopoulos and E. L. Thomas, *A Dielectric Omnidirectional Reflector*, Science, vol. **282**, p. 1679, 1998 (10.1126/science.282.5394.1679).

[282] D. N. Chigrin, A. V. Lavrinenko, D. A. Yarotsky and S. V. Gaponenko, *Observation of Total Omnidirectional Reflection from a One-Dimensional Dielectric Lattice*, Applied Physics A, vol. **68**, p. 25, 1999 (DOI: 10.1007/s003390050849).

[283] R. Biron, S. Hänni, M. Boccard, C. Pahud, G. Bugnon, L. Ding, S. Nicolay, G. Parascandolo, F. Meillaud, M. Despeisse, F.-J. Haug and C. Ballif, *Optimization of the asymmetric intermediate reflector morphology for high stabilized efficiency thin n-i-p micromorph solar cells*, IEEE Journal of Photovoltaics, vol. **3**, p. 41, 2013 (DOI: 10.1109/JPHOTOV.2012.2219502).

[284] M. Zeman, J. A. Willemen, L. L. A. Vosteen, G. Tao and J. W. Metselaar, *Computer modelling of current matching in a-Si:H/a-Si:H tandem solar cells on textured TCO substrates*, Solar Energy Materials & Solar Cells, vol. **46**, p. 81-99, 1997 (DOI: 10.1016/S0927-0248(96)00094-3).

[285] B. Vet and M. Zeman, *Sensitivity study of model parameters for high-efficient amorphous-silicon solar cells*, STW SAFE meeting, Veldhoven, the Netherlands, 2007 (http://www.stw.nl/NR/rdonlyres/ 35638258-4104-41BE-B8B3-DCB63BF7CBDC/0/vet.pdf).

[286] B. E. Pieters, M. Zeman, R. A. C. M. M. van Swaaij, W. J. Metselaar, *Optimization of a-SiGe:H solar cells with graded intrinsic layers using integrated optical and electronic modeling*, Thin Solid Films, vol. **451–452**, p. 294, 2004 (DOI: 10.1016/j.tsf.2003.11.029).

[287] S. Aljishi, J. D. Cohen, S. Jin and L. Ley, *Band tails in hydrogenated amorphous silicon and silicon-germanium alloys*, Physical Review Letters, vol. **64**, p. 2811, 1990 (DOI: 10.1103/PhysRevLett.64.2811).

[288] K. Winer, *Defects in hydrogenated amorphous silicon*, Annual Review of Materials Science, vol. **21**, p. 1, 1991 (DOI: 10.1146/annurev.ms.21.080191.000245).

[289] F. Sculati-Meillaud, *Microcrystalline silicon solar cells: theory, diagnosis and stability*, PhD thesis, Université de Neuchâtel, 2006 (http://www.unine.ch/web_pvlab/ Publications/Thesis/Thesis_F_Sculati-Meillaud.pdf).

[290] T. k. Chong, J. Wilson, S. Mokkapati, K. R. Catchpole, *Optimal wavelength scale diffraction gratings for light trapping in solar cells*, Journal of Optics, vol. **14**, 024012, 2012 (DOI: 10.1088/2040-8978/14/2/024012).

[291] S. E. Han, G. Chen, *Toward the Lambertian Limit of Light Trapping in Thin Nanostructured Silicon Solar Cells*, Nano Letters, vol. **10**, p. 4692, 2010 (DOI: 10.1021/nl1029804).

[292] K. Söderström, G. Bugnon, F.-J. Haug, S. Nicolay and C. Ballif, *Experimental study of flat light-scattering substrates in thin-film silicon solar cells*, Solar Energy Materials & Solar Cells, vol. **101**, p. 193, 2012 (DOI: 10.1016/j.solmat.2012.02.003).

[293] École Polytechnique Fédérale de Lausanne, US/2012/0186642A1.

[294] K. Söderström, G. Bugnon, R. Biron, C. Pahud, F. Meillaud, F.-J. Haug and C. Ballif, *Thin-film silicon triple-junction solar cell with 12.5% stable efficiency on innovative flat light-scattering substrate*, Applied Physics Letters, vol. 112, 114503, 2012 (DOI: 10.1063/1.4768272).

[295] O. Isabella, A. H. M. Smets and M. Zeman, *Thin-Film Silicon-Based Quadruple Junction Solar Cells with Efficiency Beyond 20%*, MRS Proceedings, *to be presented in April 2013*.

Samenvatting

Zonne-energie kan voldoen aan de energiebehoefte van de mens en een meer evenwichtige verdeling van de primaire energiebronnen veiligstellen. Momenteel domineren zonnecellen gebaseerd op wafers en dunne lagen van silicium de fotovoltaïsche markt, omdat silicium een niet toxisch is en veel voorkomt en omdat hoge conversierendementen gerealiseerd kunnen worden met op silicium gebaseerde zonnecellen. Om concurrerend te kunnen blijven met zonneceltechnologieën gebaseerd op dunne lagen of bulk kristallijn silicium, moeten zonnecellen van dunne silicium lagen een conversierendement van 20% op laboratorium-schaal behalen. Dit in ogenschouw nemende zijn lichtmanagementtechnieken essentieel om het rendement van zulke zonnecellen te verhogen, zodat de energie van de zonnestraling effectief gebruikt wordt, de absorptie in de absorberende lagen gemaximaliseerd wordt en de optische verliezen geminimaliseerd worden.

Van de verschillende lichtmanagementtechnieken die gepresenteerd worden in **Hoofdstuk 2**, is met name lichtopsluiting belangrijk voor het fabriceren van dunnere cellen met een hoog rendement en een stabiele prestatie. Het eenvoudigste lichtopsluitingsschema wordt gegeven door de willekeurige textuur van interne oppervlakken gekoppeld met een efficiënte achterreflector. Het doel van dit proefschrift is om nieuwe textuurtypes en achterreflectors te introduceren, analyseren, modelleren en toe te passen in experimentele zonnecellen. Na **Hoofdstuk 3**, waarin depositietechnieken, meetopstellingen en modelleergereedschappen worden geïntroduceerd en besproken, zal de lezer een serie thematische hoofdstukken aantreffen waar respectievelijk in detail zal worden ingegaan op periodieke diffractietralies en gemoduleerde oppervlaktetexturen als lichtverstrooiers, en diëlektrische gedistribueerde Braggreflectors en Afgevlakte Lichtverstrooiingssusbstraten als efficiënte achterreflectors.

In **Hoofdstuk 4** worden transparante rechthoekachtige 1-D periodieke tralies beschreven die werden gebruikt als *hoekselectieve* verstrooiingssubstraten in *pin* zonnecellen. Deze tralies werden zowel morfologisch als optisch gekarakteriseerd. Door gebruik te maken van het Harvey-Shack verstrooiingsmodel werd vastgesteld dat de geometrische parameters en de vorm van zulke tralies een belangrijke rol spelen bij lichtverstrooiing. Hierna werden zulke 1-D tralies voor het eerst ingezet bij de fabricatie van *pin* enkele-junctie a-Si:H zonnecellen. Deze cellen leverden een tot +13.4% hogere kortsluitstroomdichtheid dan de zonnecel met vlakke oppervlakken en vertoonden, voor golflengtes langer dan 550 *nm*, een spectrale respons die lichtelijk hoger was dan die van de zonnecel gedeponeerd op een willekeurig getextureerd substraat dat gebruikt is als referentie. Om optimale combinaties te kunnen vinden van de periode en de hoogte van de rechthoekachtige 1-D tralies en om het

potentieel van 2-D tralies te verkennen, werd gebruik gemaakt van 3-D optische modellen. Zonnecelstructuren op 1-D (2-D) tralietexturen met verschillende periodes en hoogtes werden gesimuleerd. De beste combinaties leidden tot een procentuele toename van +25.5% (+32.5%) in kortsluitstroomdichtheid ten opzichte van de vlakke cel. Binnen het raamwerk van golfgeleidertheorie laat dit resultaat zien dat zonnecellen op 2-D tralies optisch beter kunnen zijn dan willekeurige texturen gebaseerd op hetzelfde transparante geleidende oxide. De recente mogelijkheid om textuur aan te brengen in transparante substraten over grote oppervlakken opent de weg naar industriële optimalisatie van zonnecellen van dunne lagen van silicium op periodieke tralies.

In **Hoofdstuk 5** wordt het aanbrengen van gemoduleerde oppervlaktetexturen geïntroduceerd voor efficiënte lichtverstrooiing bij lange golflengtes voor multi-junctie zonnecel-toepassingen. Gebaseerd op de combinatie van twee of meerdere klassen van texturen op hetzelfde substraat baant dit concept de weg voor het realiseren van texturen die een verhoogde breedbandige lichtverstrooiing bewerkstelligen. Verschillende types van gemoduleerde oppervlaktetexturen werden gefabriceerd op geëtst glas, op 1-D tralies en op geëtste wafers van polykristallijn silicium. De mogelijkheid om de optische eigenschappen te optimaliseren door de oppervlaktetextuur te manipuleren, werd aangetoond door dezelfde natte etsprocessen te gebruiken. Zonnecellen met een enkele junctie gedeponeerd op zulke gemoduleerde oppervlaktetexturen hadden initile conversierendementen tot 9.74% en vertoonden een zeer goede opbrengst ondanks de zeer grote oppervlakteruwheid. Uit deze experimenten kon de beste gemoduleerde oppervlaktetextuur worden geselecteerd, namelijk een combinatie van geëtst glas met grote facetten op micrometerschaal en geëtst ZnO:Al met facetten op nanometerschaal. Hetzelfde type geëtst glas bedekt met getextureerd ZnO:B werd gebruikt als substraat voor de fabricatie van een tandem micromorf silicium zonnecel bij IMT-PVLAB (Zwitserland). Het resultaat was een state-of-the-art zonnecel (11.6% initieel conversierendement) waar de herverdeling van de lichtabsorptie tussen de bovenste en onderste cel gepaard ging met een breedbandige toename in de (rode) spectrale respons. Gegeven zulke conceptuele bewijzen zal de volgende stap de implementatie zijn van gerepliceerde gemoduleerde oppervlaktetexturen bedekt met zwak absorberende transparante geleidende vooroxides voor drievoudige-junctie zonnecellen.

In **Hoofdstuk 6** worden Gedistribueerde Braggreflectors bestudeerd als diëlektrische spiegels voor toepassing in zonnecellen van dunne lagen van silicium. Fysieke eigenschappen zoals de fotonische bandafstand, conditie van omni-directionaliteit en modulatie worden geanalyseerd en praktische regels voor passend ontwerp worden geëvalueerd. Gedistribueerde Braggreflectors gebaseerd op paren van a-SiN$_x$:H en a-Si:H en geoptimaliseerd voor hoge interne reflectie in zonnecellen werden ontworpen door gebruik te maken van geavanceerde optische modellen. Daarna, door gebruik te maken van een continu plasma-geassisteerd proces bij lage temperatuur, werden deze spiegels gefabriceerd, optisch gekarakteriseerd en uiteindelijk gebruikt aan de achterzijde van vlakke of getextureerde enkele-junctie zonnecellen. Door middel van spectrale en elektrische metingen werd vastgesteld dat zonnecellen met Gedistribueerde Braggreflectors even goed presteerden als de referentiecellen met zilverreflector. Toekomstige studies op deze dilektrische spiegels zullen zich richten op twee hoofddoelen: het gebruik van omni-directionaliteit en modulatieconcepten voor multi-junctie applicaties, en de toepassing van patroonmethodes die geen ge-

bruik maken van fotolithografie.

In **Hoofdstuk 7** worden Afgevlakte Lichtverstrooiingssusbstraten geoptimaliseerd voor hoog-rendement enkele-, dubbele en drievoudige-junctie zonnecellen. Dit type substraat, gebaseerd op 2-D fotonische kristallen zoals voorgesteld door AIST (Japan), is specifiek ontwikkeld voor een efficiënte en diffuse interne reflectie bij lange golflengtes, en voor de depositie van nc-Si:H van hoge kwaliteit. De studie was gebaseerd op een hybride opto-elektrisch model dat het mogelijk maakte om zowel de optische situatie als de elektrische prestatie van multi-junctie zonnecellen van dunne lagen van silicium efficiënt te simuleren. Een potentieel initieel conversierendement van 11.6%, 14.2% en 16.0% werd gerapporteerd voor respectievelijk enkele-, dubbele- en drievoudige-junctie zonnecellen op de geoptimaliseerde Afgevlakte Lichtverstrooiingssubstraten. Verdere studies op dit onderwerp zullen het modelleren van asymmetrische 2-D fotonische kristallen, het gebruik van zwak absorberende ondersteunende materialen en toepassingen in multi-juncties met tussenreflectors behelzen.

Olindo Isabella,

Delft, Januari 2013

Summary

Solar energy can fulfil mankind's energy needs and secure a more balanced distribution of primary sources of energy. Wafer-based and thin-film silicon solar cells dominate todays' photovoltaic market because silicon is a non-toxic and abundant material and high conversion efficiencies are achieved with silicon-based solar cells. To stay competitive with bulk crystalline silicon and other thin-film solar cell technologies, thin-film silicon solar cells have to achieve a conversion efficiency level of 20% on a laboratory scale. In this respect, light management techniques are essential for enhancing the efficiency of such solar devices since the energy of solar radiation is effectively used, absorption in the absorber layers is maximized and optical losses are minimized.

Among several light management techniques presented in **Chapter 2**, light trapping is especially important for fabricating thinner cells with high efficiency and stable performance. The most basic light trapping scheme is given by the random texture at internal interfaces coupled with an efficient back reflector. The aim of this doctoral thesis is to introduce, analyse, model and employ in real solar devices novel types of textures and back reflectors. After **Chapter 3**, in which deposition techniques, characterization setups and modelling tools are introduced and discussed, four thematic chapters are reported. They are focussed, respectively, on periodic diffraction gratings and modulated surface textures as light scatterers, and dielectric distributed Bragg reflectors and Flattened Light-Scattering Substrates as efficient rear reflectors.

In **Chapter 4**, transparent rectangular-like 1-D periodic gratings that were used as *angle-selective* scattering substrates in *pin* solar cells are described. These gratings were characterized from both morphological and optical perspectives. By making use of the Harvey-Shack scattering model, it was found that the geometrical parameters and the shape of such gratings play a considerable role in light scattering. Afterwards, such 1-D gratings were for the first time employed in the fabrication of *pin* single junction a-Si:H solar cells. These devices delivered up to +13.4% higher short-circuit current density than the solar cell with flat interfaces and exhibited, for wavelengths longer than 550 *nm*, a spectral response slightly higher than that of the solar cell deposited on the reference randomly-textured substrate. In order to find an optimal combination of period and height of rectangular-like 1-D gratings, and to explore the potential of 2-D gratings, 3-D optical modelling was employed. Solar-cell structures on 1-D (2-D) grating textures with different periods and heights were simulated. The best combinations led to a percentage increase of +25.5% (+32.5%) in the short-circuit current density with respect to the flat cell. In the framework of wave guide theory, this

result indicates that solar cells on 2-D gratings can be optically better than random textures based on the same transparent conductive oxide. The recent possibility to texture transparent substrates over large areas opens the way for the industrial optimization of thin-film silicon solar cells on periodic gratings.

In **Chapter 5**, modulated surface texturing is introduced for efficient light scattering at long wavelengths for multi-junction solar-cell applications. Based on the combination of two or more classes of textures on the same substrate, this concept paves the way for the realization of textures showing increased broadband light scattering. Different types of modulated surface textures were fabricated on etched glass, on 1-D gratings and on etched polycrystalline silicon wafers. The possibility to optimize the optical performance by manipulating the surface texturing was demonstrated by using wet etching processes. Single junction solar cells deposited on such modulated surface textures showed initial conversion efficiencies up to 9.74% and exhibited very good yield despite severe surface roughness. From these experiments, the best modulated surface texture could be selected, namely a combination of etched glass with large micrometer-scale features and etched ZnO:Al with nanometer-scale features. The same type of etched glass coated with textured ZnO:B was used as substrate for the fabrication of a tandem micromorph silicon device at IMT-PVLAB (Switzerland). The result was a state-of-the-art solar cell (11.6% initial conversion efficiency), where the redistribution of the light absorption between top and bottom cell occurred with a broadband increase in the (red) spectral response. Given such proofs of concept, the next step will be implementation of replicated modulated surface textures coated with low absorption front transparent conductive oxide for triple junction solar cells.

In **Chapter 6**, Distributed Bragg reflectors are studied as dielectric mirrors for thin-film silicon solar-cells applications. Physical properties like photonic band gap, condition of omni-directionality and modulation were analysed and practical rules for appropriate design were reviewed. Distributed Bragg reflectors based on pairs of a-SiN$_x$:H and a-Si:H and optimized for high internal reflectance in solar cells were designed employing advanced optical modelling. Afterwards, using a continuous plasma-assisted process at low temperature, these mirrors were fabricated, optically characterized and finally applied at the rear side of flat and textured single junction solar cells. From spectral and electrical measurements, solar cells with Distributed Bragg reflectors performed as well as the reference cells with Ag reflector. Future studies on these dielectric mirrors will focus on two main objectives: the concurrent usage of omni-directionality and modulation concepts for multi-junction applications and the development of patterning methods that do not make use of photolithography.

In **Chapter 7**, Flattened Light Scattering Substrates are optimized for high efficiency single, double and triple junction solar cells. This type of substrate, based on 2-D photonic crystals proposed by AIST (Japan), is specifically developed for effective diffuse internal reflectance at long wavelengths and for deposition of high quality nc-Si:H. The study was based on a hybrid opto-electrical model that allowed to efficiently simulate both the optical situation and the electrical performance of thin-film multi-junction silicon solar cells. A potential initial conversion efficiency of 11.6%, 14.2%, and 16.0% for single, double, and triple junction solar cells on the optimized Flattened Light Scattering Substrates, respec-

tively, was reported. Further studies on this matter will involve the modelling of asymmetric 2-D photonic crystals, usage of low-absorption supporting materials and application in multi-junctions with intermediate reflectors.

Olindo Isabella,

Delft, January 2013

List of Publications

Peer-reviewed papers

1. **O. Isabella**, H. Sai, M. Kondo and M. Zeman, *Full-wave opto-electrical modeling of optimized Flattened Light-Scattering Substrate for high efficiency thin-film silicon solar cells*, Progress in Photovoltaics: Research and Applications, 2013 (DOI: 10.1002/pip.2314).

2. **O. Isabella**, S. Solntsev, D. Caratelli, M. Zeman, *3-D optical modeling of thin-film silicon solar cells on diffraction gratings*, Progress in Photovoltaics: Research and Applications, vol. **21**, p. 94, 2013 (DOI: 10.1002/pip.1257).

3. S. Solntsev, **O. Isabella**, D. Caratelli and M. Zeman, *Thin-Film Silicon Solar Cells on 1-D Periodic Gratings With Nonconformal Layers: Optical Analysis*, IEEE Journal of Photovoltaics, vol. 3, p. 46, 2013 (DOI: 10.1109/JPHOTOV.2012.2220123).

4. M. Zeman, **O. Isabella**, K. Jäger, R. Santbergen, S. Solntsev, M. Topič and J. Krč, *Advanced Light Management Approaches for Thin-Film Silicon Solar Cells*, Energy Procedia, vol. **15**, p. 189, 2012 (DOI: 10.1016/j.egypro.2012.02.022).

5. K. Jäger, **O. Isabella**, R. A. C. M. M. van Swaaij and M. Zeman, *Angular resolved scattering measurements of nano-textured substrates in a broad wavelength range*, Measurement Science and Technology, vol. **22**, 105601, 2011 (DOI: 10.1088/0957-0233/22/10/105601).

6. **O. Isabella**, S. Dobrovolskiy, G. Kroon and M. Zeman, *Design and application of dielectric distributed Bragg back reflector in thin-film silicon solar cells*, Journal of Non-Crystalline Solids, vol. 358, p. 2295, 2012 (DOI: 10.1016/j.jnoncrysol.2011.11.025).

7. **O. Isabella**, S. Solntsev, D. Caratelli and M. Zeman, *3-D optical modeling of single and multi-junction thin-film silicon solar cells on gratings*, MRS Proceedings, vol. **1426**, 2012 (DOI: 10.1557/opl.2012.897).

8. J. Sap, **O. Isabella**, K. Jäger and M. Zeman, *Extraction of physical properties of surface textured transparent conductive oxides using variable angle spectroscopy*, Thin Solid Films, vol. 520, p. 1096, 2011 (DOI: 10.1016/j.tsf.2011.08.023).

9. S. Solntsev, **O. Isabella**, D. Caratelli, M. Kyriakou, O. Yarovyi and M. Zeman, *Advanced Optical Modeling of Thin-film Silicon Solar Cells with 1-D Periodic Gratings*, MRS Proceedings, vol. **1322**, 2011 (DOI: 10.1557/opl.2011.1298).

10. M. Zeman, **O. Isabella**, K. Jäger, P. Babal, S. Solntsev, R. Santbergen, *Modeling of Advanced Light Trapping Approaches in Thin-Film Silicon Solar Cells*, MRS Proceedings, vol. **1321**, 2011 (DOI: 10.1557/opl.2011.955).

11. **O. Isabella**, P. Liu, B. Bolman, J. Krč and M. Zeman, *Modulated surface-textured substrates with high haze for thin-film silicon solar cells*, MRS Proceedings, vol. **1321**, 2011 (DOI: 10.1557/opl.2011.945).

12. B. Lipovšek, J. Krč, **O. Isabella**, M. Zeman and M. Topič, *Modeling and optimization of white paint back reflectors for thin-film silicon solar cells*, Journal of Applied Physics, vol. **108**, 103115, 2010 (DOI: 10.1063/1.3512907).

13. **O. Isabella**, J. Krč and M. Zeman, *Modulated surface textures for enhanced light trapping in thin-film silicon solar cells*, Applied Physics Letters, vol. **97**, 101106, 2010 (DOI: 10.1063/1.3488023).

14. M. Zeman, **O. Isabella**, K. Jäger, R. Santbergen, R. Liang, S. Solntsev and J. Krč, *Advanced Light Trapping in Thin-film Silicon Solar Cells*, MRS Proceedings, vol. **1245**, 2010 (DOI: 10.1557/PROC-1245-A03-03).

15. A. Čampa, **O. Isabella**, R. van Erven, P. Peeters, H. Borg, J. Krč, M. Topič and M. Zeman, *Optimal design of periodic surface texture for thin-film a-Si:H solar cells*, Progress in Photovoltaics: Research and Applications, vol. **18**, p. 160, 2010 (DOI: 10.1002/pip.940).

16. **O. Isabella**, F. Moll, J. Krč and M. Zeman, *Modulated surface textures using zinc-oxide films for solar cells applications*, Phys. Status Solidi A, vol. **207**, p. 642, 2010 (DOI: 10.1002/pssa.200982828).

17. B. Lipovšek, J. Krč, **O. Isabella**, M. Zeman and M. Topič, *Analysis of thin-film silicon solar cells with white paint back reflectors*, Physica Status Solidi C, vol. **7**, p. 1041, 2010 (DOI: 10.1002/pssc.200982701).

18. M. Zeman, **O. Isabella**, F. D. Tichelaar and S. L. Luxembourg, *Amorphous silicon-based multilayers for photovoltaic applications*, Physica Status Solidi C, vol. **7**, p. 1057, 2010 (DOI: 10.1002/pssc.200982881).

19. K. Jäger, **O. Isabella**, L. Zhao and M. Zeman, *Light scattering properties of surface-textured substrates*, Physica Status Solidi C, vol. **7**, p. 945, 2010 (DOI: 10.1002/pssc.200982695).

20. **O. Isabella**, B. Lipovšek, J. Krč and M. Zeman, *Photonic crystals back reflectors in thin-film silicon solar cells*, MRS Proceedings, vol. **1153**, 2009 (DOI: 10.1557/PROC-1153-A03-05).

Contributions to books

- M. Zeman, O. Isabella, S. Solntsev and K. Jäger, *Design of Advanced Surface Textures for Thin-Film Silicon Solar Cells Using Computer Modelling*, Editor prof. Konagai, Tokyo Institute of Technology, Tokyo, Japan, 2013 (accepted for publication).

Proceedings papers, extended abstracts, technical digests

1. A. Ingenito, **O. Isabella** and M. Zeman, *Accurate opto-electrical modeling of multicrystalline silicon wafer-based solar cells*, 27th European Photovoltaic Solar Energy Conference and Exhibition, p. 1208, Frankfurt, Germany, September 2012 (DOI: 10.4229/27thEUPVSEC2012-2AV.6.8).

2. **O. Isabella**, H. Sai, M. Kondo and M. Zeman, *Optical modeling and optimization of Flattened Light-Scattering Substrate for thin-film silicon solar cells*, 38th IEEE Photovoltaic Specialist Conference, p. 3024, Austin, U.S.A., June 2012 (DOI: 10.1109/PVSC.2012.6318220).

3. **O. Isabella**, C. Battaglia, C. Ballif and M. Zeman, *Modulated surface-textured substrates based on etched glass for single junction and tandem micromorph thin-film silicon solar cells*, 21st International Photovoltaic Science and Engineering Conference November, ID 605, p. 1, Fukuoka, Japan, December 2011.

4. **O. Isabella**, P. Liu, B. Bolman, J. Krč, A. H. M. Smets and M. Zeman, *Modulated Surface-textured substrates with high haze: from concept to application in thin-film silicon solar cells*, 37th IEEE Photovoltaic Specialist Conference, p. 616, Seattle, U.S.A., June 2011 (DOI: 10.1109/PVSC.2011.6186029).

5. K. Jäger, **O. Isabella**, R. Santbergen, R. A. C. M. M. van Swaaij and M. Zeman, *Light Trapping in Thin-Film Silicon Solar Cells*, Colloquien der Optischen Spektrometrie (COSP), Berlin, Germany, March 2011.

6. **O. Isabella**, M. Zeman, J. Krč and M. Topič, *Advanced Light Trapping Techniques for Thin-Film Silicon Solar Cells*, 25th European Photovoltaic Solar Energy Conference and Exhibition, p. 3273, Valencia, Spain, September 2010 (DOI: 10.4229/25th EUPVSEC2010-3AV.2.44).

7. J. A. Sap, **O. Isabella** and M. Zeman, *Extraction of physical properties of transparent conductive oxides using variable angle spectroscopy*, STW Safe Workshop, Veldhoven, the Netherlands, november 2009.

8. **O. Isabella**, J. Kr, M. Zeman, *Application of Photonic Crystals as Back Reflectors in Thin-Film Silicon Solar Cells*, 24th European Photovoltaic Solar Energy Conference and Exhibition, p. 2304, Hamburg, Germany, September 2009 (DOI: 10.4229/24th EUPVSEC2009-3BO.9.5).

9. B. Vet, B. Grancic, **O. Isabella**, S. Solntsev and M. Zeman, *Optical and Electrical Simulations of Advanced Silicon Based Solar Cell Devices*, 24th European Photovoltaic Solar Energy Conference and Exhibition, p. 2682, Hamburg, Germany, September 2009 (DOI: 10.4229/24thEUPVSEC2009-3AV.2.35).

10. A. J. M. van Erven, J. Rutten, G. van der Hofstad, H. de Groot, P. Peeters, J. De Ruijter, H. Borg, S. Solntsev, **O. Isabella**, M. Zeman, G. Rajeswaran and R. Arya, *Periodic Texturing of Thin Film Silicon Solar Cell Superstrates*, 24th European Photovoltaic Solar Energy Conference and Exhibition, p. 2668, Hamburg, Germany, September 2009 (DOI: 10.4229/24thEUPVSEC2009-3AV.2.31).

11. M. Zeman, G. van Elzakker, P. Šutta, **O. Isabella** and J. Krč, *Thin-film silicon solar cells: stability and light trapping*, M I D E M 2 0 0 9 - International Conference on Microelectronics, Devices and Materials and the Workshop on Advanced Photovoltaic Devices and Technologies, Postojna, Slovenia, September 2009.

12. B. Lipovšek, J. Krč, **O. Isabella**, M. Zeman and M. Topič, *Analysis of back TCO/white paint concept in thin-film silicon solar cells*, 6th International Symposium on Transparent Oxide Thin Films for Electronics and Optics, Tokyo, Japan, April 2009.

13. **O. Isabella**, K. Jäger, J. Krč and M. Zeman, *Light scattering properties of surface-textured substrates for thin-film solar cells*, STW Safe Workshop, Veldhoven, the Netherlands, November 2008.

14. R. van Erven, R.H. Franken, J. de Ruijter, P. Peeters, W. Vugts, **O. Isabella**, M. Zeman, C. Haase, U. Rau and H. Borg, *Controlled Texturing of Thin Film Silicon Solar Cell Substrates*, 23rd European Photovoltaic Solar Energy Conference and Exhibition, p. 2096, Valencia, Spain, September 2008 (DOI:10.4229/23rdEUPVSEC2008-3CO.9.4).

15. **O. Isabella**, A. Čampa, M. Heijna, W. J. Soppe, R. van Erven, R. H. Franken, H. Borg and M. Zeman, *Diffraction gratings for light trapping in thin-film silicon solar cells*, 23rd European Photovoltaic Solar Energy Conference and Exhibition, p. 2320, Valencia, Spain, September 2008 (DOI: 10.4229/23rdEUPVSEC2008-3AV.1.48).

Invited Lectures

1. *Advanced light trapping techniques for thin-film silicon solar cells*, National Institute of Advanced Industrial Science and Technology (AIST), Tsukuba, Japan, 29th of August 2011.

2. *Advanced light trapping techniques for thin-film silicon solar cells*, Institut für Physikalische Elektronik, Stuttgart, Germany, 20th of June 2011.

3. *Advanced light trapping techniques for thin-film silicon solar cells*, ENEA Portici Research Center, Portici, Italy, 28th of September 2010.

4. *Solar cells, basic principles and main technologies*, University of Naples Federico II, Naples, Italy, 3rd of June 2009.

Acknowledgements

want to especially mention dr. Wim Soppe, dr. Maurits Heijna, dr. Edward Amers, dr. Jan Ammerlaan, dr. Herman Borg, Rob van Erven and Harry de Groot for having been such good partners. I enjoyed your company, learnt from our discussions, exulted for your own achievements.

After the end of my PhD project, I spent one year at the National Institute of Advanced Industrial Science and Technology, Tsukuba (Japan), in the laboratory of prof. dr. Michio Kondo. That was an experience I will conserve for all my life. I found there great colleagues and great men. I want to especially thank prof. dr. Michio Kondo, dr. Kenji Yamamoto, dr. Kimihiko Saito, dr. Takuya Matsui, dr. Takashi Suezaki, dr. Takashi Koida and all other staff members of PVTEC, AIST and Kaneka both in Tsukuba and Osaka. Special gratitude goes to dr. Adrien Bidiville who corrected the very first version of my dissertation and used to prepare the craziest ice creams ever. Thank you very much. A special mention goes to dr. Hitoshi Sai who let me to work on his FLiSS concept. We had a slow start, but I really enjoyed working with you and I am looking forward to cooperate with you again. During my stay in Japan, I met many people who supported me during the somewhat frustrating time which is writing the PhD thesis. Giancarlo, Stefania, Enrico, Alessio e Daniele: *Vi voglio troppo bene!* Ron, Aurélie, Yu, Yoshina, Alma: *Finally, I did it!*

Continuing with past and ongoing collaborations, I want to deeply thank Benjamin Lipovišek and prof. dr. Marko Topič from Univeristy of Ljubljana for the work done together on white paints, dr. Diego Caratelli from Delft University of Technology for the work on optical modelling done together, dr. Corsin Battaglia for having processed micromorph tandem solar cells on my etched glass substrates when still working at IMT PV-LAB (*sooner or later I shall offer you a beer!*) and Ali Naqavi for the work we have done so far in 3-D optical modeling. Finally, I want also to thank dr. Franz-Josef Haug for being such a good scientist. I thank you for teaching me always something new during our discussions!

My last year as PhD candidate was a bureaucratic jungle. I could not make it without the help of PVMD group and DIMES secretaries: you are perfect! Especially, I want to thank Laura Bruns, Marian Roozenburg-de Bree and Marysia Lagendijk-Korzeniewski for their quick reactions and problem solving attitude. Also previous years of my PhD were a jungle but rather technological. In this respect I am grateful that Martijn Tijssen and Stefaan Heirman work at PVMD group. You guys are awesome, thank you for helping me with deposition and measurement tools. I thank also Kasper Zwetsloot and Jan Chris Staalenburg for their efforts on ICT side. My experiments were carried out in Dimes Technology Center, where I met many really good people. I thank ALL OF YOU for running a complex system like a clean room environment. Especially I acknowledge Cassan Visser, Johan van der Cingel, Jan Cornelis Wolff, Mario Laros, Wim van der Vlist, Hugo Schellevis and Charles de Boer for the experiments or measurements they helped me to carry out.

I have had the honour and pleasure to work with many bright scientists at PVMD group. First of all, I want to thank my office mates for the good time shared together: Bas Vet, dr. Gijs van Elzakker, Jimmy Melskens, Joke Westra and Pavel Babal. I wish you all the best with your careers and your life. Especially, thank you, Bas, for having explained to me tips and tricks in thin-film silicon solar cells processing and thank you, Jimmy, for translating

Curriculum vitae

Olindo Isabella was born on the 12th of November 1979 in Naples (Italy). In May 2007 he received the M.Sc. degree in electronics engineering from the University of Naples Federico II. In September 2007 he joined the Faculty of Electrical Engineering, Mathematics and Computer Science at Delft University of Technology, Delft (the Netherlands), where he pursued the PhD degree within the Photovoltaic Materials and Devices group under the supervision of prof. dr. M. Zeman. During his PhD, he was visiting researcher at the National Institute of Advanced Industrial Science and Technology, Tsukuba (Japan), in the laboratory of prof. dr. M. Kondo. His areas of expertise are advanced light management techniques for thin-film and wafer-based silicon solar cells. He worked on the angle-selective scattering at periodically textured interfaces and fabricated the first solar cells on transparent periodic gratings. For this achievement he earned the best poster award during the 23rd EU-PVSEC (Spain, 2008). Next, he developed the wide-band scattering at Modulated Surface Textures. He presented this concept and its evolutions at ICANS23 (the Netherlands, 2009), MRS Spring meeting (U.S.A., 2011), 37th IEEE PVSC (U.S.A., 2011) and 21st PVSEC (Japan, 2011). He also studied highly reflective and wavelength-selective structures based on metal-free photonic crystals and manufactured photonic metal-free solar cells, showing for the first time state-of-the-art spectral and electrical performance. These results were presented at ICANS24 (Japan, 2011). Finally, by combining periodic gratings and photonic crystal-like-structures, he optimized the concept of Flattened Light-Scattering Substrate for high quality absorber layers and highly efficient solar cells. For this work he won the best student award at the 27th EU-PVSEC (Germany, 2012).